An Infrared Study of Galaxy Evolution

by

Karl Glazebrook

Presented for the Degree of Doctor of Philosophy
at the University of Edinburgh, 1991.

This thesis is solely my own composition, except where specifically indicated in the text.

July, 1991.

ABSTRACT

This thesis describes a large-area 2μm survey undertaken on the U.K. Infrared Telescope in Hawaii, using a new infrared imaging camera. The survey covers $594\Box'$ and is complete and uniform to a limit of K = 17. The main aim of the survey was to construct a sample of galaxies, selected by their 2μm flux, for studies of galaxy evolution. The subsidiary aim was to survey the 2μm Universe and search for any new populations of infrared objects, such as protogalaxies and brown dwarf stars.

The first half of this thesis is concerned with the analysis of astronomical data. The detailed methods for constructing the infrared survey are described, including flatfielding, astrometry, mosaicing and photometry. Also described are optical CCD observations which cover the survey area to provide optical-infrared colours of almost all the objects in the sample. The methods of reducing, calibrating and matching the CCD data with the infrared data are detailed. For the study of galaxy evolution the redshifts of 53 K band selected galaxies, with a well defined completeness, were measured using multiple object spectrographs. The reduction of the spectra and the methods used for securing the redshifts, including the cross-correlation technique, are described.

The second half of this thesis is about the scientific results from this survey. Firstly, it appears that no new large populations of objects appear, in particular there appear to be no objects *only* detected in K. A few extremely red objects objects are found, however their true nature is unclear in the absence of spectra. The best evidence is that a few of them are very cool stars. Secondly the galaxy population appears to have very red R – K colours, although not necessarily so red in B – K, and the K band number-magnitude counts exhibit a much smaller excess over the no-evolution prediction than do the B band optical counts. The K band counts are consistent with only a small amount of luminosity evolution.

It is possible to reconcile the B counts, K counts, and the colours of the galaxies, by introducing a model of galaxy merging in which galaxy numbers per unit volume are no longer conserved with lookback time. This model naturally predicts the surprisingly low redshifts found by other workers in B band selected redshift surveys. This model also predicts that the mean redshift of a K selected survey should be *less* than the no-evolution prediction. This is indeed found — the redshift distribution for the sample studied here is less than the no-evolution model at the 5% significance level.

Finally the limitations of this survey are reviewed, and the prospects for future deep infrared and spectroscopic surveys discussed.

To my parents

Just remember you are standing on a planet that's evolving
and revolving at 900 miles an hour,
That's orbiting at 19 miles a second, so it's reckoned,
a Sun that is the source of all our power.

The Sun, and you and me, and all the stars that we can see
are moving at a million miles a day*,
In an outer spiral arm at 40,000 miles an hour*
of the galaxy they call the Milky Way.

Our Galaxy itself contains a hundred billion stars
it's a hundred thousand light years side to side,
It bulges in the middle 16,000 light years thick
but out by us it's just 3000 light years wide.

We're 30,000 light years from Galactic central point
we go round every 200 million years,
And our Galaxy is only one of millions of billions
in this amazing and expanding Universe.

The Universe itself keeps on expanding and expanding
in all of the directions it can whizz,
As fast as it can go, the speed of light you know
12 million miles a minute and that's the fastest speed there is.

So remember when you're feeling very small and insecure
how amazingly unlikely is your birth
And pray that there's intelligent life somewhere up in space
'cause there's bugger all down here on earth!

---

* More like 600,000 miles an hour and 15 million miles a day!

TABLE OF CONTENTS

1 INTRODUCTORY REMARKS

We live in a dynamic, evolving universe. As a science extra-galactic astronomy is only 70 years old, but despite this relatively short temporal baseline it is possible to observe the evolution of galaxies in the Universe directly. With modern telescopes and instrumentation we can study galaxies over large cosmological distances. Due to the finite speed of light we see them as they were when the Universe was only a fraction of its present age.

Apart from rare classes of active galaxies, such as radio galaxies, Seyfert galaxies and quasars, the bulk of a galaxy's luminosity comes either directly from stars or from starlight reradiated from gas or dust. Historically the most detailed information about stellar populations has come from studies in optical light (3000–8000 Å), not because this is necessarily the best part of the spectrum for such studies, but because of the practical constraints of detector technology and atmospheric transmission.

The work presented in this thesis describes one of the first attempts at a systematic study of faint galaxies at cosmological distances in the near-infrared spectral window, more specifically at a wavelength of 2 μm. This was made possible by the development of infrared array detectors which allow a large area of sky to be surveyed quickly and galaxies to be *selected* by their infrared flux. Stellar luminosity is a steep function of temperature and in the optical galaxy light is dominated by the youngest, hottest stars. Conversely in the infrared the light comes mainly from much older and cooler stars. Thus this survey complements evolutionary studies in the optical because one is observing different stellar populations. By comparing evolution in the optical and infrared it is possible to investigate the nature of observed evolution.

Number-magnitude and number-redshift counts of faint galaxies have historically been one of the classical tools of cosmology, their use was pioneered by Hubble & Tolman in 1935. In principle the counts can be used to measure how the volume of space scales with redshift, this gives the curvature of space and hence the cosmic density (see below). In practice this is difficult because of the effect of galaxy evolution with redshift. However if counts of galaxies could be made in a band insensitive to evolution, such as the near-infrared, then this technique could be revived.

Such a survey also presents the possibility of serendipitous discovery of new classes of objects, which could be absent or very faint in the optical. For example it might be possible to detect the first galaxies in the process of formation. If these were formed sufficiently early in the universe then the light from their young stars would be so redshifted that most of it would emerge in the infrared. Another possibility is the discovery of very cool brown dwarf stars, objects too cool for main sequence nuclear combustion. These and other objects can be selected by searching the survey for objects with very red optical-infrared colours and then followed up, either via further photometry or spectroscopy, to reveal their true nature.

1.1 The Big Bang Cosmology and Galaxy Formation

It is useful at this point to mention briefly the issues which are now considered important in cosmology and review the currently accepted paradigm, as this forms an implicit background to the rest of the thesis. For a more detailed review of cosmological models and standard Big Bang cosmology the reader is referred to Weinberg (1972) and Gunn *et al.* (1978). A good review of galaxy formation models, dark matter and inflation is given by Efstathiou and Silk (1983) and a more recent book by Kolb & Turner (1990). Also White (1989) gives a useful overview of the Big Bang cosmology, cosmological tests and Dark Matter.

The deepest assumption behind current descriptions of the Universe is the "Copernican Principle" which states that our Galaxy is at no special place in the Universe and that the view from any other galaxy would look very much the same. If the Universe appears isotropic to all such observers then it follows that it must be homogenous. However if it appears the same this does not require homogeneity: it is possible for the galaxy distribution to follow a self-similar fractal pattern in which case the distribution would never become uniform on large-scales.

In fact the best evidence that the Universe is indeed isotropic comes not from studies of the galaxy distribution, but from the smoothness of the microwave background (see below). Given homogeneity and isotropy the spatial geometry of the Universe takes a particularly simple form, described by the Robertson-Walker metric, of a 3D space with constant curvature. Our current picture of the universe follows from two principal observations:

1) **The Universe is expanding.** What were previously called the "starry nebulae" were first established as lying outside our Galaxy in the 1920's when Hubble first measured the distance to the Andromeda nebula. Further measurements of galaxy distances established that their recession velocities, the redshift, was proportional to distance and that the Universe was undergoing a uniform global expansion. This fits in with Einstein's General Theory of Relativity, which when combined with the Robertson-Walker metric (i.e. the uniformity and isotropy assumptions), naturally results in expanding and contracting solutions. The dynamics is governed by Hubble's constant (H_0), giving the rate of expansion at the present time, and the Universe's energy density.

The energy density can be split into 3 components, matter, radiation and vacuum all of which give differing dynamics when dominant. Estimates of the radiation energy density in the microwave background (see below) give values much smaller than the present matter density, all other electromagnetic backgrounds contribute much less. The vacuum energy density is equivalent to the "Cosmological Constant", introduced by Einstein to produce a static Universe before before the expansion of the Universe was established. It is known from the various geometrical tests that matter and vacuum are at least within a factor of 10–100 in energy density (see White 1989), this implies that in natural energy density units of c^7/hG^2 the cosmological constant has a value of $\sim 10^{-122}$. It seems likely that its value is identically equal to zero, and there is no compelling case for introducing it from studies of the geometry. (This issue is touched on again in chapter 5.) This would imply that the Universe is now dominated by matter. The density is usually referred to by the ratio, Ω, of the density of the Universe to the critical density at which gravity will be strong enough to eventually reverse the expansion. The notation Ω_0 refers to Ω at the present epoch.

2) **The Cosmic Microwave Background.** In 1965 Penzias & Wilson discovered that the Universe is filled with a thermal bath of radiation at a temperature of 3 K. This provided the first direct evidence for the Hot Big Bang model of the origin of the Universe in an initial singularity, first suggested by George Gamow in 1948. This background is observed to be remarkably smooth and isotropic. Apart from a dipole caused by the Earth's motion relative to this frame, the latest results (e.g. Readhead *et al.*, 1989, Davies *et al.*, 1987, Smoot *et al.*, 1991) show that any anisotropies are $\lesssim 2 \times 10^{-5}$ from scales of 10′–2° (for fluctuations) up to the *entire* sky (the quadrapole).

This smoothness results in a problem. The radiation originates on a surface of last scattering, at $z \simeq 1000$, where the primordial matter cooled below 4000 K and protons and electrons combined to make hydrogen. At this time the Universe ceased to form a plasma and became optically thin. Applying the standard cosmological models it transpires that at this redshift patches of sky $> 2^\circ$ apart could *never* have been in causal contact at an earlier time, and hence there is no means where they could become isotropic.

Another problem with the standard Big Bang cosmology is the *flatness* problem. It is known that Ω_0 in observed matter is at least greater than ~ 0.01 (see below). However in the standard model the difference of Ω from unity evolves $\propto (1+z)$ at the present time and $\propto (1+z)^2$ in the radiation dominated past. Even if $\Omega = 0.01$ at the present time then by $z = 1000$ $\Omega = 0.9$, at the epoch of nucleosynthesis (see below) $z = 10^8$ giving $|\Omega - 1| \sim 10^{-14}$ and at the Planck time ($\sqrt{hG/c^5} = 10^{-43}$ s) $|\Omega - 1| \sim 10^{-61}$. The problem is that at any natural early timescale, where the initial conditions would be set, Ω has to be fine-tuned very close to unity, regardless of the uncertainties in its present day value. An alternative way of stating the same problem is why is the Universe 10^{61} times older than the natural, Planck time?

These problems, and others, have motivated the two principal cosmological developments of the 1980's — the Inflationary Universe Model (Guth, 1981) and non-baryonic Dark Matter. Inflation assumes that at very early epochs ($\lesssim 10^{-35}$ s) the energy density of the Universe was dominated by the zero-point vacuum energy of some exotic fundamental particle. The resulting equations of motion give an exponential expansion which can inflate a very small initial volume up to produce the entire observed universe now. This explains the large-scale smoothness of the microwave background as the opposite sides of the sky *were* in causal contact in the past with the different time evolution. Inflation also naturally predicts $\Omega = 1$ as the curvature goes exponentially to zero as the universe inflates, irrespective of its pre-inflationary value. Given this, Ω still has to be equal to unity now to avoid having to fine-tune the amount of inflation.

The mass corresponding to the visible light in the universe can be measured by taking galaxy luminosities and fitting to their spectra stellar populations with known mass-to-light ratios. These methods give a density of $\Omega_0 = 0.003h^{-1}$ in stars, introducing the notation $h = H_0/100\,\mathrm{km\,s^{-1}\,Mpc^{-1}}$ which parameterises the present day uncertainty in Hubble's constant ($0.5 < h < 1$, see Rowan-Robinson, 1986, for a detailed discussion).

Galaxies can be weighed directly by their rotation curves (e.g. Sancisi and van Albada, 1987) which gives an estimate $\Omega_0 \lesssim 0.02h^{-1}$ and establishes the presence of at least some dark matter in galaxy haloes.

It is also possible to get an independent estimate of the density of *baryons* in the Universe from Big Bang nucleosynthesis theory. Because the rate of nuclear reactions depends critically on the baryon density, the observed primordial abundances of the light elements deuterium, ^{3}He, ^{4}He and ^{7}Li matches the standard theory only if $0.010 < \Omega_b h^2 < 0.035$ (e.g. Yang *et al.*, 1984). Thus inflation leads us to expect some form of non-baryonic dark matter to make up 95–99% of the Universe.

The actual form of the dark matter is not specified. Many varied candidates from the particle physics zoo have been suggested. However dark matter theories of galaxy formation can be broken down into two principal types, which predict quite different power spectra of primordial fluctuations (Bond *et al.* 1982) and hence large-scale galaxy structure:

1) **Hot Dark Matter.** In this scenario the dark matter is assumed to have a low rest mass and hence be relativistic. One candidate particle would be the neutrino if it had a rest mass of a few eV. This has the merit that at least it is known to exist. Because of the relativistic thermal velocity of the light neutrinos they damp out the formation of small structures and the intial structures which form are large — protoclusters and superclusters forming large pancakes (White, 1986). Then individual galaxies from by fragmentation in a top-down process. This model has serious difficulties in that it makes the Universe excessively inhomogeneous on large scales, of order 10–100 Mpc (White *et al.* 1983) and that it takes a long time for individual galaxies to form ($z_f \lesssim 2$), which is difficult to reconcile with the observed existence of quasars and radio-galaxies at $z \gtrsim 3$.

2) **Cold Dark Matter.** This has become the most successful theory of galaxy formation in the 1980's and is the standard benchmark against which observations are compared. It uses particles with larger masses and hence smaller random velocities. Candidate particles from Grand Unified Theories and Supersymmetric theories include photinos, gravitinos, axions, scalar neutrinos, Higgsinos, and other even more exotic beasts. The standard model with a scale-invariant adiabatic spectrum of initial fluctuations produces objects of roughly galactic mass and reproduces the small-scale clustering and internal dynamics of galaxies (Blumenthal *et al.* 1984). There is mounting evidence, however, that

this produces too *little* power on large scales as evidenced by the galaxy-galaxy correlation function (Maddox *et al.* 1990, Collins *et al.* 1991) and cell-counts of IRAS galaxies (Saunders *et al.*, 1991). This may not be a fatal problem as the model retains the freedom to renormalise to match large-scale power while the smaller scales can be brought down by non-linear effects. This can be matched in N-body simulations provided the simulations are run for long enough (Couchman & Carlberg 1991).

To summarize, the favoured view of the Universe at the beginning of the 1990's is that it originated in a Hot Big Bang, after passing through an inflationary phase, that its density is equal to the critical density and that it is dominated by non-baryonic Cold Dark Matter.

1.2 Protogalaxies

From an observational point of view protogalaxies can be defined as high-redshift galaxies undergoing their initial and most luminous phase of star formation. They are the early precursors of galaxies such as the Milky Way, known to be at least 10 Gyr old. PG searches are useful because detecting them will directly establish the epoch of galaxy formation, and of course having some actual examples of forming galaxies would provide new constraints on theories of galaxy formation (Baron & White, 1987).

It is possible to make some educated guesses about what the spectrum of a PG should look like. Partridge & Peebles (1967) proposed that the spectrum should be similar to that of a giant HII region. The light would come from the first burst of stars and so the would be dominated by luminous and massive O and B stars. Thus the continuum would have a blackbody shape with a temperature of $\sim 40\,000$ K — almost flat in f_ν. This would be modified by the presence of even a slight amount of gas to give a large discontinuity at the Lyman limit (912 Å rest) of a factor of 5 or more. Most of this energy would be reradiated in a strong Lyman-α line (1216 Å) with a large equivalent width of ~ 100 Å. Much of the continuum between Lyman-α and the Lyman limit should be eaten away by absorbing clouds of hydrogen along the line of sight, as has already been observed in high-redshift quasars. PGs would be discriminated from other high redshift objects, such as the quasars, by having narrow emission lines characteristic of the velocity dispersions of galaxies, i.e. $\lesssim 500\,\mathrm{km\,s^{-1}}$.

Their appearance in the observed frame depends on the redshift of formation. In the original Partridge & Peebles model this was at $z = 20$–30 and so they would appear to be very red as the blue light would be completely redshifted out of the optical. They would also appear very large ($\sim 30''$) as the angular diameter-distance relation turns over at such large redshifts. Alternatively, if galaxy formation occurs much later ($z = 2$–3), the PG's would be smaller (2–3″) and bluer, because the rest frame ultraviolet emission is now observed in the optical.

Previous optical surveys for PGs fall into two main classes. Firstly deep broad band photometric surveys which attempt to distinguish PGs by their flat spectrum plus break spectral energy distribution. Secondly there are narrow-band imaging surveys and spectroscopic surveys of blank portions of sky to search for the Lyman-α line, taking advantage of its large equivalent width. For a detailed review of optical surveys using these methods the reader is referred to Koo (1986). Suffice to say that no PGs have yet been found.

The motivation for extending such searches into the infrared is to extend searches for primeval galaxies to higher redshifts. It is known that at least *some* galaxies exist at high redshifts because of the recent discovery of quasars at redshifts > 4 (e.g. Warren *et al.*, 1987) and the discovery of radio galaxies at $z > 3$ with evidence for old stellar populations (Lilly 1988), although there is some controversy about the age issue (Chambers & Charlot 1990). At high redshifts the rest frame blue stars are shifted out of the optical and the PGs would appear as objects with very red optical-infrared colours. Indeed the K band is sensitive to such objects out to very large redshifts ($z \sim 20$). Little previous work has been done in the infrared and so this is relatively unexplored territory. Collins & Joseph (1988), using a single-channel photometer, surveyed $0.4\square'$ down to K = 18.2 and found only 1 normal galaxy. Cowie *et al.* (1990) have surveyed $1.4\square'$ down to K = 21.4 and found no objects with odd PG-like colours. Thus there is a strong motive to search a large area infrared survey and explore a new region of parameter space for peculiar objects.

1.3 Brown Dwarf Stars

Brown dwarves* are sub-stellar objects whose mass is too small for the core temperature to rise above that required for main sequence hydrogen fusion. They are commonly distinguished from planets by also requiring that they form from the same fragmentation process as the stars, and not via some secondary solar system formation mechanism (Black 1986). Such objects would derive the bulk of their radiant energy from deuterium fusion and gravitational collapse.

There is no physical reason why the star-formation process should cut off at masses just below observable stars, and indeed it is possible that such objects could make up the missing mass in galactic disks (Bahcall 1984). Reid & Gilmore (1982) constructed the first substantial colour selected survey for very faint main sequence stars and concluded that there were no significant stars below $M_V = 15$ and $0.1 M_\odot$. However Hawkins & Bessel (1988) in a much larger survey ($85 \square°$) found that the luminosity function continues to $M_V = 18$ and that the faint stars had a lower velocity dispersion indicating that they were younger objects and more likely to be brown dwarves than M stars.

Other types of survey have found a handful of brown dwarf candidates. The earliest such discovery was the object VB8B, detected by speckle interferometry (McCarthy *et al.* 1985). This caused much excitement at the time but later work, including that by the original discoverers, failed to confirm it. A more recent example is the infrared excess from the white dwarf G29-38 observed by Zuckerman & Becklin (1987) and interpreted as a brown dwarf companion. A possible direct brown dwarf detection is the companion to the white dwarf GD165 resolved via infrared imaging (Becklin & Zuckerman, 1988). The JHK infrared colours of this object indicate that it is the coolest dwarf star discovered and theoretical models show that it is consistent with a brown dwarf of 0.06–$0.08 M_\odot$.

A K band infrared survey presents the possibility of detecting such objects in the field and hence at least obtaining constraints on the luminosity function. The advantage of working at K is that this is where the blackbody flux from these objects peaks, hence optical-infrared colours are very efficient at selecting cool stars. The only colour confusion of these objects is with faint high-redshift galaxies, which it should be possible to distinguish by image size.

---

* The convention for the plural of "dwarf" follows Tolkien 1937.

1.4 The Evolution of Faint Galaxies

The principal aim of the survey work presented in this thesis was to make one of the first deep studies of galaxy evolution from the near-infrared. The advent of CCD detectors in the 1980's has had a major impact on the study of galaxy evolution in the optical by allowing genuine spectroscopic redshifts to be obtained for galaxies fainter than B = 20 and by improving the depth and reliability of photometric surveys. Such work, in the optical, has started to present a picture of a considerable amount of evolution in the galaxy population by a redshift of $z = 1$.

1.4.1 Cluster galaxy evolution

Rich clusters of galaxies can be recognised out to $z \sim 1$ and provide statistical samples of large numbers of galaxies at similar redshifts. These can be then be compared with their counterparts at low redshift to look for evidence of galaxy evolution.

The first realistic models of galaxy spectral evolution (Tinsley & Gunn 1976) suggested that there was little spectral evolution in early type elliptical galaxies at redshifts $z < 0.5$. Rich clusters are dominated by such galaxies so it was expected that little evolution would be seen in their populations. However when Butcher and Oemler (1978) measured the colour distributions of high-z clusters they found a significant blue tail of galaxies, which they interpreted as star-forming spirals ancestral to S0 galaxies abundant in today's clusters.

Subsequent spectroscopic work (e.g. Dressler & Gunn 1982, Couch & Sharples 1987, Lavery & Henry 1987) showed that these galaxies were indeed cluster members, and not just chance projections, thus confirming the effect. However they also found that rather than being star-forming spirals with strong emission lines the sample was dominated by galaxies with strong Balmer *absorption* lines, indicative of a population of young A type stars (hence "*E+A*" galaxies). These lines imply that the galaxies have a recently formed population of young blue stars, the absence of emission lines showing that the actual star-formation has stopped. This leads to the conclusion that the B-O effect is produced by more common short starbursts in the past and not by a process of continuous star-formation.

There are two principal hypotheses that have been advanced to explain this starburst phenomenon. Firstly mergers and galaxy collisions could be a trigger (Lavery & Henry 1988). However there is no evidence in favour of an enhanced number of near-neighbours, even for emission line galaxies caught during the burst. Secondly it is possible that starbursts could be caused by some kind of interaction with the intracluster medium (ICM), either by shocks propagating through the cluster (Evrard 1989), or by infall of gaseous field galaxies into the dense ICM. These both imply a larger velocity dispersion for $E+A$ galaxies and there is evidence that this is indeed the case (Dressler & Gunn 1990).

It is intriguing that the evidence for the evolution of cluster galaxies seems to mirror the activity of galaxies in the field, which is discussed next.

1.4.2 Field galaxy evolution

The first evidence for considerable evolution in the field galaxy population came from deep optical galaxy counts as a function of magnitude. This is the easiest cosmological observation in that it requires the least amount of telescope time.

The first detailed predictions of deep counts were published by Brown & Tinsley (1974) who showed that the number-magnitude counts of faint galaxies were sensitive to evolution beyond B = 20, and were in fact more sensitive to luminosity evolution in the galaxy population than to the cosmology. Tinsley (1977) gave count predictions down to 24^{th} magnitude for models with different redshifts of formation. The amounts of luminosity evolution were derived from the stellar population models developed in Larson & Tinsley (1974) and Tinsley & Gunn (1976).

The first deep data were based on photographic surveys. Examples are Jarvis & Tyson (1980), Peterson *et al.* (1979) and Kron (1978, 1980) which provided counts from B = 18 to B = 24. The availability of CCD detectors allowed the extension of the counts down to 28^{th} magnitude by workers such as Tyson (1988), Yee and Green (1987), Lilly *et al.* (1991) and Hall & Mackay (1984). The current picture is summarised in figure 5.11 in chapter 5, which discusses the galaxy counts in more depth. The observed slope is remarkably constant over 10 magnitudes and is much steeper than that predicted without evolution. It was also established that the faint galaxies had bluer rest-frame optical colours than local galaxies (Tyson 1988).

The initial interpretation was that the excess was due to luminosity evolution from more active star-formation in the past, producing the bluer colours. The counts were probing large numbers of galaxies beyond $z \sim 1$, brightened by luminosity evolution, although it was difficult to produce the lack of slope features without very high redshifts of formation. However other interpretations are possible because the number-magnitude relation actually contains very little information by itself. One example is the idea that the deep counts were picking up a population of local dwarves whose abundance is poorly determined in local redshift surveys (Kron 1982). Blue dwarves are almost unaffected by redshift dimming because of their relatively flat spectra and so would have a near-Euclidean slope, steepening the combined relation.

The way to deproject the galaxy counts and to remove the degeneracy between possibilities was to undertake deep *redshift* surveys to see if the blue galaxies at faint magnitudes really were at $z \sim 1$, or much more local. Such redshift surveys were made possible only by the development of multiple object spectrographs (see chapter 4) as the exposure times required to obtain spectra to $b_j = 22$ were of order 10–20 000 s on a 4 m telescope. The deepest published spectroscopic work is that of Broadhurst *et al.* (1988) and Colless *et al.* (1990) which reach limits of $bj < 21.5$ and $bj < 22.5$ respectively. These gave the surprising result that the *redshift* distribution of faint galaxies is entirely consistent in shape with that predicted by the non-evolving model, although, of course, the normalisation was up by a factor of two. Neither a high-redshift tail, as would be predicted by luminosity evolution, nor a low redshift hump from local dwarves were found.

Examination of the spectra of these faint blue galaxies showed many of them to be dominated by strong [OII] emission lines, indicating the possibility of them suffering short starbursts. This led Broadhurst *et al.* to propose a model of differential luminosity evolution where the dwarf galaxies evolved most with redshift. They painted a picture in which the dwarves periodically suffered small starbursts which caused them to be, on average, brighter and so gradually dominate the faint counts. Their model was consistent with the counts down to their magnitude limit and successfully mimicked the no-evolution redshift prediction.

It is possible to go still deeper with multi-colour surveys, the technique here is to try and fit the spectral energy distributions (SEDs) to generate photometric redshifts. The best recent example of this is the work of Lilly *et al.* (1991) who constructed a SED based

redshift distribution from UBVI colours at $23 < B < 24$. Even at these magnitudes the redshift distributions are still consistent with the non-evolving distribution and $\bar{z} \simeq 0.4$. SED fitting procedures can be very unreliable, particularly when the galaxies are blue as the flat spectrum results in a poor constraint on the redshift. However Lilly *et al.*'s result is strengthened by the fact that it fits the null hypothesis, i.e. that no evolution is occurring and that the SEDs of faint galaxies are similar to those of local ones. They also found that the SEDs of the faint galaxies they fitted were predominately blue dwarf types, Scd and Ir galaxies, which supports Broadhurst *et al.*'s hypothesis. However to apply the Broadhurst *et al.* model at these magnitudes requires brightening galaxies from fainter and fainter down the luminosity function to generate the sheer numbers of galaxies observed.

An alternative, more straightforward, interpretation of the counts is that we are witnessing some kind of *density* evolution with redshift, so that there were simply more galaxies in the past through some kind of history of galaxy mergers (Koo, 1990). Then the count prediction would be exactly that observed — a steeper number-magnitude relation with the number-redshift distribution consistent with no-evolution, apart from the normalisation. However by itself this will not produce bluer colours and the steepening of the number-magnitude relation will be the same in all passbands. Of course it is possible to combine these hypotheses as merging is a possible mechanism for inducing starbursts in galaxies and this would increase the luminosity and make the colours bluer. Obviously such a model would require a lot of poorly understood physics to relate the B luminosity to star-formation rate to merging rate to a theory of evolution of fluctuations in an expanding Universe.

1.5 Galaxy Evolution from a Faint Near-Infrared Survey

There are obvious ways one can proceed to investigate galaxy evolution further. One method is simply to attempt deeper spectroscopic redshift surveys in the optical. At present such surveys are limited by sheer light collecting power. To push redshifts down beyond $B \sim 23$ probably requires a new generation of 8 m telescopes. Another method is to study galaxies in other wavebands and try to understand the colour evolution.

Stellar evolution modelling is a very complex subject, and a large amount of detailed

computation is necessary to go from a star-formation rate to fluxes in different wavebands. The reader is referred to section 5.3.3, and references therein, later on in this thesis, for a more detailed discussion of these models.

However it is possible to make some qualitative statements about the behaviour of galaxy light in different bands, which agree to first order with the models. This serves to give a feeling for how the various bands probe evolution.

A large fraction of the B light from a galaxy comes from short lived (i.e. a few million years) hot OB stars — this component becomes more dominant as one sees galaxies at higher redshifts where the observed light is now from the rest-frame ultraviolet. Because of the short life times, the light curve with time from a short burst of star-formation is similar to a narrow delta function. Thus, qualitatively, the light is effectively proportional to the instantaneous star-formation rate.

What happens as one proceeds to redder wavelengths? Then the light becomes dominated by stars with progressively longer lifetimes. The near-infrared light from a galaxy is dominated by the "old-stellar population". This consists of old, evolved, stars on the giant branch with lifetimes of gigayears. Thus the relative contribution from on-going star-formation to the total light will be much less. In the I band ($\sim 1\mu$m) the excess in the counts over no-evolution is already much less than in the B band (e.g. Tyson, 1988).

This leads us to expect that the K band light will be relatively insensitive to star-formation for redshifts $z \lesssim 1$. Of course this is only an approximation, even old stars must evolve and it is possible that the picture could be considerably more complex. This is discussed in detail later on in this thesis. However we are led to several key reasons for studying galaxies selected in the K band:

1) **Geometry.** As has already been mentioned, the insensitivity to evolution means the counts are possibly an excellent probe of the geometry of the Universe. It may be possible to obtain new constraints on Ω_0, and also test non-standard world models such as those including the Cosmological Constant.

2) **Normalisation.** One vexed issue in evolutionary studies is what the present absolute space density of galaxies actually is. The range of differing estimates typically vary by a factor of two (see chapter 5). For number-magnitude count predictions

this normalisation is usually allowed to float — instead the models are normalised to the data at some intermediate magnitude. This of course affects the size of the excess over no-evolution and, hence, the amount of evolution required. The problem is that if the models are normalised at faint enough B magnitudes to avoid problems from local fluctuations in galaxy density, then one is sufficiently deep that evolution is already important. As there should be less evolution in K it would be possible to obtain a more reliable normalisation, on larger scales, and transfer this to the B band to determine just how much evolution is actually needed.

3) **Extinction.** Another advantage of selecting galaxies at 2μm is its relative insensitivity to extinction caused by dust — the extinction (in magnitudes) is only 10% that in the visual band. And unlike longer *far-infrared* wavelengths, such as those surveyed by the IRAS satellite, there is little thermal *emission* from warm dust ($\lesssim 100\,\mathrm{K}$). Thus there would be no preferential selection of the *dusty* starburst galaxies seen in the IRAS sample.

4) **Luminosity evolution.** The K data should allow the quantification of just how much luminosity evolution, in the B light of galaxies, is allowed. This should manifest itself in a greater excess over no-evolution in the B number-magnitude counts than in K, and, equivalently, in the evolution of the B – K colours. Also by selecting galaxies in a band insensitive to star-formation it should be possible to find out the true fraction of objects with strong emission lines such as [OII] which make up such a large proportion of the Broadhurst *et al.* and Colless *et al.* samples.

5) **Density evolution.** The K data should also allow the determination of the amount of evolution in the space density of galaxies. This will cause an excess in the number-magnitude counts over no-evolution which, unlike luminosity evolution, will be the *same* in B and K.

Of course luminosity and density evolution are not independent — if density evolution occurs via mergers then associated star-formation will cause luminosity evolution. However the B and K galaxy data should allow us to constrain these modes separately, and measure how much galactic evolution is going on in our Universe in a simple way, relatively unaffected by the more complex details of stellar evolution. This is the prime aim of the rest of this thesis.

1.6 Thesis Organisation

The organisation of this thesis is as follows:

1) **Chapter 1** presents the background to the work described in this thesis. Short reviews of the history of the Big Bang cosmology and studies of galaxy evolution are given, together with a discussion of the types of exotic objects which could be picked up in an infrared survey. The chapter concludes with a brief outline of the various other chapters of the thesis.

2) **Chapter 2** discusses the construction of the infrared survey. The choosing of field centres from Schmidt plates and the method adopted for observing are discussed. The data reduction procedures peculiar to infrared array detectors are detailed and the methods of mosaicing and performing photometric and astrometric calibrations are elaborated.

3) **Chapter 3** describes the CCD observations that were performed to obtain accurate colours for all the infrared selected objects. Photometry, astrometry and matching with the infrared data are detailed.

4) **Chapter 4** discusses the spectroscopic survey. The method of sample selection and the techniques used for making multifibre and multislit observations are presented and data reduction methods are outlined. The methods used for redshift determination, including the cross-correlation technique, and their reliability, are examined.

5) **Chapter 5** derives the infrared star and galaxy counts for the survey and corrects them for observed error rates, from the spectroscopy, in star-galaxy classification. Galaxy count predictions are developed from literature spectral evolution models and compared in K and b_j with the survey data and other published data. More general parametric models of density and luminosity evolution in the galaxy population are also developed and compared with the data.

6) **Chapter 6** analyses the colours and redshifts of the survey galaxies. The colour-magnitude and colour redshift diagrams are shown and compared with the predictions from spectral evolution. The very reddest objects in the survey are examined and the results of further JHK photometry and its implications are mentioned. Finally the number-redshift relation is analysed and compared with the evolutionary models of chapter 5.

7) **Chapter 7** sums up the conclusions of the thesis and presents some suggestions for future work.

8) **Appendices.** Appendix A gives a complete list of the positions, infrared magnitudes and optical magnitudes of the survey objects. Appendix B gives a list of objects in the spectroscopic survey and gives the line identifications and redshifts. The spectra of objects with determined redshifts are also plotted.

2 THE INFRARED SURVEY

2.1 Introduction

In undertaking a blank-field galaxy survey in the infrared three important questions have to be answered—what wavebands, what area and what limiting magnitude? Obviously given a finite amount of observing time these three parameters trade off against each other.

Infrared surveys have been pushed very deep in very small areas of the sky — for example, recently, Cowie *et al.* (1990) have observed $1.6\Box'$ to a limiting K magnitude of 21.4 (5σ in a $3.5''$ diameter aperture) with a total exposure time of 22.4 hours. The problem with this approach is in the additional observations needed to identify the types and redshifts of the objects detected in the infrared. As will be demonstrated, because of the greater sky coverage of the detectors, it is possible to get deep broad band optical UBVRI colours for essentially all the objects in an infrared sample in approximately the same amount of observing time on a large (2 m or bigger) optical telescope.

These colours can be used to derive the spectral energy distribution (SED) of the object but this conveys only very limited information on redshifts and types. Ideally one would like to obtain proper spectra and this is where the problem comes in. On a 4 m optical telescope it is possible to get a spectrum good enough to get a redshift from absorption features in a night's observing (30 000 s) down to $B \simeq 23.5$ or even $B \simeq 24$ if the object has very strong emission lines.

For the Cowie *et al.* survey above this gives a $B - K \simeq 2$ limit, redder than which it is very difficult to determine redshifts spectroscopically for the fainter objects. Indeed none of the infrared objects in their survey were this blue. Thus if one goes too faint in the infrared it becomes difficult to select a complete sub-sample for follow-up spectroscopy. As will be demonstrated in chapter 6 completeness is vital, having a colour bias greatly reduces the ability of an infrared selected sample to constrain galaxy evolution. In addition the number of objects in a deep sample rises less than $\propto t$, the integration time, because it is background limited by the sky. For a simple Euclidean universe the rise is $\propto t^{\frac{3}{4}}$ which

is an upper bound in the absence of strong luminosity or number density evolution in the sources with redshift.

To address the question of galaxy evolution, redshifts are required for a fairly large sample with no colour bias. Approximately 50–100 galaxies were hoped for and spectra were desirable. It was decided that the survey limit would be K $\simeq$ 18, enabling spectra of even very red objects (B – K $\simeq$ 5.5) to be obtained. Given an estimated surface density at K=18 of about 1 galaxy/$\Box'$, several hundred $\Box'$ would have to be surveyed. Even with the availability of 62 × 58 infrared detectors the area per integration is small and so it was decided to observe as large an area as possible in one infrared band only (the K band) and to supplement this with optical observations. The standard optical imaging detector is a CCD, or *Charged Coupled Device*, which covers a much larger area of sky. The CCD system on the Isaac Newton Telescope (INT) used for this survey (see chapter 3) had 512 × 320 pixels and covered 6.4′ × 3.9′.

2.2 Observational Strategy

The infrared observations for this project were all made using the 3.8 m United Kingdom Infrared Telescope. This is situated on the dormant volcanic caldera Mauna Kea on the Big Island of Hawaii. The site is at an altitude of 4200 m above sea level, which is above 60% of the earth's atmosphere and results in some of the best conditions in the world for infrared astronomy. The atmosphere is very stable which gives very good astronomical seeing (usually 0.5 – 1.4″) and it is also very dry, which is very important for infrared astronomy as water vapour is responsible for much of the extinction in these passbands. Figure 2.1 shows the profiles of the JHK filters used and the atmospheric transmission (at Mauna Kea) in the near-infrared.

In 1986 IRCAM (standing for Infrared Camera) was installed on the U.K. Infrared Telescope. IRCAM uses a 62 × 58 indium antimonide (InSb) array for imaging observations in the 1–5 μm band. Unlike optical CCD detectors it is a direct readout device; each pixel is read out separately by the hardware via a direct connection with no charge transfer along rows and columns. It has a readout noise of 450 e^-, a dark current of 100 $e^- s^{-1}$ and in the infrared K band (2.2 μm) the quantum efficiency is about 70%. It was one of the first of a new generation of infrared array detectors. Previously infrared astronomy

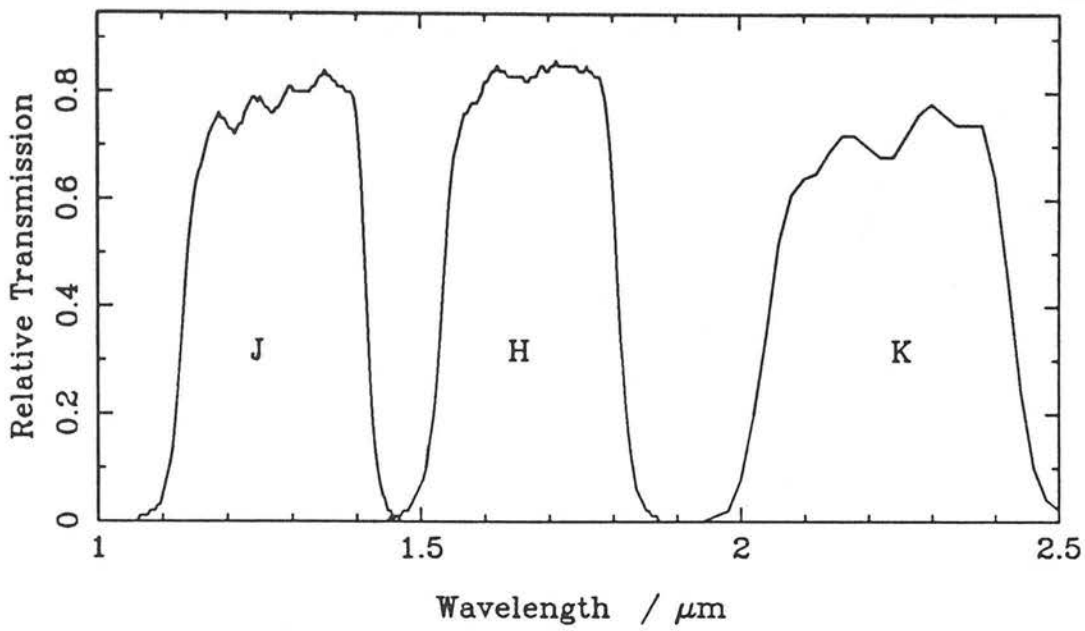

Fig. 2.1a Profiles of the JHK filters used in IRCAM.

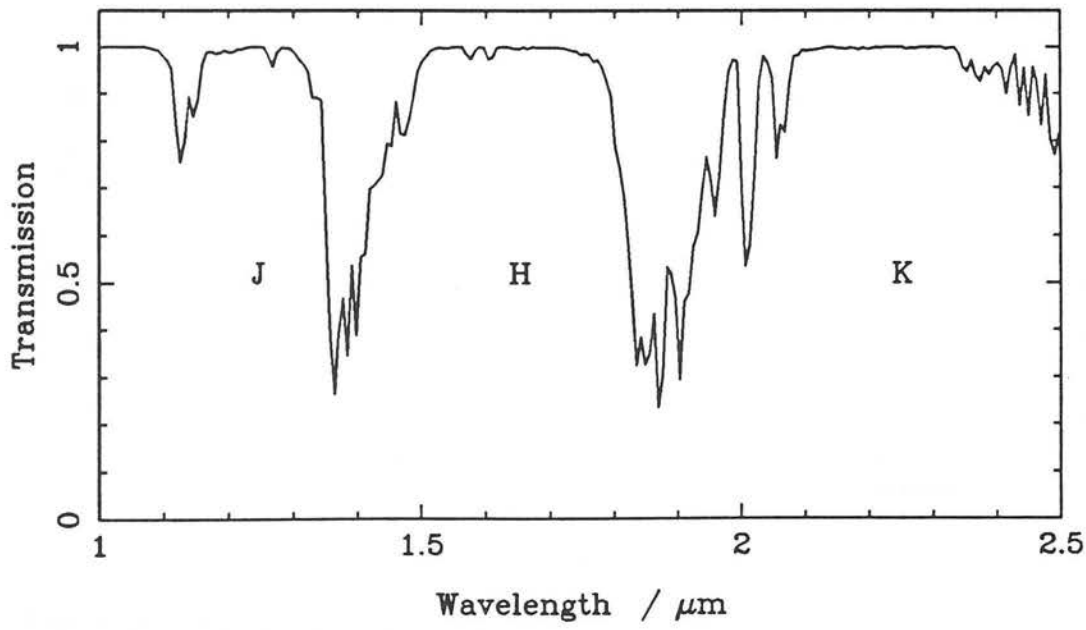

Fig. 2.1b The atmospheric transmission at Mauna Kea, Hawaii in the near-infrared.

was done using single element instruments; an example is the photometer UKT9 (also on UKIRT) which contains a single InSb detector. Measurements could only be made in a large aperture ($\geq 8''$) and any detailed mapping of the sky had to be done by stepping the position of the telescope on the sky. With 3596 detectors IRCAM made it possible to carry out an infrared imaging survey covering a much larger area than any previous work. IRCAM can be used at three different pixel scales of 0.6″, 1.2″ and 2.4″. For this project the 1.2″ scale was used in order to give the best compromise between areal coverage and reasonable sampling of the objects detected.

2.2.1 Detector sensitivity

The maximum sensitivity of a telescope/detector combination is usually given by the 1σ 1s figure which is the rms background noise in one pixel from the sky photons + dark current shot noise and the readout noise, obtained during the maximum possible on-chip exposure, scaled by $1/\sqrt{t}$ to 1 s. In magnitude units this is is given by :

$$1\sigma\ 1\mathrm{s} = -2.5\log_{10}\left[\frac{\sqrt{\eta a^2 10^{-0.4m_s} N\Delta_e A_e + D + R^2/t_b}}{\eta N\Delta_e A_e}\right]$$

where
- η is quantum efficiency
- a^2 pixel area in □″.
- m_s sky brightness in magnitudes/□″.
- N photons sec^{-1} $\mathrm{Å}^{-1}$ m^{-2} at bottom of atmosphere from a star of 0 magnitude.
- Δ_e effective filter bandwidth in Å.
- A_e effective aperture of telescope (m^2) = geometrical collecting area × efficiency.
- D dark current in $\mathrm{e}^-\ \mathrm{s}^{-1}$.
- R RMS readout noise from detector in e^-.
- t_b The maximum possible on chip exposure time (secs) for individual integrations.

Note for IRCAM the counts from the sky are so much larger than that from the dark current that the contribution of dark current to the total shot noise can be neglected. In

the background limited case where readout noise is negligible compared to the shot noise then this reduces to the simple formula:

$$1\sigma\,1\mathrm{s} = \frac{1}{2}(m_z + m_s) - 2.5\log_{10} a$$

where m_z is the zeropoint which converts *photons* to magnitudes and is given by:

$$m_z = 2.5\log_{10}(\eta N \Delta_e A_e)$$

In the K band ($\simeq 2.2\,\mu$m) the combined background from the telescope and the night sky gives a brightness of 12.5 mags/□″ or 9.5×10^{14} photons $\mathrm{m^{-2}Hz^{-1}sr^{-1}}$ (taking an absolute zeropoint from Tokunaga, 1986) for UKIRT/IRCAM. This should be compared with the typical optical sky brightness, for example 22.3 mags/□″ or 7.4×10^{11} photons $\mathrm{m^{-2}Hz^{-1}sr^{-1}}$ (zeropoint from Hayes & Latham, 1975) in B ($\simeq 4400$ Å). The infrared night sky is much brighter, chiefly due to the presence of many strong OH emission lines. The K band window also suffers from the high frequency blackbody tail from thermal radiation of the atmosphere, telescope and IRCAM optics.

Because of this large sky background the IRCAM detector saturates on the sky in a 20 second exposure. To avoid this longer exposures are made up of a large number of short "coadds" which are separately stored and combined in the hardware control system IRACS (*Infrared Array Control System*) before being stored permanently on disk. As each coadd carries a readout noise penalty the individual exposures can not be made too short. An acceptable compromise of 10 seconds/coadd was used. In this time the sky fills about 70% of the wells of the detector and gives a saturation limit of $\mathrm{K} \lesssim 12.5$ mags/□″ or $\mathrm{K} \lesssim 11.5$ for point sources in 2″ seeing. The appropriate value of t_b in the sensitivity formula is then 10 s which gives approximately equal readout and photon shot noise contributions to the 1σ 1 sec figure.

For IRCAM at K in the 1.2″/pixel mode $1\sigma\,1\,\mathrm{s} = 17.8$ mags (*IRCAM users guide*, Casali *et al.*, 1987). The limiting K magnitude is given by

$$\mathrm{K_{lim}} = \mathrm{K}_{1\sigma\,1\,\mathrm{s}} - 2.5\log_{10}\left[\left(\frac{\mathrm{Signal}}{\mathrm{Noise}}\right)\sqrt{\frac{\mathrm{N_{pixels}}}{(\mathrm{t}/1\,\mathrm{sec})}}\right]$$

which also holds for multiple coadds.

In a 4″ diameter aperture covering $\simeq 9$ pixels a 5σ detection corresponds to K = 18.0 in a 5 minute exposure. If 6–7 hours/night could be spent integrating (after allowing

for overheads such as moving the telescope and taking standards) 400 frames could be obtained covering $600\,\square'$ of sky.

It should be noted that since these observations were made the IRCAM readout noise has been greatly reduced by the implementation of non-destructive readout technology. This works by reading out each coadd many times during the course of the integration. As the read is non-destructive the final signal is unaltered but the readout noise is reduced by a factor of $\sqrt{N}$ where N is the number of reads. This reduces the readout noise sufficiently that it is negligible compared to the shot noise and means IRCAM is now essentially a pure photon limited device for deep observations.

2.2.2 Blank field positions

As a blank-field survey allows considerable freedom in location in the sky it is possible to optimize it by careful consideration of field location. The criteria that were used were —

1) Availability of fields at low airmass throughout the night.

2) High galactic latitude ($b > 30°$) so as to minimize galactic extinction and reddening.

3) Equatorial (DEC $\simeq 0°$) so as to be easily accessible from telescopes in the North and South hemispheres.

4) Availability of useful data from other work.

5) Absence of very bright stars.

In section 2.3 it can be seen that two sets of fields were picked for observing runs six months apart. In October the Sun has a RA of 14^h and in March 0^h. In order to have fields available less than 60° from the zenith (2 airmasses) throughout the night this requires 3–4 fields at 1–2^h separation. The RA range for October works out at 20^h–6^h and for March 6^h–16^h. However the galactic plane crosses the celestial equator at 7^h and 19^h and so restricting to a high galactic latitude ($b > 30°$) gives the RA ranges 21^h–4^h and 9^h–16^h respectively.

For the October fields it was decided to use Kapteyn's Selected Areas (Kapteyn, 1906) for our survey zones. These areas were compiled by Kapteyn in 1906 in order to study

the distribution of stars in the Milky Way and are chosen to be uniformly distributed across the sky. The centres are about 15° apart. Astronomers commonly use these fields for survey work as they are a small subset of the sky making up an unbiased sample and agreeing on a common standard increases the chance of different astronomical studies complementing each other.

For the March fields a different strategy was adopted. The primary fields selected were in areas which were to be surveyed with the *Low Dispersion Survey Spectrograph*, or LDSS (R.S. Ellis, 1988, private communication) which is a multislit aperture mask instrument (for further details see chapter 4). It was anticipated that useful spectral data from this survey might be obtained on objects in our fields. Because there were only a few of these areas and they only covered RA's 10^h–13^h additional non-LDSS fields (labelled "STARS") were chosen near these zones and also at RA's 9^h20^m and 17^h20^m so as fill in the beginning and the end of the nights observing. Unfortunately the 17^h20^m field was at a relatively low galactic latitude ($b = 20°$) but this was unavoidable at this time of year at the end of the night — only an equatorial field with low b field would be sufficiently close to the zenith.

Since the IRCAM detector only covers $1.2' \times 1.2'$ of sky, a large-area survey has to cover the sky with some kind of mosaic pattern. Ideally one would simply fill in the sky with a rectangular grid with some overlap between frames as, inevitably, some data would be obtained under non-photometric conditions. Objects in common in the overlap could then be used to calibrate the magnitudes of non-photometric data from the photometric data. They would also be crucial in providing a positional reference so as to allow the removal of small telescope pointing errors, which is important for later pairing of objects in different wavebands. This is the technique usually adopted with CCD surveys.

In order to estimate the expected number of bright stars in an IRCAM area the stellar distribution models of Bahcall & Soneira (1980) were used. These predicted 0.3–1 stars/$\Box'$ in the fields brighter than B = 20. Although these are optical and not infrared estimates it was necessary to have accurate positions of these stars in advance measured off sky-survey plates so the optical figure was the appropriate one. This is too small to allow for their use as a reference. For example if the upper limit of 1 star/$\Box'$ is assumed then from Poisson statistics an IRCAM image will contain a suitable reference star only 63% of the time.

Because of this problem it was decided to use a sparse rather than a full mosaic strategy. In this the mosaic was constructed in a 2 × 2 pattern around bright stars so that each frame would have the star in one of its four corners. This reference star was $\simeq$ 10 pixels in from the edge of the chip so each 2 × 2 mosaic would be $\simeq$ 100 × 100 pixels, or $4\Box'$, with 32% of the "4-mosaic" covered twice and 4% covered four times. Each quarter was to be observed on different nights so that even if only one night in four was photometric then the zeropoint of the non-photometric data could be determined from the reference star, the reference star also serving as a positional reference.

Thus the sky is filled in less efficiently with gaps in regions devoid of bright stars. Although this introduces a bias towards bright stars, they can be removed as their positions are known. Galaxy positions are not correlated with those of bright stars so they are unbiased by this procedure although the stars may be owing to the effects of star clusters and multiple-star systems. As stars were not of prime interest in this survey this was felt to be unimportant.

The detailed selection of these reference stars was based on SERC (*Science and Engineering Research Council*) sky survey plates taken by the United Kingdom Schmidt Telescope Unit at Siding Spring, Australia. As well as being available for visual inspection, COSMOS scans were made of the plates to construct computer catalogues. COSMOS (standing for COordinates, Shapes, Magnitudes, Orientations and Sizes) is a high-speed automatic plate measuring machine at the Royal Observatory Edinburgh. It scans a Schmidt plate with a light beam to measure the density of the photographic emulsion at each point and hence digitizes the plate.

Objects are detected by using a threshold above a local sky background (see section 2.5.1 for a detailed description of this technique) and their positions, geometric parameters, and instrumental magnitudes are stored in a computer catalogue. These raw magnitudes are non-linear and have an unknown zeropoint so they are usually calibrated via CCD sequences for scientific projects. However in this case it was not necessary as only positions of stars and rough optical magnitudes were required. The calibration was done by transforming the observed number-magnitude relation for stars onto that predicted from the model of Bahcall & Soneira (1980) at the appropriate galactic latitude and longitude using a spline fit to the observed relation. Although this was crude the ± 0.5 mag error was quite acceptable for these purposes.

Areas of $0.5° \times 0.5°$ were identified within the chosen fields which were free from the very brightest stars. All stars between certain magnitude limits were initially selected and then any that were too near other bright stars (such that their 4-mosaics would overlap) were rejected. As this does not take into account mutual overlaps between rejected stars this algorithm is rather overzealous. However a more sophisticated algorithm to reclaim some of these stars was not warranted initially as the total area covered would still be much greater than would be possible to observe.

The plate faint magnitude limits were varied between R = 17 and R = 18, depending on the field, for reference star selection so as to produce a similar number of candidate centres in each field. The bright limit was set 1–2 magnitudes above the faint limit so as to avoid saturating the IRCAM detector.

Because of the large number of frames to be taken it was essential to observe efficiently by having the telescope computer control system automatically step through a list of frame positions, moving the telescope and integrating at each one. It is not possible to do this with UKIRT over the whole sky as in order to achieve a sub-arcsecond pointing accuracy it is necessary first to go to a star near ($\lesssim 1°$) the field desired, centre manually on the star using the TV finder and zero the pointing system. There exists a large catalogue of these "nearstars" in the control computer for this purpose.

The control software does, however, include a mosaicing routine for small areas. The telescope is moved to the start point of the mosaic and then the system steps through a file containing a list of X,Y offsets from the centre taking an exposure at each one. The restriction is that the offsets must be $< 500''$. To meet this each field was divided up into 9 (3×3) subfields of size $10' \times 10'$. The mosaic positions were then stored as lists of offsets from these subfield centres. A separate mosaic file was constructed for each quarter of the 4-mosaic (see section 2.4.3). These were referred to as PP, MM, MP and PM as to whether the centre of the chip was a plus/minus offset in RA/DEC from the reference star.

After the first observing run an improvement was made in this strategy. The mosaic centres were moved, where possible, from the subfield centre to the position of a bright star ($R \lesssim 12$) within $200''$ (this limit being set by the maximum offset size) of the centre. A star this bright was easily visible on the TV and could be used for correcting the

positioning of the telescope after each mosaic instead of going to a nearstar, with the attendant overheads that involved. This star was chosen off the same Schmidt plate data as those used for the reference stars so this had the extra advantage that the coordinate system of the telescope would match that of the reference stars.

For the second observing run in the October fields (see section 2.3) a refinement to the reference star selection process was required to select additional fields for observing over those used in 1987. All of the 9 subfields observed then had been covered in deep R band CCD imaging (see chapter 3) in a filled-in grid pattern. The optimum observing strategy was then to try and fill in the gaps in the subfields from the 1987 data with new 4-mosaic centres while minimizing the overlap with existing data. While much of the existing infrared data were known to be affected by problems (see section 2.3) at that time it was only possible to make a preliminary assessment of what data might be usable and the gaps were based on this assessment.

The algorithm adopted for reference star selection was as follows:

1) All the stars in the appropriate magnitude range were selected as frame centres.

2) For each frame i, using the list of already observed positions of possible usable quality, the fractional area overlap f_i of all the new frames with all the old frames if frame i was removed from the list was computed.

3) The frame with the lowest f_i was removed from the list.

4) Steps 2–3 were iterated until the overlap f_i dropped to an acceptable fraction which was set at 20% as a compromise between having enough fields and minimizing the overlap.

Both the new interleaved subfields and some of the old subfield positions were observed in the very successful October 1988 run.

Table 2.1 shows the subfields that were covered in all the observing runs. Each subfield is the centre of a $10' \times 10'$ box in which the centres of the 4-mosaics lie.

Table 2.1: Field centres for blank field mosaics

	Field	RA	DEC
October fields	SA114_3	$22^h38^m56.0^s$	$+0°36^m\ 0^s$
	SA114_4	$22^h40^m16.0^s$	$+0°26^m\ 0^s$
	SA114_5	$22^h39^m36.0^s$	$+0°26^m\ 0^s$
	SA114_6	$22^h38^m56.0^s$	$+0°26^m\ 0^s$
	SA92_2	$0^h52^m20.0^s$	$+0°20^m\ 0^s$
	SA92_4	$0^h53^m\ 0.0^s$	$+0°10^m\ 0^s$
	SA93_1	$1^h53^m16.0^s$	$+0°45^m\ 0^s$
	SA93_5	$1^h52^m36.0^s$	$+0°35^m\ 0^s$
	SA93_8	$1^h52^m36.0^s$	$+0°25^m\ 0^s$
March fields	851STARS_1	$9^h18^m24.5^s$	$-0°21^m55^s$
	851STARS_2	$9^h18^m39.0^s$	$-0°\ 3^m\ 3^s$
	855LDSS_1	$10^h43^m55.4^s$	$+0°\ 5^m33^s$
	855LDSS_2	$10^h43^m\ 6.2^s$	$-0°\ 8^m15^s$
	855LDSS_4	$10^h44^m\ 3.3^s$	$-0°20^m26^s$
	855STARS_1	$10^h41^m59.2^s$	$-0°13^m26^s$
	864LDSS_1	$13^h41^m57.7^s$	$+0°\ 6^m25^s$
	864LDSS_2	$13^h41^m\ 9.1^s$	$-0°\ 0^m16^s$
	864LDSS_3	$13^h41^m\ 8.8^s$	$+0°10^m18^s$
	864STARS_1	$13^h39^m20.8^s$	$+0°18^m48^s$
	864STARS_2	$13^h40^m10.8^s$	$-0°\ 2^m57^s$
	875STARS_5	$17^h19^m59.3^s$	$+0°10^m19^s$

2.3 Observing Log

The infrared survey observations for this project were performed in three observing runs over the years 1987–1988. These are listed below:

9–13th October 1987. A total of 262 individual frames were obtained in five nights on this run covering $\simeq 270\,\Box'$ (counting overlaps once only) using five minute integrations with the FPA61 InSb array. The observations were split among the three October fields. However the run was affected by weather and severe detector problems. Intermittent cloud cover was present on all nights and the zenith extinction was observed at the telescope to vary by ± 1 mag. This was subsequently confirmed when the data were reduced fully and the standard star zeropoints analysed. The survey observations were all affected at some level by electronic problems with the detector and control system. This manifested itself in image background patterns which changed amplitude and shape between integrations. These were impossible to remove fully. Approximately 30% of the time was lost as the computer control system kept crashing. Detector problems were believed to be associated with this fault. Although these data were reduced none were used in the final survey catalogue due to the background problems, lack of depth and the fact that much better data were obtained at a later stage.

25–29th March 1988. A total of 205 individual frames in the March fields were obtained in five nights covering $\simeq 236\,\Box'$ using 2.5 minute integrations with the FPA118 InSb array. 18 frames were covered twice to give 5 minutes on each field. Weather was a severe problem on this run. Only 65 frames were obtained on the first three nights and there was a large amount of intermittent cloud cover. Because of limited depth and difficulty of calibration these were not included in the final survey. The fourth night (and nearly the observers!) was lost entirely due to a blizzard. However the last night was clear and photometric and 158 frames were obtained using 2.5 minute integrations. The shorter integration time was used due to the adverse conditions as it was decided that areal coverage was more important than depth.

26–30th October 1988. This observing run contributed the bulk of the infrared data to the final survey. A total of 662 frames, mostly 2×2.5 minute integrations were obtained covering $\simeq 420\,\Box'$ with the FPA118 InSb array. Two whole nights were perfectly photometric, most had only slight extinction due to cirrus cloud and only two-thirds of a

night was unusable. The October fields were concentrated on although some of our March fields at low RA (851 and 855) were also observed towards the end of the night. The only problem with the detector was a horizontal streak that appeared in the top right corner of some of the images due to readout problems associated with an electronics fault. This was cured when it appeared by changing to the L′ filter and taking a quick exposure to saturate the chip.

In summary 1147 IRCAM frames were obtained of which 72% were included in the final survey. The total area surveyed was $\simeq 594\,\Box'$ of which 64% was observed twice to give 5 minutes on target. Table 2.2 summarizes the areas covered.

2.4 Data Reduction

The procedure for reducing IRCAM data is in some respects quite similar to that for optical CCD data. Bias and dark current frames are subtracted and the data are divided by a flatfield frame. However all these steps are much more critical in the infrared than they are in the optical. While it is possible to display a raw CCD image about the mean level and easily see stars and galaxies this can not be done with an IRCAM image — the size of the variations introduced by bias, dark and flatfield effects (see section 2.4.3) is much bigger than those due to even very bright objects. For a quick-look display at the telescope it is possible to difference two frames and display them. The bias and dark variations then cancel out and so does the flatfield to first order due to approximate sky-subtraction. If the image is then displayed about the mean level faint objects (both positive and negative) can then be seen and this forms a useful procedure at the telescope to check on the observing while it is in progress.

The full reduction procedure followed for IRCAM images is outlined below together with the differences from standard CCD procedures. All the reductions were carried out with the FIGARO (Fast Interactive Graphics And Reduction Operations) data reduction system created by K.S. Shortridge at the Anglo-Australian Observatory. This provided standard sets of routines for the manipulation of images and spectra (for example addition, multiplication, display, etc.) and was easy to extend as necessary by adding new routines.

Table 2.2: Approximate[1] areal coverage of survey

October fields

N_q	N_f	N_5	$N_{2.5}$
4	35	35	—[2]
3	10	10	—
2	44	14	—
1	42	40	62
	366□′	280□′	89□′

March fields

N_q	N_f	N_5	$N_{2.5}$
4	22	18	—
3	—	4	—
2	33	—	33
1	30	10	24
	228□′	105□′	126□′

N_q = Number of quarters of 4-mosaic filled in (see section 2.2.2).
N_f = Number of positions with this fill-in factor.
N_5 = Number of these positions with 5 minute integrations at this fill-in factor.
$N_{2.5}$ = Number of these positions with 2.5 minute integrations at this fill-in factor.

Notes:

1.) The areas are only approximate as they do not take into account the overlaps between separate 4-mosaics which will reduce the total slightly.
2.) $N_f \neq N_5 + N_{2.5}$ as some of the second passes on the mosaics were only partially complete. Thus frames can appear in different rows in different columns.

2.4.1 Bias and dark removal

The bias level of a CCD detector should be just a constant DC level set electronically to ensure that only positive numbers result from the digitization process. In practice there is a residual pixel-pixel variation that must be subtracted from the data. The standard procedure is to read out an empty frame of 0 secs exposure which becomes the bias frame. As the normalisation tends to drift throughout the night this bias frame is first scaled before subtraction — the scaling being determined by reading out the last 20–30 columns of each frame twice to determine the overall bias level.

For IRCAM there is also an electronic bias that must be removed from the data. This has a much larger pixel-pixel variation but is relatively stable throughout the night. The mean levels from bias frames taken at the beginning and end of the night generally agree so the nights were generally treated as a unit with master biases and darks being constructed for each one by stacking them in order to reduce the readout noise. However there were occasional problems when there had been a crash in the computer control system and the electronics had to be reset. In this case the levels change so new biases and darks were taken and the night divided up appropriately.

IRCAM has a dark current of about $100\,e^{-}\,sec^{-1}$ compared with about $4–12\,e^{-}\,sec^{-1}$ for different types of CCD. This is another additive correction that must be subtracted from the data.

In order to achieve correct subtraction of bias and dark frames, two important points must be considered:

1) The minimum exposure on a bias is actually 130 ms due to hardware overheads. This means that the bias contains 130 ms worth of dark current on top of the offset values.

2) Each coadd is actually a separate readout operation and contains its own bias level. So the total bias level scales with the number of coadds.

The procedure that was followed in subtracting the bias and dark frames is outlined below:

1) A master bias frame was prepared for each group of frames by taking the median of several (typically 4–6) 100 coadd × 130 ms bias frames. This was scaled to the

correct number of coadds and subtracted off the very short exposure ($< 1\,s$) frames which were taken on the bright standard stars as the dark current was negligible for these.

2) As IRCAM has a slightly non-linear dark current for long exposure frames ($> 1\,s$) a separate frame should ideally be taken with the shutter closed and the same exposure time. This contains the combined bias and dark and is subtracted off after scaling to the same number of coadds. This was used for the deep sky data and for the faint standard stars. Usually several darks were taken and median filtered to reduce the noise and remove hot pixels (see section 2.4.4).

2.4.2 Non-linearity correction

For the frames taken in March 1988 with the FPA118 array it was necessary to apply a correction for non-linearity in the detector (M.M. Casali & I.S. McLean, 1988, private communication). To correct for this each pixel in the bias and dark subtracted frame was multiplied by the correction factor f given by the equation:

$$f = 1.0 - 2.308 \times 10^{-9}\, C + 8.689 \times 10^{-11} C^2 + 2.281 \times 10^{-14} C^3 - 1.687 \times 10^{-18} C^4 + 4.287 \times 10^{-23} C^5$$

where C = counts/coadd in the pixel.

The non-linearity was unexpectedly strong for this type of device — the factor f reaches 1.09 at 70% full well. It was due to a voltage in the electronics being incorrectly set and was subsequently rectified.

For the October 1988 run another, much smaller, non-linearity was removed from the data. This was done at the telescope using a standard procedure.

2.4.3 Flatfielding

Two-dimensional electronic detectors used for astronomy usually have pixel-pixel gain variations that must be calibrated out. For example optical CCD detectors generally have 1–5% variations both on pixel-pixel scales and large-scale across the whole of the chip. It is possible to make CCDs which are much more uniform than this, indeed these are the ones used in commercial TV cameras, but to do this requires the sacrifice of quantum efficiency.

In practice it is possible to remove the variations by dividing by a "flatfield" which is an exposure of the chip on a uniformly illuminated background. The detector response depends on wavelength so in broad band work the ideal flatfield has to have the same spectral energy distribution as the object of interest. For deep integrations the night sky emission dominates over that from objects so the ideal flatfield for this sort of work would be a featureless piece of night sky. Unfortunately it is difficult to find such a piece as any exposure long enough to get good S/N on the sky generally detects stars and galaxies which contaminate the flatfield.

The usual fix is to use a "dome-flat" which involves looking at a piece of the telescope dome illuminated by a white light source or a "twilight-flat" in which the twilight sky is observed (as this is much brighter than the night sky individual objects are not seen). However in neither case does the spectral shape adequately match that of the night sky. The natural light in the dark night sky contains auroral emission from the ionosphere; a white light source usually has a hot thermal or a fluorescent spectrum while the twilight contains a larger contribution from scattered sunlight.

In the infrared it is much more important to get a correct flatfield as the sky is so much brighter. The greater number of photons means that the fractional $\sqrt{N}/N$ shot noise is reduced so the flatfield has to be more accurate to reduce the systematic errors below this limit. A technique has been developed in recent years for deep optical CCD surveys (for an example see Tyson, 1988) which allows the obtaining of true night sky flatfields. To achieve this the deep data frames are taken with positional offsets with respect to each other. The flatfield is then constructed in the following way:

1) Each frame in the sequence is normalised by dividing each one by the sky level

worked out in some box on the chip (the *same* box on each chip for consistent normalisation). This is *not* determined by working out an average — mean values tend to be highly skewed by a small number of very high data values such as might be produced by cosmic ray impacts on a few detectors or the presence of a few very bright objects. The *median* value is used in preference because for any distribution which is even approximately normal the median lies close to the mode (and is easier to calculate) and is not affected greatly by a few anomalously high values. In addition some kind of iterative rejection of points greater than a couple of standard deviations away from the median is employed to improve the sky determination even more.

2) Each pixel in the flatfield is then obtained as the median value of the same pixel in each of the frames in the sequence, again with some kind of iterative rejection. As the frames have positional offsets any object which appears in one frame at that pixel position does not appear in any of the other frames at that position. Median filtering effectively removes the objects and leaves an empty night sky frame if the object density is sufficiently low that the frames are mostly sky.

The data frames are then flatfielded with this frame and mosaiced together to remove the positional offsets and increase the final signal/noise.

Using these techniques in the optical it has been possible to reduce the systematic flatfield residuals below 0.03% and obtain photon shot noise limited imaging as faint as B = 29 mags/□″.

In the infrared the sky spectrum is brighter and much more variable as the bandpasses contain a larger number of airglow lines. These vary in strength on time-scales of the order of 20–30 minutes so a new flatfield has to be constructed at least this often.

Each of the mosaic sequences consisted of 8–16 frames. The intended approach was to construct a flatfield via the median filtering technique for each group of 4–5 frames. A slight complication was caused by the presence of the reference stars. As mentioned in section 2.2.2 a mosaic sequence was constructed for each quarter of the 4-mosaic. If the same quarter was used on the first, second, third etc... position in the mosaic then the reference star will always appear in the same approximate position on the chip in

consecutive exposures and will contaminate the flatfield because no sky is available to be sampled at that point.

For the initial October 1987 run the solution that was adopted to combat this problem was to move the reference star alternately to opposite corners as the mosaic was stepped through. This ensures that the sky is available at the reference star position on half the frames and a suitably modified version of the median filtering program could ignore pixels near reference stars. Then the PP, MM, MP and PM terminology refers to the reference star position on the first frame only. If all four of these mosaics are taken then all the 4-mosaics on all the reference stars are still completely filled. Typically 4–6 five minute exposures were combined to generate a flatfield.

However the frames near the edge of each group tended to be more poorly flatfielded and it was decided that the time resolution was too coarse. On subsequent runs the integration times were reduced to 2.5 min exposures, each mosaic being observed twice, and this cured that problem. Also the frames were still rather poorly flatfielded around the reference stars due to the availability of only 2–3 sky positions. This was solved after the first run by moving the reference star around all four corners of the chip instead of just alternating corners. Then 3 out of 4 positions where reference stars occur had sky data. Again each group of 4–5 frames were combined via median filtering to generate a flatfield for the group.

The technique worked well. On frames that were unaffected by detector problems the RMS noise of the frames was consistent with that which would be expected from the combination of photon shot noise and readout noise indicating that the flatfield noise was well below this level ($\lesssim 1$ part in 10^4). After flatfielding each frame was normalised to 1 second 1 coadd.

2.4.4 Bad pixel removal

Each of the detector arrays had a known set of non-functional pixels. There are two approaches for dealing with these, other than simply ignoring them. The rigorous approach is to flag the pixels so that any scientific analysis program, for example to measure magnitudes or fit profiles, will ignore them. The other approach is to interpolate over them in some fashion and then hope that this will have no serious affect on the results.

However the first approach was impractical. The data reduction system used for reducing the data, FIGARO, did not have the facility at that time for handling flagged values. Adding this would have required a major rewrite of the entire software package and none of the other potential packages had this capability either. As only typically 10–15 pixels out of 3596 were affected it was decided to interpolate over them. In addition 1–2 rows on some of the chip edges were relatively insensitive and were removed in the same way.

The algorithm used for the interpolation was to replace each bad pixel value with the median value of the data values in a 5×5 box surrounding it, excluding other bad pixels.

IRCAM also suffers from a species of intermittent bad pixel known as "hot" pixels. These vary in location from frame to frame and manifest themselves as pixels with abnormally high sensitivity, appearing as bright specks of 1–2 pixels in the frame. These were removed as best as possible in the image detection stage of the reduction (see section 2.5.1).

2.4.5 Standards and calibration

Two sets of standard stars were used to calibrate the photometry. The UKIRT standard star list provided a list of commonly used bright ($K \simeq 6$–7) standards. In addition fainter stars from Leggett & Hawkins (1988) and from Hawkins (private communication, 1988) were used which provided stars in the North and South Galactic Poles and Hyades cluster areas. These have magnitudes in the range $K \simeq 10$–14 and using them meant that the linearity of the detector could be checked to faint magnitudes.

Each standard was observed twice with a 20″ offset between them so that each frame could be used to flatfield the other while still giving two independent flux measurements.

Fixed size apertures were to be used for the aperture photometry of the survey objects (see section 2.5.2). In order to determine which aperture size to use extinction curves of zeropoint against airmass were plotted for a series of increasing apertures (4″,5″,6″,8″,10″ and 12″). As the apertures get bigger the RMS scatter about the best fit line tends to a constant. This is because small variations in seeing, which change the light lost outside the aperture, are having a progressively smaller effect and the result is tending to the intrinsic scatter in the data. The chosen aperture size is a compromise between having a large aperture which minimizes this seeing RMS and gives a correct total galaxy magnitude

Table 2.3: Extinction terms for photometric nights

Date	Aperture	α	C	RMS
29/3/88	8″	0.065	20.319	0.037
27/10/88	4″	0.082	20.068	0.067
28/10/88	4″	0.085	20.048	0.080

and having a small aperture to avoid including too much sky noise. The seeing values for the infrared *and* the optical data were considered together as for meaningful colours the aperture sizes must be matched.

In order to estimate the effect of seeing variations on the standard star zeropoints, the plots shown in figure 2.2 were made. These show the magnitude errors caused by different sized fractional seeing variations versus aperture size. For example the 10% curve is the magnitude error caused by the seeing being ±10% from the mean value, the maximum of the errors caused by positive and negative fluctuations being plotted. The upper plot is for a standard Gaussian point spread function and the lower is for a slight broader PSF ($e^{-r^{1.7}}$) which causes larger errors. It can be seen that adopting an aperture of twice the mean seeing causes $\simeq 0.05$ mag errors if the variation is 10%.

The infrared and optical data in the October fields had typical seeing values in the range 1–2″ so it was decided to use a 4″ diameter aperture. Unfortunately in the March data the seeing was a lot worse — as bad as 3–4″ sometimes in both the infrared and optical data and so an 8″ aperture was used.

Using the measured counts from the standard stars in the chosen apertures a standard extinction law was fitted to the data using least-squares. This has the form:

$$\Delta = C - \alpha \sec z$$

where the variables are

Δ	=	Given K Magnitude + $2.5 \log_{10}$ Counts/sec
$\sec z$	=	sec(Zenith angle) (= airmass)
C	=	Zeropoint at zero airmass
α	=	Extinction in magnitudes/airmass

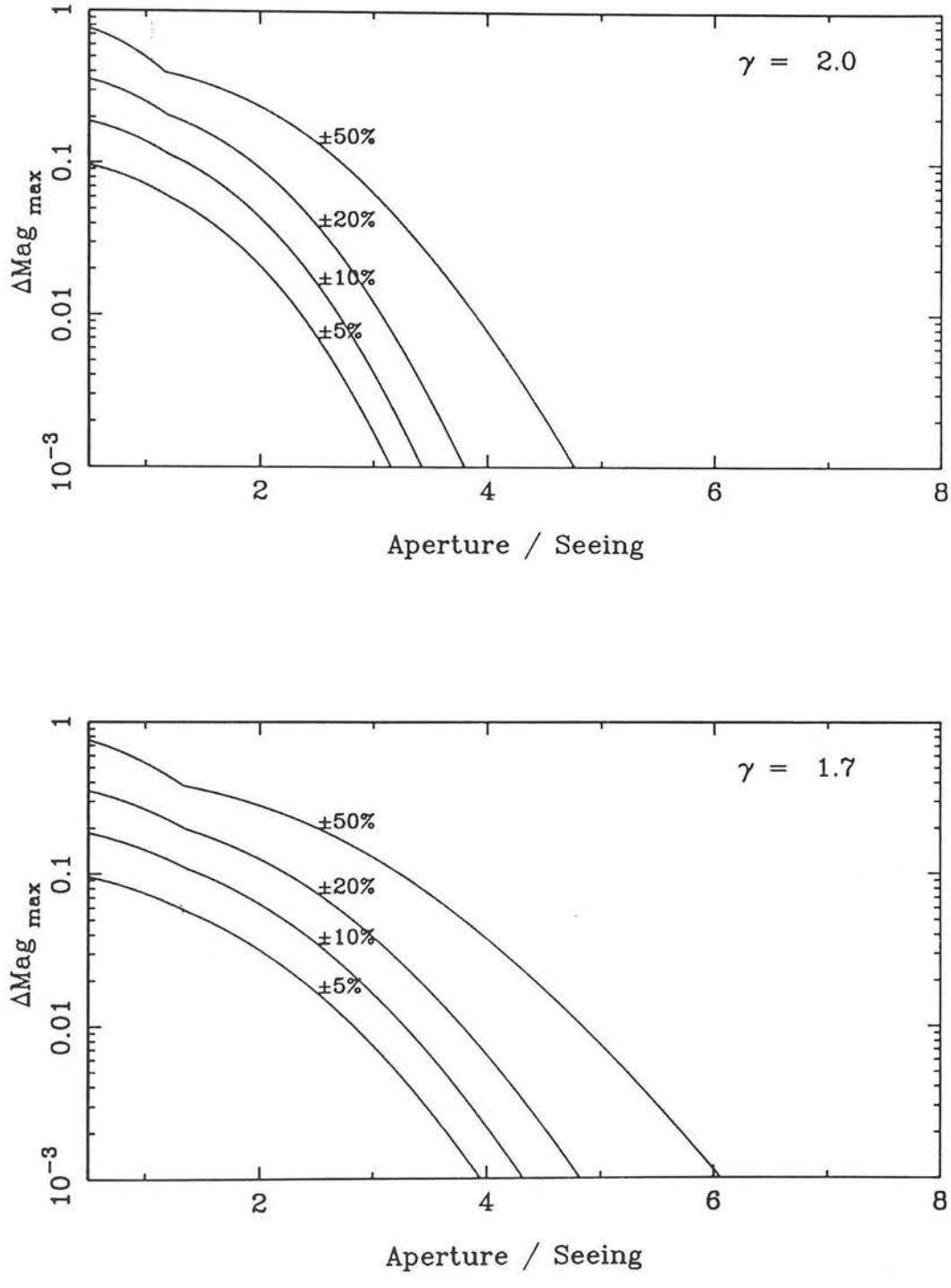

Fig. 2.2 The theoretical magnitude errors derived for progressively larger seeing variations (see text). The point-spread function is of the form e^{-r^γ}.

C and α are the parameters to be determined in the fit.

Table 2.3 shows the extinction parameters determined for the photometric nights. It can be seen that the RMS scatter is consistent with the size of the errors expected from seeing variations of $< 10\%$. No evidence of any residual non-linearity was found.

2.5 Photometry

The calibration procedure employed was quite complex as it involved image detection and photometry on all the individual frames, zeropoint cross-calibration using the reference stars, mosaicing together of the 4-mosaics with the correct zeropoint weights to go as deep as possible and then a further round of image detection and photometry. This is outlined in further detail in the rest of this section.

2.5.1 Image detection

Since about 800 frames were included in the final survey, going through and selecting all the images by hand was not feasible as well as being highly subjective, so some kind of automatic computer algorithm was needed. The most common technique in the literature is based on thresholding (e.g. Tyson, 1988). A threshold is set (above the sky background) and all the pixel values higher than it are joined up and groups of these are separated into discrete objects. The centroid and area (i.e. number of pixels > threshold) of each object is then returned.

The approach adopted here for the IRCAM survey was based on this using a modified image detection program from the COSMOS suite of software for the automatic analysis of Schmidt plate data. The steps are outlined below:

1) The local sky background was removed by subtracting from each pixel the median of a 17 × 17 box (20″ × 20″) centred on the pixel. Such a low-pass filter removes only large-scale variations and only affects the photometry of very bright objects which, in effect, bias up their local sky levels. Such objects are likely to be highly saturated so their magnitudes are incorrect anyway. Some of the IRCAM images were slightly vignetted resulting in a slight sky gradient across the chip. The frames

where these effects were major problems were not used and only those where the effect was minor and easily removed by the filter were used.

2) The RMS pixel-pixel sky variation was computed for each frame in a 30×30 box at the centre of the chip (away from the reference stars). In the box the median and 67% deviation (i.e. that deviation from the median encompassing 67% of the pixel values) were computed instead of the mean and standard deviation. For a normal distribution these are equivalent, but the median and deviation are much less sensitive to the departures from normality caused by the presence of bright objects and "hot" pixels. The median and deviation for each frame were output and it was checked that:

   a.) The medians were consistent with zero (as they should be from (1)) within the measurement error.

   b.) The deviations had consistent values from frame to frame.

   If all was well then the 67% deviation was adopted as the "RMS" sky background.

3) The frames were then subjected to object detection with a threshold of $2 \times$RMS and a minimum area size of 3 pixels which corresponds to a $3.5\,\sigma$ detection level. These values were determined to be optimum after much experimentation with displaying images and overlaying the positions of detection. A 2 pixel area of detection brought in too many hot pixels while a higher area lost too many objects.

4) The X,Y position was computed as the intensity weighted centroid of each object on the frame.

Figure 2.3 shows the results of the thresholding and object detection algorithm on a typical image from the survey. The thresholded image and the final object detections are indicated.

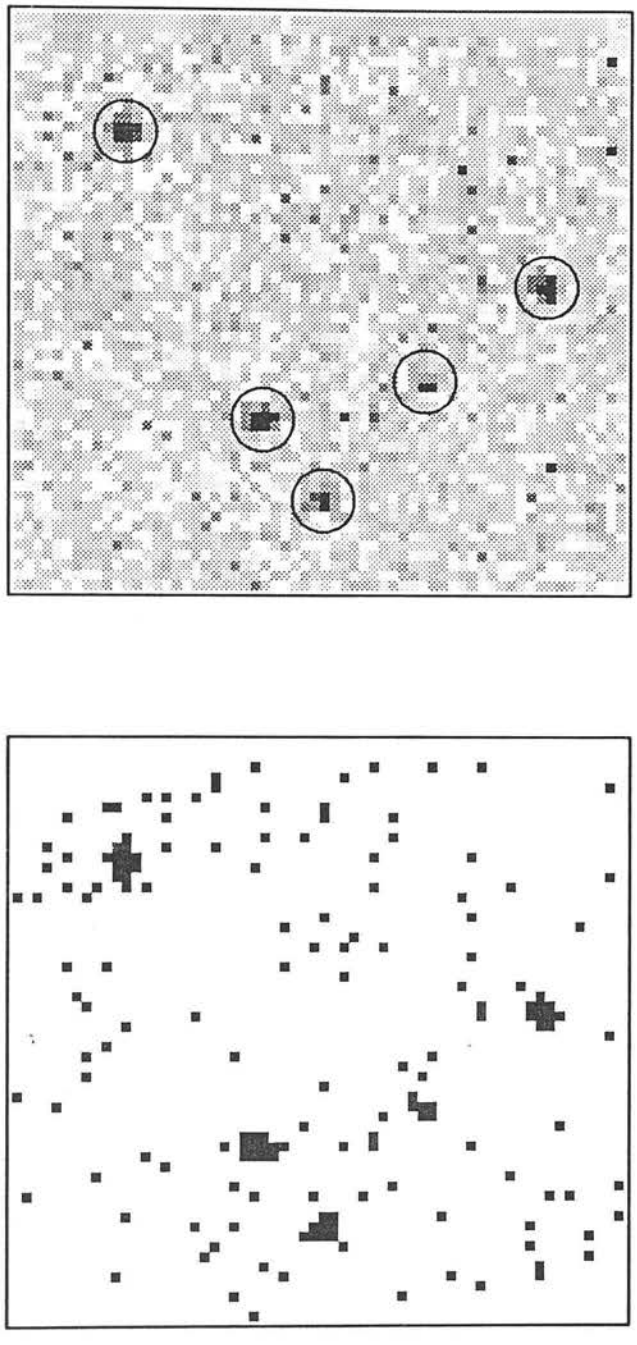

Fig. 2.3 A typical IRCAM image is shown at the top together with the objects detected by the thresholding algorithm. Below is shown the same image with the pixels above the adopted threshold shown in black.

2.5.2 Photometry of individual images

For a combined survey of galaxies and stars the correct weighting scheme for the photometry is uniform — i.e. use a simple aperture magnitude. The error was determined from the global RMS of the image as computed in section 2.5.1 scaled by $\sqrt{N}$, where N is the number of pixels in the aperture. This corresponds to the combined readout, sky shot and flatfielding noise. There is also shot noise from the photons from the object itself but since the objects are faint this is negligible compared to that from the sky.

In the absence of redshift information it was not possible in advance to scale the galaxy magnitudes to a fixed metric aperture so there were three possible approaches to the photometry of faint objects:

1) Derive a growth curve (magnitude as a function of aperture) and try to extrapolate to the total magnitude as the aperture $\rightarrow \infty$. This must be done for each object separately since if the galaxies are resolved they have different orientations and shapes (if they are unresolved this is the same as (2) below anyway). If the objects are highly non-spherical this procedure breaks down. As the objects are faint simply using a very large aperture introduces a large amount of sky-noise and contamination from other objects.

2) Use a fixed size aperture (in arcseconds) for all objects and adopt a zeropoint from the standard stars calibration at the same aperture. This is chosen to be larger than the faint objects of interest although it systematically underestimates the total flux from bright galaxies. However these are likely to be saturated anyway. A fixed aperture magnitude has the great advantage that it provides a number which is easy for other observers to check.

3) Use an isophotal magnitude scheme where all pixels above an intensity threshold are summed up. This systematically underestimates the total magnitudes of faint objects as the area above the threshold gets smaller with magnitude. There is another systematic effect which partially compensates for this which is that an isophote can only include *positive* and never negative sky noise. Isophotal magnitudes are difficult to check or interpret as the position of the isophote varies depending on the noise.

It was decided to use scheme (2) as being the most reliable at faint magnitudes, the actual size being determined partly by the seeing (see section 2.4.5) for the data in question. Using the centroids determined in section 2.5.1 aperture magnitudes were determined. If the data were taken on the photometric nights zeropoints from table 2.3 were applied at the appropriate airmass.

2.5.3 Non-photometric zeropoint determination

The data taken in non-photometric conditions had to be calibrated against the photometric data using the reference stars. The approximate position of these on the frames were known in advance and they were identified automatically on each frame using a criterion of looking for bright (S/N $>$ 10) objects near ($<$ 5 pixels) the predicted position. In principle then all that was necessary would be to take the magnitude difference with respect to a photometric calibrated frame in order to determine the zeropoint.

One complication was that sometimes the reference stars were not bright enough to do this accurately. As the original selection could only be done using optical (Schmidt plate) data it was unavoidable that some stars would be sufficiently blue that they would be faint in K.

In order to salvage these data it was decided to combine the zeropoints over neighbouring frames. The zeropoint was determined for each frame where the reference star was brighter than $10\,\sigma$ using the magnitude offset with respect to the reference stars on overlapping frames taken on photometric nights. As there were usually several of these their median was taken. The scatter among these different zeropoints gives an extra cross-check on the reliability of our photometry. Figure 2.4 shows the RMS scatter of the zeropoints about the median plotted against K magnitude. As expected for a $10\,\sigma$ limited sample most of the points fall within $\Delta K \lesssim 0.1$.

To determine zeropoints for the runs with faint reference stars the median zeropoint of each group (in run order) of five bright reference stars was first determined to reduce the intrinsic scatter. Then each run was zeropointed by interpolating between these medians.

Figure 2.5 shows the zeropoint plotted against run number for an example photometric night and a non-photometric night. The dots are the zeropoints determined from the

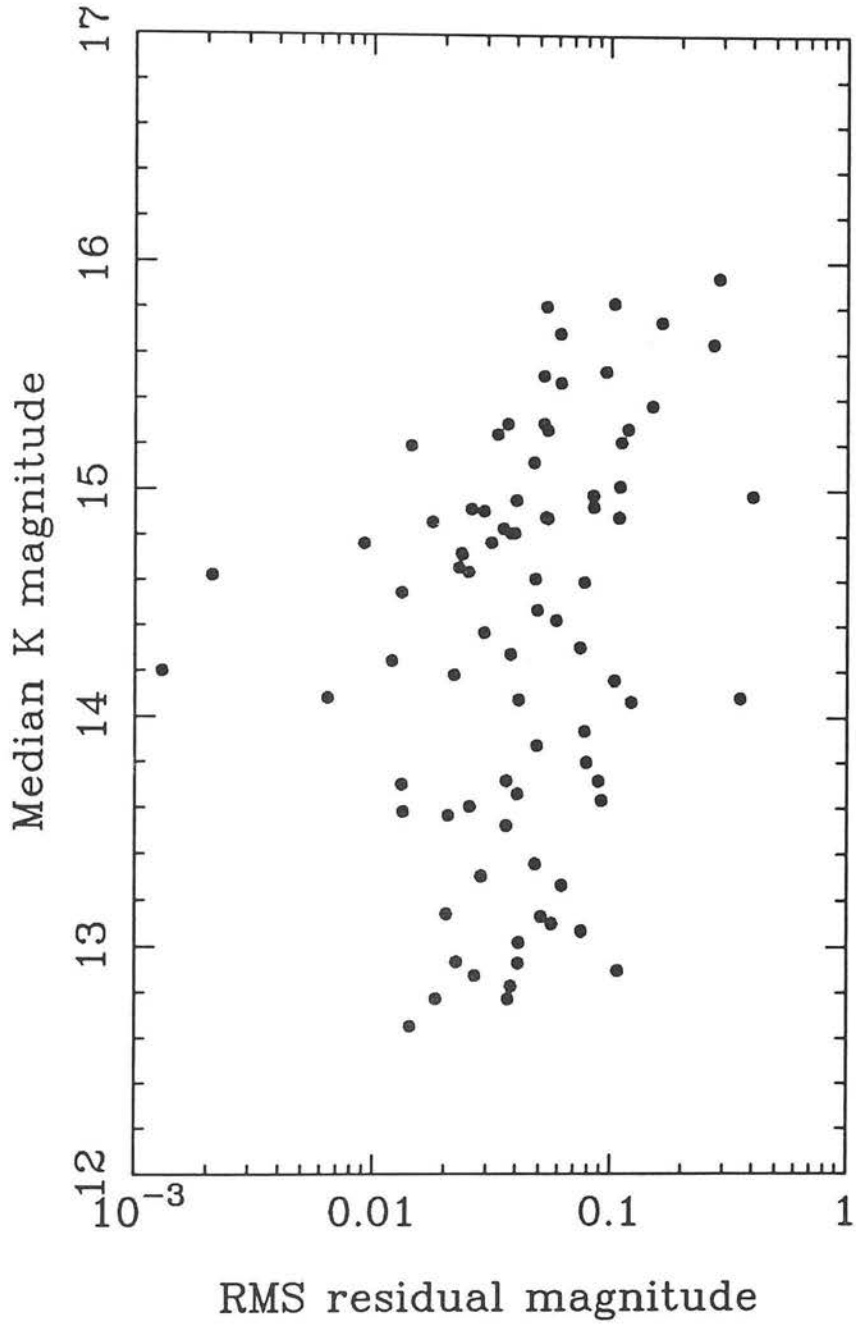

Fig. 2.4 RMS scatter of separate determinations of reference star K magnitudes (brighter than $10\,\sigma$) about their median plotted against K magnitude.

bright reference stars and the solid line is the median filtered interpolation. It can be seen for the photometric night that this curve is close to a straight line at the abscissa while, on the non-photometric night, the line makes large scale excursions from the abscissa of the order of ± 0.5 mag. The typical scatter about the lines is about 0.1 mag as would be expected from $10\,\sigma$ objects

2.5.4 Constructing the mosaics

Once the zeropoints were determined for each of the components of the 4-mosaic it was possible to correctly mosaic the images together and preserve the absolute photometry. Up to 8 sub-images had to be mosaiced together — 2×2.5 minute exposures of the 2×2 mosaic. The steps used were:

1) Using the reference star centroids the sub-images were registered to 1 pixel accuracy. Dividing up each pixel and registering to sub-pixel accuracy was experimented with but was found to be unnecessary. No sky levels had to be worried about as this was removed before the initial image detection stage (see section 2.5.1).

2) The resultant flux $f(x, y)$ in each mosaic pixel was computed as the weighted sum of the counts in each pixel $f_j(x, y)$ in sub-image j:

$$f(x,y) = \frac{\sum_j w_j Z_j f_j(x,y)}{\sum_j w_j}$$

The weights w_j for each sub-image were taken as:

$$w_j = \frac{1}{(\mathrm{RMS}_j)^2}$$

The Z_j values were scaling factors determined from the zeropoints which convert counts to flux units.

3) For convenience in the photometry the mosaics were scaled so that the zeropoint was 20 magnitudes. As the zeropoints were applicable to the chosen aperture this is correct for the same aperture.

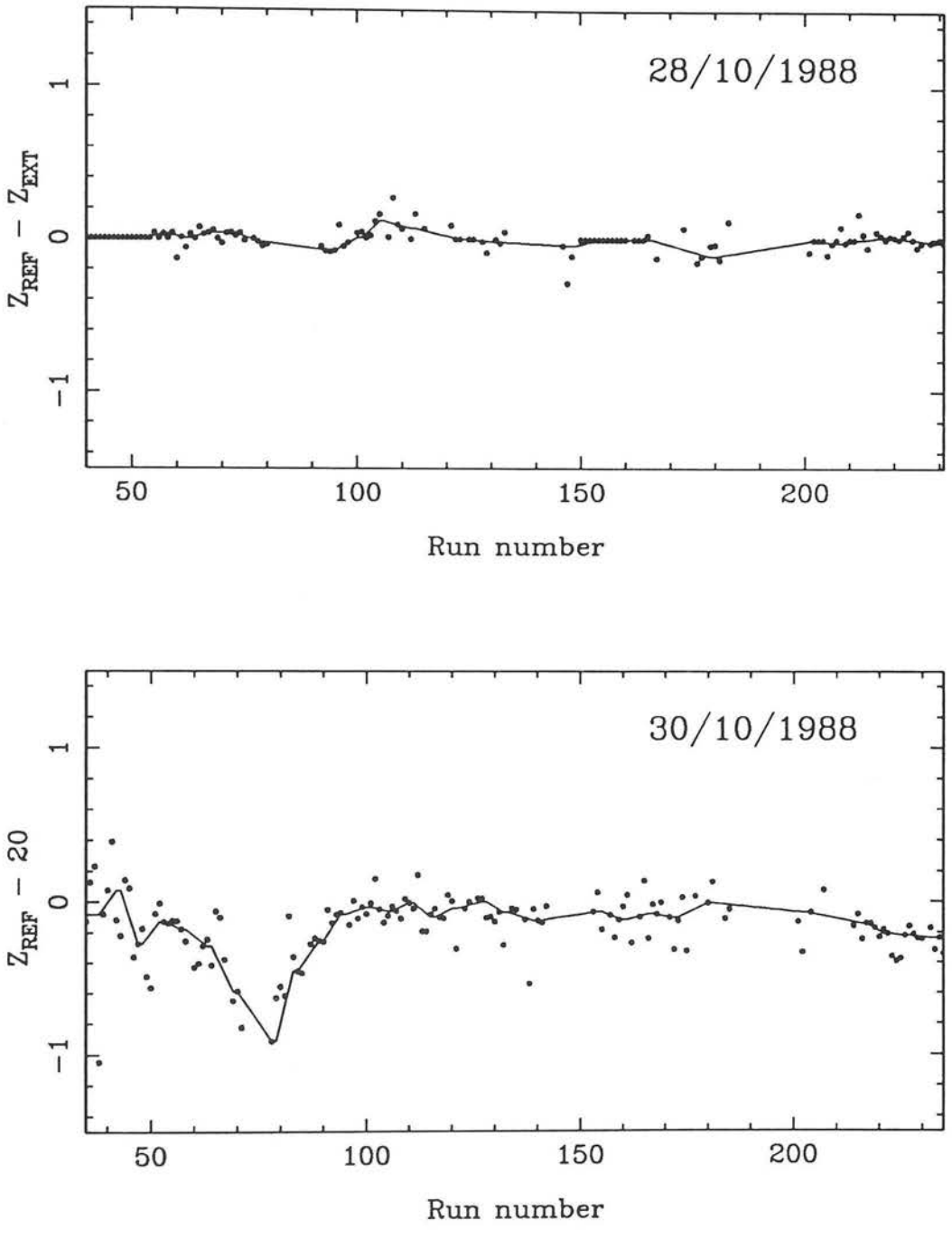

Fig. 2.5 The zeropoints determined by cross-night calibration of reference stars with S/N > 10 plotted against run number . The upper plot is for one of the photometric nights and shows the difference of this zeropoint from that determined from the extinction curves. The lower plot is for one of the non-photometric nights — the drift of the zeropoint with time is clearly visible. The solid line shows the median filtered interpolation adopted.

2.5.5 Mosaic image detection and photometry

This proceeded more or less as for the individual sub-images. One complication is that some portions of the mosaic with different overlap factors have different amounts of noise and this had to be allowed for in the image detection, though this was not so important for the photometry.

This was done by diving each image by a "mask" image, whose pixel values reflected the local noise average and then using the result for the image detection. Then using these coordinates the photometry was performed on the original image.

The mask was constructed as

$$f(x,y) = \sqrt{\langle f(x_i,y_i)^2 \rangle_\Box}$$

where $\langle\rangle$ means median instead of mean and the pixel values $f(x_i, y_i)$ are combined over a box centred on pixel (x, y). It was found by experimentation that a 9×9 box worked best and was least sensitive to objects while correctly reflecting the local RMS.

The typical RMS on a twice-covered (i.e. 5 minutes total exposure) portion of a mosaic was $\simeq 25\,e^-$ which was equivalent to a $3\,\sigma$ limiting magnitude of K = 17.5 in a 4″ aperture. This is well within the factor of 2 uncertainties typical of S/N calculations.

Of course the mosaicing procedure introduces slightly different depths in different parts of the survey. This has to be allowed for in the analysis of the scientific results.

2.6 Construction of Object Catalogues

2.6.1 Coordinate transformations

To go from X,Y coordinates on the 4-mosaics to accurate RA and DEC coordinates it was decided to check for possible small chip rotations with respect to the North-South axis and deviations from the nominal image scale.

The measurements were performed with respect to the original Schmidt plate catalogues used to select the reference stars. These have RA and DEC coordinates accurate to $\simeq 0.5''$ and are normalised to 1950.0 coordinates.

First the RA and DEC coordinates were computed for each object in each 4-mosaic assuming zero rotation, a scale of 1.2″/pixel and with the reference star having its nominal Schmidt plate coordinates. Then each 4-mosaic catalogue was paired up with the Schmidt plate catalogues using a tolerance $(\Delta\mathrm{RA}, \Delta\mathrm{DEC}) = 2''$.

The general coordinate transformation is given by:

$$\begin{pmatrix} x' \\ y' \end{pmatrix} = \begin{pmatrix} \alpha & \beta \\ \gamma & \delta \end{pmatrix} \begin{pmatrix} x \\ y \end{pmatrix} + \begin{pmatrix} a \\ b \end{pmatrix}$$

This allows the inclusion of rotation, shear and scale changes and since it is linear is easy to fit in one step by least-squares. The disadvantage is that it has 6 free parameters and so they are poorly constrained if there are only a few pairs on each image, as is the case with IRCAM.

By constraining the axes to be orthogonal the two shear parameters can be discarded resulting in:

$$\begin{pmatrix} x' \\ y' \end{pmatrix} = (1+R) \begin{pmatrix} \cos\theta & -\sin\theta \\ \sin\theta & \cos\theta \end{pmatrix} \begin{pmatrix} x \\ y \end{pmatrix} + \begin{pmatrix} a \\ b \end{pmatrix}$$

where $(1 + R)$ is the multiplicative change in the scale factor, θ is the rotation angle and a,b are constant offsets. Unfortunately this is now a *non-linear* problem and the exact solution via least-squares would require iteration. However the chip should be quite accurately aligned N-S E-W to start with so if θ is assumed to be small we can expand the trigonometric functions to first order giving:

$$x' = x + xR - \theta y + a$$
$$y' = y + yR + \theta x + b$$

This is now a linear transformation and a least-squares solution for R, θ, a and b can be obtained from the data in a one step solution. From the matching we have a set of pairs for each 4-mosaic with original coordinates (x_i, y_i) and transformed coordinates (x'_i, y'_i).

Minimising:

$$S = \sum_{\text{pairs}} \left[(x' - x - xR + \theta y - a)^2 + (y' - y - yR - \theta x - b)^2 \right]$$

by differentiating S with respect to R, θ, a and b in turn and equating to zero we get after some algebra:

$$\theta = \frac{\sum(x\Delta y - y\Delta x) - \left[\frac{\sum x \sum \Delta y - \sum y \sum \Delta x}{n}\right]}{\sum(x^2+y^2) - \left[\frac{\left(\sum x\right)^2 + \left(\sum y\right)^2}{n}\right]}$$

$$R = \frac{\sum(x\Delta x + y\Delta y) - \left[\frac{\sum x \sum \Delta x + \sum y \sum \Delta y}{n}\right]}{\sum(x^2+y^2) - \left[\frac{\left(\sum x\right)^2 + \left(\sum y\right)^2}{n}\right]}$$

where

$$\Delta x = x' - x$$

$$\Delta y = y' - y$$

and the sums are over all pairs on the 4-mosaic matched with the Schmidt plate.

When the least-squares derivation is gone through in detail it is found, as may be expected, that θ and R are independent of each other (i.e. the formula for each is unchanged if the other is regarded as a given parameter rather than one to be determined). Also we get for arbitrary θ, R (i.e. either a given or a free parameter):

$$a = \frac{1}{n}\left(\sum \Delta x - R\sum x + \theta \sum y\right)$$

$$b = \frac{1}{n}\left(\sum \Delta y - R\sum y - \theta \sum x\right)$$

The least-squares fit R and θ was determined for each 4-mosaic and a histogram of these values is shown in Figure 2.6. It can be seen that $\theta = 1°$ at a $2\,\sigma$ detection level. Also R is only $\simeq 1\,\sigma$ off zero. It can thus be seen that the initial assumption of small (R, θ) was correct. The validity of the one-step solution was checked by applying the (R, θ, a, b) coordinate transformation and repeating the least-squares minimization to give new values

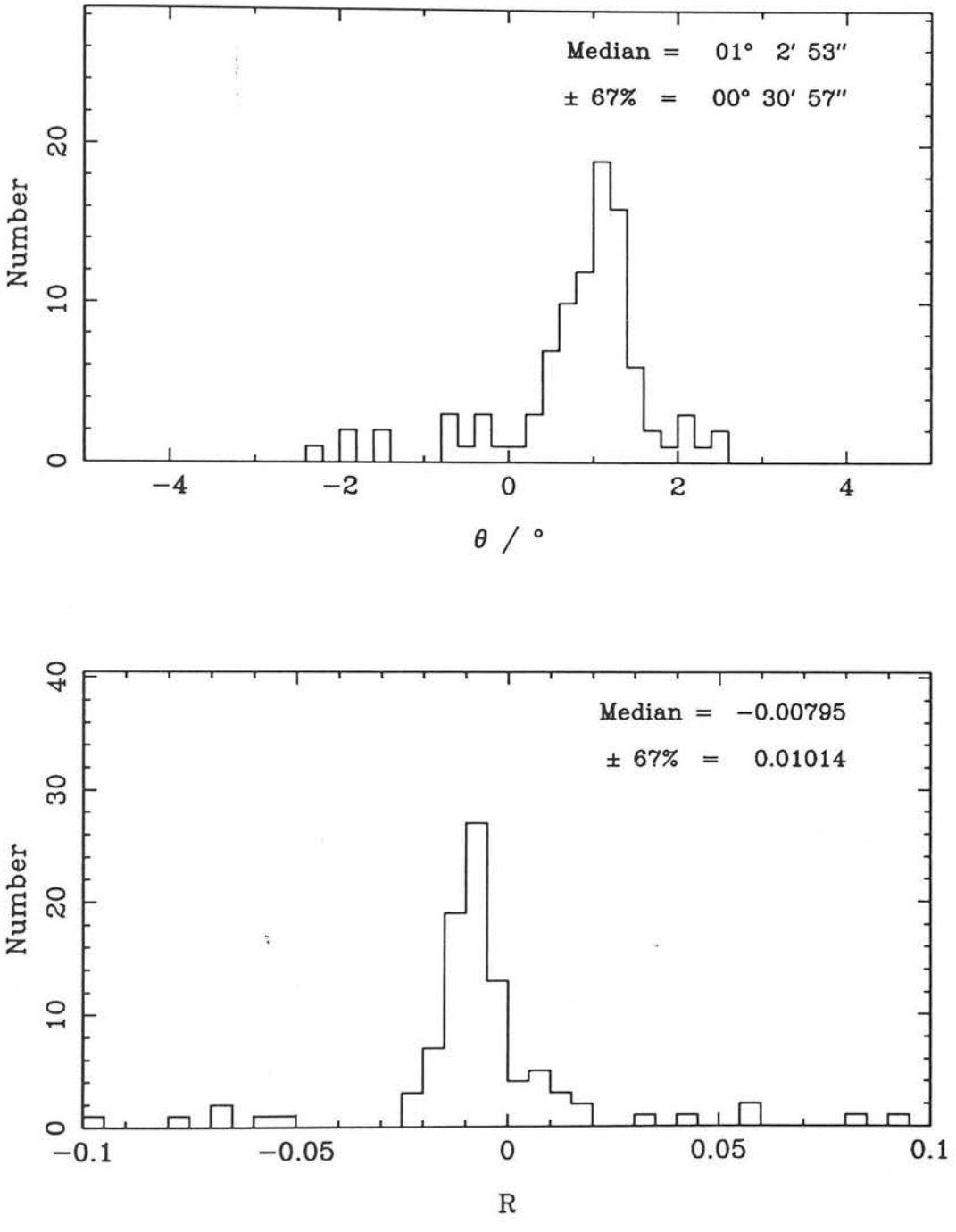

Fig. 2.6 The histograms of the best fit transformations in rotation (top) and scale factor (bottom) of each IRCAM 4-mosaic onto the Schmidt plate coordinate system. This is for all the 4-mosaics in the combined October and March fields having ≥ 3 pairs with Schmidt plate objects.

(R', θ', a', b'). These were close to zero and the RMS residual $\sqrt{S/N_{\rm pairs}}$ was unchanged. So the one-step solution was good enough and no more iterations were required.

The initial assumed scale factor was 1.2″/pixel so the best fit pixel scale was 1.19″/pixel, $\simeq 5\,\sigma$ away from the 1.24″/pixel claimed in the IRCAM users guide. The large scatter is due to the small number of objects (2–3) paired up on each mosaic with Schmidt data. The histograms were also replotted for different RA bins and night bins. Although the individual samples were then smaller and noisier no systematics effects were detected with RA or night. The derived histograms were also consistent, within the errors, between the different observing runs. These scale and rotation effects cause positional errors of $\simeq 1''$ across the whole width of the IRCAM chip and are small enough that they were unnoticed in normal use. However if the nominal 1.24″/pixel figure had been blindly believed the total error across the chip would have been 3″ which would have seriously compromised the later catalogue pairing.

The best fit values of R and θ were adopted for each run and the pairing and least-squares analysis were repeated with these fixed to obtain the best offsets a and b which were then applied to each 4-mosaic catalogue. The typical RMS positional residuals after the transformation were also calculated and output as a check. They were typically 0.3″–0.7″ as expected.

All the mosaic catalogues were then stacked up to produce two master catalogues — one for the October fields and one for the March fields.

2.6.2 Removal of duplicated catalogue objects

Most of the overlaps in the infrared dataset were internal to the 4-mosaics and were thus removed by the mosaicing procedure. However there was a small amount of overlap between adjacent 4-mosaics which resulted in the same object appearing twice in the catalogue occasionally. To remove these correctly would have required the mosaicing together of the separate 4-mosaics over each 0.5° × 0.5° field which was not feasible with the computational resources available.

A simple procedure was adopted to remove this minor contamination — for all objects any object on a *different* 4-mosaic which was within 3″ of it was expunged from the catalogue.

2.7 Summary

A total area of 594$\Box'$ was surveyed with 826 IRCAM images. Using a median filtering technique the images were flatfielded to $\lesssim 1$ part in 10^4 and all the frames were essentially limited by sky shot and readout noise. The limiting depth was K = 17.5 ($3\,\sigma$ in a $4''$ aperture) over 64% of the area and K = 17.1 over the rest.

576 objects were automatically detected in the October fields with fluxes $> 5\,\sigma$ ($4''$ aperture) and 312 were detected in March fields ($8''$ aperture). Using cross-calibration techniques the magnitude zeropoints on all the frames were determined to $\lesssim 0.1$ mag and photometric catalogues were constructed with a positional accuracy of $\simeq 0.5''$.

3 CCD IMAGING OBSERVATIONS

3.1 Introduction

In order to relate the properties of an infrared selected sample of galaxies to those of galaxies seen in deep optical CCD surveys it is necessary to have deep broad band optical colours for the objects. Spectroscopy at these faint magnitude limits requires hours of 4 m telescope time per object and so the most efficient way of obtaining some spectral information is via broad band UBVRI colours. Because of the large areal coverage of the CCD compared to IRCAM the survey area can be covered very quickly in several broad bands. The colours can then be compared with those of model galaxy spectra to look at the evolution of the galaxy population with survey depth.

Even if only one optical magnitude is obtained for each infrared object this is still important as the infrared survey is probing an unknown region of parameter space. There might be new populations of very red objects that have extreme optical-infrared colours or even not appear at all in the optical. Examples include primeval galaxies at high redshift (see chapter 1) and cool brown dwarf stars in the local Galaxy.

Finally optical data provides the possibility of carrying out star/galaxy separation on the survey objects. This is based on the relative sizes of star and galaxy profiles and since the star profile changes from image to image due to seeing variations it is best to try and define the star profiles separately on each image and this requires a sufficiently large number of objects. It would be be less reliable to do this on the IRCAM frames as each one only contains 1–2 objects. In addition the pixel scale on the CCD is smaller (area is not as big a consideration as for IRCAM) and thus the profiles are better sampled.

3.2 Observations

All the CCD observations were performed on the 2.5 m Isaac Newton Telescope (INT). This telescope is situated at an altitude of 2400 m at the Observatorio Astrofisico del Roque de los Muchachos on the island of La Palma in the Canary Islands.

3.2.1 Integration times and strategy

The INT has a choice of two CCD detectors — the RCA SID 501 and the GEC PS603. It was decided to use the RCA chip primarily because it has a much higher quantum efficiency (about double at 7000 Å and more at shorter wavelengths) and covered a larger area on the sky due to its larger pixels. The GEC has a much smaller readout noise but because the observations would be sky background limited this was irrelevant. The RCA is 512 × 320 pixels with a scale of 0.74″/pixel at the INT prime focus. The quantum efficiency ranges from about 40% at 4000 Å to 70% at 6000 Å.

In order to obtain accurate colours at the survey limit of K = 18 for even very red objects the integration times in table 3.1 were aimed for.

It was not possible to get complete coverage of all the IRCAM data in all 4 optical bandpasses due to time and weather. It was decided that the most important optical band was R since for the primeval galaxy part of the program (see chapter 1) this best matched the redshift range of interest ($z > 4$) and the I band required much longer integration times. The next choice was B partly because this provided some information on primeval galaxies but mainly because for the study of galaxy evolution B − K colours provide the most sensitive measure of star formation. In addition the existing studies of faint galaxy magnitude and redshift distributions were predominately based either on Schmidt plate data (using the close b_j filter) or deep CCD B counts. Next came V and I CCD images.

Because of the high density of IRCAM fields in the October data it was decided to cover the 9 existing 10′ × 10′ fields using a filled-in grid pattern. We were then able in October 1988 to get IRCAM data in areas where we already had optical data from September 1988 by filling in between the existing gaps in the infrared data. Figure 3.1 shows an example of one of our October fields with the CCD and IRCAM positions shown. The CCD coverage is in a 2 × 4 pattern.

Table 3.1: CCD integration times used

Band	Sky brightness[1]	$1\sigma 1s^2$	t_{int}	Mag. limit[3]
B	22.3	24.4	600 s	25.0
V	21.4	23.7	600 s	24.3
R	20.4	23.1	600 s	23.7
I	19.3	22.0	2000 s	23.2

Notes:

1.) For dark of moon. Calculated from Table 2 in Wall & Laing 1986 and expressed in mags/□″.
2.) Calculated noise/pixel expressed in magnitudes.
3.) Limiting magnitude is for a 3 σ detection in a 4″ aperture.

In contrast the March fields had a much lower density and the optimum strategy was to carefully place the CCD so as to maximize the number of IRCAM fields. The overlaps were still quite large and could be used for cross-calibration. A number of the positions were taken with short exposures and were carefully placed to overlap a number of other images so as to allow their calibration. Figure 3.2 shows an example of one of the March fields.

3.2.2 Observing log

Three observing runs, of four nights each, were awarded for this project between 1988 and 1989. The details are given below:

9–12th April 1988. 16 positions were taken in R (2 × 300 s), 16 in B (2 × 500 s), 18 in V (2 × 300 s) and 14 in I (4 × 500 s). All four nights suffered from various degrees of cloud problems although continuous observation was possible. In addition there was evidence for the presence of some sub-Saharan dust in the atmosphere. Unfortunately the millisecond timer on the CCD camera was defunct for the first three nights and so all the exposure times had ±0.5 s random errors making absolute photometry impossible.

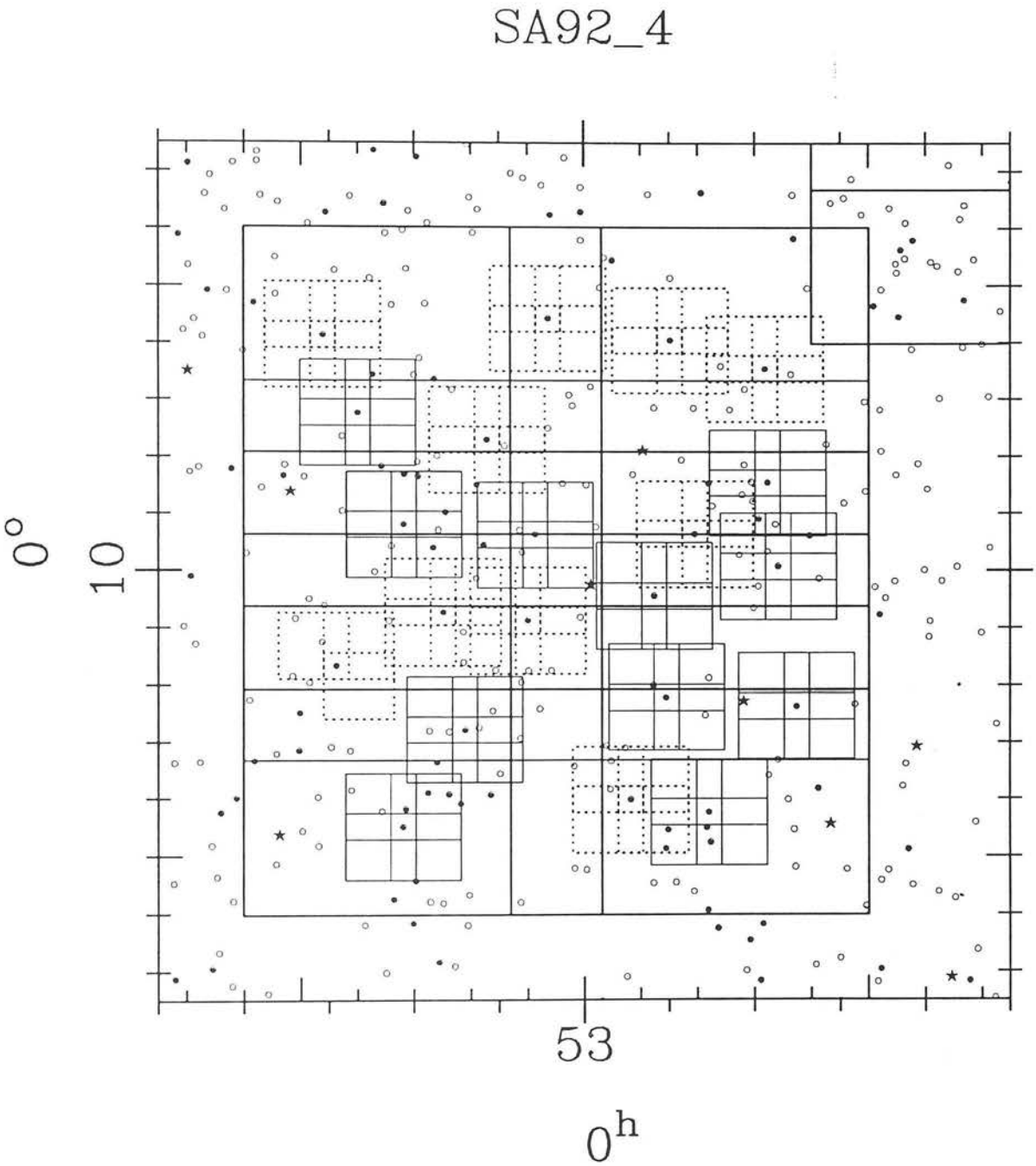

Fig. 3.1 The CCD positions (thick solid lines), IRCAM positions from the October 1988 run (thin solid lines) and IRCAM positions from the October 1987 run (thin dotted lines) in one of the October fields. The field of view is $15' \times 15'$.

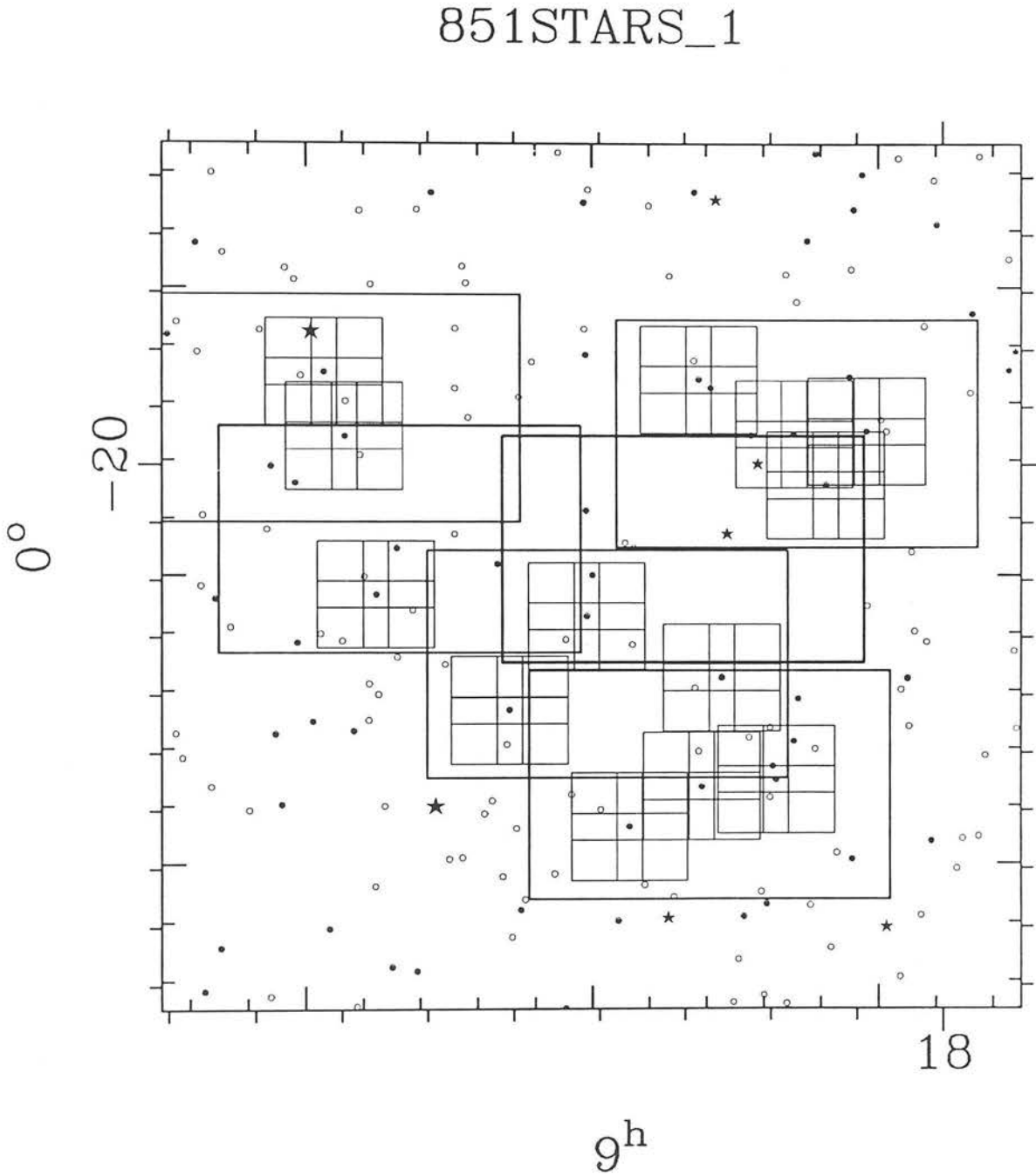

Fig. 3.2 The CCD positions (thick solid lines) and IRCAM positions (thin solid lines) in one of the March fields. The field of view is 15′ × 15′.

The photometry of the last night was checked and showed large (0.5 magnitude) zeropoint variations leading to the conclusion that this night was non-photometric also.

5–10th September 1988. This run was performed jointly with another University of Edinburgh project which was awarded 2 nights. The other project involved absolute photometry of radio galaxies and so it was decided, in order to make the most efficient use of the time, to observe infrared fields whenever the conditions looked non-photometric as these could be cross-calibrated. The first 2 nights turned out to be photometric and 1.5 nights were lost completely due to cloud cover. In the R band 72 positions (600 s exposures) were observed giving complete coverage of the October infrared fields of which 17 were observed in B (600 s exposures). Because of the grid mosaicing strategy adopted all the zeropoints could be tied down via cross-calibration.

5–8th April 1989. 46 positions were taken in R, 48 in B, 5 in V and 5 in I. The first night was clear and photometric with good seeing ($\simeq 1''$) and so the observations concentrated on deep 600 s exposures of fields that had not been covered the previous April. The second night suffered throughout from patchy cirrus and more deep 600 s exposures were taken in B and R. On the third night conditions were again photometric but the seeing was unexpectedly poor ($\simeq$ 2–3″). It was decided to take short 100-300 s exposures at strategically placed positions in order to calibrate the data from April last year and some of that taken the previous night. No observations were possible on the fourth night due to blizzard conditions.

To summarize 134 positions on the sky were observed in the R band, 81 in B, 23 in V and 19 in I. The overlaps were such that it was possible to accurately obtain zeropoints for all the frames. All the infrared fields had R band coverage while in the March fields all of them had B as well.

3.3 Data Reduction

The images were reduced following standard CCD procedures. They were bias and dark frame subtracted and then divided by a flatfield. A master flatfield was constructed for each night by median filtering the normalised data frames in each band as described in section 2.4.3 and the photon shot noise limit was reached. The RCA chip had one bad column which was interpolated over using the method described in section 2.4.4.

3.3.1 Standards and calibration.

The standard stars used were selected from the list of Landolt (1983) according to current hour angle and colour $0.5 < \mathrm{B} - \mathrm{R} < 1.5$ to match the colours typical of faint galaxies.

On plotting Δ (= Real magnitude $+ 2.5 \log_{10}$(Counts/sec)) as a function of airmass ($\sec z$) for the photometric nights it was found that the residual RMS scatter about the best fit line was about 3–5 times greater in the B band than in R. It was suspected that there was a residual colour term between the Landolt and CCD magnitude systems due to the difference in detector response curves (Landolt used a photoelectric detector for his work). This was investigated by fitting (using least-squares) a 3 parameter model:

$$\Delta = C - \alpha \sec z - \beta(\mathrm{B} - \mathrm{R})_{\mathrm{LAN}}$$

It was found for all the nights that β was $\simeq 0$ in R and that the effect on the size of the RMS was negligible. This was also true in V and I. However in the B band a colour term of $\beta \simeq -0.1$ was typically found and the RMS was reduced to a value comparable to the other bands. Table 3.2 shows the colour and extinction terms derived for each photometric night in the survey.

It is important to note that only the *extinction* corrections were applied to the data, i.e. a CCD magnitude system was defined where

$$\mathrm{B_{CCD}} = C_{\mathrm{B}} - 2.5 \log_{10} (\mathrm{Counts/sec})_{\mathrm{B}} - \alpha_{\mathrm{B}} \sec z$$

$$\mathrm{R_{CCD}} = C_{\mathrm{R}} - 2.5 \log_{10} (\mathrm{Counts/sec})_{\mathrm{R}} - \alpha_{\mathrm{R}} \sec z$$

Table 3.2: Colour terms and extinctions for photometric nights

Date	Band	Aperture	α	β	C	RMS
5/9/88	B	4″	0.281	−0.105	23.901	0.039
5/9/88	R	4″	0.106	—	23.836	0.016
6/9/88[1]	R	4″	0.190	—	23.937	0.013
5/4/89[2]	B	8″	0.205	−0.070	23.990	0.015
5/4/89	R	8″	0.144	—	23.959	0.024
7/4/89[3]	B	8″	0.218	−0.070	24.045	0.059
7/4/89	V	8″	0.141	—	24.072	0.030
7/4/89	R	8″	0.133	—	23.949	0.050
7/4/89	I	8″	0.037	—	23.259	0.026

Notes:

1.) This night was photometric apart from at the start when there was thick cloud. Exclusion of standards from this part gives a good fit. The data taken in the first part of the night was assumed to be non-photometric.

2.) For consistency with the other March field data an 8″ aperture was used despite the good seeing on this night. The extinction and colour terms were taken from fits at asymptotically large apertures (which made negligible difference).

3.) On this night the points at the highest airmass had the worst seeing. This gives an ambiguity for small apertures as to whether or not light loss at high airmass is due to extinction or not. To circumvent this problem the extinction value determined at asymptotically *large* apertures was force-fitted to the data at the 8″ aperture, ignoring the high airmass points ($\sec z > 1.5$). As all the data frames were taken at $\sec z < 1.5$ this gives the best fit. In addition the colour term from 5/4/89 was used to reduce the number of free parameters in the fit.

This is then related to the Landolt system by the colour equations :

$$B_{LAN} = B_{CCD} - \beta(B - R)_{LAN}$$
$$R_{LAN} = R_{CCD}$$

which can be inverted to give :

$$B_{LAN} = B_{CCD} - \frac{\beta}{1+\beta}(B - R)_{CCD}$$

The magnitude of an A0 star is zero in the CCD systems by virtue of the way it was defined, so the CCD system is a proper magnitude system obeying all the rules for magnitudes. Transforming all the magnitudes onto Landolt would have required B and R data for all the objects in the survey which was not available so the data were left in the natural CCD system. Neither system is in any fundamental sense better than the other, it just has to be remembered when interpreting the magnitudes what their exact definition is.

As an example of this later chapters will compare the observed galaxy colours with those of model spectra. To compute a magnitude requires the flux of the galaxy integrated through the filter profile ratioed with that of an A0 star integrated through the same filter. As CCD magnitudes are being compared with, the filter profile used was the standard Kitt Peak profile for the appropriate band multiplied by the response of the RCA CCD detector. This then gives the correct magnitude in the CCD system.

3.4 Construction of Optical Object Catalogues

The image detection proceeded exactly as described in section 2.5.1 for the infrared images except that the RMS for the thresholding was computed from a bigger box (100 × 100 pixels). Indeed the optical performance was better because the pixels were smaller (0.74″) and so the object profiles were better sampled. Less real objects were lost and less spurious features were picked up, which was verified by visual checking of the images. Some of the frames suffered from background variations induced by the presence of dust on the camera window. These were effectively removed by the 20″ × 20″ median filtering.

Aperture photometry was performed on the objects using a 4″ diameter aperture for the October data and 8″ for the March data and object catalogues were constructed for each image. These were then paired with Schmidt plate data to obtain the rotation and scale transformations as described in section 2.6.1 for the infrared data.

Example R and θ histograms for one of the observing runs are shown in figure 3.3. The typical $|\theta|$ values are in the range 0.5–1° for different observing runs with errors of the order of 5–8′. It was not unexpected that the value would change because unlike IRCAM which has a fixed base (it has no need to rotate being almost square) the INT prime focus CCD system is mounted on a movable rotator and its orientation is constantly being changed for different observing programs. The R values were constant at a value of 0.006 ± 0.002. This corresponds to a scale at prime focus of 0.7444 ± 0.0015″/pixel. After applying the best fit values for each observing run these errors correspond to a positional error of $\simeq 1$″ across the full length of the chip. The typical RMS position residual after application of this procedure was 0.5-0.7″.

Next the data had to be calibrated with the previously determined zeropoints. Note this was done after image detection and cataloguing and not before (by scaling the images). This was because most of the data was not taken on photometric nights and the zeropoints for these had to be determined by cross-matching object lists with photometric data. This was done in slightly different ways for the October and March datasets, this is detailed below.

3.4.1 Cross-calibration of October fields data

The data consisted of 9 fields each with 8 CCD positions arranged in a 2×4 grid pattern almost completely filled in R but with only a few positions in B. Only some of the data were taken on photometric nights and had zeropoints. The procedure adopted to obtain the magnitude offset between two images was first to pair the objects with a tolerance of 3″. Then the median magnitude difference of the brightest 10 objects were taken as the zeropoint and the weighted (with respect to the magnitude errors) RMS residual about this was taken as the error. This was found, after some experimentation, to be the optimum scheme. Extending the pairing to fainter objects tended to make the errors worse.

As a test of the errors involved in using this procedure to obtain relative zeropoints it

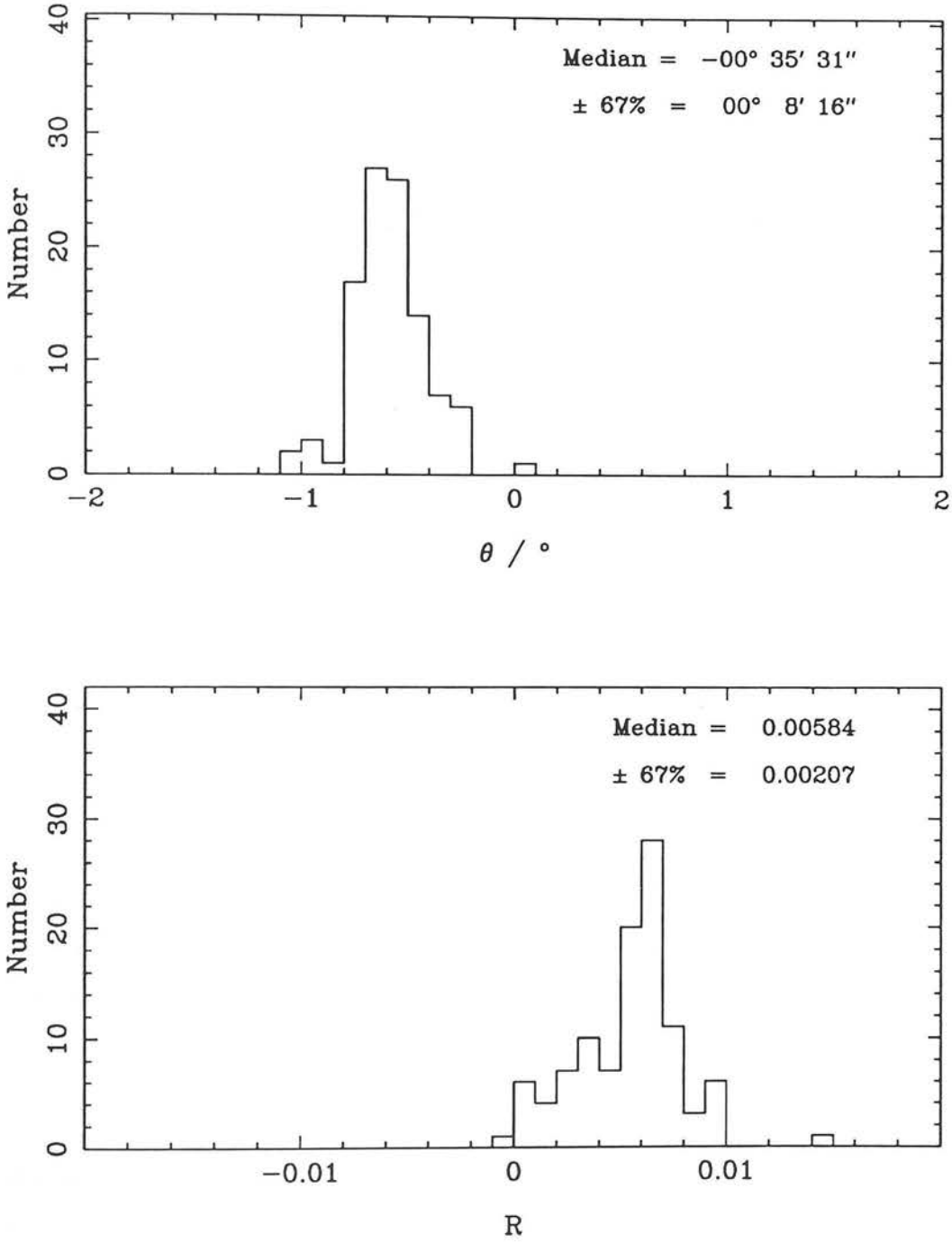

Fig. 3.3 The histograms of the best fit transformations in rotation (top) and scale factor (bottom) of each CCD catalogue having ≥ 3 pairs with Schmidt plate objects onto the Schmidt plate coordinate system. This is for the data taken in the April 1989 observing run.

was applied to all the *photometric* data. These were matched with their photometric neighbours (if any) and the magnitude offset found. Apart from the first part of night 2, which was mentioned in note 1 of table 3.2, the typical shifts were of the order ± 0.05 mags — this can be seen in the upper plot of figure 3.4. Thus if a series of images are calibrated across the error will grow as a random walk — i.e. $0.05\sqrt{N}$.

The non-photometric images were then paired onto the photometric data. The order in which images were matched up was determined by the particular geometry of the individual subfields, i.e. which parts were photometric, in order to minimize the number of frames being calibrated across to reach a desired frame. The errors associated with each matching are about 0.05 mags as can be seen in the lower plot of figure 3.4 which are of the same order as the photometric–photometric relative zeropoints. This is what is expected if the difference in these relative zeropoints comes primarily from the error in the cross-calibration. The few anomalously high values are caused by 1–2 objects being mispaired. Inspection of plots produced for each overlap match showed that the median magnitude shift taken was hardly affected by this although the RMS about this median was spuriously high. The maximum number of images matched across to calibrate a particular image was 5 in a few extreme cases — this would give a systematic error of 0.1 mags in the zeropoint at most.

As a check on the astrometry the RMS *position* residuals between the paired overlap objects was examined and was found to range from 0.5–1.5″for different overlaps. This is slightly worse than $\sqrt{2}\times$ that found when calculating the coordinate transformations with respect to Schmidt plate data, probably because the CCD overlap objects are biased towards the edge of the chip.

3.4.2 Cross-calibration of March fields data

As can be seen by comparing figures 3.1 and 3.2 the geometry of the CCD arrangement is considerably more complex in the March fields. The prospect of going through each one and choosing complex matching orders (in up to 4 bandpasses) was not attractive and so a more sophisticated algorithm was invented.

The allowed the zeropoints of all the non-photometric frames to be free parameters and then finding a least-squares solution for them which minimizes the magnitude overlap

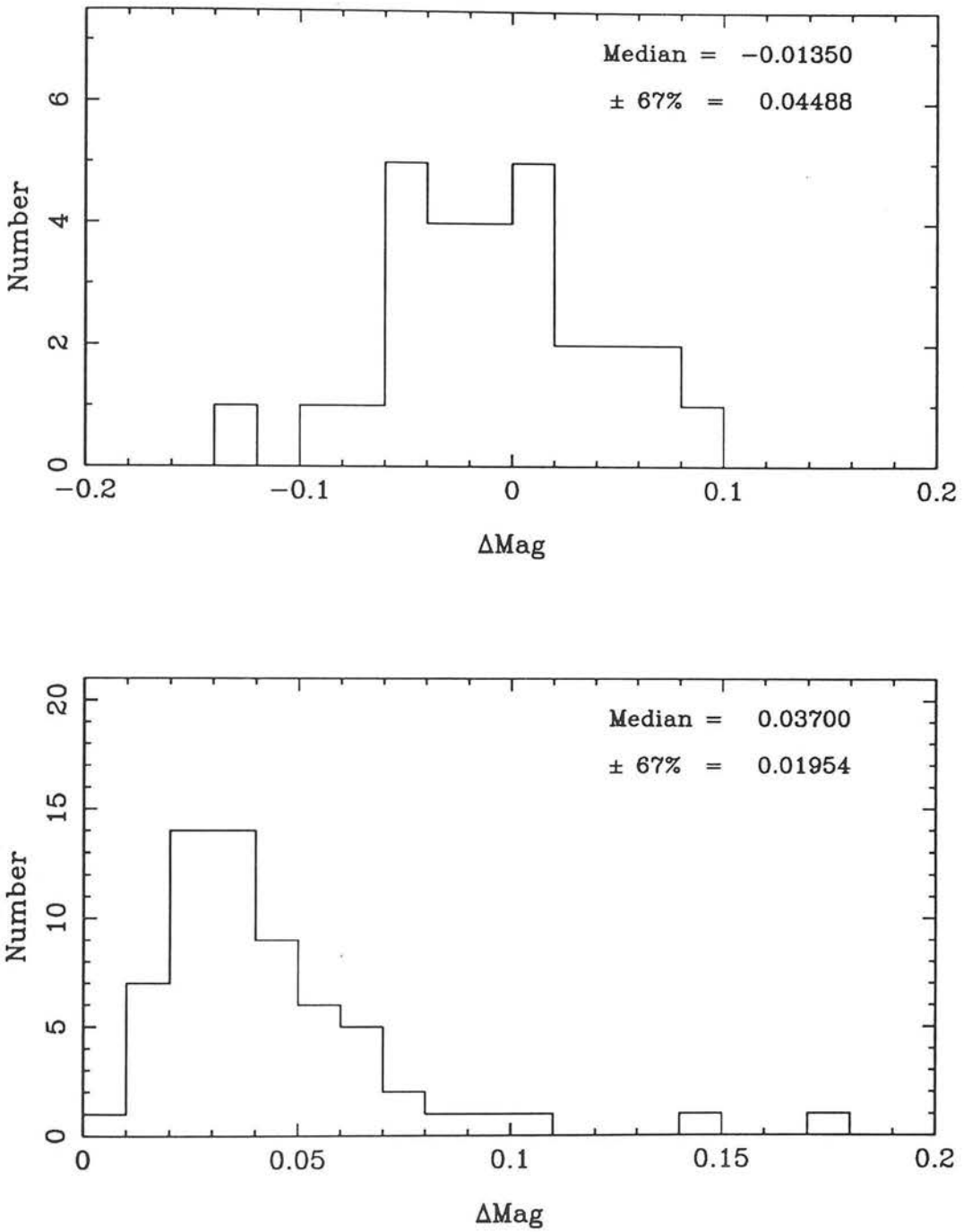

Fig. 3.4 The errors on the magnitude calibrations in R for the October CCD images. The upper histogram shows the distribution of the magnitude differences between overlapping *photometric* images and the lower histogram shows the errors on the magnitude differences on the overlaps used to calibrate the catalogues.

residuals via a matrix inversion.

Consider n frames of which $(1 \ldots m)$ are uncalibrated and $(m+1 \ldots n)$ are calibrated.

Let Δ_{ij} be the magnitude difference between frames i and j. This difference was determined, as for the October data, by taking the median magnitude difference of the 10 brightest objects in the overlap, paired with a tolerance of 3″.

$$\Delta_{ij} = \langle \mathrm{Mag_i} - \mathrm{Mag_j} \rangle_{\mathrm{pairs}} \qquad (\text{Note: } \Delta_{\mathrm{ij}} = -\Delta_{\mathrm{ji}})$$

Let a_i be the floating zeropoint of frame i. Therefore we have $a_i = 0$ if $i > m$.

If we define the overlap function:

$$\theta_{ij} = \begin{cases} = 1, & \text{if frames } i \text{ and } j \text{ overlap} \\ = 0, & \text{if no overlap} \\ = 0, & \text{if } i = j \end{cases}$$

Then the sum of squares to be minimized is:

$$S = \sum_{i=1}^{n} \sum_{j=1}^{n} w_{ij} \theta_{ij} (\Delta_{ij} + a_i - a_j)^2$$

where w_{ij} are the weights used for each match. In this case they were set equal to 1 though they could, for example, be set according to the errors on each overlap.

Differentiating with respect to a_i gives the m linear equations:

$$\frac{\partial S}{\partial a_i} = 4 \sum_{j=1}^{n} w_{ij} \theta_{ij} (\Delta_{ij} + a_i - a_j) = 0$$

This gives:

$$\sum_{j=1}^{n} w_{ij} \theta_{ij} \Delta_{ij} + a_i n(i) - \sum_{j=1}^{n} a_j w_{ij} \theta_{ij} = 0$$

where

$$n(i) = \sum_{j=1}^{n} w_{ij} \theta_{ij}$$

In the case where $w_{ij} = 1$ this is the number of *other* frames which overlap with frame i.

Now since

$$\sum_{j=1}^{n} a_j w_{ij} \theta_{ij} = \sum_{j=1}^{m} a_j w_{ij} \theta_{ij}$$

and

$$\sum_{j=1}^{n} w_{ij} \theta_{ij} \Delta_{ij} = \sum_{j=1}^{n} w_{ij} \Delta_{ij}$$

then one obtains the result

$$\sum_{j=1}^{m} (w_{ij} \theta_{ij} - \delta_{ij} n(j)) a_j = \sum_{j=1}^{n} w_{ij} \Delta_{ij}$$

This gives the set of matrix equations:

$$\sum_{j=1}^{m} A_{ij} a_j = b_i$$

$$A_{ij} = w_{ij} \theta_{ij} - \delta_{ij} n(j)$$

$$b_i = \sum_{j=1}^{n} w_{ij} \Delta_{ij}$$

The matrix **A** is $m \times m$ and the vector **b** is $m \times 1$. This can be inverted by standard algorithms, such as Gaussian Elimination, to give the a_i values in a one-step solution. It is not required that the CCD frames be contiguous — i.e. all connected together. If there are disconnected groups of frames then the matrix becomes block-diagonal and the different solutions become independent of each other. If there are uncalibrated frames which do not join up in any way onto calibrated frames then the matrix becomes singular so it cannot be inverted. These frames have to be removed from the list.

The overall RMS residual of the solution is given by:

$$\mathrm{RMS} = \frac{\sum_{i=1}^{n} \sum_{j=1}^{n} w_{ij} \theta_{ij} (\Delta_{ij} + a_j - a_i)^2}{\sum_{i=1}^{n} \sum_{j=1}^{n} w_{ij} \theta_{ij}}$$

A simple example is useful in order to clarify this technique. Consider the following arrangement of CCD images, where the * marks the calibrated images:

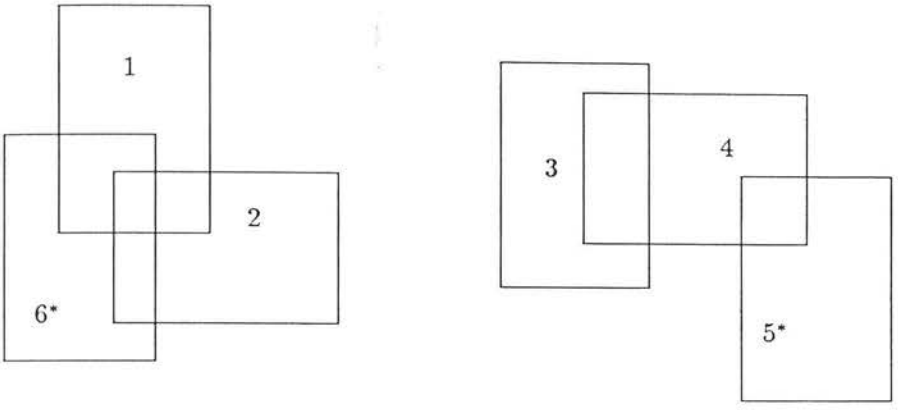

It is quite straight forward to work through the least-squares solution explicitly. For the left hand group,

$$S = (\Delta_{12} + a_1 - a_2)^2 + (\Delta_{16} + a_1)^2 + (\Delta_{26} + a_2)^2$$
$$\frac{\partial S}{\partial a_1} = 0 \quad \Rightarrow \quad a_2 - 2a_1 = \Delta_{12} + \Delta_{16}$$
$$\frac{\partial S}{\partial a_2} = 0 \quad \Rightarrow \quad a_1 - 2a_2 = \Delta_{21} + \Delta_{26}$$

which results in the solutions:

$$a_1 = \frac{2}{3}\Delta_{61} + \frac{1}{3}(\Delta_{21} + \Delta_{62})$$
$$a_2 = \frac{2}{3}\Delta_{62} + \frac{1}{3}(\Delta_{12} + \Delta_{61})$$

For the right hand group,

$$S = (\Delta_{43} + a_4 - a_3)^2 + (\Delta_{45} + a_4)^2$$
$$\frac{\partial S}{\partial a_3} = 0 \quad \Rightarrow \quad a_3 - a_4 = \Delta_{43}$$
$$\frac{\partial S}{\partial a_4} = 0 \quad \Rightarrow \quad a_3 - 2a_4 = \Delta_{43} + \Delta_{45}$$

which results in the solutions:

$$a_3 = \Delta_{43} + \Delta_{54}$$
$$a_4 = \Delta_{54}$$

It can be seen that these results make intuitive sense. In the first case the offsets are linear combinations of the offsets along two different paths from the calibrated image. In the

second case there is only one path and the offsets are just the sum of the individual offsets along that path.

Now we can do the whole thing in one go via the general matrix method outlined above. The overlaps give:

$$n(i) = (2, 2, 1, 2, 1, 2)$$

which together with the overlaps result in the matrix equation:

$$\begin{pmatrix} -2 & 1 & 0 & 0 \\ 1 & -2 & 0 & 0 \\ 0 & 0 & -1 & 1 \\ 0 & 0 & 1 & -2 \end{pmatrix} \begin{pmatrix} a_1 \\ a_2 \\ a_3 \\ a_4 \end{pmatrix} = \begin{pmatrix} \Delta_{12} + \Delta_{16} \\ \Delta_{21} + \Delta_{26} \\ \Delta_{34} \\ \Delta_{43} + \Delta_{45} \end{pmatrix}$$

It can be seen by inspection of the matrix elements that this is exactly the same set of linear equations as above and thus the solution is the same. The matrix has decomposed into block-diagonal form as the two groups of frames are disconnected. The RMS magnitude residual on each image from *different* overlaps can be computed as:

$$\mathrm{RMS}_i = \frac{\sum_{j=1}^{n} w_{ij}\theta_{ij}(\Delta_{ij} + a_j - a_i)^2}{\sum_{j=1}^{n} w_{ij}\theta_{ij}}$$

Figure 3.5 shows histograms of the magnitude residuals in BVRI bands after applying this least-squares solution to the March data. It can be seen that the typical RMS is about 0.02–0.04. This is due to a combination of the errors on the zeropoints in the photometric data and those due to the finite S/N of the paired objects in the overlaps. This is a much more aesthetically pleasing technique compared to that used for zeropointing the October data and with hindsight should have been developed and used for that. However it is not magic and is subject to the same limitations as the other method — namely that if one matched across a series of frames the cumulative zeropoint error grows as $\sqrt{N}$. This is easy to check visually by plotting out all the fields and marking the photometric frames. The situation is actually better than for the October data as there are less frames per field. So in the worst cases only 2–3 frames had to be matched across to derive zeropoints.

In conclusion it appears that the zeropoint errors on the non-photometric data have been determined to < 0.05 mags by two similar methods in the October and March fields.

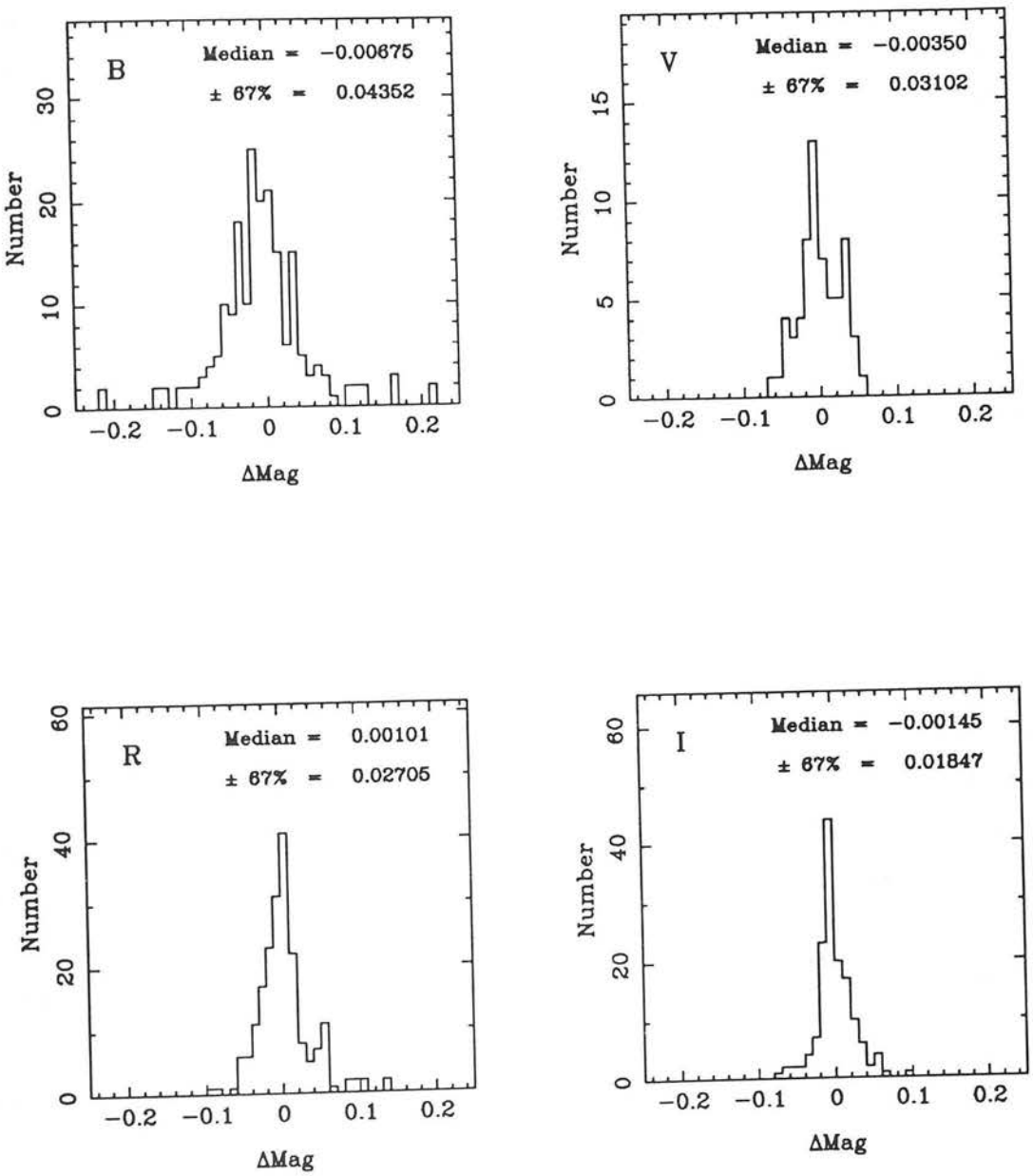

Fig. 3.5 The RMS magnitude residuals in BVRI for the March data after solving for the zeropoints via least-squares.

3.4.3 Removal of duplicate catalogue objects

October fields data

The duplicate objects were removed as part of the cross-calibration procedure. As the CCD overlaps were matched up the objects paired in the overlap (for the magnitude offset determination) only had one of each pair assigned to the output catalogue. Thus the duplicates were automatically removed.

March fields data

It was not possible to easily remove the overlap duplicates as part of the calibration procedure due to the much more complex geometry in the March fields data. The alternative procedure would have been to go through each object and scan the rest of the catalogue for duplicates as was done for the IRCAM data. However since these catalogues were much bigger, of the order of several thousand objects, such a procedure would have taken about 100 times as much computer time.

Obviously as the duplicates were only separated by a few arcseconds it is not necessary to check each object against every other one. The catalogue could have first been binned according to position and then checked with a slightly more complex algorithm. However it was decided not to do this. The ultimate fate of the optical data was be paired up with the infrared data, in which case the nearest object to the infrared position of any duplicates would be taken. Since the infrared was the primary data this gave a smaller chance of incorrect matching. As long as there was no problem with duplicates in the prime infrared dataset then there would not be any in the final multicolour catalogues.

3.4.4 Magnitude limits

October data

The final catalogues of objects with fluxes $> 3\sigma$ contained 11860 objects in the R band and 2311 in the B band. Plotting the number of objects against magnitude and examining the cutoff allowed the approximate magnitude limits to be estimated as R = 23.3 and B = 23.7. All the exposures were 600 s and the aperture was 4″ so these figures can be

Table 3.3: Empirical sensitivity figures

September 1988 data.

Band	Sky brightness	1σ1s	t_{int}	Mag. limit
B	21.2	23.5	600 s	23.9
R	20.6	23.2	600 s	23.8

April 1989 data.

Band	Sky brightness	1σ1s	t_{int}	Mag. limit
B	22.0	23.9	600 s	24.3
V	21.0	23.6	600 s	24.1
R	20.5	23.2	600 s	23.8
I	19.2	22.4	2000 s	23.6

compared directly with the theoretical estimates in table 3.1. R agrees with expectations but the performance appears to be 1.3 magnitudes worse in B than predicted.

3.4.5 March data

The final 3σ catalogues contained 8509, 3447, 12172 and 7893 objects in B, V, R and I respectively. The estimated magnitude limits were B = 23.4, V = 22.7, R = 22.8 and I = 22.1 for typical exposure times of 600, 300, 600 and 500 seconds respectively. Correcting these to a 4″ aperture and the exposure times of table 3.1 gives limits of B = 24.2, V = 23.8, R = 23.6 and I = 23.6. As with the October data there is a large loss of B performance — 0.8 magnitudes.

Table 3.3 shows a revised version of table 3.1 with the figures now determined empirically from the sky values of the data. The figures are shown separately for the September 1988 and April 1989 photometric data, both of these runs were during dark of moon. It can be seen that the R and I sky brightnesses are similar to those of table 3.1, however the 1989 data has B and V $\simeq$ 0.4 magnitudes brighter and the 1988 data has B 1.2 magnitudes

brighter. The latest official night sky figures for 1989 (from the La-Palma online information system) also give B and V 0.4 magnitudes brighter than for 1984, which were the figures used by Wall and Laing. This was attributed to the maximum of the solar cycle in 1989. It is not known why the 1988 B sky was so bright — possible explanations include enhanced auroral activity or a small enough amount of haze to increase scattered light while preserving photometric conditions. In 1990 the sky was reported to be 1 magnitude brighter in B than in earlier years (N. Metcalfe, private communication) indicating that the likely explanation is the solar cycle, causing the sky to be bright and variable in B.

Regardless of this there is still a problem with the B sensitivities — the $1\sigma 1$ s figures for B are still consistently worse than those calculated from Table 2 of Wall and Laing for the same sky brightness. The origin of this discrepancy turns out to lie in the zeropoint. The zeropoint used here was determined from the standards and is around 23.6–23.8 at a zenith distance of 30° for the different nights. However the figures in Table 2 of Wall and Laing are equivalent to a B zero point of 24.29, hence the anomaly. There is also a slight contribution from readout noise in B and V due to the lower sky background — amounting to increasing the noise by 0.2 magnitudes in a 600 s exposure. The $1\sigma 1$ s figures are corrected for this to reflect true background limited performance.

3.5 Construction of Multicolour Catalogues

The steps so far have resulted in object catalogues in B, V, R, I and K. The procedure for constructing a merged multicolour dataset was quite simple. First one of the catalogues (K to produce the infrared selected catalogue) was chosen as the primary dataset. Secondly one of the other catalogues (e.g. R) was paired with it with a certain pairing tolerance (typically 1–5″) to generate an output merged catalogue. This is the same as the primary catalogue with additional entries for the position, magnitude, etc. of the object in the secondary catalogue (these are null if there is no match). In the case of multiple matches then the nearest secondary object to the primary position was taken. This procedure was then repeated pairing each of the other catalogues with the merged catalogue (always based on the very first *primary* position) generating a new merged catalogue at each step.

Thus the final merged catalogue is a multicolour catalogue containing all the object information (position, magnitude, etc...) in each of the bands selected by pairing with the

position in the first band. Note all the information was retained at each step including the location of each object detection in each band in terms of x, y coordinates on a specified IRCAM or CCD image. Thus it was possible, for any given catalogue entry, to display the actual object in any colour; and a program was written to make this easy. Sample plots from this program are shown in figures 3.6 and 3.7 for some bright, decorative spiral galaxies in the survey area. These nicely illustrate the difference between the infrared and optical views of the universe.

This was very useful for objects of unusual colour — human inspection of the original data allowed the elimination of things such as unrejected cosmic rays/hot pixels, blended objects and diffraction spikes.

3.5.1 October data

A 576 object catalogue KRBPAIR3 was generated by pairing the IR data (cut at flux$> 5\sigma$) with the R and B band optical data at 3″ tolerance. The optical coverage was almost complete in R but only partial in B. In the catalogue 167 objects (the "K-only"objects) were detected solely in the K band and not in R or B. This was far to many to be put down to the insignificant area covered only in K and so for some reason there were IR detections which were not present at R < 23. Of course if these were genuine galaxies they would have to be very red (R $-$ K $\gtrsim 6$) and so they would be very interesting as candidate protogalaxies (see chapter 1).

The images were examined visually to try and ascertain whether these were due to any obvious flaw in the reduction procedures. This was not quite straight forward because obviously an unpaired infrared object has no catalogue pointer to the appropriate part of the optical CCD frame. What was done was to construct a separate catalogue of K-only objects. This was then paired with the R and B data as before but this time with a *large* tolerance — 30″ to produce the catalogue K_ONLY30. This had the effect of pairing with the *nearest* optical object and in almost all cases there was some match, unless it was in one of the few fields not covered in the optical. The optical information then gives the appropriate CCD image and then the K and optical images could be displayed about the K position showing the possibly blank optical area. Other objects in the field would then reveal whether or not there were any gross errors in the IR-optical coordinate system. In

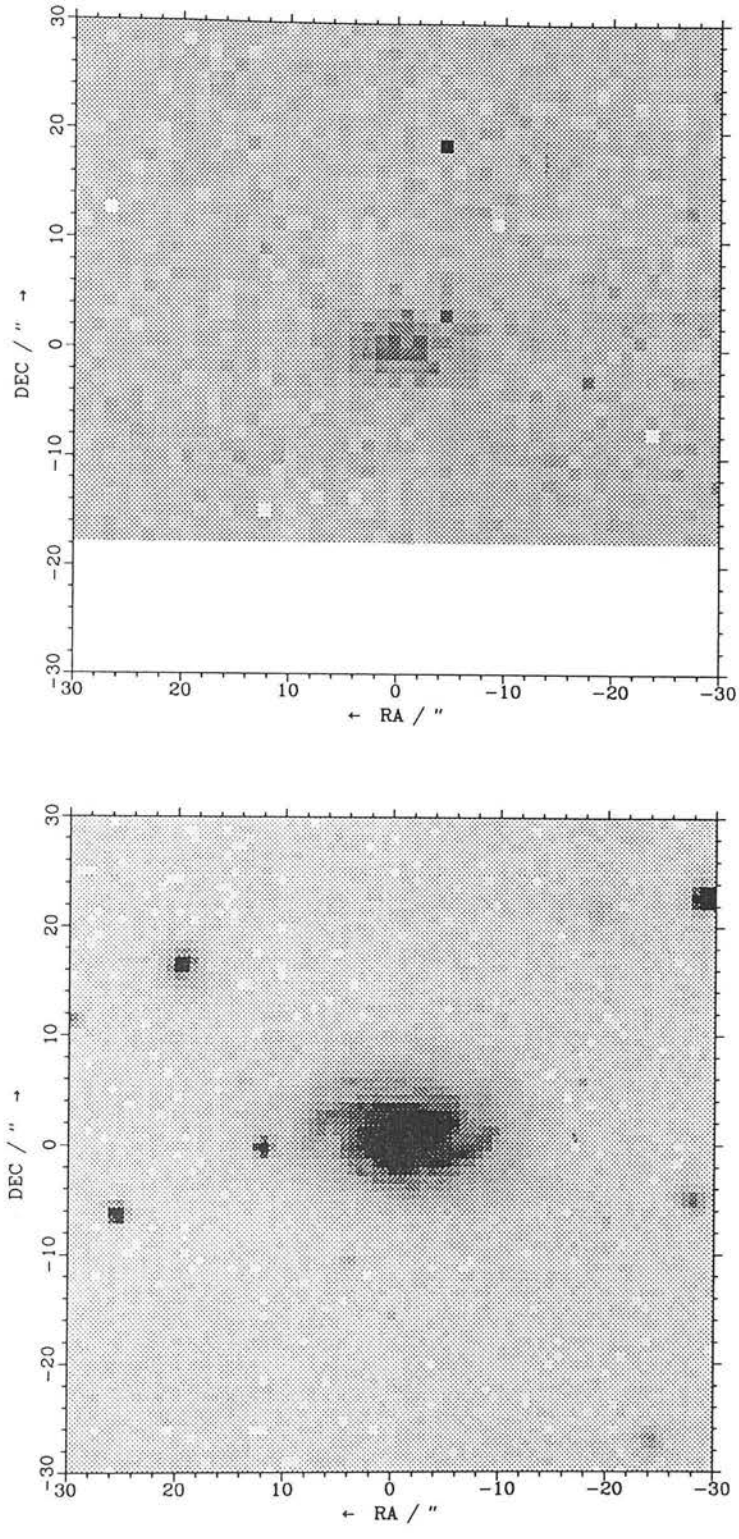

Fig. 3.6 K (top) and R (bottom) images of OCTKR#558 a bright (K = 15.4, R = 17.8) spiral galaxy in the survey. Note the contrast between the red central bulge and the blue spiral arms.

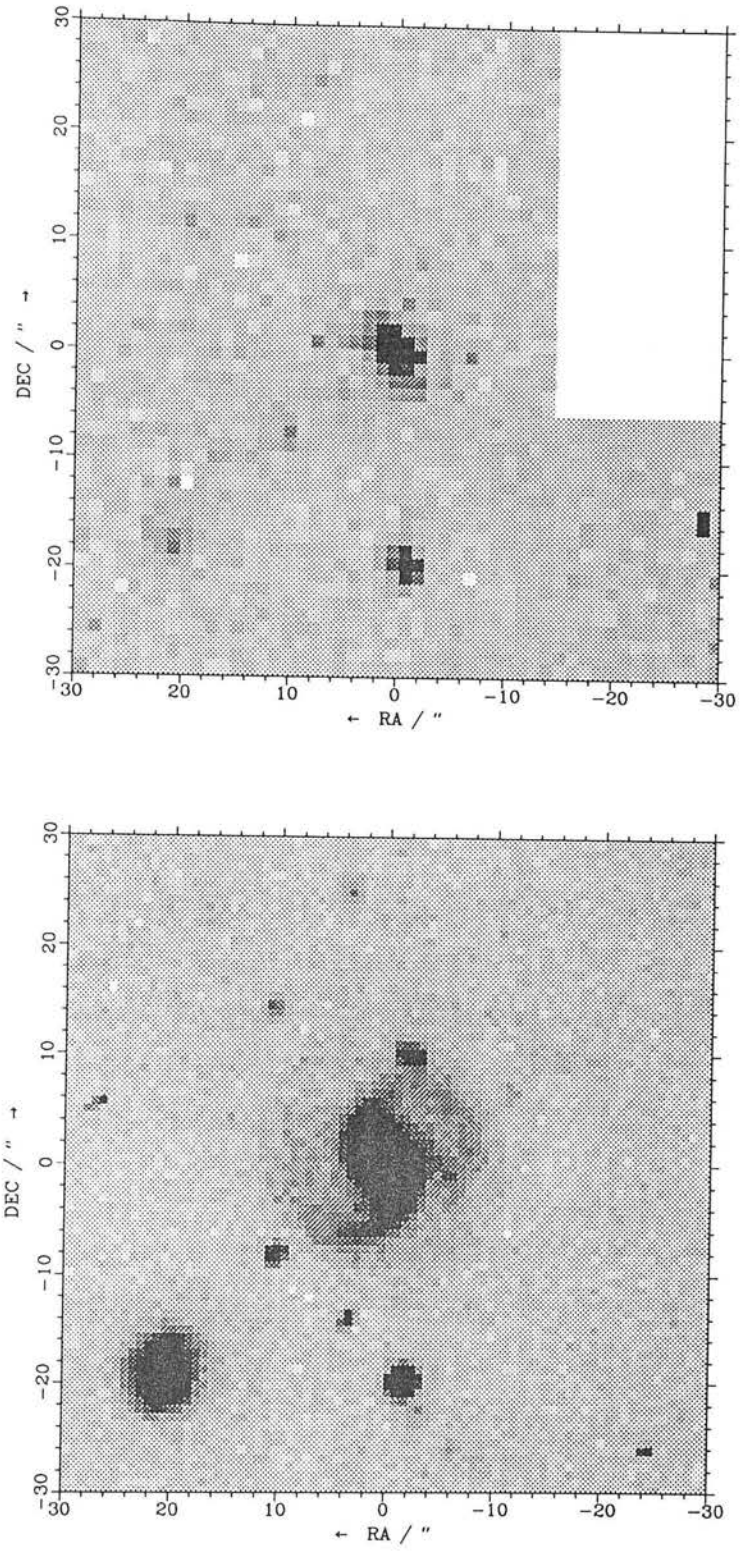

Fig. 3.7 K (top) and R (bottom) images of OCTKR#302, another bright (K = 14.2, R = 17.0) spiral galaxy in the survey.

fact this was never found to be the case in any of the catalogues, verifying the original astrometric procedures.

It was found that most of the K-only objects ($\simeq$ 95%) were found *not* to be due to real objects, but to a variety of image artifacts. The principal ones are:

1) **"Cosmic Rays".** These manifest themselves as spikes consisting of usually 1, but occasionally a group of 2–3, bright pixels. Whether or not they are associated with cosmic rays, like optical CCD detectors, or whether they are caused by some feature of the InSb detector is unclear. However the effect is similar to that of cosmic rays on CCDs. Despite the 3-pixel area cut in the object detection many of them still make it into the catalogue.

2) **Blends.** These were due to the faint isophote scheme used in the object detection. Where there were two close objects they would be separately detected at K but not in the optical. This is because for bright K the corresponding optical objects would be many magnitudes above the sky if they had normal colours, so merging into a single R detection leaving one surplus K detection.

3) **Noise features.** Some frames seemed to have large-scale correlated noise streaks, possibly associated with the readout electronics, which were broken up into a large number of spurious objects by the image detection program. At the detection stage it was attempted to compensate for these to some extent by throwing away particularly bad images and subtracting a sky background via a median filter from the rest.

4) **Ghosts.** These are caused by multiple reflections within the camera which allows bright stars to produce secondary ghost images. These are discussed further in section 6.3.

Before the later service observations (see section 6.3) the ghosting problem was not known about. However excluding these 146/167 of the K-only objects could be accounted for leaving 21 candidate objects, of which 7 later turned out to be ghosts. For later spectroscopic work objects were selected by being paired in K and R (404 objects). These objects were also checked visually, and the above problems with the K-only objects were not found to be significant.

3.5.2 March data

This data was reduced later than the October data and with the hindsight provided by the earlier work a slightly different strategy was adopted. For selection for a spectroscopic run it was decided to cut deeper into the signal/noise and avoid the extra spurious objects by tightening the optical pairing constraint. This is discussed further in section 6.3. The final catalogue, KBVRIPAIR2, which was generated with fluxes$> 2.5\sigma$ and $2''$ pairing tolerance, contained 663 objects of which 281 were detected in at least one of the optical bands. If the catalogue is restricted to 5σ then there are 312 objects of which 195 were paired in at least one optical band. 74 of these K-only objects were checked visually (the other 43 being due to the lack of optical coverage in one field) and only 4 emerged as candidate objects, the other being ghosts, cosmic rays, etc.

It is possible to estimate the contamination of the paired objects, given that the K-only objects are all spurious. Given a R band optical density of $\simeq 8$ objects/$\Box'$ down to the flux limit, and the pairing box size, then the number of spurious K pairs is $\simeq 0.04\times$ the number of spurious K-only objects. Thus in the 2.5σ catalogue (256 K,R pairs) there are $\simeq 15$ spurious *pairs*. This can be checked by increasing the pair box to $3''$, as the positional accuracy is good to $0.5''$ then the increase in K,R pairs should be predominately due to the random matching up of genuine R objects with spurious K-only objects. Thus $\simeq 19$ extra pairs are expected whist 17 are found, which confirms the estimate of contamination.

3.5.3 On nomenclature

Later on objects are referred to for brevity as OCTKR#$< n >$ for objects in the KRB-PAIR3 catalogue, OCTK#$< n >$ for objects in the K_ONLY30 catalogue and MAR#$< n >$ for objects in the KBVRIPAIR2 catalogue. The integer n is simply the entry number in the catalogue and has no special ordering except that the fields occur in RA order. For example in the MAR catalogue the fields occur in the order 9^h, 10^h and 13^h although the objects are not RA ordered *within* the fields.

3.6 Star-Galaxy Classification

Some sort of automatic classification of objects into stars and galaxies is essential in order to improve the efficiency of spectroscopic observations and to allow the determination of galaxy number-magnitude counts (see chapter 5). One common technique is simply based on image size (e.g. Heydon-Dumbleton *et al*, 1989) and this was the technique employed here. The area, in pixels, above the threshold isophote was determined for each catalogue object as part of the object detection stage and retained in the final catalogue. At bright magnitudes galaxies should have a much larger area than stars so if number of objects was plotted against area a strong bimodality should be observed. As one goes fainter the galaxy peak comes down in area and merges with the stellar peak as the galaxies become unresolved.

For each object, with magnitude M and on image j a parameter y was calculated:

$$y = \log_{10}[\text{Object area}] - \log_{10}[A_\star(M, j)]$$

where $A_\star$ is the averaged area of an object on the stellar locus at that magnitude on the same image. Since the point-spread-function varies from image to image this locus is calculated separately for each one.

It was decided to do the star-galaxy separation on the paired R band CCD data rather than directly on the K data as each CCD image had a much larger numbers of objects per image (several hundred as opposed to 1–2) which made the determination of the stellar locus less noisy. Also the CCD data was better sampled than the IRCAM data.

The procedure adopted was to read in all the optical objects (*not* just those paired with IR objects) and bin them according to image number, magnitude and $\log_{10}$[image area]. Next the binned data was first smoothed slightly in magnitude space by applying a top hat filter of width 1 magnitude (note 0.25 magnitude binning was used). Then the stellar locus in each (magnitude, ID) skewer was taken as the area below which lay 2 objects (i.e. the median of the bottom 3 objects) (if the total number of objects in the skewer was > 10) or the area of the lowest object (if total ≤ 10). Figure 3.8 shows plots of y vs R magnitude for the October and March data. It can be seen that there is a well defined

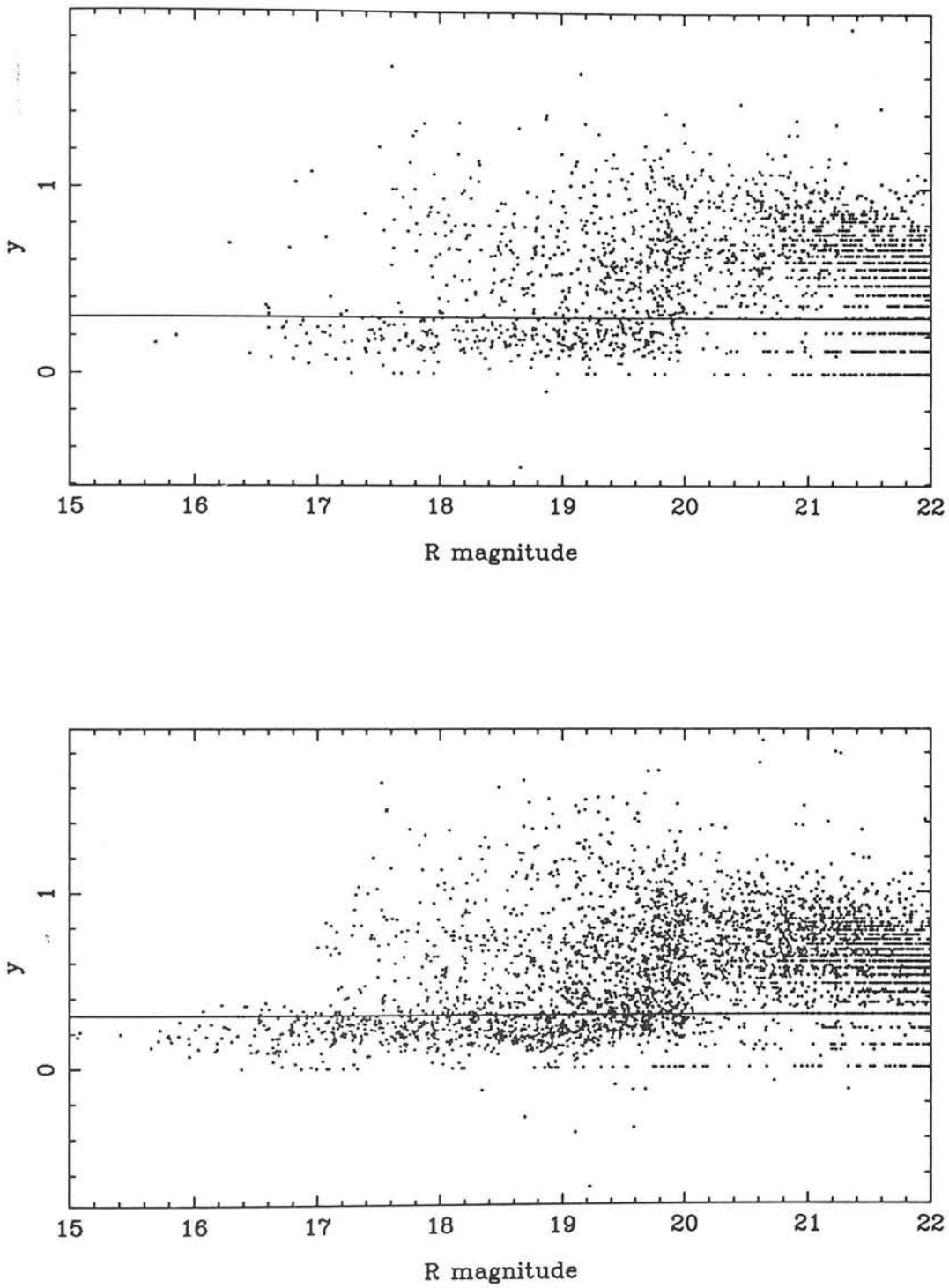

Fig. 3.8 Plots of the star-galaxy separation parameter (y) vs R magnitude for the October fields data (top) and the March fields data (bottom).

stellar locus down to R $\simeq$ 20. Fainter than this the galaxies become unresolved (for 2-4″ seeing) and the quantisation of area becomes apparent in the plots. However at these magnitudes galaxies dominate stars. A conservative (in the sense of including stars rather than missing galaxies) value of y=0.3 was chosen to separate "stars" from "galaxies". Additionally in the final selection all objects which were saturated on the R band CCD image were classified as "stars".

3.7 Summary

A total of 134 positions on the sky were observed using R band CCD imaging covering $\sim 2200\,\square'$ (assuming a very approximate estimate of 30% overlap). 81 of these positions were observed in B, 23 in V and 19 in I (mostly in March fields). This provided complete CCD coverage of virtually all the IRCAM data. The CCD data was zeropointed by overlap matching to an RMS accuracy of $\simeq$ 0.05 mags despite only 3/11 nights being photometric. A positional accuracy of $\simeq$ 0.5″ was achieved which allowed reliable pairing of optical and IR objects. Finally automatic star-galaxy classification based on image area was performed down to R = 20.

4 THE SPECTROSCOPIC SURVEY

4.1 Introduction

This chapter describes the follow-up spectroscopic observations that were made of a sub-sample of infrared selected galaxies. These were undertaken primarily to determine the redshifts of the galaxies. As discussed in chapter 1, redshifts are essential for the understanding of the evolution of the luminosity function. Indeed, the zero redshift K band luminosity function has not even been properly determined yet.

At the K = 17.5 limit of the sample these galaxies are very faint in the optical (R = 20–22) and very long exposures, of order 10 000–20 000 s, are required on a 4 m class telescope to secure redshifts. If the redshifts were determined one at a time it would take about a month of telescope time to observe 50 galaxies. However in recent years various types of multiple object spectrograph have been developed which allow the recording of spectra for a large number of neighbouring objects *simultaneously* using 2 dimensional detectors. These give the multiplex advantage that used to be confined to imaging and have been used to secure redshifts of large numbers of faint optically selected galaxies (e.g. Broadhurst *et al.*, 1988, Colless *et al.*, 1990). There are two generic types of instrument:

1) **Multifibre.** In this system fibres are used to feed the light from the objects to the spectrograph. The input ends are placed in the image plane of the telescope and the output ends are stacked along the slit of a long-slit spectrograph. A large format 2D array detector such as a CCD or an IPCS (*Image Photon Counting System*) device is used to record all the spectra. Several fibres are placed in object-free positions to record spectra for sky-subtraction. The principal advantage of fibres is the efficiency with which spectra can be packed on the detector and the relative lack of constraint on the geometry of the field objects compared to multislit instruments. Another advantage is that the fibre positioning can be automated and so changed in real-time at the telescope. The principal disadvantage of fibre systems lies in the difficultly of achieving accurate sky-subtraction. The fibres cannot be perfectly aligned along

the input slit of the spectrograph and this causes small wavelength shifts between sky and object spectra. Also the relative transmissions change unpredictably by about 5–10% through the night due to flexure as the telescope tracks across the sky which makes accurate normalisation and sky-subtraction difficult. The other main disadvantage is that 40% of the light is lost through the fibre system.

2) **Multislit** In this system a metal plate is placed in the image plane of the telescope with slits cut into it at the positions of the objects. The efficiency is the same as for a single-slit spectrograph and the sky-subtraction is much better than with fibres, because the sky sees the same transmission with no wavelength shift. However the number of objects that can be accommodated on a 2D detector is greatly reduced as the slits cannot overlap in the spatial direction. Also the object position spread in the spatial direction can not be too great in order to accommodate a desired wavelength range on the detector. The main disadvantage of this system is that it is harder to automate than fibres and so is less flexible.

Both types of multiobject spectrograph were used to obtain redshifts for this project — the *AUTOFIB* multifibre system and the LDSS multislit system. Both of these were common user instruments on the 3.9 m *Anglo-Australian Telescope* (AAT), which is situated on Siding Spring Mountain (altitude 1164 m above sea level) near Coonabarabran in New South Wales, Australia. Although the site is rather low and has mediocre seeing compared to newer sites the telescope and instrumentation are first class. The survey objects were easily accessible from the southern hemisphere as they had been chosen in equatorial fields for this very purpose (see chapter 2).

4.2 AUTOFIB Observations

The *AUTOFIB* instrument is an automatic fibre positioning system developed by the Anglo-Australian Observatory and Durham University. *AUTOFIB* consists of a robot positioner which can automatically place fibres anywhere in the 40′ Cassegrain field of the AAT. The fibre ends are held in place by magnetic buttons attached to a metal plate. This gives it much more flexibility than earlier systems which used fixed mountings prepared in advance. *AUTOFIB* has six special multifibre bundles which are devoted to autoguiding on stars. There are 60 usable fibres and it takes about 15 minutes for the

robot to position all of them. A more complete description of the instrument can be found in Parry & Sharples (1988).

There are some mild geometric constraints in selecting the objects to be observed, such as a minimum separation of 30″, set by the size of the buttons, and various constraints to do with fibre crossover and length. A sample configuration for one of the survey fields is shown in figure 4.1. The additional light loss through the fibre system is about 40% due mainly to focal ratio degradation from irregular internal reflections in the fibre and reflection losses at the fibre input and output faces. The focal ratio degradation was slightly better than it could have been as the fibre input to the spectrograph was specially designed with faster collimating optics. This is at the expense of lower spectral resolution due to a larger projected slit size. The actual transmission of the fibre material is close to 100% for wavelengths longer than 5000 Å. Since optical fibres were originally developed for long distance communications across oceans the loss over a distance of 3 m to the spectrograph is entirely negligible.

4.2.1 Object selection

The infrared selected population is very red, as will be shown in chapter 6, and has median colours $R - K = 3.5$ and $B - K = 5.5$ at $K = 17$. To be complete to $K = 17.5$ requires redshifts to $R = 23$ and $B = 25.5$. In contrast the deepest B survey to date is that of Colless *et al.* (1990) who reached B of 22.5. Clearly completeness requires restricting the sample to brighter K magnitudes and the optimum strategy is to use a red sensitive detector such as a CCD rather than a blue sensitive detector such as the IPCS. For object selection the best guide as to the probability of securing a redshift for a particular object is then the R magnitude.

The fields configurations for *AUTOFIB* are prepared interactively. An example configuration is shown in figure 4.1. The user has the ability to generate a set of fibre-object assignments automatically and then modify them interactively using the cursor on a display device. An initial set of configurations were prepared to take to the telescope, however it was anticipated that these would be modified as necessary during the run. This initial selection was based on paired K and R objects regardless of star/galaxy classification. As discussed in sections 3.5.1, 3.5.2 and 6.3 the evidence is that most of the "objects" only

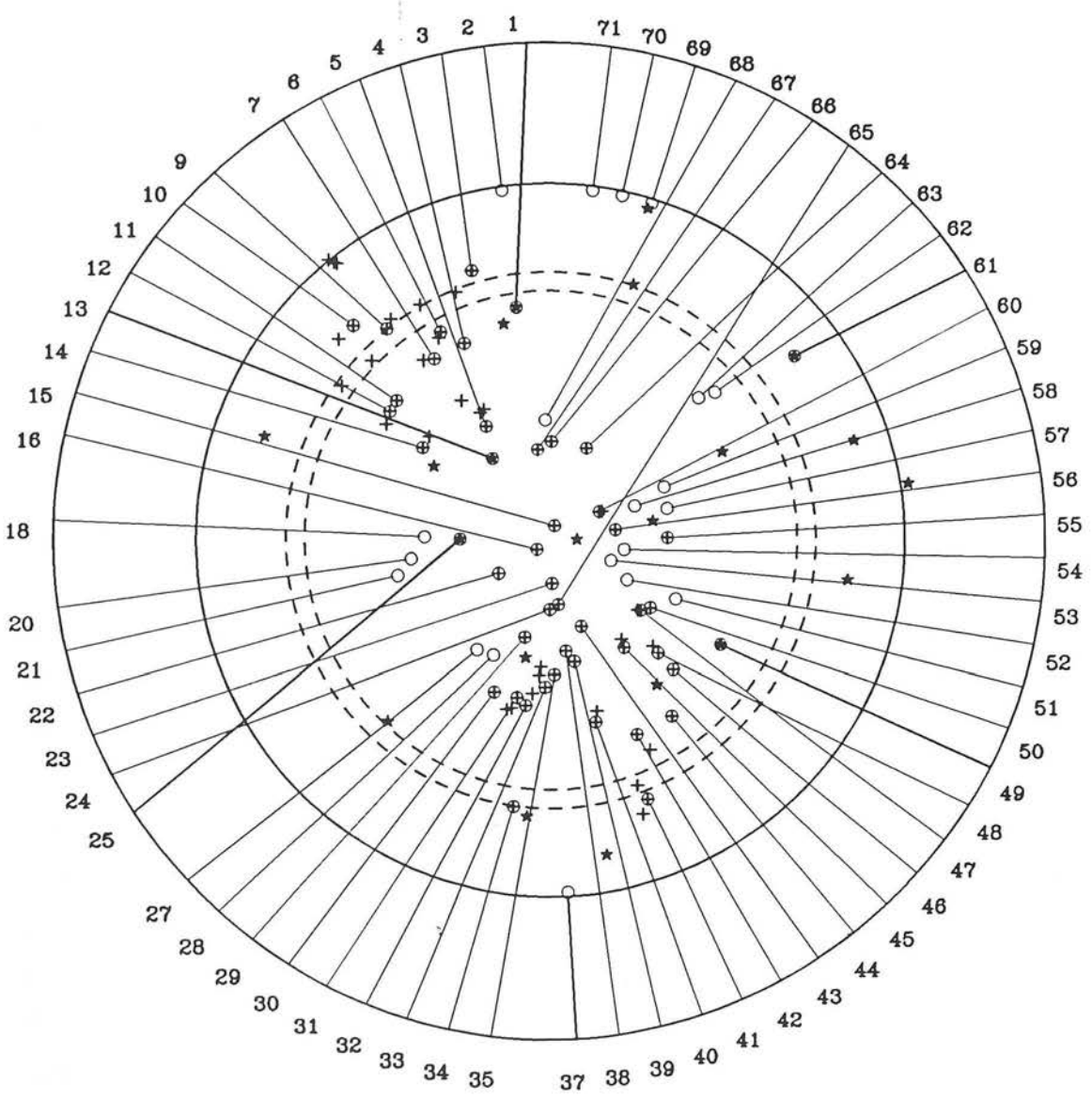

Fig. 4.1 One of the field configurations used in the *AUTOFIB* run. The field diameter is 40′. The target objects are shown as crosses and the possible guide stars are shown as stars. Object fibres are shown as thin lines and the special guide probe fibres are shown as thick lines, both terminating in circles indicating the fibre buttons. The dotted lines indicate the position of a step in the metal plate, on which the fibres rest, that provides some correction for field curvature.

detected in K are artifacts and not real. In any case they would have to be fainter than R = 23, much fainter than could possibly be achieved spectroscopically. The star/galaxy classification was ignored because at the time it was not known what the reliability of it would be.

The K selection limit was varied between K = 15.5 and K = 16 to get a similar number of objects per field. This corresponds to an R limit of 20.5 for the reddest K objects at these magnitudes, for which it was estimated that a 10σ continuum detection could be achieved with *AUTOFIB* in 20 000 s.

4.2.2 Observational details

The *AUTOFIB* data were acquired in a 4 night run over 27^{th}–30^{th} October 1989 of which about half a night was lost to weather. About 20 hours (66%) were spent integrating on targets. The fibre system was used with the RGO spectrograph and the GEC 584 × 386 CCD. The 270 R grating was used giving a dispersion of 142 Å mm^{-1} resulting in a spectral resolution of 9 Å with 3× oversampling and a 1800 Å spectral range.

With *AUTOFIB* the fields are acquired using 6 special guide fibre bundles. At least 4 of these are placed at the position of bright fiducial stars in the target field and their light is fed into the finder TV. Each bundle consists of a ring of 6 fibres arranged around a central fibre and has a total field of view of 5.3″. The fields is configured and the telescope pointing model is set up in the normal way using astrometric stars and the direct viewing TV. Then the telescope is sent to the nominal field position and because the pointing model is normally accurate to 1–2″ the guide star images can then be seen down the fibres. These are then brought to the centres of the bundles and then used for autoguiding and correcting field rotation. If there is a problem in acquiring the field the area can be viewed in TV-direct mode to see if it can be recognised.

At first the brighter objects in each field were observed. After a sequence of integrations the frames were coadded and spectra extracted to see which objects had sufficient signal/noise for an identification to be possible. Then the fibres were reconfigured replacing identified objects with fainter unidentified objects. A spectral range of 4500–6500 Å was used on the first night, 5600–7400 Å on the second night and 5100–6900 Å on the last two nights. The changes were made to optimise the detection of features at different redshifts based on

experience gained on previous nights. Also the first fields included far too many stars, the star-galaxy classification proving very reliable. Thus the proportion of these were reduced in the later field configurations.

4.2.3 Bias subtraction and flatfielding

The CCD frames were bias subtracted and divided by a flatfield in the standard way for CCDs. One point worth mentioning is that the data were extracted before flatfielding. Here "extraction" means tracing each spectrum along the dispersion direction, allowing for small wiggles, and summing across it to produce a 1D spectrum. Using the white light flatfield as a reference a file was produced containing polynomial coefficients (6^{th} order) which described the trace of each spectrum on the detector. These coefficients were then used to reduce each raw image to a 2D "extracted" image where each row represents an individual 1D spectrum. Dispersion was along the X axis. Dividing the extracted object spectrum by the extracted flatfield is exactly equivalent to normal flatfielding provided the spectrum position is stable (which it is) and has the advantage of avoiding the division by zero problem in the inter-fibre gaps on the original images.

4.2.4 Coaddition of data

It was found that the spectra positions were stable throughout the night which enabled each field configuration to be coadded before performing the other steps. With several frames available it is possible to perform the coaddition in such a way as to automatically reject cosmic rays at the same time instead of simply interpolating over them first. There are various methods that could be used for doing this. One approach might be to take a median — however this requires that each frame be suitably normalised first because unlike the mean the median is not simply proportional to the sum of the data. It is not clear what the correct normalisation method is, for example if there was a small amount of cirrus contaminating one frame then the sky level would get *brighter* while the object level would get *fainter*. While one could subtract the sky before coadding it would be preferable not to as one would have better signal/noise on object and sky in the final summed image and it would be better to do sky-subtraction on that.

The approach taken here was to sum up the data values in each pixel, rejecting cosmic rays as being a certain amount above the *median* value, and summing up again. The sum is then renormalised to allow for the number of rejected points. This works because the cosmic rays represent comparatively large deviations. A very good method of testing such schemes is to "blink" the coadded image and a normal straight sum on the image display so the rejected cosmic rays stand out. It can also be seen whether real features such as emission lines are being removed.

Various criteria were tested to find the best way of choosing the "certain amount". It was found not to be advisable to reject values greater then a certain number of standard deviations above the pixel median as the number of frames was quite small (2–3) and hence the standard deviation at each pixel poorly determined. It was also not realistic to compute the standard deviation in a small neighbourhood as for 2D spectra this is dominated by the variations in sky background due to emission lines and not the random noise. Empirically it was found that by far the best way was to set the rejection level at 30–50% above the pixel median.

4.2.5 Sky-subtraction

For each configuration about 10 fibres were devoted to sky spectra. However it was not possible to subtract a mean sky directly due to the problem of relative fibre-fibre transmission variations. These are of the order of 5–10% and depend on the field configuration. This is because the component of the fibre loss due to focal ratio degradation from internal reflections changes as the fibres flex.

In order to subtract a correctly scaled sky spectrum from each object spectrum these variations must be calibrated out. This is done by taking "offset sky" exposures at regular intervals. These consist of 4 exposures offset by 30″ North, South, East and West from the object positions. Since the sky can be assumed to be constant across the 40′ field then the sky levels in each spectra in principle give the normalisation. About 15% of the total integration time on each field was devoted to obtaining the offset sky exposures.

The sky continuum level for each fibre in each offset sky frame was determined by taking a median to remove any effect from varying sky emission lines. Then for each fibre the median of the 4 continuum levels was determined. Next any continuum level > 10% above

the median was rejected as being likely to have been contaminated by some random object and the median redetermined to provide the final normalising level. Then each row in each object spectrum was divided by the appropriate normalising levels.

Using this procedure it was found that the offset sky pattern was stable for a given field on a given night for the period it was observable. It also gave the best results on sky-subtraction. So a master set of 4 offset skies were prepared by coadding the offset skies like the data and these were used to determine the final normalising levels. Figure 4.2 shows an example of the normalising levels for two different fibre configurations taken on the same night.

After dividing by offset sky frames the data were wavelength calibrated and rebinned (see section 4.2.6) and then a median sky spectrum was determined for each data frame from the sky fibres and subtracted. Inspection of the sky-subtracted sky fibres showed a mean level of zero and a RMS scatter about this consistent with that expected from photon shot noise.

4.2.6 Wavelength calibration

Cu Ar arc spectra were taken at regular intervals and it was found that the arc line positions were stable throughout the night. However the fibres are not perfectly lined up down the slit and this results in small shifts of 2–3 Å between spectra in neighbouring rows. The calibration procedure employed was first to coadd all the arcs for one field and then manually calibrate one of the arc spectra near the middle using a low order polynomial fit to the dispersion. Next a program was used which automatically located the same lines nearby on the other spectra to generate individual polynomial fits to each row. The typical RMS fit residual achieved by this procedure was 0.4–0.6 Å. Then each image was linearly rebinned with a pixel scale of 3 Å (close to the mean of the original).

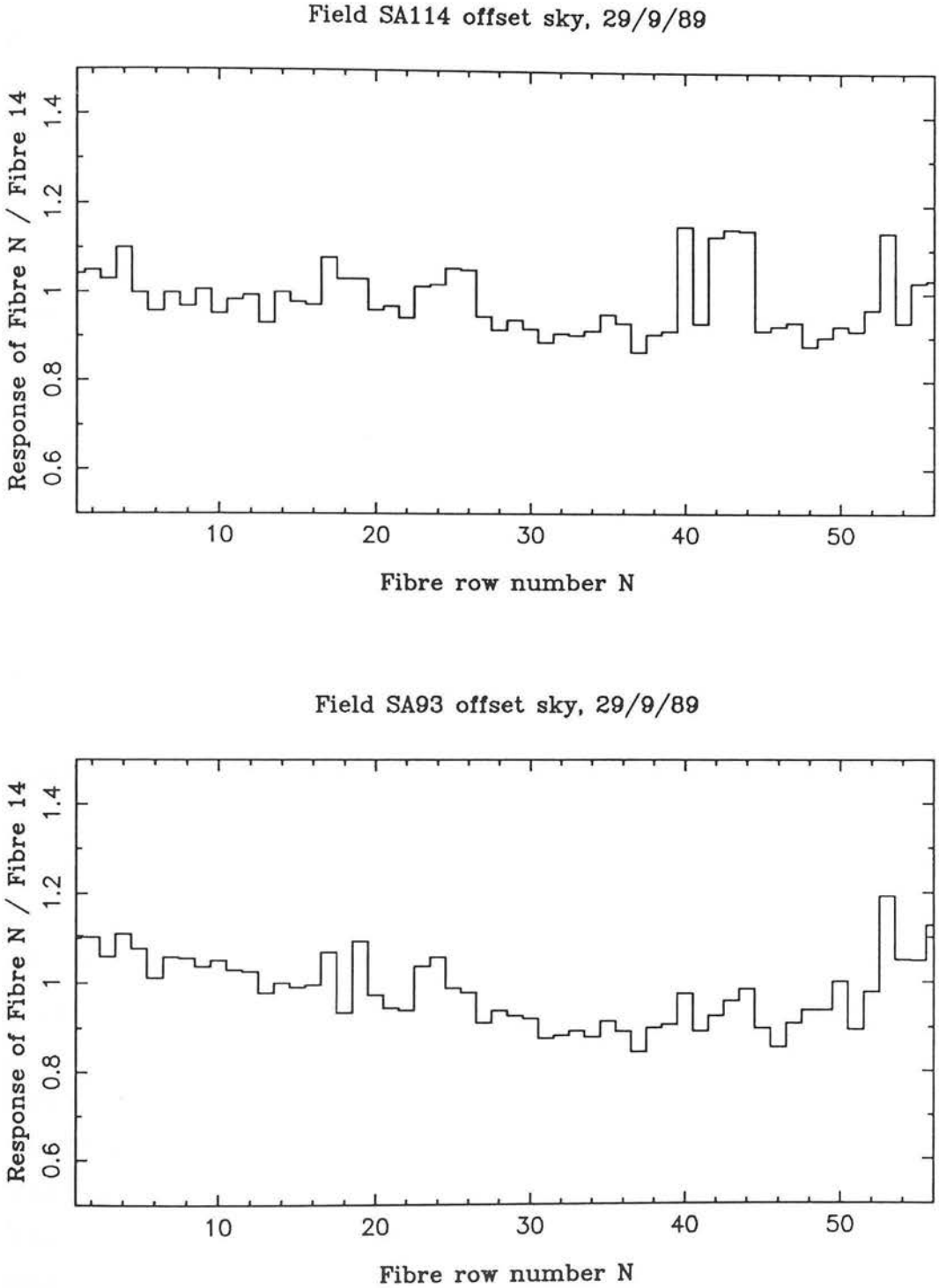

Fig. 4.2 The relative fibre-fibre transmissions plotted against fibre number. These are for two different field configurations on the same night. Note the variations caused by different flexures in the fibres.

4.2.7 Final combination

Each individual spectrum was automatically extracted and all the separate spectra of the same object on the same night were added (across different configurations). Now different wavelength ranges were used on different nights to try and optimise the detection of spectral features at different redshifts. So if the wavelength range was different then the spectra were added in the overlap region, normalised appropriately and joined. Note that at the wavelength calibration stage the end points for the linear rebinning on each night were chosen so that the bins would be the same in the overlap regions.

4.2.8 Fluxing

A smooth spectrum standard star, LTT2415 from Stone & Baldwin (1983), was taken on each night to derive the CCD response. There was a slight variation between nights, probably due to variations in the flatfield lamp. A smooth curve was adopted between the different curves, shown in figure 4.3a, to provide an approximate relative fluxing which was applied to the data.

4.3 LDSS Observations

The *Low Dispersion Survey Spectrograph*, or LDSS, is a multislit spectrograph developed jointly by Durham University and the Royal Greenwich Observatory. It was designed as a highly efficient faint object spectrograph for the AAT, with a wide field of view of up to 12.3′. This is due to the use of re-imaging optics which reduce the focal ratio from $f/8$ at the Cassegrain focus to $f/2$. The large field of view allows the efficient use of multislit masks. Operation of LDSS requires the presence of an observer in the telescope's Cassegrain cage as all the basic controls for changing the masks, changing grisms and inserting/removing the grism are via mechanical levers and knobs on the outside of the instrument box. A fuller description of the instrument together with the procedure for mask design and field aquisition can be found in Colless *et al.* (1990) and Wynn & Worswick (1988).

The instrument's backplane can accept a variety of large-area detectors. In this case the Thomson-CSF 1024 × 1024 pixel CCD was used giving a field of 8.5′ × 8.5′. The masks

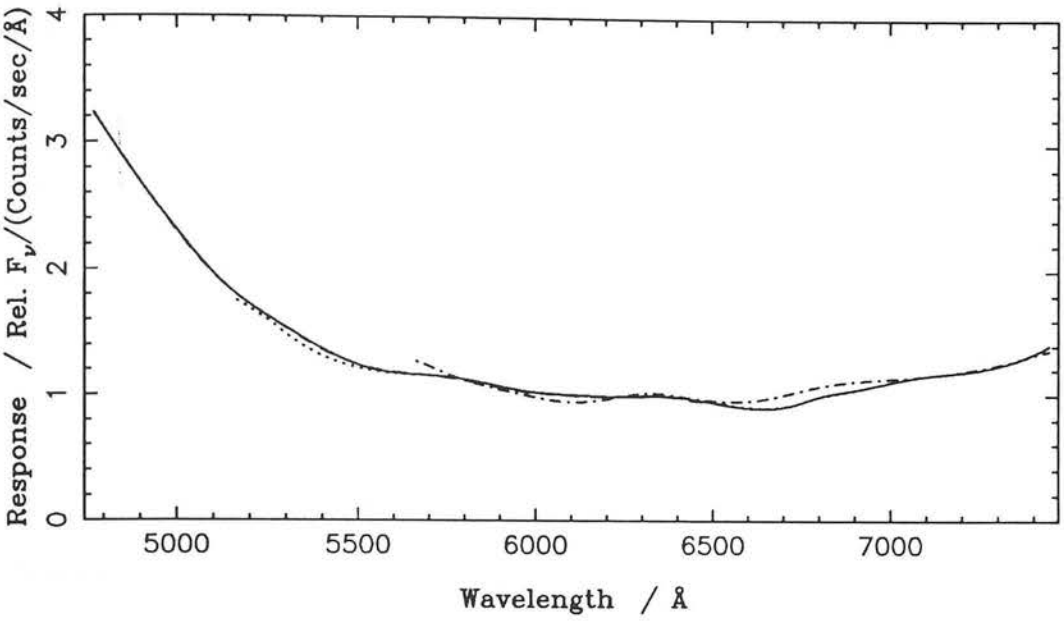

Fig. 4.3a The sensitivity curves derived from observations of the standard star LTT2415 on three different nights during the *AUTOFIB* run. The solid line shows the adopted interpolation.

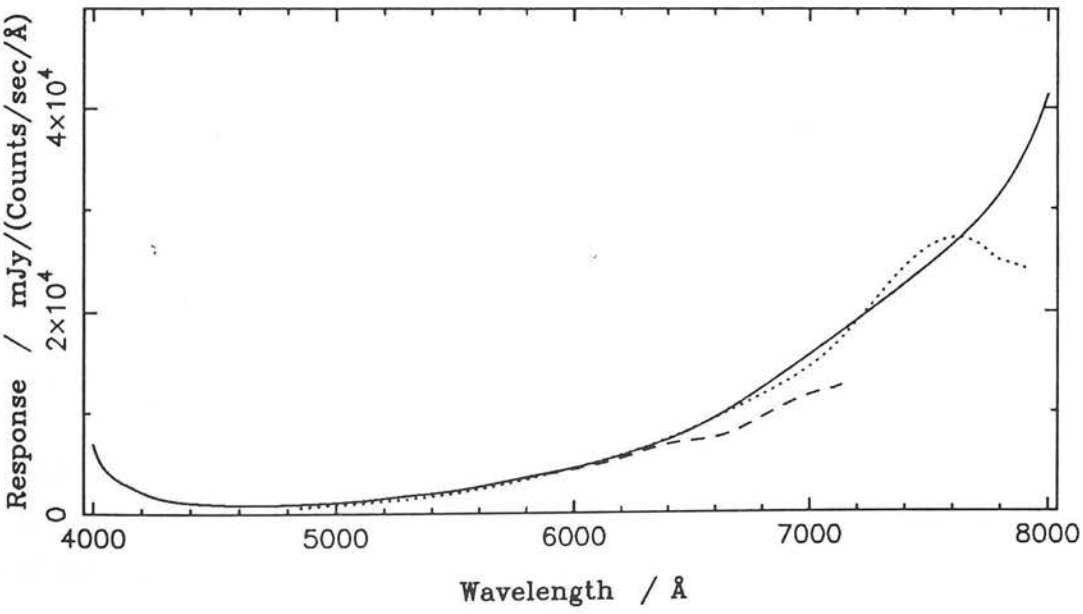

Fig. 4.3b The sensitivity curves derived from LTT2415 (dashed) and Feige 110 (dotted) on two different nights (and on different slits) during the October 1990 LDSS run. The solid line shows the adopted interpolation.

are commercially manufactured by photochemically etching the slits into a steel template. These were made with a slit size of 1.7″ (0.25 mm) and a minimum slit length of 15″ (2.2 mm) for accurate sky-subtraction. The slits were oriented North-South in order to minimise the atmospheric differential refraction since with a multislit it is not possible to continually rotate to the parallactic angle (only one slit can be on the rotation axis of the CCD). The 165 Å mm^{-1} grism was used giving a spectral range of 5000–7000 Å which matches the maximum sensitivity of the CCD and the likely range of redshifted spectral features as determined from the *AUTOFIB* data. Obviously due to the RA spread of the slits there would be additional blue or red portions in the spectrum. With this grating the spectral resolution was 10.6 Å with 3× oversampling — very similar to that of the *AUTOFIB* setup.

The motivation for using LDSS was to extend the redshift survey to fainter magnitudes. The *AUTOFIB* data were found to be limited to $R \lesssim 19$ (see section 4.5), with LDSS it was anticipated that R = 21 would be reached, giving completeness at $K \simeq 16.5$. There are two reasons principal why LDSS can go so much fainter:

1) The efficiency is so much greater due to the absence of fibres and the overall design of the instrument — LDSS was specially designed for faint object work, unlike the RGO spectrograph, and hence has less internal losses from the optical system.

2) The sky has a brightness of R = 20.4 magnitudes/□″ so with typical seeing (2″ at the AAT) the count rate from an object with R = 21 is only 15% that from the sky. Clearly accurate sky-subtraction is a vital component for obtaining good spectra and hence the use of slits is essential at these faint magnitudes.

4.3.1 Object selection

The mask design program works by assigning priorities to different classes of objects. It then assigns all the priority 1 objects it can, subject to the slit positional constraints, then all the priority 2 objects, and so on down the priority list.

The first run was in March 1990 to observe objects in the March fields (see section 4.3.2). For the mask design the priorities were:

1) Objects classified as galaxies brighter than R = 21.

2) Fainter "galaxies" with $21 < R < 22$.

3) Stars $R < 21$.

4) Stars $21 < R < 22$.

It was worth including stars at low priority, so they had slits placed on them when there was no available galaxy, because this provides a useful check on the star-galaxy classification. The stars also allow the wavelength calibration to be checked via their absorption lines. Despite this there were still areas of the mask where no slits could be placed due to the geometrical arrangement of the IRCAM frames. So as not to waste this an additional set of blue optical objects were selected using the criteria $B - R < 0.5$ or $R - I < 0.2$ to see if strong starburst galaxies at $z \gtrsim 0.5$ could be identified.

A slightly different set of priorities were used for the mask design in the October fields:

1) Red objects with $R - K > 4$. These were included at *highest* priority; because there were only 1–2 per LDSS field this ensured that they were all included. It was possible that some of these might be protogalaxies at very high redshift (see sections 1.2 and 6.3) with strong Lyman-α emission lines in the R band. These objects were also selected for a run of JHK photometry at UKIRT, a month earlier, which was totally wiped out by bad weather.

2) All objects $16 < R < 21.5$, excluding those classified as stars for $R < 20$. It was known from the *AUTOFIB* run in the October fields that the star-galaxy classification was reliable down to these magnitudes, in any case the proportion of stars was expected to be small for $R > 20$.

3) All objects with $R > 21.5$.

4) All the remaining objects classified as stars.

About 10–15 objects per mask were usually obtained. Figure 4.4 shows an example of one of the resulting CCD images from the October fields. 17 individual slit spectra dispersed along the X-axis can be clearly seen, together with the predicted positions from the mask design.

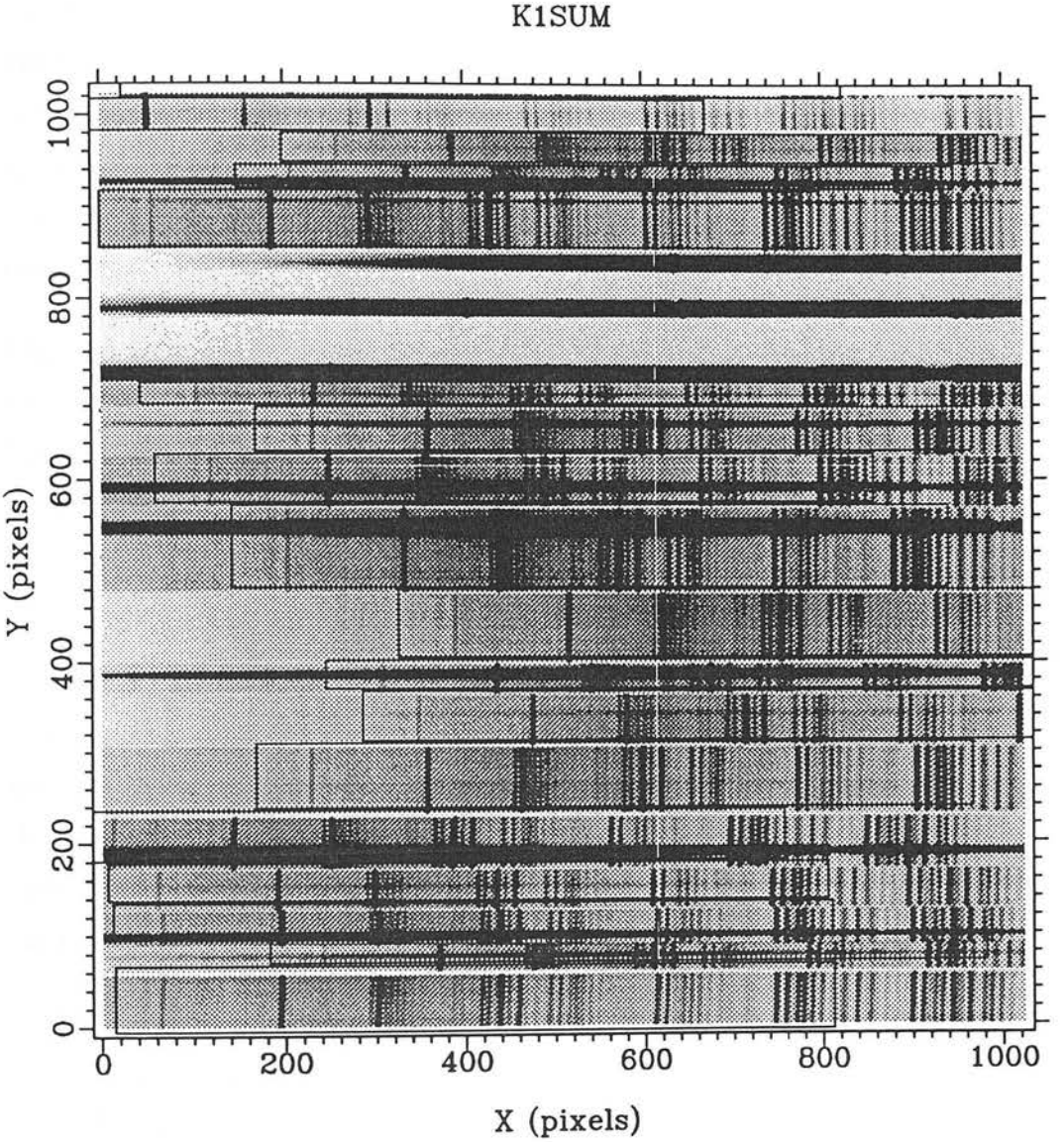

Fig. 4.4 A plot showing the predicted and actual positions of the spectra on the Thomson CCD for one of the LDSS masks. The dispersion is in the horizontal direction and North is at the top, each box corresponding to one slit with a range from 5000–7500 Å. This is a 15 600 s exposure on 17 objects. With these display levels the continua of most of the objects can be seen. The bright night sky emission lines are easily visible and their number grow rapidly longwards of 7000 Å. In the top middle can be seen the light from acquisition stars coming down the fiducial holes and being dispersed.

Note the horizontal and vertical white lines are caused by a subtle bug in the GKS graphics library, which the LEXT package uses (D.L. Terrett, private communication, 1991).

4.3.2 Observational details

Two LDSS observing runs were awarded for this project. The first was 26^{th}–29^{th} March 1990 which was adversely affected by weather. Only one 2000 s integration in poor seeing (3″) was obtained. Fortunately 6000 s on one of the March field masks was kindly provided by R.S. Ellis and M. Colless from an observing run one month later in 1.5″ seeing. The second run was 19^{th}–22^{nd} October 1990 of which 1.5 nights were lost to weather. The seeing was 2–2.5″.

The data reduction is summarised below where it differs from standard spectroscopic procedures. The data were reduced using an amalgam of standard FIGARO, specially written FIGARO and the dedicated LDSS data reduction package LEXT. Identical procedures were employed for the April and October data.

4.3.3 Field acquisition

The hardest part of observing with LDSS is acquiring the fields with sufficient accuracy that the light from the objects comes through all the slits. It is not possible to view the field and the slit positions on the TV system simultaneously, in any case most of the objects would be too faint, so the procedure employed makes use of direct imaging with the LDSS detector. The steps are as follows:

1) During the mask design stage each mask has 2 or 3 large circular holes (diameter 10″) included at the known positions of bright stars ($14 < R < 16$) in the field. For this project the stars were selected from the same Schmidt plate scans used to select the fields for the original infrared observations. Thus the internal astrometric accuracy is good to $\lesssim 0.5$″.

2) The telescope is moved to the nominal field position in the normal way. The grism is removed and a quick direct image is taken of the mask illuminated by white light from the chimney flatfield lamp. Then another quick image of the field viewed through the mask is taken. Then the grism is put back in and a long integration ($\sim$ 2000 s) is started straight away, in order to save time if the subsequent stages of analysis (which can take a few minutes) prove the alignment to be correct.

3) The field image is examined to see whether or not stars are visible through the fiducial holes. As the AAT pointing model is accurate to $\sim 1''$ this is usually the case. If they are not, then the current integration is aborted. It is then possible to remove the mask and grism and take images of the field to compare with finding charts and try and track down the source of the error.

4) If the stars are visible then an interactive LEXT procedure is run to work out the offsets and field rotation required to bring the stars into the exact centres of the holes. The star positions are determined by centroiding or Gaussian fitting and the hole centres are similarly determined by centroiding the white light frame.

5) The computed offsets and field rotation are applied to the telescope. If they are small (1–2″) then the current exposure is left to continue. Otherwise the integration is aborted and the acquisition procedure is repeated from step 2 as a check.

Generally field acquisition takes about 10 minutes if everything goes as expected. If the stars are not found first time it can be more efficient to try another field rather than wasting valuable integration time hunting around with direct imaging to try and identify the field. As an example, it was found to be impossible to acquire one of the fields used for this project, a problem which was subsequently tracked down to an incorrectly manufactured mask with the holes 1 cm out of place.

4.3.4 Bias subtraction and flatfielding

Bias subtraction was performed using standard CCD procedures. Flat fields were taken of a dispersed white light source through the mask as in the single slit procedure. Normally in the single slit case the flat field is summed along the spatial axes and a low-order polynomial is fitted to the resultant spectrum, which is then divided into the flat field image to normalise it. For multislit data it is incorrect to fit a separate polynomial to each slit and since the data were eventually fluxed this step was left out — the data were simply divided by the raw flatfield. One disadvantage of doing this is that the flatfielded spectra are not in counts which can be useful for estimating poisson errors. However if necessary this can be done on the raw image.

For LDSS data flatfielding also has the effect of removing amplitude variations along the slits caused by imperfect manufacture which give the slits ragged edges as compared to

the dekker in a conventional single slit spectrograph. Since the pattern of the slits on the CCD appeared to be stable between different nights a master flatfield for each mask was prepared by adding all the flatfields for that mask from different nights.

4.3.5 Coaddition of data

Before coadding integrations on the same field the data had first to be corrected for small position shifts of up to 2–3″ of the objects along the slits. These were usually manifest between the same field on different nights. Because the aquisition testing procedure was somewhat time consuming small pointing errors along the slit direction were left physically uncorrected. Instead the flatfielded data were shifted in software before coadding. Of course this causes some overlap in the summed image at the edges of each slit with the sky of adjacent slits reducing the region of valid sky. However since the slits were at least 15″ long to start with this made little difference to accurate sky-subtraction.

The actual coaddition proceeded in the same way as for the *AUTOFIB* data (see section 4.2.4) to ensure optimum cosmic ray removal. Again this was tested by a blinking the coadded data against the straight sum.

4.3.6 Wavelength calibration

Cu He and Cu Ar arc spectra were taken for each of the masks. Using LEXT it is possible to take one of the spectra, fit the arc lines using a low order polynomial, automatically locate the same lines in all the other spectra (using the theoretical shifts between them) and fit them. This failed to work as advertised so two modifications were made to LEXT to rectify this:

1) The line centre finding algorithm was changed so that instead of simply taking the intensity weighted centroid in a small box as the line centre it took the median position of the 3 brightest channels.

2) An option was added so that it was possible to get a first approximation to the fit using a few bright, well separated lines and then using this fit as a starting point track down all the fainter lines and use these to refine it.

The fitting was done using the Cu Ar arcs since a more extensive line list was available allowing the identification of 23 lines for use in the fit. This gave a RMS residual in the range 1.5–2 Å for the fits to each spectrum. An independent check of the wavelength calibration was then made using the Cu He arc. In the Colless data only Cu He arcs were available of which only 8 He lines could be identified. In order to provide an additional constraint *between* spectra, the wavelengths of 11 unknown but bright lines were measured by fitting Gaussian profiles. The typical RMS obtained was about 1 Å.

Once a list of coefficients had been generated, each slit spectrum was extracted and written to a separate 2D FIGARO image file with associated wavelength information derived from its coefficients for each channel. They could then be treated individually as single slit spectra for the purposes of sky-subtraction and object extraction.

4.3.7 Sky-subtraction

The standard sky-subtraction procedure employed was to visually identify object flux free regions each side of the spectrum, take the median sky and subtract. If the spectrum was not visible easily to the eye a median was subtracted first which usually rendered it visible. In some cases there was a perceptible sky gradient left in the slit direction so a linear interpolation was used instead. It was suspected that this was due to some residual gradient in the flat field lamp. A straight least squares fit was *not* used as such things are easily lead astray by defects and cosmic rays. The usual recourse would have been "sigma-clipping", with some iteration, however the more general iterative reweighting scheme of P. Stetson (1990) was used instead.

In this method sigma-clipping is replaced by a smooth function which goes to zero at large multiples of sigma. This avoids problems associated with "sigma-clipping" such as possible non-uniqueness of the solution converged to from different starting points. With an appropriately chosen function, scaled by the RMS residual at each iteration, it can be arranged that large residuals eventually contribute only their *sign* to the fit weighting while small ones are unaffected. This provides what is effectively a *median* line fit to the data. This is a very robust estimator and is quite effective in eliminating the effect of spikes on line fitting.

4.3.8 Object spectrum extraction

In principle an increase in signal/noise of order $\sim \sqrt{2}$ can be achieved by performing a *weighted* spectrum extraction, rather than simply adding all the flux in the spatial direction across the object. The optimum scheme, for maximum signal/noise, is to weight according to the spatial brightness profile. It is very easy to see this must be the case. First take the errors on each point as being approximately constant, since they mainly come from sky shot noise and readout noise. Now imagine each flux value in a cross-section f_i is divided by the averaged profile, $P(x_i)$, so that the flux is now approximately constant across it, with the errors now growing as $\sigma_i \propto P(x_i)^{-1}$. Now the optimal scheme is to take a mean using reciprocal variance weighting, i.e.,

$$\langle f \rangle = \sum_i \frac{1}{\sigma_i^2} \left(\frac{f_i}{P(x_i)} \right) = \sum_i P(x_i) f_i$$

These profiles were automatically generated for each object by summing the sky-subtracted image in the wavelength direction between 5000 and 7000 Å (where the CCD is most sensitive), excluding regions far from the object or near bright sky lines which are poorly subtracted. Each profile was plotted out for visual checking to see if it looked sensible, and then used for optimal extraction. The improvement in signal/noise was of order 20–30% over a simple box extraction.

4.3.9 Fluxing

Two smooth spectrum standards were observed — LTT2415 (Stone & Baldwin, 1983) and Feige 110 (Stone, 1977). The technique for taking standards with LDSS is to place the star on one or two of the slits. LTT2415 was observed on one slit and Feige 110 was placed on a bluer slit on a different mask and the resultant sensitivity curves are shown in figure 4.3b. Note that the LTT2415 curve was scaled to match that of Feige 110 in the overlap since the available data table for LTT2415 was only given in relative flux units.

The discrepancy between the two curves is small except near the chip edges. This is probably due to two effects which cannot easily be distinguished. Firstly the spectral shape of the white light lamp could have been different between the flatfields of the two different masks. Secondly the spectral response of the chip could vary between the two

different slit positions. As the prime aim of the project was redshift determination only a crude relative fluxing was desired, in order to give a rough continuum shape as an aid to identification. So the compromise curve shown in figure 4.3b was adopted as the final calibration.

4.4 Redshift Determination

The identification and redshift determination of each object was done in two ways. Firstly each spectrum was identified manually by plotting it on an image display and secondly by cross-correlating each spectrum with a library of template spectra.

Before running an automatic technique such as cross-correlation any residual sky features have to be patched out. Poor sky-subtraction arises from the bright emission lines due to [OI] (5577 Å, 6300 Åand 6363 Å) and Na D (5892 Å). Also there are various atmospheric absorption bands which start at 6800 Å. Although in principle it is possible to remove the bands from the data by measuring them in the standard star and dividing out, in practice it did not work very well. This is because the band profiles change slightly through the night and also because there is a change in pixel sampling between the standard and the object, requiring a rebinning which introduces systematic errors. These were left in for the manual identification so they were at least recognisable. For the cross-correlation the emission and absorption features were removed by linear interpolation.

No correction of the redshifts was made to a heliocentric coordinate system. The Earth's orbital velocity is $\simeq 30\,\mathrm{km\,s^{-1}}$ which corresponds to a redshift error of $\Delta z \simeq 10^{-4}$. Moreover for actual observations this is reduced further, e.g. for an observation near midnight the component of telescope velocity towards an object directly overhead is ~ 0. There was also no need to correct the spectra to vacuum wavelengths. Tabulated values of wavelengths of emission and absorption lines in galaxies, and those of wavelengths of arc lines, are both given as air values in standard conditions. Hence the effect on the redshift cancels out.

4.4.1 Manual identifications

This was based on the list of absorption features provided by Corwin & Emerson (1982) and the list of emission lines from Costero & Osterbrook (1977). These are summarised in table 4.1. Figure 4.5 shows a sample absorption and emission line galaxy spectrum from the LDSS data demonstrating these features. It should be noted that about 30% of the galaxies turned out to have emission lines. This is discussed further in chapter 6.

The method used was to measure the wavelengths of features with the cursor on the image display, guess at their identities, and look for other features. Clues were provided by such things as the 4000 Å break (a continuum break due to a change in overall blanketing by hosts of metallic lines (e.g. FeII) which undergo a large increase in density near 4000 Å) and the distinctive calcium H and K doublet (3933 Å and 3969 Å). Once the redshift has been determined the scatter of the measured line positions gives an estimate of the errors, which were typically $\Delta z \simeq 0.0005$–0.001 (depending on magnitude). This was found to be of the same order as that from the cross-correlation technique.

The strongest common absorption features are Ca H and K, G band, Hβ, Mg b and Na D. In emission Hα, [NII] and the [SII] doublet were the strongest followed by [OII] 3727 Å, [OIII] 5007 Å, Hβ and [OIII] 4959 Å. The nature of the spectra, and their relation to galaxy colours is discussed in detail in section The serious question of incompleteness arises here — are there redshift ranges for certain objects which would result in no significant features for redshift measurement? This is discussed further in sections 4.4.4 and 6.5.1.

4.4.2 The cross-correlation method

This technique involves finding the convolution of a galaxy spectrum with that of a template galaxy spectrum of known redshift, the actual convolution being done with Fast Fourier Transforms. The result, or cross-correlation function (CCF), has a peak corresponding to the redshift at which the template best matches the galaxy spectrum. A full description of this technique, together with the error analysis, can be found in Tonry & Davis (1979). To summarize:

1) The continuum has to subtracted from galaxy and template. This was done by fitting a fourth order polynomial to the spectrum and subtracting. The results are

Table 4.1: Common absorption and emission line features in galaxies

Absorption		Emission	
λ/Å	Feature	λ/Å	Feature
3742.5	Fe I (+Ti II ?)	3346	[Ne V]
3769.0	Hλ + Fe I	3426	[Ne V]
3794.5	Fe I	3727	[O II]
3798.6	Hθ	3869	[Ne III]
3827.0	Fe I	3889	He I
3834.7	Hη (+Mg I + Fe I)	3967	[Ne III]
3879.1	Fe I	3970	Hϵ
3888.7	Hζ	4071	[S II]
3933.4	K (Ca II)	4102	Hδ
3969.2	H (Ca II + Hϵ)	4340	Hγ
4071.1	Fe I	4363	[O III]
4102.8	Hδ	4686	He II
4227.8	g (Ca I)	4861	Hβ
4272.1	Fe I + Cr I	4959	[O III]
4298.1	G_1^* (CH etc.)	5007	[O III]
4304.4	G (CH etc.)	5199	[N I]
4310.4	G_2^* (CH etc.)	5309	[Ca V]
4340.5	Hγ	5721	[Fe VII]
4376.7	Fe I + CH	5876	He I
4384.1	Fe I	6087	[Fe VII]
4864.5	Hβ	6300	[O I]
5166.6	b_1^* (Mg I)	6364	[O I]
5174.0	b (Mg I)	6374	[Fe X]
5183.2	b_2^* (Mg I)	6548	[N II]
5268.6	Fe I + Ca I (or MgH)	6563	Hα
5591.0	Ca I + Ni I	6583	[N II]
5709.9	Fe I + Mg I (+Ni I ?)	6716	[S II]
5847.6	Fe I (+ Ni I ?)	6731	[S II]
5856.3	Ca I + Fe I (or TiO)		
5892.4	D (Na I)		
5917.6	Fe I ?		
5948.2	Si I ?		
5955.3	Fe I + Ti I		

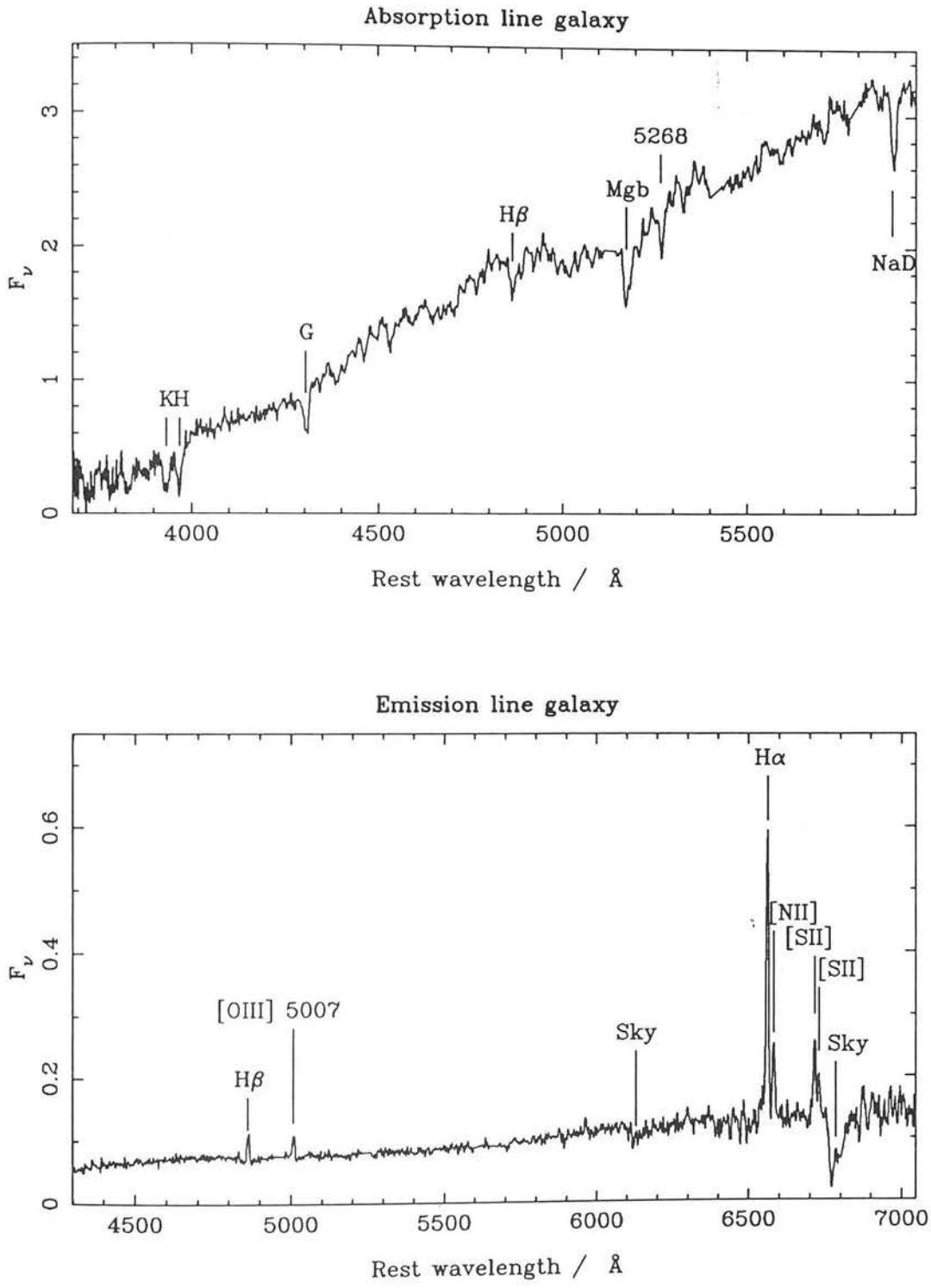

Fig. 4.5 Spectra of a bright absorption line galaxy (top) and a bright emission line galaxy (bottom) from the LDSS sample showing typical spectral features.

insensitive to the exact order of the polynomial.

2) The spectra have to be apodised — i.e. any remaining discontinuity between the opposite ends of the spectra has to be removed. This is because a discrete Fourier transform is employed and the spectrum is made periodic by identifying the ends. Any discontinuity would look the same as a genuine break in the galaxy spectrum, such as the 4000Å feature, only sharper, and so introduce spurious correlations. The apodisation was done by multiplying by a 10% "cosine-bell" function which is equal to unity for its 90% central portion and goes smoothly to zero at the edges. The previous continuum subtraction is sufficiently accurate that this is enough to remove any trace of a residual step while introducing negligible distortion of its own.

3) The spectra are rebinned into *logarithmic* bins, i.e. the bin centres follow a geometric progression. This is vital because cross-correlation measures a *shift* between spectra while the effect of redshift is a *multiplication* by $(1 + z)$. Note what is returned is the redshift directly and not a velocity. It is important to emphasize this — in the course of this programme it was discovered that the cross-correlation routines in use at the author's institution were being used incorrectly! How this happened was that the logarithmic rebinning program returned a "velocity shift per bin" in units of $\mathrm{km\,s^{-1}}$ and the cross-correlation program returned a relative shift in bins. These were then multiplied to give a "velocity" in $\mathrm{km\,s^{-1}}$ and "velocity" was taken as cz. Of course this is wrong as it is not velocity which is being measured but redshift directly. If the rebinning is done as

$$N_{bin} = A \ln \lambda + B$$

then the correct formula for the shift is:

$$\Delta N_{bin} = A \ln(1 + z)$$

The incorrect formula was:

$$\frac{v}{c} = \frac{\lambda'}{\lambda} - 1 = e^{A^{-1}} - 1$$

$$\Delta N_{bin} = \frac{cz}{v} = \frac{z}{e^{A^{-1}} - 1}$$

where λ'/λ is the ratio of consecutive bins. As can be seen the incorrect formulae boil down to a first-order doppler formula together with an incorrect linear extrapolation of "velocity/bin". It can be seen that the redshift is correct to first order, however the second order error is $\simeq \frac{1}{2}z^2$ which amounts to $\Delta z \sim 0.1$ at $z = 0.5$. The cross-correlation program was modified so that it automatically deduced A from the rebinning and output its results directly as a *redshift.*

4) Each spectrum is scaled by its RMS deviation from zero. This normalises it so that the autocorrelation function of the spectrum with itself will have a peak value of 1 at $z = 0$.

5) The spectra are Fourier transformed and the transform of the galaxy spectrum is multiplied by the complex conjugate of the transform of the template spectrum. At this point there is an optional multiplication by a bandpass filter designed to cut off high and low frequency components. The low frequency cutoff removes any residual continuum variations and the high frequency cutoff is equivalent to smoothing in data space with the instrumental profile. Note this destroys the normalisation of the two spectra.

6) The result is transformed back and the real part is taken as the CCF. The CCF is searched through to identify the highest peak and the redshift and error are determined by fitting a parabola in the neighbourhood of this peak. Optionally the entire CCF is stored as a "spectrum" of correlation coefficient (r) vs redshift. This can be inspected to determine the redshifts of other peaks if required.

4.4.3 Cross-correlation results

It should be emphasized that cross-correlation is not a magic technique for extracting redshifts out of random noise. There need to be observable features in the spectrum to make it work. It is not obvious how one should interpret the value of r in terms of reliability of the redshift. The solution adopted was to cross-correlate with many different templates. If these gave the same results then the redshift was taken to be secure. It was found empirically that $r > 0.2$ generally gave good results.

Some experimentation was made with the filtering. It was found that it made little difference to the consistency of the redshifts, the main effect being a scaling of r. This is

to be expected as noise at a higher frequency than the instrumental resolution will just be uncorrelated.

On comparison with objects with secure manual redshifts it was found that they gave broadly similar results. The formal errors on the cross-correlation redshift, based on peak width, were of order $\Delta z \simeq 0.0005$ and at least 4–5 of the galaxy templates gave consistent results. Typical correlation peak amplitudes were > 0.25 and the scatter in peak positions between the correct templates was of order $\Delta z \simeq 0.0005$, consistent with the internal error estimates.

Only in a very few cases was it possible to get a similarly secure cross-correlation redshift from a spectrum which had defeated manual methods. More usually the peak heights were < 0.2 and only 2–3 templates would give the same redshift at best. The errors would be larger and plotting the spectrum scaled to rest wavelength would fail to show expected features. Instead parts of the spectrum where bright night sky lines had been patched out by interpolation would be commonly identified as spurious absorption features.

Table 4.2 lists all the templates together with their rest spectral ranges that were used at some point in the analysis of the *AUTOFIB* and LDSS data. The cross-correlation work for the *AUTOFIB* data was mainly done with bright radio-galaxy templates derived from other projects at the author's institution. Because the LDSS data were deeper and had a greater spectral range it was found that these templates did not go blueward enough. Additional templates were derived from bright galaxies in the LDSS survey and these gave excellent results. Figure 4.6 shows an example of a faint LDSS galaxy together with a template and the CCF between them.

Note some stellar templates were also used since if the correlation peak was higher with a star than with a galaxy then one should be worried! Also because many faint M stars were found in the survey, looking at the strength of the correlation with an M star template enabled these to be picked out. Cross-correlation with a standard sky spectrum was done for the same reason since sometimes the cross-correlation can result in a best match of template features onto residual sky features. Experiments were also made with cross-correlating emission line galaxies. As expected this was unsuccessful because, apart from the emission lines themselves, the spectra were usually just a featureless continuum. Another experiment involved using some synthetic galaxy spectra based on the models of

Table 4.2: Cross-correlation templates

Template	Description	λ_{min}/Å †	λ_{max}/Å †
0207_LNR	Absorption line radio galaxy	4611	6049
0208_LNR	Absorption line radio galaxy	4463	5854
ESO_0602	Absorption line radio galaxy	4451	5839
ESO_0605	Absorption line radio galaxy	4421	5800
ESO_0625	Absorption line radio galaxy	4420	5798
ESO_0816	Absorption line radio galaxy	4480	5877
JAP	Mean abs line RG from IPCS + FOS data	3000	9000
OCTKR#563	Hα emission line galaxy	4421	6890
OCTKR#295	Bright LDSS absorption line galaxy	3399	5502
OCTKR#312	Bright LDSS absorption line galaxy	3593	5503
OCTKR#406	Bright LDSS absorption line galaxy	3748	5673
OCTKR#455	Bright LDSS absorption line galaxy	3482	5638
MAR#550	Bright LDSS absorption line galaxy	3686	5957
AATSKY	Summed sky line spectra from *AUTOFIB* data	4776	7443
GSTAR	Bright ~G type star from *AUTOFIB* data	4776	7443
MSTAR	Bright ~M type star from *AUTOFIB* data	4776	7443
GLA1_10	UV-cold elliptical model after 10.47 Gyr	2000	7000
GLA1_15	UV-cold elliptical model after 15.47 Gyr	2000	7000

† Rest wavelength

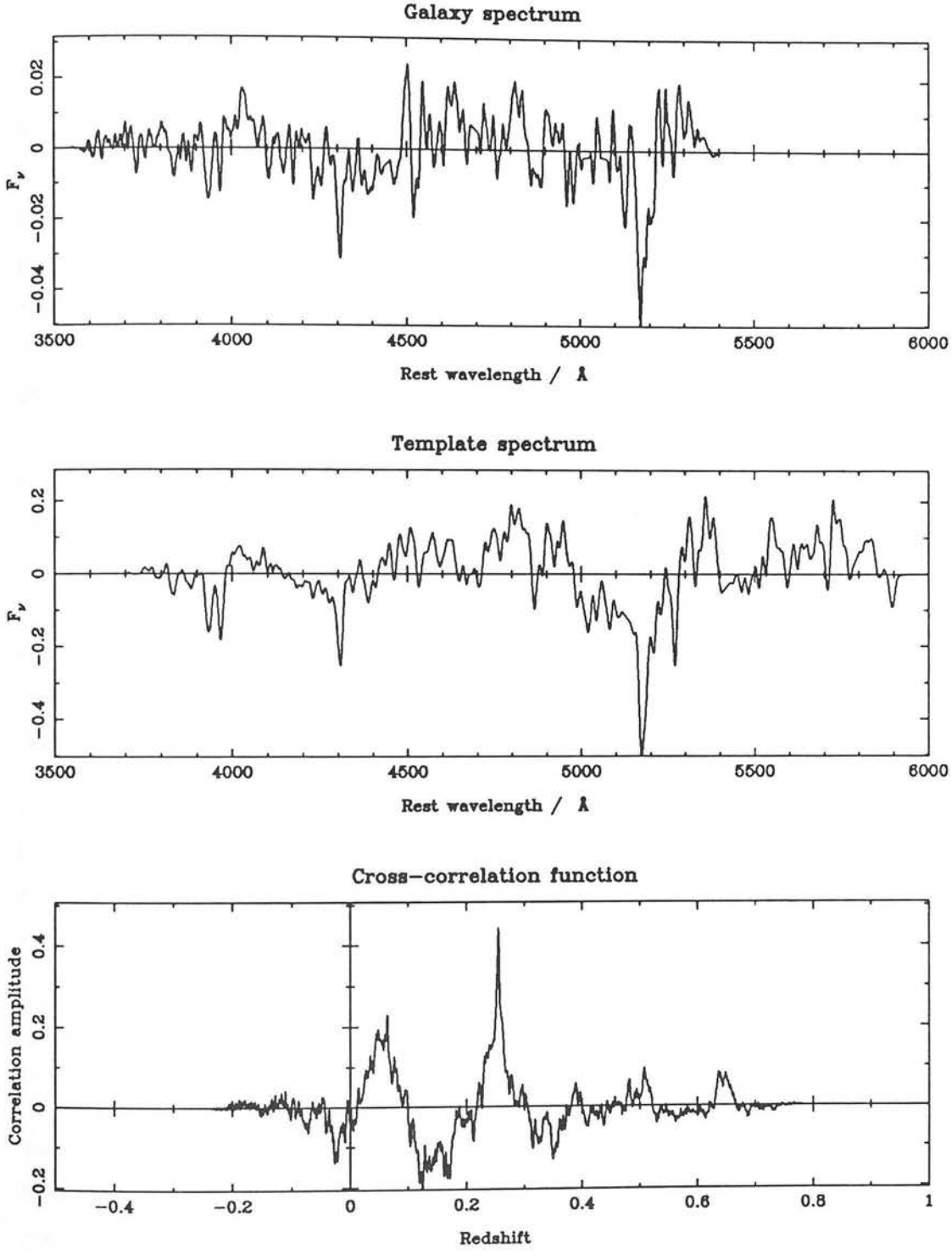

Fig. 4.6 The spectrum of a faint LDSS galaxy ($z = 0.2551 \pm 0.0003$, R = 20.0) is shown (top panel) together with the template MAR#550 (R = 16.7) (middle) and the cross-correlation function between them (bottom). Both spectra have been continuum subtracted, apodised, shifted to zero redshift (based on the CCF peak) and smoothed with the instrumental profile (10 Å FWHM Gaussian) for ease of visual comparison.

Rocca-Volmerange & Guideroni (see section 5.3.3 for details). These gave redshift results consistent with the real templates.

4.4.4 Completeness

It is possible to make a quantitative assessment of the depth reached in each field by plotting identification rate, i.e. fraction of objects identified in a given magnitude bin, against magnitude in the fields. This is done for the LDSS data in figure 4.7a. Because of the small number of objects in each LDSS field this will be somewhat noisy, it is possible to do better by incorporating the information that the relative depths of each field is predominately a function of exposure. There are other factors such as seeing and atmospheric transparency, but these can be neglected since each field was observed under similar conditions. Thus the R flux limit scales as $\sqrt{t}$, where t is the exposure time. This is done in figure 4.7a, folding this in results in a smoother curve with a sharper turnover as expected. The identification rate includes stars and galaxies in order to reduce the noise, cool M-type stars are easier to identify at faint magnitudes than galaxies, because of their strongly sawtooth shaped continuum, so this probably results in a small overestimate of the limit.

Figure 4.7b shows the *completeness*, i.e. fraction of objects identified brighter than a limiting magnitude, plotted against the limiting magnitude. Taking from figure 4.7a a limit of R = 21, corresponding to an identification rate of 58%, the completeness down to this magnitude comes out at 87%. This limit can then be scaled back to work out the R limit in each field, this is given in table 4.3 (see section 4.5). These figures agree, within ± 0.1 magnitudes, with the author's own hand estimates for the individual fields based on the *galaxy* data, indicating stars are not a problem.

Turning to the *AUTOFIB* data the identification rate is plotted against R magnitude in figure 4.8a, with cumulative completeness shown in figure 4.8b. It is not possible to break the *AUTOFIB* data down by field, because the same objects were observed in different wavelength ranges to different depths in different field configurations, and they were all joined for the final identification (see section 4.2.7). This results in the flux limit being less sharp. However adopting the same 87% cumulative completeness criterion used for the LDSS data gives $R_{lim} = 19.1$. At this magnitude the identification rate is 55%, consistent

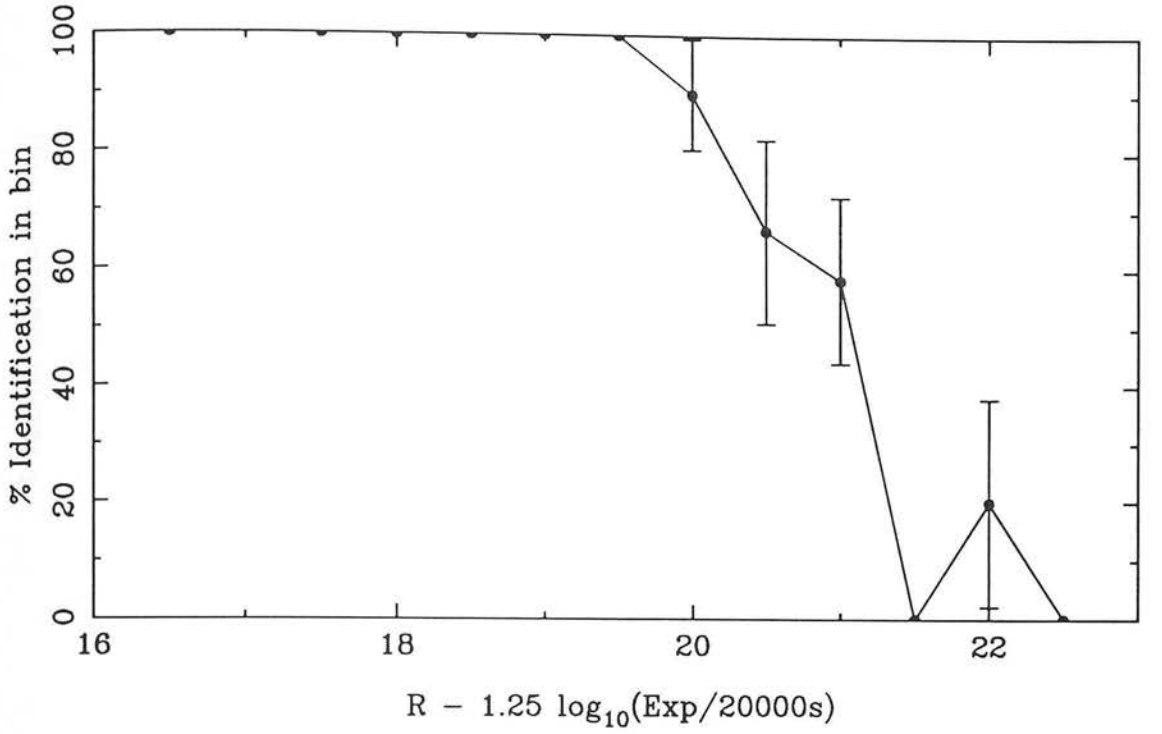

Fig. 4.7a The object identification rate for the LDSS fields vs R magnitude, corrected for the differences in exposure time.

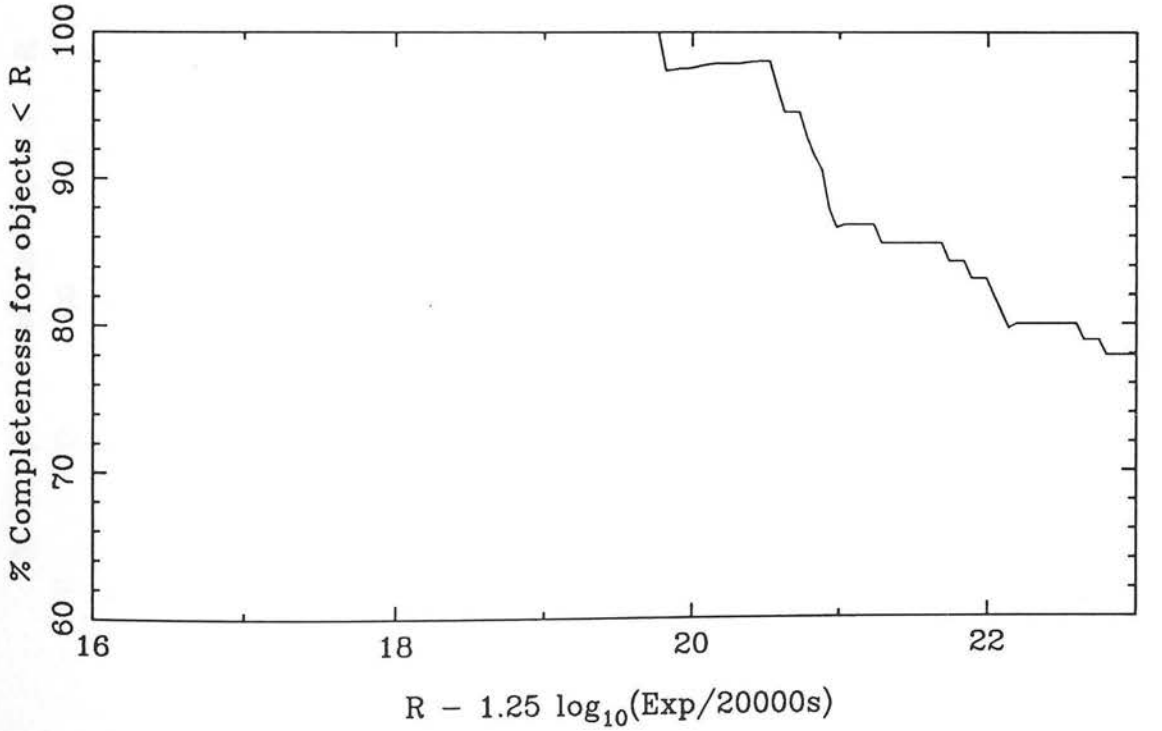

Fig. 4.7b The cumulative completeness (i.e. fraction of objects identified brighter than this magnitude) vs exposure corrected R magnitude.

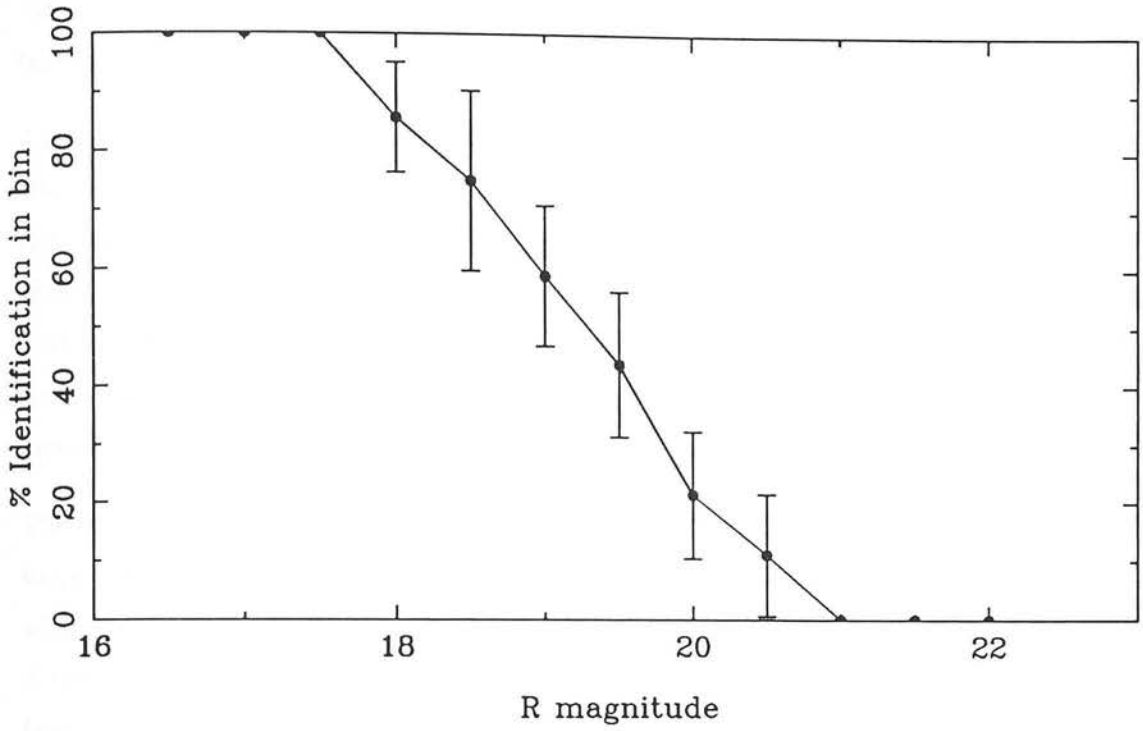

Fig. 4.8a The object identification rate for the *AUTOFIB* fields vs R magnitude.

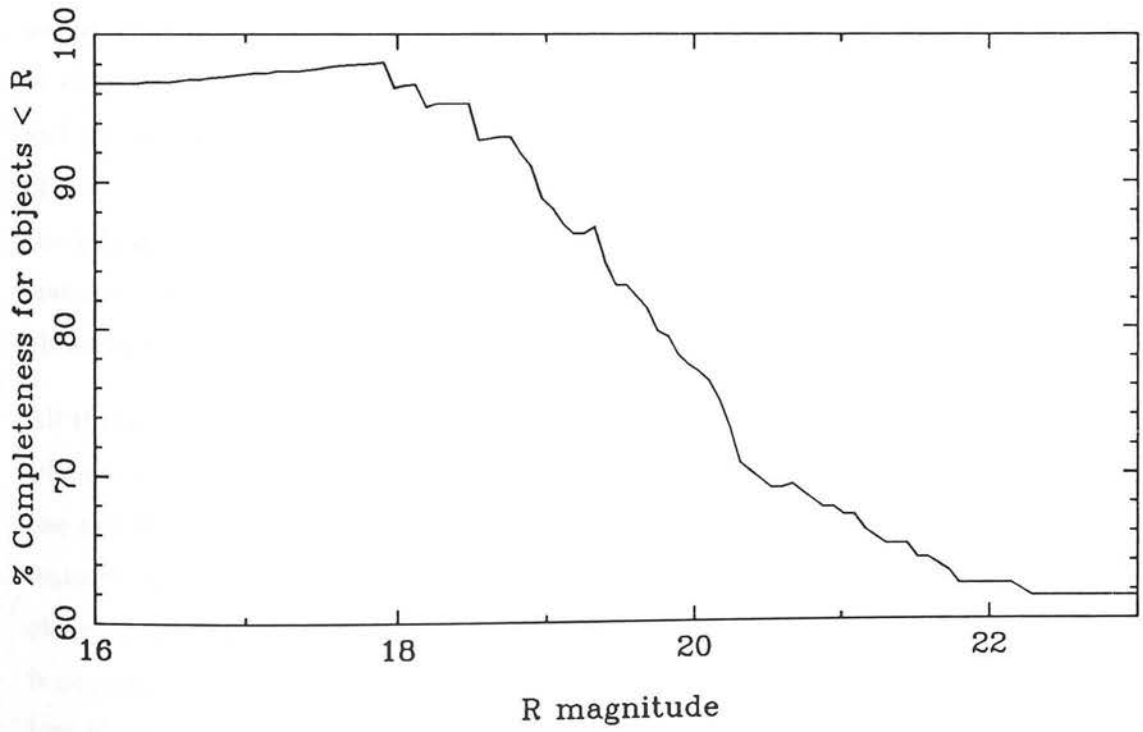

Fig. 4.8b The cumulative completeness (i.e. fraction of objects identified brighter than this magnitude) vs R magnitude.

with the LDSS data and the authors hand estimate from the galaxy data alone. The faintest identified galaxy in the *AUTOFIB* data has a R magnitude of 19.8.

Another question that arises is whether completeness is purely a function of magnitude. Obviously as a galaxy is redshifted different features of varying strength are redshifted through the observed spectral window. Figure 4.9 shows two spectra at the limit of identification, from the same mask, K5. These are OCTKR#314 ($z = 0.4705$, R – K = 3.04) and OCTKR#321 (unidentified, R – K = 3.6), both with R magnitudes of 20.1 and similar signal/noise. At this magnitude in this field an identification rate of $\simeq$ 60% is expected from the completeness plots.

The identified galaxy has obvious H,K and G band lines, although the 4000 Å break is weak. OCTKR#314 is one of the bluer galaxies for its redshift (the colour is consistent with a non-evolving Scd) , so it is understandable that the 4000 Å break would be weaker if there was a young stellar component. The unidentified galaxy has tentative absorption features at 5231 Å, 5509 Å and 6578 Å. The object is redder in R – K than the identified galaxy so if it was an early type galaxy one would expect *stronger* 4000 Å break, H and K features. Possibly the redshift could be greater than 0.82, in which case the said features would be redshifted out of the spectral window and a range less than 2400–4000 Å would be observed. In early-type objects the spectral features are weak in this wavelength range and securing a redshift would be difficult. Alternatively it could be a member of the class of emission line galaxies (see section 6.4.3 for a detailed discussion of the spectral types of the galaxies) with a red continuum, strong Hα, weak Hβ forbidden lines and absorption features. Finally, of course, it is always possible that important spectral features could be obscured by the night sky emission lines.

All this is rather unsatisfactory; however a good way of testing the effect of the spectral window is provided by the V/V_{max} test. As well as specifying K and R flux limits per field one can also calculate the z_{max} out to which one could redshift the galaxy and have the features which determine the redshift, selected according to *observed* type, remain in the observed spectral window. This is done in section 6.5.1 where it is shown that the effect is negligible. As it is there are only 3 galaxies at $z > 0.6$, whereas $z \sim 0.8$ is required to lose H and K. If a deeper redshift sample were to be constructed then the effect would become important, however it does not bias this sample.

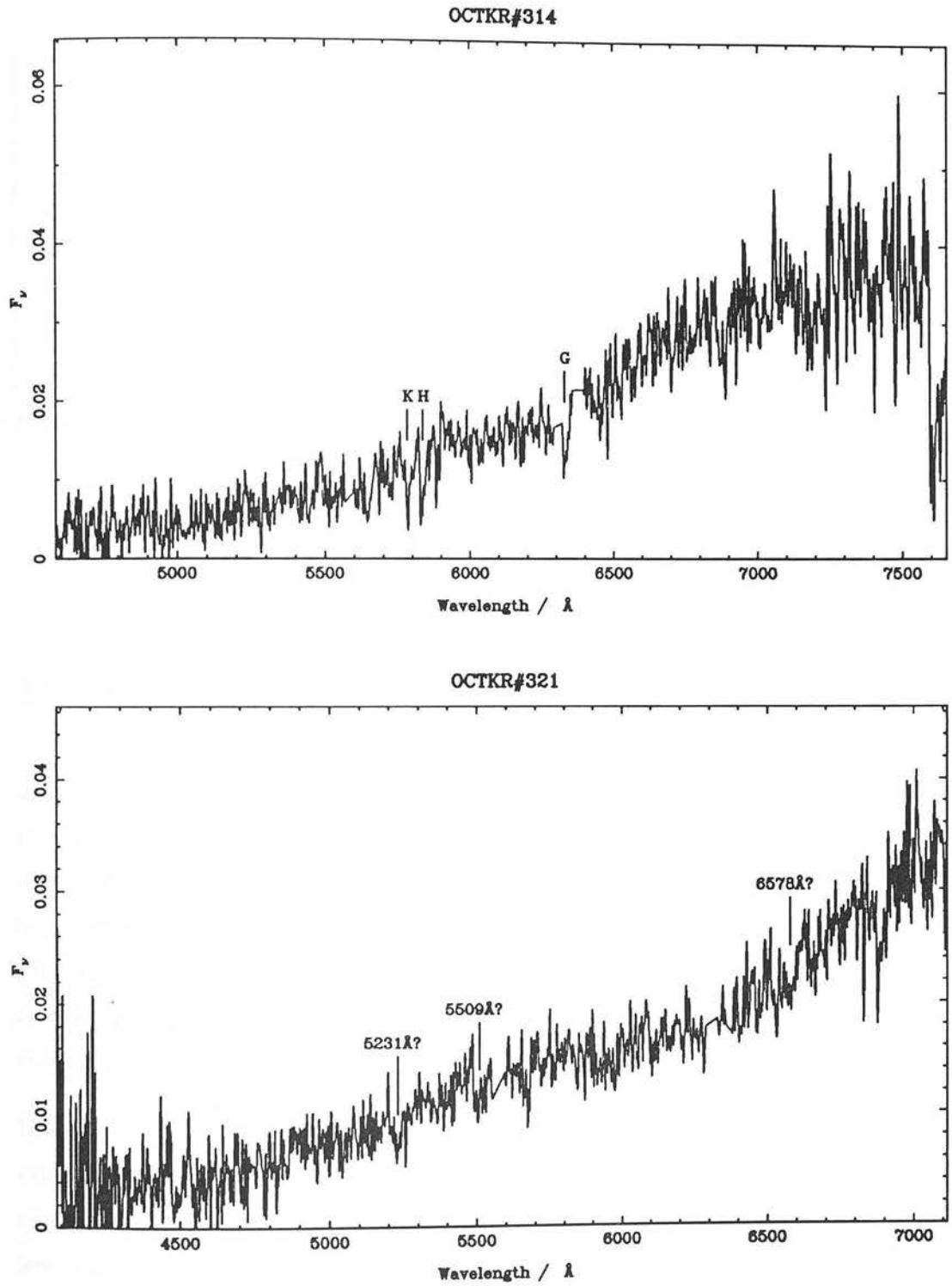

Fig. 4.9 Examples of two spectra near the limit of identification on mask K5. Both have R = 20.1, the upper spectrum was identified as a galaxy at $z = 0.4705 \pm 0.0005$, the lower spectrum remains unidentified.† Tentative absorption features are marked. The spectra have been slightly smoothed to bring out weak features.

† A small prize is offered to any examiner who can identify the object.

Table 4.3: Spectroscopic results summary

Field	Exp/s	Galaxies	Stars	UnId	Total	$\sim R_{lim}$
AUTOFIB	~20000	22[1]	72[1]	74	165	19.1
LDSS K1	15600	4	10	3	17	20.9
LDSS K5	6000	10	7	1	18	20.3
LDSS K6	6540[2]	2	5	9	16	20.2
LDSS K7	18600	12	2	3	17	21.0
LDSS F5	6571	5	4	2	11	20.4
		55	101	88	244	

Notes

1) 2 galaxies and 6 stars are in common in the *AUTOFIB* and LDSS data.
2) Very poor seeing (3.5″) on one 1540 s frame, effective exposure taken as 5000 s.

4.5 Results

Table 4.3 summarizes the depth reached in each field and the number of redshifts obtained, the identification rate down to these R magnitude limits is 87% (see section 4.4.4). It can be seen that the LDSS data reach about two magnitudes fainter than the *AUTOFIB* data in a similar order of integration time due to the increased efficiency. A comparison of two galaxies observed with both *AUTOFIB* and LDSS is shown in figure 4.10 demonstrating the much greater signal/noise achieved with LDSS. A full listing of all the redshifts is given in Appendix B.

Using these data it is possible to put figures on the reliability of the star-galaxy classification. Stars were observed intentionally to check on this — rather more, with hindsight, than should have been in the *AUTOFIB* run as initially it was decided to observe regardless of S/G classification due to some uncertainty about its reliability. Also in the LDSS run some slits were placed on "stars" as it was impossible to place them all on "galaxies" for geometric reasons. Overall $4 \pm 2\%$ of the identified objects classified as "stars" turned out to be galaxies. This rises to $7 \pm 4\%$ if we exclude the 36 objects which were saturated in the R band, all of which turned out to be stars. In the other direction $20 \pm 6\%$ of the

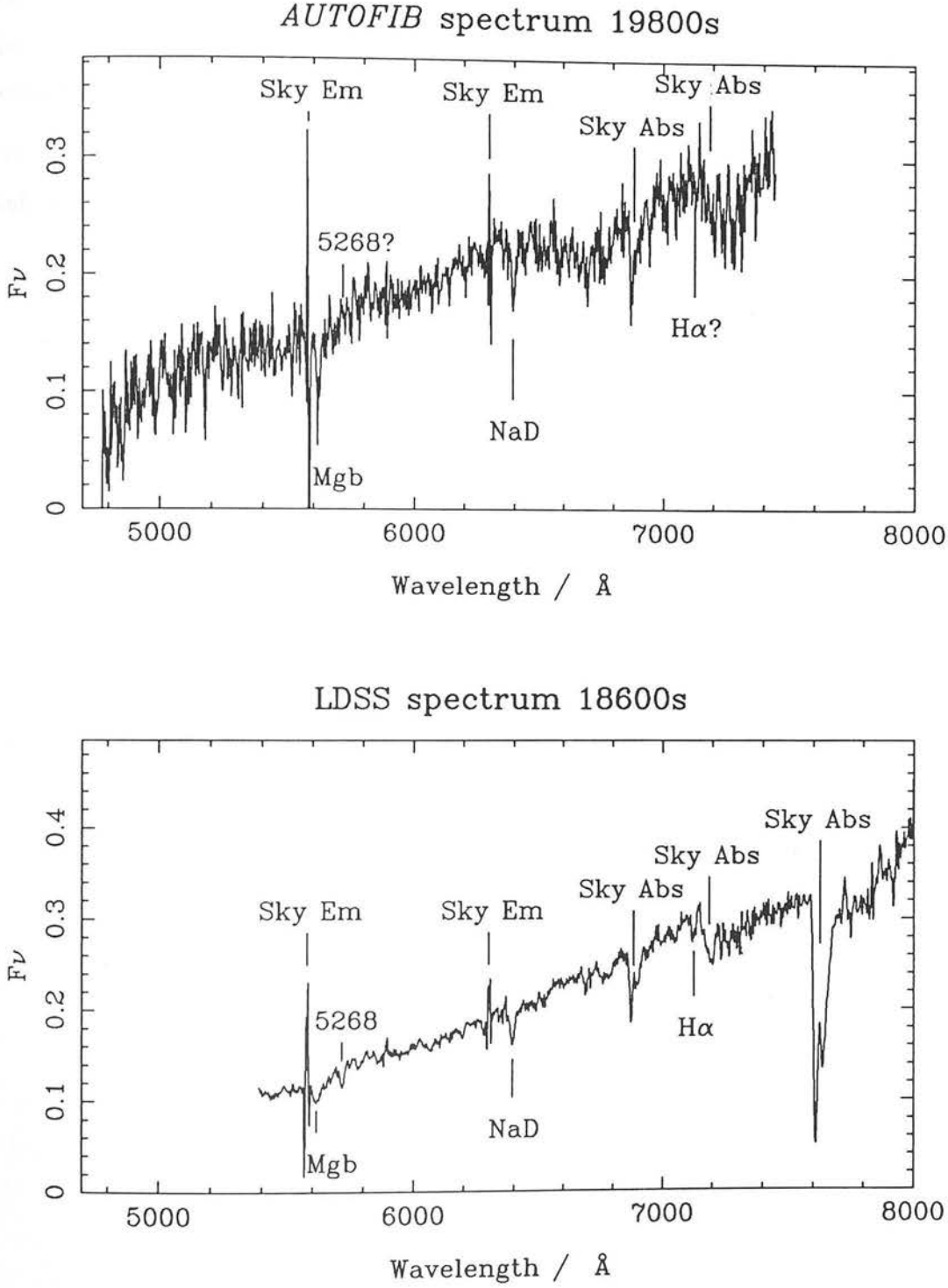

Fig. 4.10 A comparison of the galaxy OCTKR#411 ($z = 0.0853 \pm 0.0003$, R = 17.4) observed with *AUTOFIB* (top) and LDSS (bottom). Raw spectra are shown, unpatched near the bright sky emission lines. The much better efficiency and sky-subtraction of the LDSS system can be easily seen.

identified objects classified as "galaxies" turned out to be stars. This is consistent with the pre-spectroscopy assessment that the classification was conservative in the sense of including stars rather than missing galaxies. The effect of this on the number-magnitude counts is discussed further in chapter 5.

To summarize a total of 53 galaxy redshifts were obtained down to R = 20–21 from the infrared selected sample.

5 THE 2 μm GALAXY COUNTS

5.1 Introduction

This chapter presents the 2 μm galaxy counts determined from the infrared survey. This is the first determination of the galaxy counts from a large-area infrared survey and when combined with deep K count data published in the literature allows the determination of the galaxy counts over a range of 10^4 in flux.

As is described in chapter 1, galaxy counts are a classical tool of cosmology. The determination of the 2 μm counts is important because, in principle, they are much less sensitive to the evolution of stellar populations than the optical galaxy counts. This allows them to be used as a direct test of cosmological models as well as to probe galaxy evolution. There has been little work done in this area until recently, because the recent arrival of infrared array detectors only now allows a large area to be surveyed quickly.

Counts of galaxies allow the determination of the geometry *if* the evolution can be accounted for. In the optical b_j band the effects of evolution completely overwhelm the effects of geometry and much effort has been spent on constructing sophisticated models of spectral evolution of galaxies in order to allow for this (e.g. Guideroni & Rocca-Volmerange 1990, Bruzual 1983). However the evolution is so dominant that the uncertainties in the models have greater effects than Ω_0.

In this chapter the galaxy counts are modelled in b_j and K using various evolutionary schemes, including spectral evolution models from the literature. The availability of an infrared passband, insensitive to spectral evolution, enables a better constraint on the geometry to be obtained. In addition it is possible to remove the degeneracy between *luminosity* evolution in the galaxy population, due to their on-going star-formation and stellar evolution; and *number-density* evolution in the galaxy population which might, for example, be due to a history of galaxy mergers.

5.2 The Raw Data

The raw counts of galaxies and stars are shown in Figures 5.1 and Figure 5.2. In total there are 174 galaxies and 114 stars in the October fields, and 132 galaxies and 61 stars in the March fields. These are counts for objects paired in the K and R bands; as is discussed in 6.3 there is no evidence that any of the unpaired K detections are real, and the number of K-only objects unaccounted for is sufficiently low to have negligible effect. As is the usual convention, $\log_{10}$ of the *differential* counts (i.e. number per unit magnitude — determined by binning) is plotted against magnitude. The low value beyond K=17 is due to the survey area being non-uniform with depth at the faintest magnitudes. The error bars are simply $\sqrt{N}$ Poisson errors determined from the number of objects in each bin. The real errors will be somewhat larger of course due to the effect of clustering.

The "galaxies" are defined as in section 3.6 by adopting the criterion $y \geq 0.3$. Star-galaxy separation is vital to the counts as stars outnumber galaxies for K $<$ 16. The counts exclude objects used as "reference stars" (see section 2.2.2) in the IRCAM mosaics; these mainly affect the range K = 15–16. The reference stars provide a useful independent check on the R CCD star-galaxy classification as they were independently classified by the COSMOS image analysis software based on the Schmidt plate data. There were 37 "galaxies" out of 116 reference objects in the October fields, of which 3/21 identified spectroscopically turned out to be real stars after all. In the March fields the galaxy fraction was 11/63; none of these "galaxies" was identified spectroscopically. It appears that the misclassification rate of the CCD star-galaxy separation is consistent between the reference objects and the rest (see below), and that the COSMOS classification is much less reliable than the CCD classification. This is to be expected as the CCD data are deeper and much more linear.

The CCD failure rate can be estimated from the spectroscopic results given in section 4.5. We can define parameters α as the fraction of "stars" which turn out to be really galaxies and β to be the fraction of "galaxies" which turn out to be really stars. For the entire identified spectroscopic sample $\alpha = 4 \pm 2\%$ and $\beta = 20 \pm 6\%$, the errors being based on Poisson statistics. β is much larger than α because a deliberately conservative star-galaxy cut was chosen for completeness reasons, i.e. to include stars rather than lose galaxies. The magnitude of this error in the galaxy counts is about half that of the Poisson

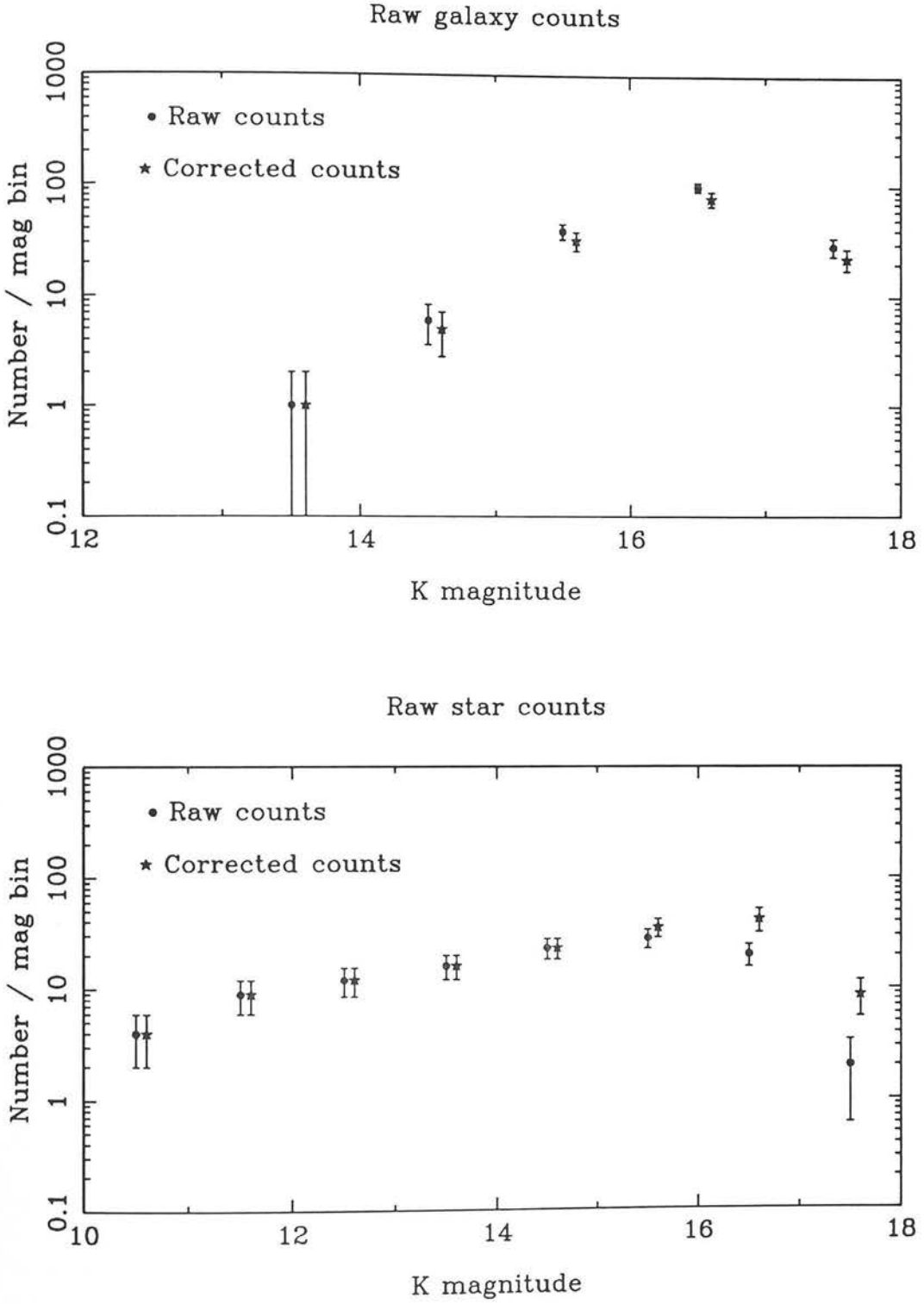

Fig. 5.1 The K counts in 1 magnitude bins for galaxies (top) and stars (bottom) for the October fields. The raw counts and counts corrected for star-galaxy misclassification (offset by 0.1 magnitudes for clarity) are shown.

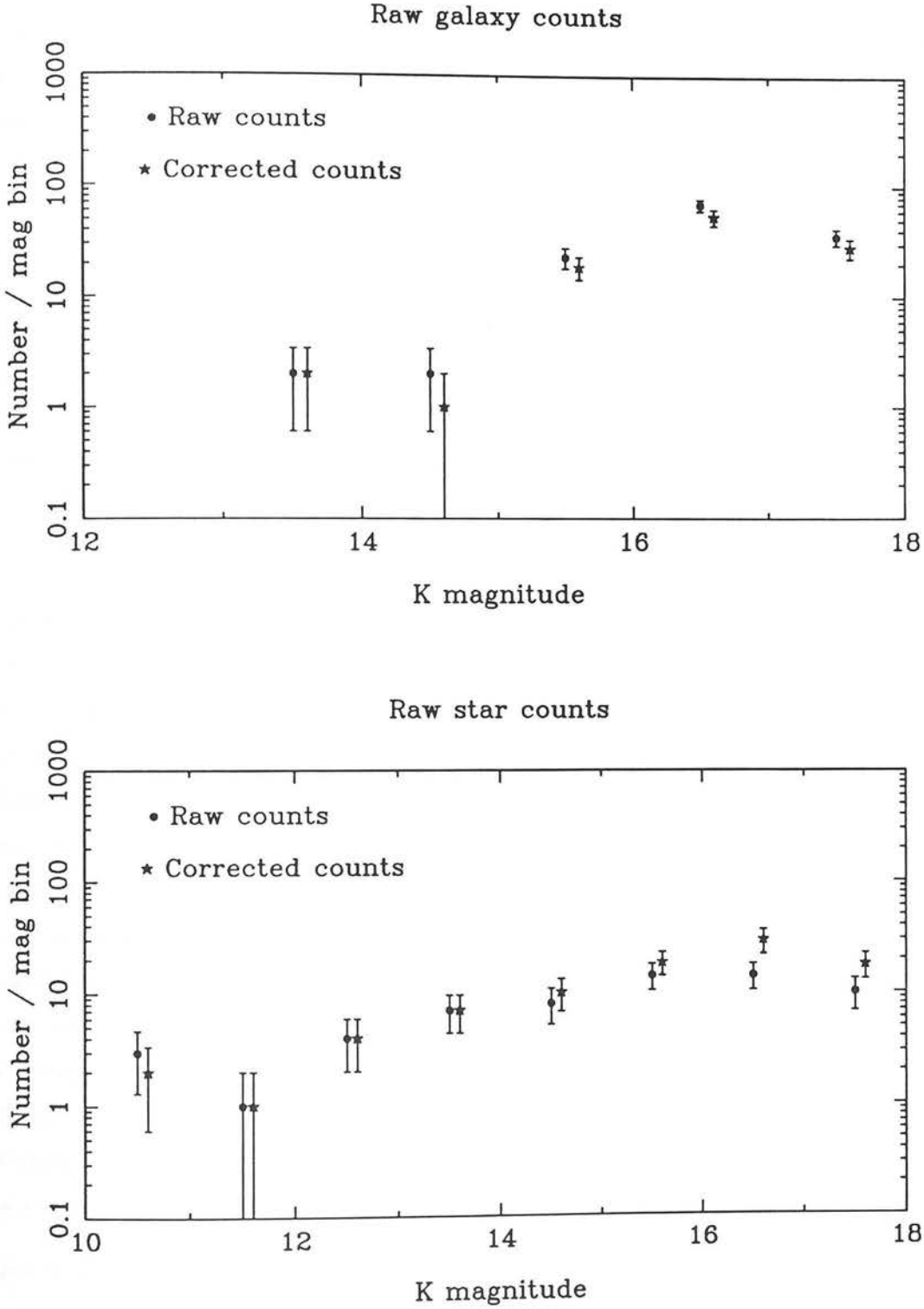

Fig. 5.2 The K counts in 1 magnitude bins for galaxies (top) and stars (bottom) for the March fields. The raw counts and counts corrected for star-galaxy misclassification (offset by 0.1 magnitudes for clarity) are shown.

errors in each magnitude bin. However what is most important is the *differential* change in star-galaxy misclassification with K magnitude — the slope of the galaxy relation is much more important than the normalisation. This misclassification can be corrected for by using the relations:

$$N'_g = N_g(1-\beta) + \alpha N_s$$
$$N'_s = N_s(1-\alpha) + \beta N_g$$

where N_s and N_g are the original star and galaxy numbers in each magnitude bin and N'_g and N'_s are the corrected values (note $N'_s + N'_g = N_s + N_g$ of course). The errors $\Delta\alpha$, $\Delta\beta$, $\sqrt{N_s}$ and $\sqrt{N_g}$ can all be folded in to give errors on N'_g and N'_s which are now slightly in excess of their Poisson values. (Note on these plots the corrected error bars appear smaller. This is not in fact the case as this is a log plot: the actual absolute errors increase).

It can be seen from figure 5.3, which plots the classification image-area parameter y against K magnitude that the star and galaxy loci are well separated down to K $\simeq$ 15 and that the misclassification should apply mostly in the K $>$ 15 regime. In the spectroscopic sample 12 out of 15 of the misclassified objects had K $>$ 15. For the final corrected counts all objects with K $<$ 15 (94) were inspected visually to check for errors and only 4 were found. The K $>$ 15 counts were corrected using the values $\alpha = 7.7 \pm 7.7\%$ (1 object) and $\beta = 23.3 \pm 8.8\%$ derived from the spectroscopy in this magnitude range. Figures 5.1 and 5.2 show the effect on the counts from applying these corrections and table 5.1 gives these in numeric form. It is evident from the graph that the major effect is just a small change in the normalisation due to β. Figure 5.4 compares the galaxy counts for both halves of the survey normalised according to area. Note that the galaxy counts have the same shape and normalisation for both halves, within the errors, while the star counts differ for the two halves. This also demonstrates that the effect of misclassification is minor, otherwise the star counts would cause the galaxy counts in the two halves to be different.

Note there seems to be an anomaly in the star counts in the March field in the very brightest bin (see figure 5.2). This is not caused by a star cluster as the three objects involved are all in different RA fields. The most probable explanation is that this is an effect of the residual stellar bias mentioned in section 2.2.2. Although the reference stars have been selected out of these counts there will still be a bias from stellar binaries and

Table 5.1: Galaxy and star counts for the infrared survey.

October fields						
K range	N_g	N_s	N'_g	$\Delta N'_g$	N'_s	$\Delta N'_s$
$10 \leq K < 11$	0	4	0.0	—	4.0	2.0
$11 \leq K < 12$	0	9	0.0	—	9.0	3.0
$12 \leq K < 13$	0	12	0.0	—	12.0	3.5
$13 \leq K < 14$	1	16	1.0	1.0	16.0	4.0
$14 \leq K < 15$	6	23	5.0	2.2	23.0	4.8
$15 \leq K < 16$	39	28	32.1	6.3	34.9	6.5
$16 \leq K < 17$	99	20	77.5	11.7	41.5	10.0
$17 \leq K < 18$	29	2	22.4	4.9	8.6	3.1
	174	114	138.0	14.4	149.0	14.7

March fields						
K range	N_g	N_s	N'_g	$\Delta N'_g$	N'_s	$\Delta N'_s$
$10 \leq K < 11$	0	3	0.0	—	2.0	1.4
$11 \leq K < 12$	0	1	0.0	—	1.0	1.0
$12 \leq K < 13$	0	4	0.0	—	4.0	2.0
$13 \leq K < 14$	2	7	2.0	1.4	7.0	2.6
$14 \leq K < 15$	2	8	1.0	1.0	10.0	3.2
$15 \leq K < 16$	23	14	18.7	4.3	18.3	4.3
$16 \leq K < 17$	69	14	54.0	8.9	29.0	7.3
$17 \leq K < 18$	36	10	28.4	5.6	17.6	4.6
	132	61	104.1	11.5	88.9	10.8

Total Survey						
K range	N_g	N_s	N'_g	$\Delta N'_g$	N'_s	$\Delta N'_s$
$10 \leq K < 11$	0	7	0.0	—	6.0	2.4
$11 \leq K < 12$	0	10	0.0	—	10.0	3.2
$12 \leq K < 13$	0	16	0.0	—	16.0	4.0
$13 \leq K < 14$	3	23	3.0	1.7	23.0	4.8
$14 \leq K < 15$	8	31	6.0	2.4	33.0	5.8
$15 \leq K < 16$	62	42	50.8	7.6	53.2	7.8
$16 \leq K < 17$	168	34	131.5	14.7	70.5	12.4
$17 \leq K < 18$	65	12	50.8	7.4	26.2	5.5
	306	175	242.1	18.4	237.9	18.3

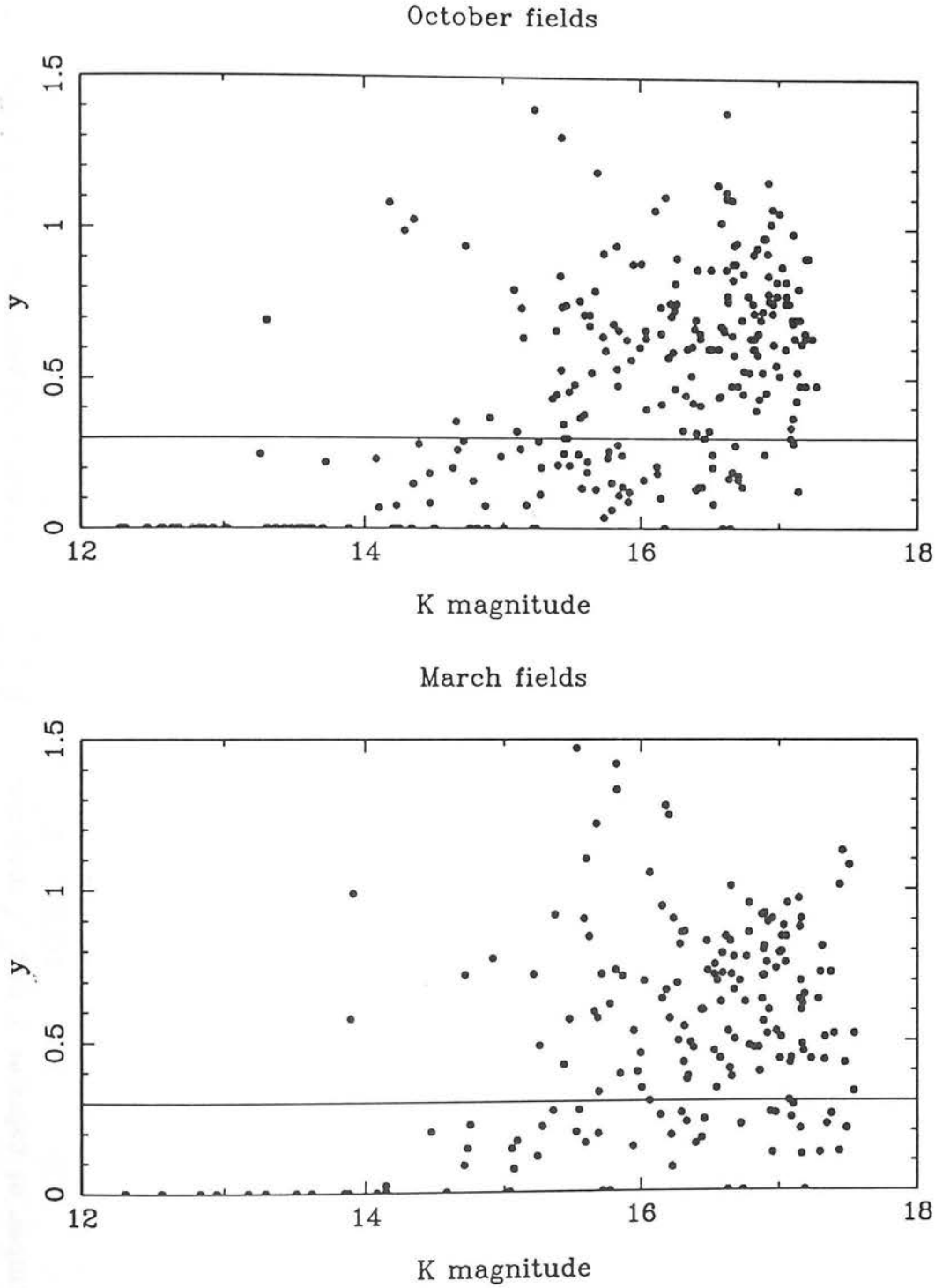

Fig. 5.3 The star-galaxy separation parameter y parameter plotted against K magnitude for all the objects in the October fields (top) and March fields (bottom). The adopted separation between stars ($y < 0.3$) and galaxies ($y \geq 0.3$) is shown. Objects on the $y = 0$ axis are saturated on the R CCD image and are classed as stars. The separate star and galaxy loci can be clearly seen.

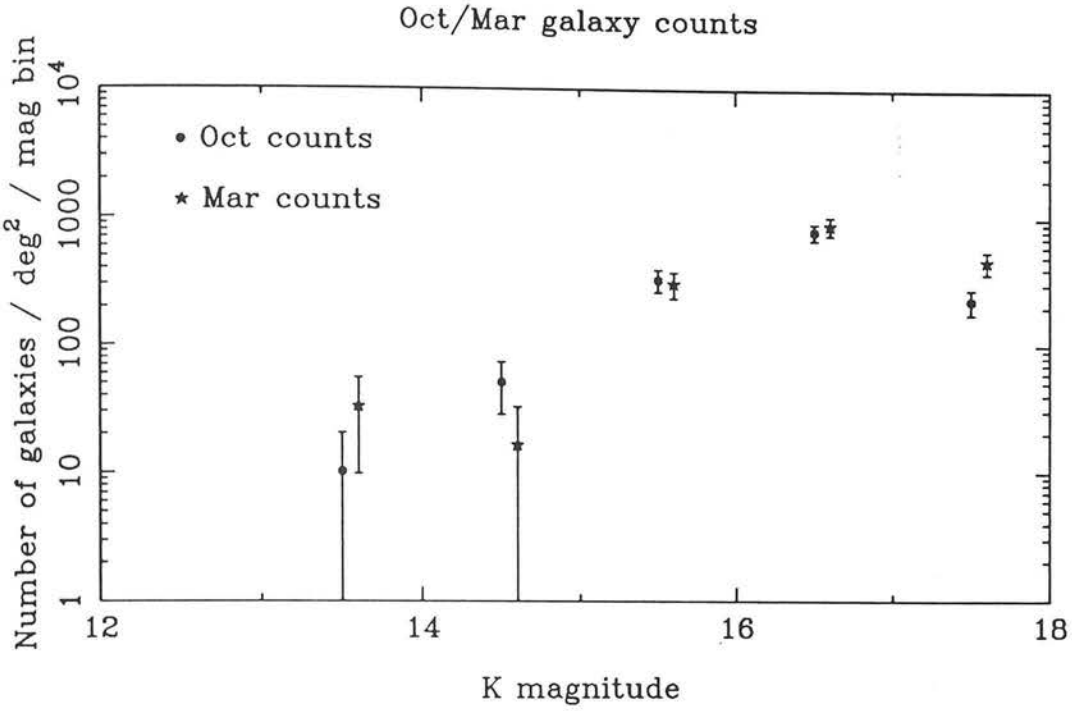

Fig. 5.4a A comparison of the star-galaxy misclassification corrected K galaxy counts, in 1 magnitude bins, for the October and March fields normalised to 1□°. The March points are offset by 0.1 magnitudes from the October points for clarity.

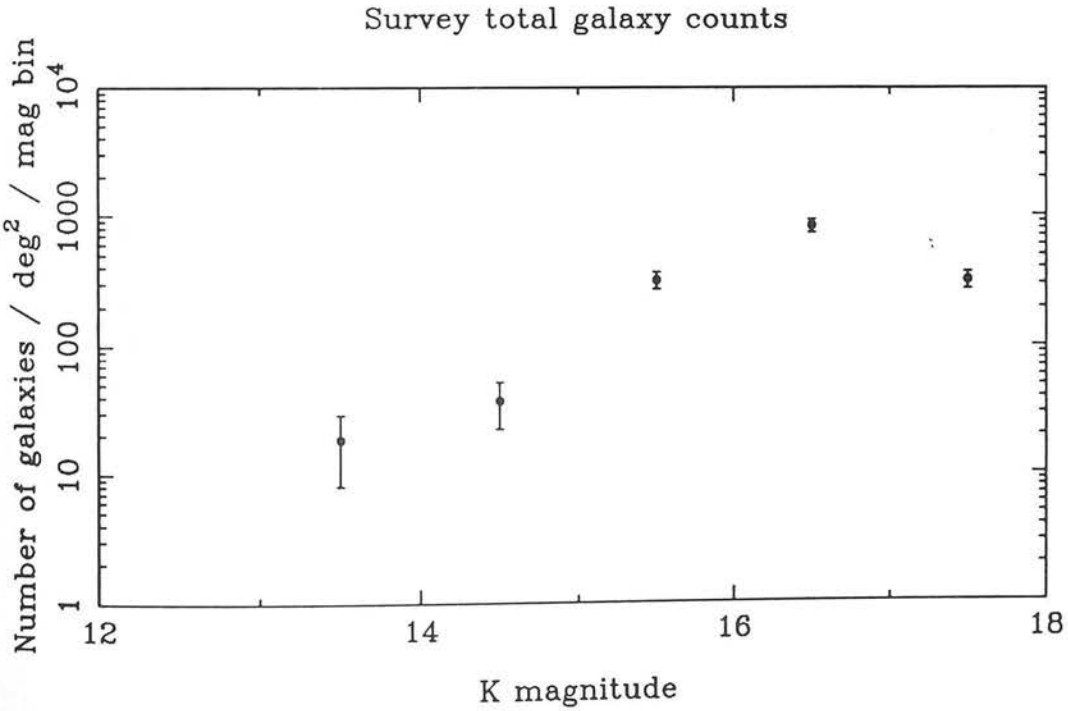

Fig. 5.4b The K galaxy counts in 1 magnitude bins for the whole survey corrected for star-galaxy misclassification.

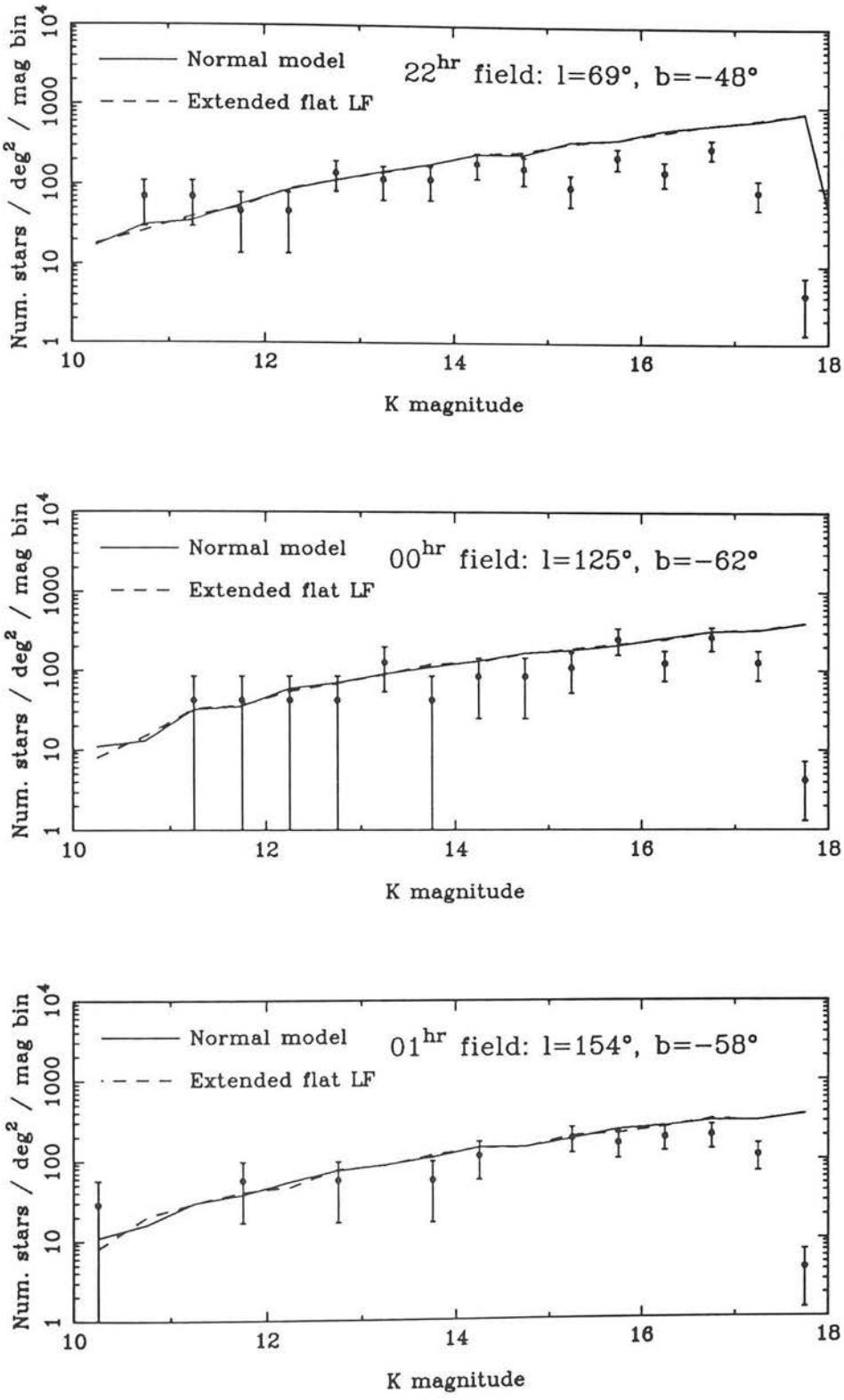

Fig. 5.5 Star counts in the various October fields compared with models supplied by I.N. Reid.

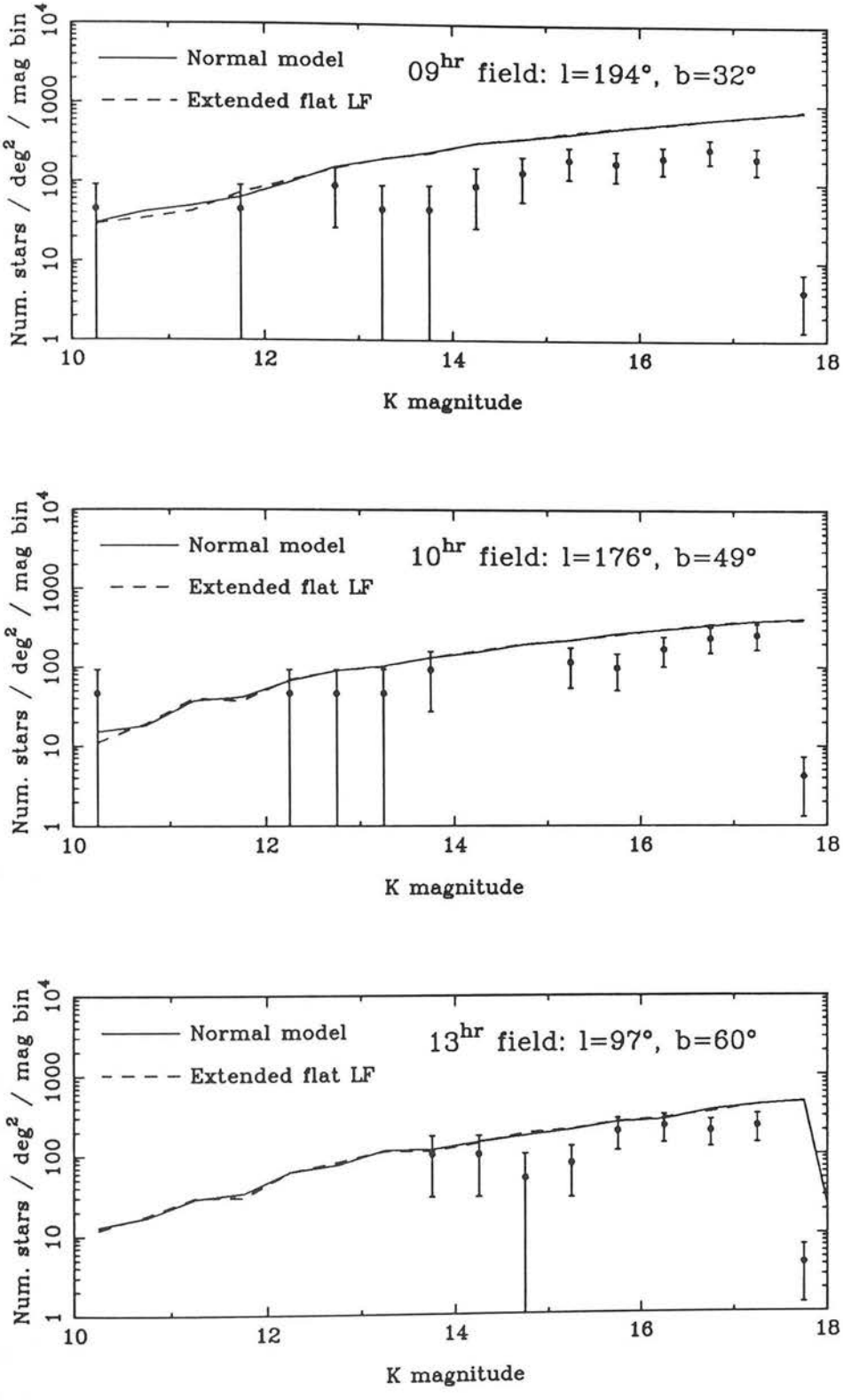

Fig. 5.6 Star counts in the various March fields compared with models supplied by I.N. Reid.

clusters. Nevertheless, the star counts can be compared with the model of Bahcall & Soneira (1980), these were modified to the infrared by I.N. Reid (private communication, 1990). This is shown in figures 5.5 and 5.6 for the individual RA fields. It can be seen that in most cases the agreement is good though the normalisation in the model appears to be slightly too high in each case. This is worse in the 09^h field which is also the field at lowest galactic latitude.

To summarise it appears that the star-galaxy classification has been very successful and reliable. It has been possible to correct for the observed error rate in star-galaxy separation — the only important effect being a drop in normalisation of $\simeq 20\%$ in the galaxy counts. The resultant star counts agree with model predictions and the galaxy counts are consistent between the two different halves of the survey.

5.3 Modelling Technique

5.3.1 Basic principles

Modelling the number-magnitude counts involves integrating the galaxy luminosity function over redshift at a fixed observed magnitude. In a Friedmann model the relation between luminosity and observed flux is given by (Weinberg 1972):

$$S_{\rm BOL} = \frac{L_{\rm BOL}}{4\pi D_L^2}$$

where $S_{\rm BOL}$ and $L_{\rm BOL}$ are *bolometric* flux densities and luminosities, i.e. integrated over all wavelengths. D_L is known as the luminosity distance and is given conventionally in a Friedmann cosmology by

$$D_L = \frac{2c}{\Omega^2 H_0}(\Omega z + (\Omega - 2)(\sqrt{1+\Omega z} - 1))$$

However this formula is undefined as $\Omega \to 0$, an algebraically equivalent formula which is better behaved is given by:

$$D_L = \frac{cz}{H_0}\frac{(1+\sqrt{1+\Omega z}+z)}{(1+\sqrt{1+\Omega z}+\Omega z/2)}$$

This formula was taken from Peacock (1987): it is a modification of one due to Terrell (1977) given by Schmidt & Green (1983). Using the luminosity distance one can then simply relate absolute (M) and apparent (m) magnitudes:

$$(m - M)_{\rm BOL} = 5\log_{10}\left(\frac{D_L}{10\,{\rm pc}}\right)$$

In the real world, only a flux in a finite wavelength range can be measured. In this case the distance modulus becomes:

$$m - M = 5\log_{10}\left(\frac{D_L}{10\,{\rm pc}}\right) + K(z) + E(z)$$

where $K(z)$ is the ill-named K-correction which takes account of the redshifting of the galaxy spectrum through the observed band and $E(z)$ is the evolutionary effect from observing a galaxy at large lookback times (Bruzual 1983b). If the spectrum of the galaxy is $f_\lambda(t)$, where $t(z)$ is the lookback time at a given redshift, then $K(z)$ and $E(z)$ are given by:

$$K(z) = -2.5\log_{10}\left[\frac{1}{(1+z)}\frac{\int_{-\infty}^{\infty} T_\lambda f_{\frac{\lambda}{(1+z)}}(0)d\lambda}{\int_{-\infty}^{\infty} T_\lambda f_\lambda(0)d\lambda}\right]$$

$$E(z) = -2.5\log_{10}\left[\frac{\int_{-\infty}^{\infty} T_\lambda f_{\frac{\lambda}{(1+z)}}(t)d\lambda}{\int_{-\infty}^{\infty} T_\lambda f_{\frac{\lambda}{(1+z)}}(0)d\lambda}\right]$$

$K(z)$ and $E(z)$ might be separately calculated, for example $K(z)$ from a low-redshift galaxy template and $E(z)$ from some simple parameterisation of luminosity as a function of z. Alternatively if a galaxy spectral evolution code is used it is more sensible to combine them as:

$$R(z) = K(z) + E(z)$$

where $R(z)$ is given as :

$$R(z) = -2.5\log_{10}\left[\frac{1}{(1+z)}\frac{\int_{-\infty}^{\infty} T_\lambda f_{\frac{\lambda}{(1+z)}}(t)d\lambda}{\int_{-\infty}^{\infty} T_\lambda f_\lambda(0)d\lambda}\right]$$

If we then take $\phi(M)$ as the luminosity function in terms of *magnitudes* (i.e. number of galaxies per unit comoving volume per unit magnitude) then the number of galaxies per unit magnitude is:

$$n(m) = \int_0^\infty \phi(M) dV$$

There are two limiting cases worth noting which have simple analytic forms. At bright magnitudes the counts tend to the Euclidean case; when $\phi(M)$ is described by a Schechter function (see section 5.3.2) this becomes:

$$n(m) \Rightarrow \frac{4\pi}{5} (\ln 10)\, \Gamma(\alpha + \tfrac{5}{2})\, \phi^*\, 10^{0.6(m-M^*-25)} \qquad \text{as } m \Rightarrow -\infty$$

i.e. the counts have a slope of 0.6 if $\log n$ is plotted against m.

Secondly if $\alpha = -1$ the counts tend to a constant value at faint magnitudes (if the Schechter function is not truncated at faint luminosities):

$$n(m) \Rightarrow 0.4\, (\ln 10)\, \phi^*\, V(z_{max}) \qquad \text{as } m \Rightarrow \infty$$

These provide an important check on the program which computes $n(m)$, and in particular ensures that the normalisation is correct for given Schechter parameters. This is very important in going from the B counts to the K counts (see section 5.4.1).

It is also worth noting that if $n(m)$ is parameterised as $10^{\alpha m}$ (so $\log_{10} n$ vs m is a line of slope α), as is quite common in the literature, then the total *surface brightness* of the night sky becomes:

$$S_{TOT} = \int_{-\infty}^{\infty} S(m) n(m) dm = \int_{-\infty}^{\infty} 10^{-0.4m} 10^{\alpha m} dm$$

which is divergent if $\alpha \geq 0.4$. The Euclidean case ($\alpha = 0.6$) violates this which, of course, is more familiar as one form of Olber's paradox.

Knowledge of the comoving volume element (dV) is what allows the galaxy counts to be used, in principle, as a cosmological test and is given for a Friedmann model by:

$$\frac{dV}{dz} = 4\pi \left(\frac{c}{H_0}\right)^3 \frac{z^2}{(1+z)^3} \frac{1}{\sqrt{1+\Omega z}} \frac{(1+\sqrt{1+\Omega z}+z)^2}{(1+\sqrt{1+\Omega z}+\Omega z/2)^2}$$

It can now be seen that the term in ${H_0}^3$ goes away in the normalisation. The normalisation of the luminosity function is given by local galaxies, i.e. by $n(m,z)$ at some low-z and bright magnitude so $\phi(M) \propto {H_0}^3$ which cancels the ${H_0}^{-3}$ dependance of dV/dZ. Similarly the H_0 dependence in the distance modulus $m - M$ is cancelled by that of M^* in the luminosity function (see section 5.3.2). The only remaining H_0 dependence is in the evolutionary corrections $E(z)$ where the change in the galaxy spectrum depends on its age at a given redshift.

5.3.2 Luminosity function

An analytic form which provides a good fit to the luminosity distribution of galaxies is given by Schechter (1976):

$$\phi(L)dL = \phi^* \left(\frac{L}{L^*}\right)^{\alpha} e^{-L/L^*} d\left(\frac{L}{L^*}\right)$$

where $\phi(L)dL$ is the comoving number density of galaxies with luminosity between L and $L + dL$. In terms of magnitudes instead of luminosities this becomes:

$$\phi(M)dM = 0.4 \ln 10 \, \phi^* \, 10^{-0.4(\alpha+1)(M-M^*)} \, e^{-10^{-0.4(M-M^*)}} dM$$

which gives

$$\log \phi = -\underbrace{(\log e) 10^{-0.4(M-M^*)}}_{\text{Exponential break}} - \underbrace{0.4(\alpha+1)(M-M^*)}_{\text{Faint end slope}} + (\text{consts.})$$

It can be seen by inspection that if M is fainter than M^* then $\log \phi$ vs M tends to a line of slope $\propto (\alpha + 1)$. If $\alpha = -1$ then the slope is 0 and if $\alpha < -1$ then the slope is positive. For $M \leq M^*$ there is a strong exponential downturn in the curve giving a "knee-shaped" luminosity function.

At this point a word about H_0 conventions is necessary. Usually H_0 is parameterised in terms of $h = H_0/100\,\mathrm{km\,s^{-1}\,Mpc^{-1}}$ and ϕ^* is given in units of $h^3\,\mathrm{Mpc^{-3}}$, which is the convention adopted here. M^* scales as $M^* + 5\log_{10} h$, where numerical M^* values are given in the rest of the text they are for $H_0 = 100\,\mathrm{km\,s^{-1}\,Mpc^{-1}}$. To re-emphasise the point made in section 5.3.1 in actual number-magnitude and number-redshift predictions the h dependencies in the luminosity function cancel out.

$\phi(M)$ has been determined for field galaxies from several flux limited surveys in the optical. A Schechter function provides a satisfactory fit but there is some question as to the dependance of M^* and α on morphological type. For example King & Ellis (1985) give $M^*_{b_j}$ ranging from -19.59 for ellipticals to -19.39 for Sc types ($\alpha = -1.0$, $H_0 = 100\,\mathrm{km\,s^{-1}\,Mpc^{-1}}$) based on data from the Durham/AAT redshift survey (*DARS*). Efstathiou *et al.* (1988), however, applying clustering-insensitive maximum likelihood estimators to a variety of flux limited samples including *DARS*, finds $\alpha = -1.07 \pm 0.05$, $M^*_{b_j} = -19.68 \pm 0.10$ and $\phi^* = (1.56 \pm 0.34) \times 10^{-2} h^3\,\mathrm{Mpc}^{-3}$ with no evidence of dependence on morphological types earlier than Sc.

For predicting the infrared galaxy counts the luminosity function should be determined self consistently from an infrared selected redshift survey. The only work which has been done on this is that of B. Mobasher, R.M. Sharples and R.S. Ellis based on an K selected complete subset of the DARS sample ($\overline{z} \sim 0.05$) (private communication). The resulting K luminosity function is identical to the optical luminosity function shifted by type-dependant $b_j - \mathrm{K}$ colours. In this chapter the luminosity function is constructed in this way using $b_j - \mathrm{K}$ colours derived from the same model spectra used to predict the b_j and K number-magnitude counts. This provides a self-consistent approach to jointly modelling the b_j and K counts. Of course this approach is only valid if the optical-infrared colours of the models accurately reflect those of the data. This is discussed further in chapter 6.

5.3.3 Spectral evolution models

The principles behind models of galaxy spectral evolution are very simple. They usually adopt a semi-empirical technique called evolutionary synthesis, which bypasses the present lack of detailed knowledge of the star formation process by choosing an arbitrary analytic form for the star formation rate. These are formed with an assumed initial mass function (IMF) and then the stars are followed along their well known evolutionary tracks in the Hertzsprung-Russell diagram and the stellar mix is determined as a function of galactic age. From the mix and a library of observed stellar spectra of different stellar types the galaxy spectrum at each age is obtained.

The models used here are those of Guideroni & Rocca-Volmerange (1987, hereafter GRV)

Table 5.2: The old and new galaxy spectral evolution models

The available old GRV models of stellar evolution. Each consists of 16 synthetic galaxy spectra with $\Delta t_{gal} = 1\,\mathrm{Gyr}$, from age $t_{gal} = 0.47\,\mathrm{Gyr}$ to $15.47\,\mathrm{Gyr}$. Note $g(t) = M_{gas}(t)/M_{tot}$ and t is in Gyr.

Colour Class	SFR $\tau(t)$	$b_j - \mathrm{K}^*$
Burst	1 for $0 < t < 1$, 0 otherwise.	3.51
UV-cold Elliptical	$\exp(-t)$	4.06
UV-hot Elliptical	$0.37\exp(0.37t)$	3.94
SO/a	$0.4g(t)$	3.91
Sa	$0.3g(t)$	3.79
Sb	$0.2g(t)$	3.61
Sc	$0.1g(t)$	3.26
Sd	0.048	2.85
Im	$4 \times 10^{-4}t^2$	2.22

* at 15.47 Gyr.

The available new improved models from RVG. Each consists of 20 synthetic galaxy spectra with $\Delta t_{gal} = 1\,\mathrm{Gyr}$, from age $t_{gal} = 0.12\,\mathrm{Gyr}$ to $19.12\,\mathrm{Gyr}$.

Colour Class	SFR $\tau(t)$	$b_j - \mathrm{K}^*$
Burst	1 for $0 < t < 1$, 0 otherwise.	3.99
UV-cold Elliptical	$\exp(-t)$	3.90
UV-hot Elliptical	$1g(t)$	3.83

* at 15.12 Gyr.

---

and the newer ones of Rocca-Volmerange & Guideroni (1988, hereafter RVG). These are superior to earlier models (e.g. Bruzual 1983a, b, c, and references therein) in several important respects, summarized below:

1) The models use Scalo's (1986) observationally determined IMF, which has different

slopes for different mass ranges:

$$\frac{dN}{d\ln m} \propto m^{-x} \begin{cases} x = 0.25, & \text{if } 0.1\,M_\odot < m < 1\,M_\odot; \\ x = 1.35, & \text{if } 1\,M_\odot < m < 2\,M_\odot; \\ x = 1.7, & \text{if } 2\,M_\odot < m < 80\,M_\odot. \end{cases}$$

as opposed to Bruzual's single-slope IMF (Salpeter 1955).

2) The models include the late post-Giant Branch stages of stellar evolution such as the Asymptotic Giant Branch whose light is an important contribution in the infrared.

3) The models use a stellar library with greater resolution (~ 10 Å as opposed to the $20 \rightarrow 50$ Å used by Bruzual) and extends further into the UV.

Table 5.2 summarizes the available models, which were obtained in machine readable format from the authors. The reader is referred to the GRV and RVG for a full discussion of the fitting of the models to the optical spectra and colours of galaxy samples. Dunlop *et al.* (1989) and Dunlop (1987) also give a useful description of the models and their use in modelling the evolution of optical-infrared colours of radio galaxies. The terms "UV-cold" and "UV-hot" refer to star-formation laws chosen so that the UV spectra of the models bracket the ranges of UV excess observed in elliptical galaxies. Unlike the Bruzual models the UV excess is modelled by a population of young stars rather than by "adding-in" a population of hot Horizontal Branch stars. The differences between the old and new models are primarily:

1) Smaller time steps (0.2 Gyr) used in the modelling of the stellar tracks. This reduces the problem in quantisation noise which cause irregularities in the colours of successive epochs. When the old models were used (see later on in this chapter) this was counteracted by smoothing the spectra across neighbouring epochs.

2) A newer functional form for the UV-hot model was used which gives a better fit to the observed UV-excesses of elliptical galaxies.

3) The extension of the models to the near infrared is based on observed JHK colours of stellar types (Johnson 1966, Lee 1970, Frogel *et al.* 1978 and Engels *et al.* 1981) instead of assuming the near infrared spectra of stars to be blackbodies.

This last difference has a particular importance for the K galaxy counts as the K-correction is determined from the spectra of the models at late epochs, at which ages the optical

colours and line ratios match nearby galaxy samples (again see GRV). Although all galaxies have similar spectra in the near infrared as shown by their J – H and H – K colours (e.g. Glass 1984, Aaronson 1978) the form of the spectra *in between* the atmospheric J, H and K windows is poorly known. In such previous infrared studies of galaxies the populations were very local (typically $z \sim 0.005$) and the infrared K-corrections were minor. They were usually done with a spectrum of a star, of some intermediate spectral type, observed from a space-borne telescope. Predicting galaxy counts down to K = 17 and beyond requires the K correction for $z \gtrsim 0.5$ and getting it right is vital. The best that can be done is to take the model spectra at late epochs and compare them with known (J – H, H – K) of galaxy samples. If the models appear to have the correct colours it is then reasonable to use them for the K-correction.

Figure 5.7 shows the (J – H, H – K) colours of the model spectra at an age of 15 Gyr redshifted from $z = 0$ (on the left side of the diagram) to $z = 1$ (right) for both the old and new spectral evolution models. Also shown is the "Frogel Ellipse" which defines the spread in (J – H, H – K) colours of local galaxies. The Frogel ellipse shown (taken from Collins 1986) is for the UKT9 JHK filter system on UKIRT, so for consistency the model colours are calculated for this plot in this filter system rather than the IRCAM JHK filters used for the other plots. The difference between the colours in the two filter systems is of the order of 0.1 magnitudes at the Frogel ellipse centre. The old models have a track with redshift that follows an approximate blackbody curve, as would be expected from the method of construction of the infrared stellar spectra. The old model $z = 0$ colours are very different from the Frogel ellipse being $\simeq 0.5$ magnitudes too blue in J – H; the new models provide a much better match at $z = 0$. The derived K-correction from the old and new models can be seen in figure 5.8. The K-correction can be seen to be highly insensitive to the spectral type of the models although the difference between the old and new models is very significant, at $z \sim 0.2$ the difference between the old and new model K-corrections is $\Delta K \simeq 0.3$ magnitudes. The K-correction is also insensitive to age past 15 Gyr, the new models are extended out to 19 Gyr but if the K-corrections or spectra are plotted out little difference is found between 15 and 19 Gyr.

The model JHK colours can be compared with some others in the literature. For example Yoshii and Takahara (1988) predict K band counts using a K-correction based on their model spectra of present day galaxies. Their models have zero redshift infrared colours of

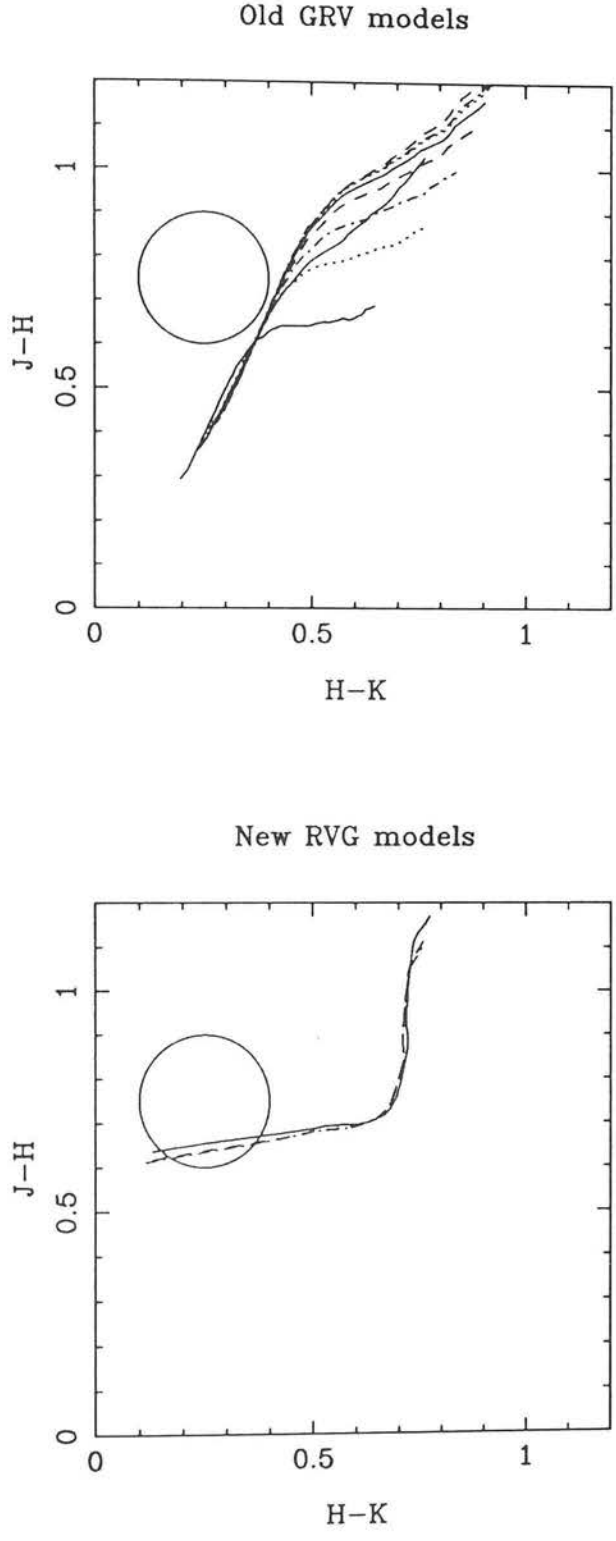

Fig. 5.7 (J − H, H − K) colour diagrams showing the track of the 15 Gyr model spectra, used for the K-correction, with redshift from $z = 0$ (left) to $z = 1$ (right).

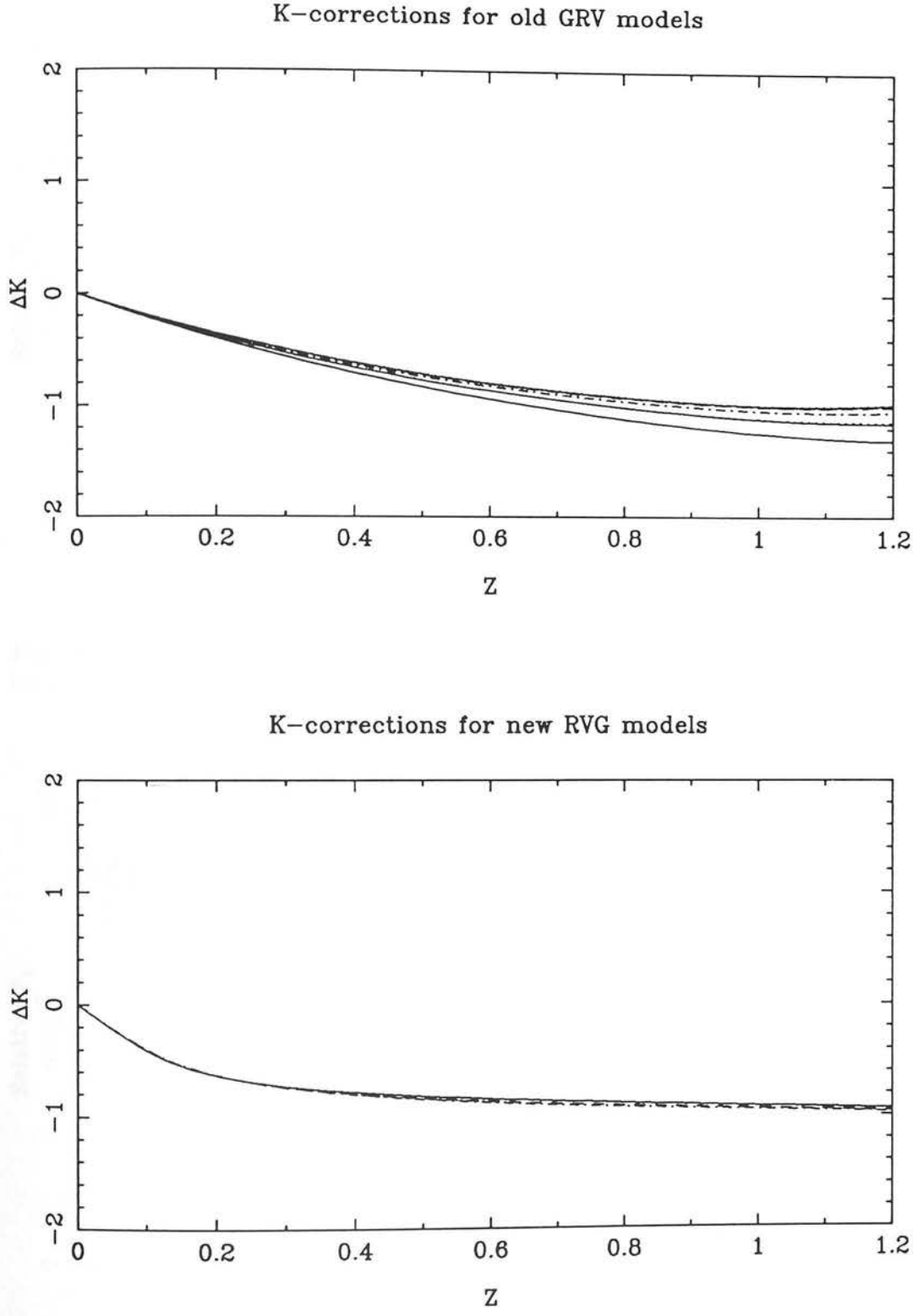

Fig. 5.8 The derived K-correction from the old and new model spectra at 15 Gyr.

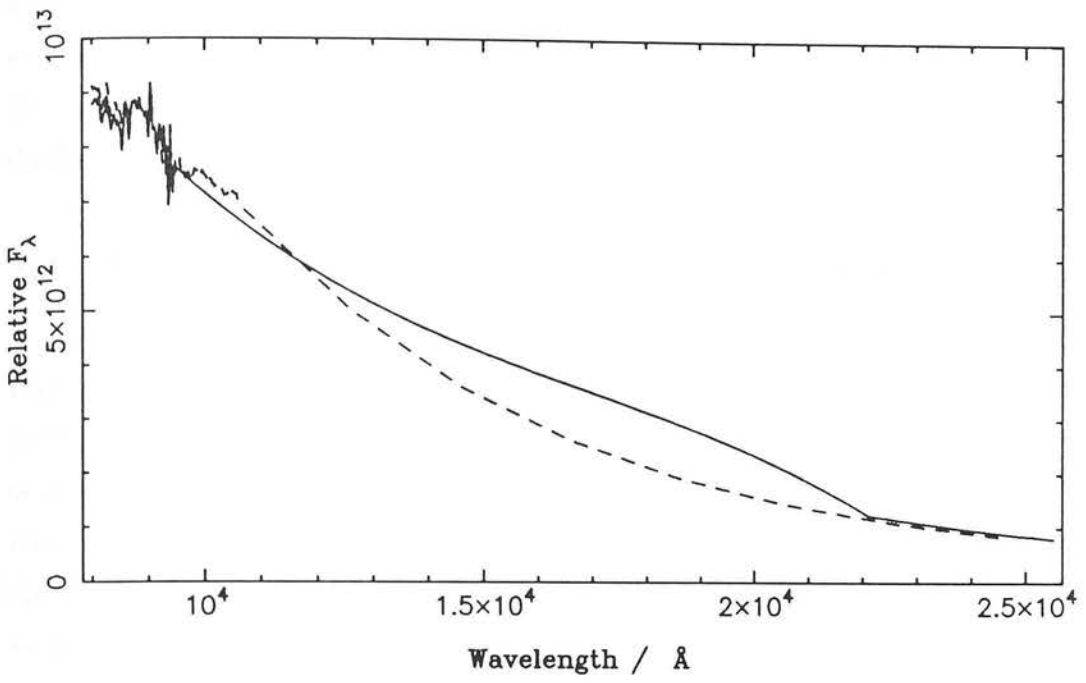

Fig. 5.9a A comparison of the infrared spectra of the new RVG models (solid line) and the older GRV models (dashed line). These are for a 1 Gyr burst models at age 15 Gyr.

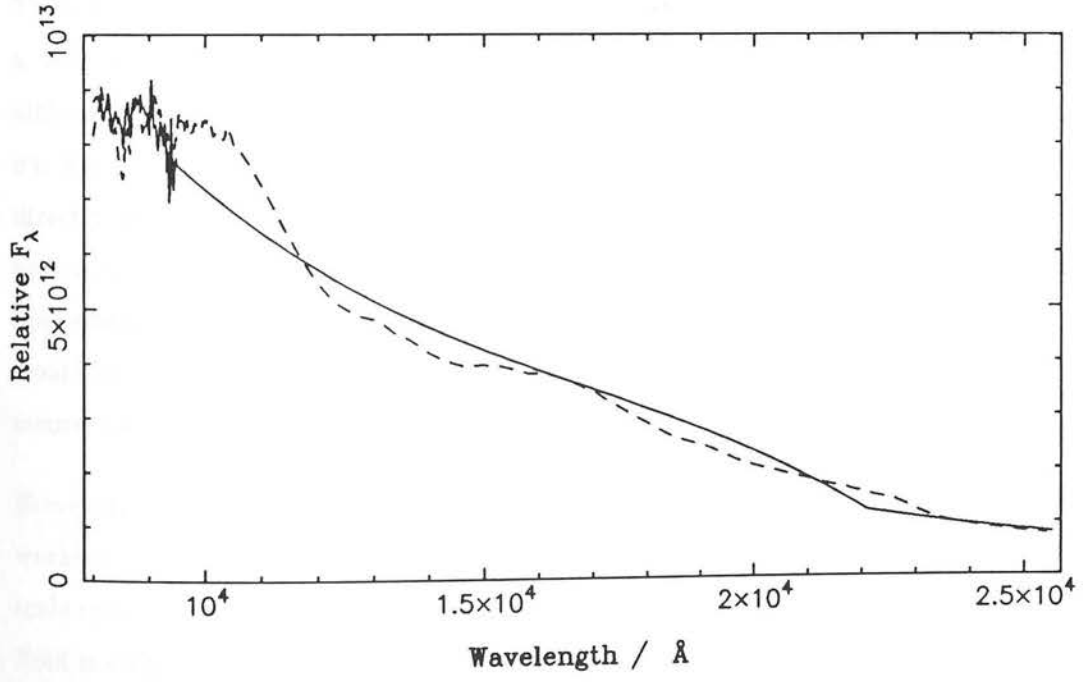

Fig. 5.9b A similar comparison of the infrared spectra of the RVG (solid line) and Bruzual models (dashed line), again these are 1 Gyr burst models at age 15 Gyr.

J – H = 0.52 and H – K = 0.35, which are a much poorer match than those of the RVG models. The older Bruzual models are better — they have rest colours of J – H = 0.65 and H – K = 0.25. Examples of the spectra of the GRV, RVG and Bruzual models are given in figure 5.9. The near infrared shapes of the Bruzual and new RVG models are very similar which is why they have similar JHK colours and hence give similar K-corrections.

5.4 Model Fits

Figure 5.10 shows the K counts determined from this survey and that of Cowie *et al.* (1990) and Cowie (1991). Note that although Cowie *et al.* do not give errors, the number of objects in each magnitude bin has been reconstructed from their Figure 3, together with other information in their paper, and minimal Poisson errors determined. Also shown are the number-magnitude determination of Jenkins & Reid (1991) based on a survey of 0.9□′ to K = 19 using the single channel photometer UKT9 on UKIRT with a 20″ diameter aperture. Jenkins & Reid analysed the flux density distribution and fitted a parametric form to $n(m)$ (after allowing for predicted star counts), $\pm 1\sigma$ errors being determined from Monte-Carlo simulations.

Their final results, with errors, are shown in Figure 5.10 as solid lines. Note there is a very satisfactory agreement between the 3 independent determinations in the slope although Jenkins & Reid's normalisation is about a factor of 2 higher (about 2 of their σ). This could be due to stellar contamination, as they could not generate the star counts directly, however this is unlikely as their stellar models (see section 5.2) seem to give good agreement with the survey direct star counts. The only apparent discrepancy is in the opposite direction, i.e. their models predict too many faint stars rather than too few which would increase their galaxy counts. It is also possible that they have underestimated their errors, a difficult task in a fluctuation analysis.

However, similar variations in normalisation have been commonly seen between different workers in optical counts in the past and this has been interpreted as being due to large-scale structure (e.g. Jones *et al.* 1991, Metcalfe *et al.* 1991). The survey area of Jenkins & Reid is only 0.9□′, however this is distributed over 11 widely separated patches of sky in an attempt to get a fair sample. The work presented here is based on 594□′ and is almost equally distributed over 6 patches spaced around the celestial equator at high galactic

latitude. Thus it is not clear who has the fairest sample, for the present purposes the normalisation based on the larger area will be adopted.

The optical b_j galaxy counts are shown in figure 5.11. This is a new compilation of the most recently available data and matches well previously published compilations. The faint points are taken from the deep CCD counts of Tyson (1988), Lilly *et al.* (1991) and Metcalfe *et al.* (1991). At intermediate magnitudes are the counts of Jones *et al.* (1991) based on deep AAT plates. The brightest points are taken from the two largest surveys in existence, both based on southern Schmidt plate data, the 946□° Edinburgh-Durham Southern Galaxy Catalogue (Collins & Nichol, 1991) and the 4300□° APM Galaxy Survey (Maddox *et al.* 1990). Note these two surveys are not independent: the EDSGC sky coverage is a smaller subset, though more accurately calibrated, of the APM survey.

The errors bars are determined from the observed field-field RMS scatter where given. All the counts have been transformed to the b_j band using the transformations given in the references. The agreement between the normalisation of different determinations is now of the order of $\lesssim 50\%$, much better than in previous compilations of older data.

5.4.1 Non-evolving prediction

The first case to be discussed is the null hypothesis. How well does the model which assumes an unchanging luminosity function, derived from the local galaxy population, fit the data? The results of this exercise is shown in figures 5.10 and 5.11. Initially the same luminosity function as that tabulated in Guideroni & Rocca-Volmerange (1990) (hereafter GRVb) was used in order to allow a direct comparison of the b_j prediction with that given in GRVb. The type-dependent luminosity function they use was taken from King & Ellis (1985) with the relative mix of morphological types calculated from that observed in the local population ($b_j < 16.75$) by Shanks *et al.* (1984). This is summarized in table 5.3. This luminosity function is very similar to the ones used by Broadhurst *et al.* (1988) and also gives agreement with the K luminosity function derived from the $b_j - K$ colours of the DARS survey.

GRVb use the new models throughout and model ellipticals with their UV-hot model. For the curves shown here, the old models had to be used for the spiral types but for these, in the optical, the difference between the old and new models is smallest. The

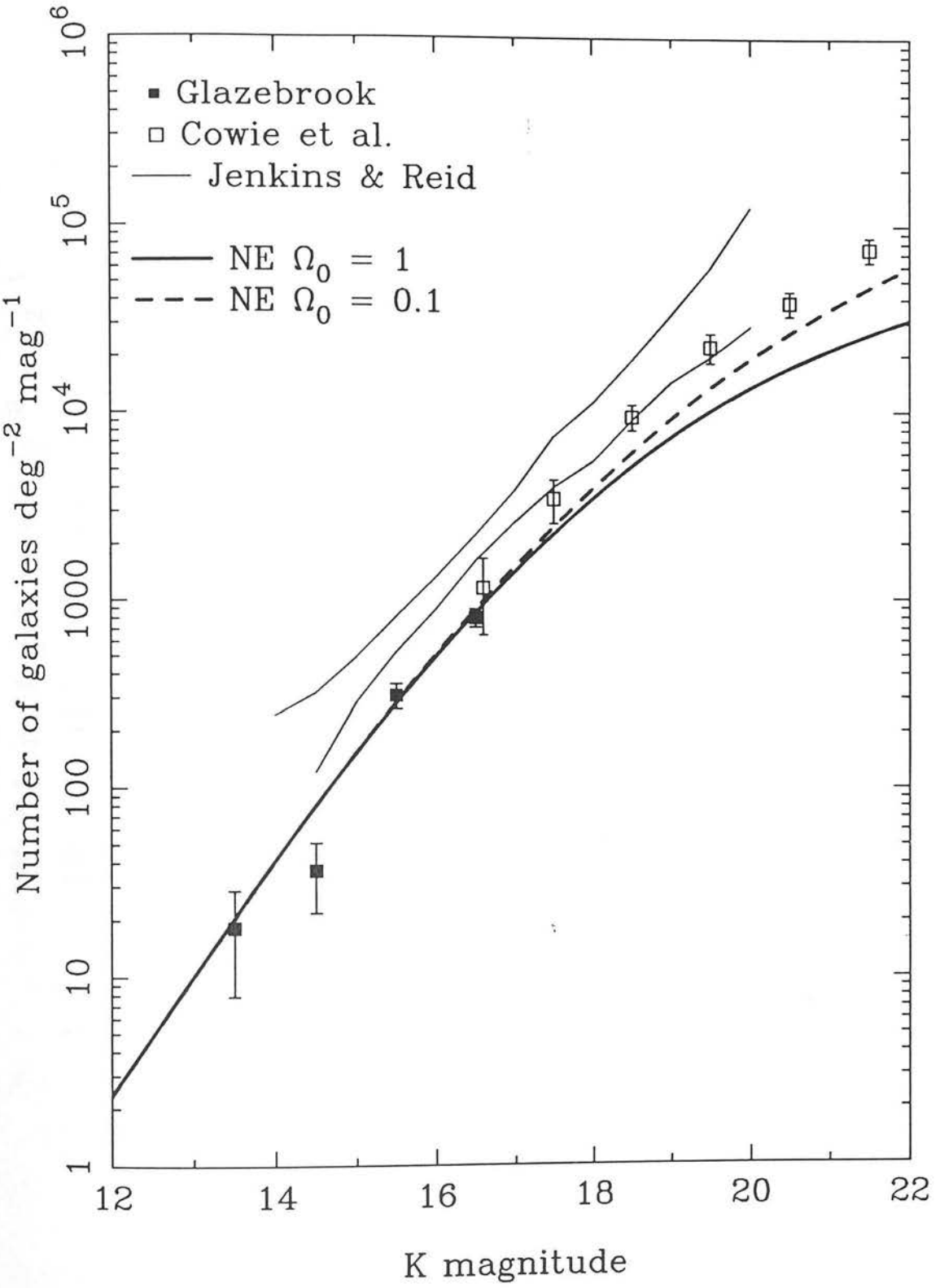

Fig. 5.10 The observed K band number-magnitude counts.

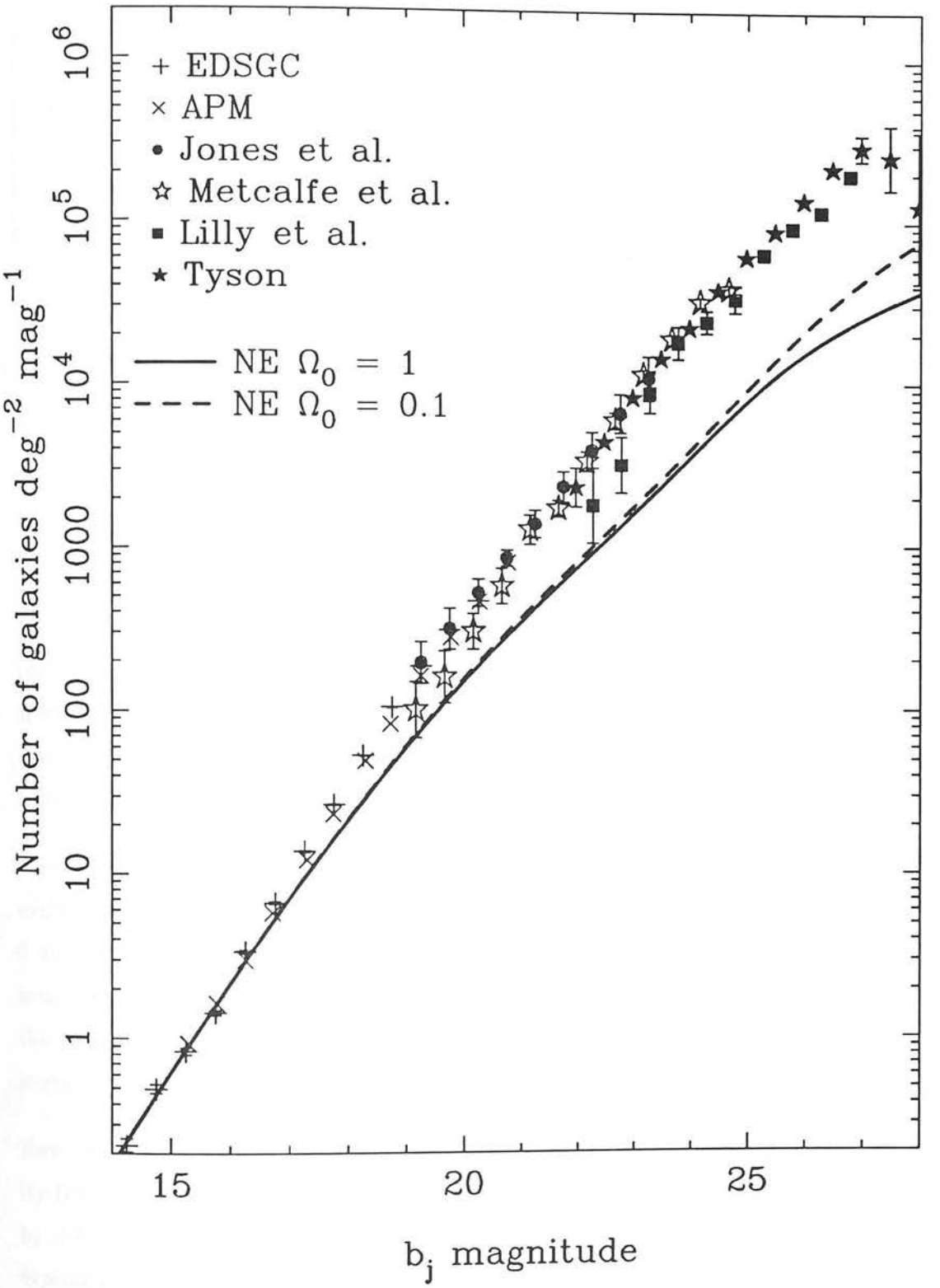

Fig. 5.11 The observed b_j band number-magnitude counts.

Table 5.3: Galaxy mix for type-dependent luminosity function

Type	Fraction	$M^*_{b_j}$ †
E/SO	0.35	−19.59
Sa	0.07	−19.39
Sb	0.19	−19.39
Sc	0.18	−19.39
Sd	0.09	−18.94
Im	0.04	−18.94

† $\alpha = -1.00$, $H_0 = 100\,\mathrm{km\,s^{-1}\,Mpc^{-1}}$.

curves are shown for $\Omega_0 = 0.1$ and $\Omega_0 = 1$ cosmologies normalised at $b_j < 16$ with $\phi^* = 1.5{\times}10^{-2}\,h^3\,\mathrm{Mpc}^{-3}$. The b_j curves are completely in agreement with those of GRVb.

For the infrared counts the luminosity function is constructed by applying the $b_j - \mathrm{K}$ colours for each type given in table 5.2 to the optical $M^*_{b_j}$ for that type. However the K-correction is taken from the *new* UV-hot model (at 15 Gyr) for *all* the types. As is discussed in section 5.3.3 the new models provide a better match to the near infrared colours and the K-correction is insensitive to type in the infrared.

The b_j counts show the well-known result of a huge galaxy excess compared to the non-evolving prediction. If the curves are normalised as shown then this excess is a factor of 3 at $b_j = 22$ and 10 at $b_j = 28$. It can be seen at once that the observed K counts are a much better match for the non-evolving prediction than are the counts in b_j. This follows the trend seen in optical counts in other bands (e.g. Tyson 1988) where the galaxy excess is greatest in b_j and progressively less in R and I filters.

How sensitive is this result to the assumptions that have been made about the luminosity function? To illustrate the effect of this figure 5.12 shows the effect of varying $M^*_{b_j}$ by ± 0.25 magnitudes, for the $\Omega_0 = 1$ case. This encompasses the range of uncertainty typically found in differing estimates of $M^*_{b_j}$, including the difference from the constant $M^*_{b_j}$ given by Efstathiou *et al.* (1988). At this point a new way of plotting the number-magnitude counts is introduced. The plot is now normalised by dividing by the Euclidean

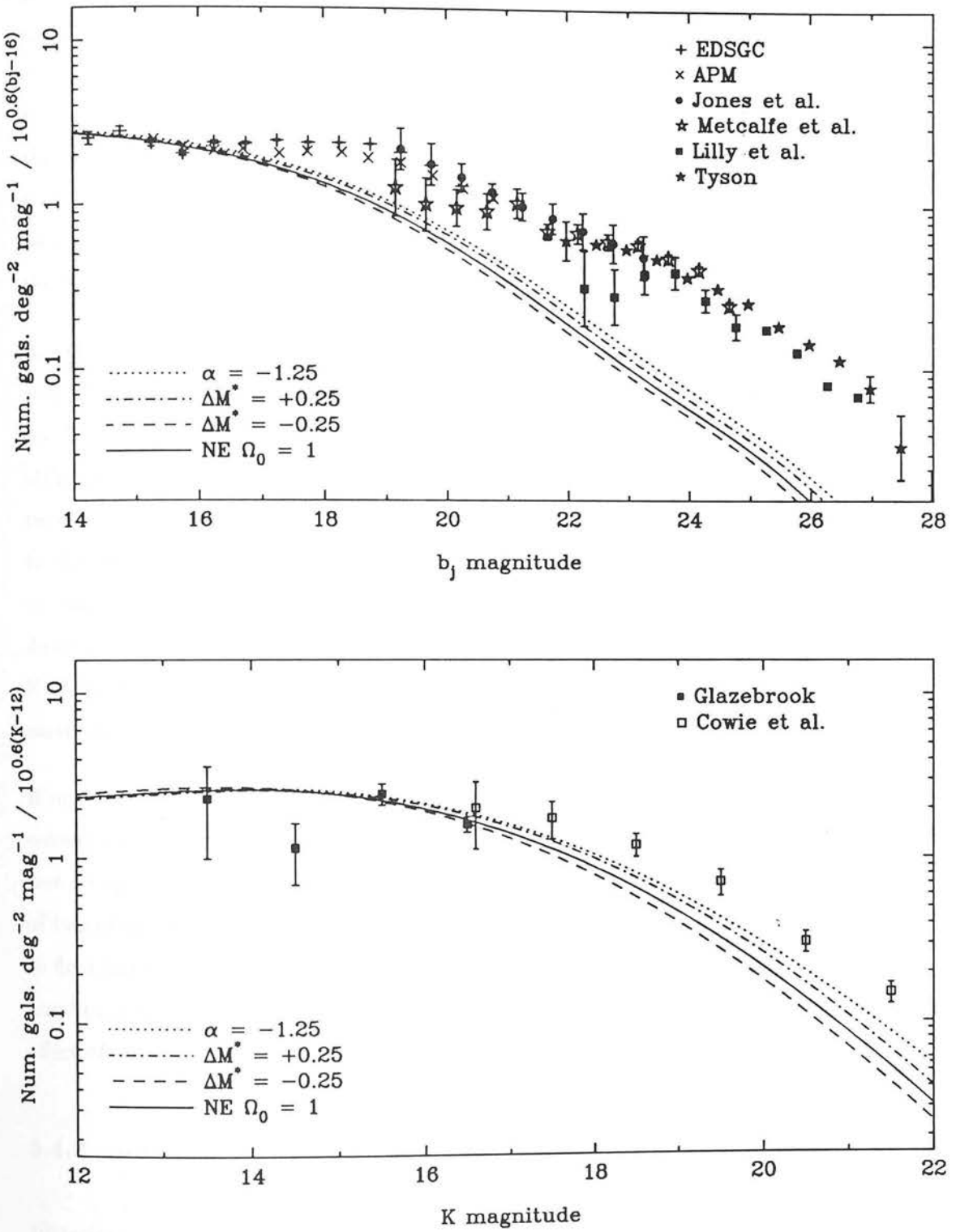

Fig. 5.12 The effect of varying M^* and α on the b_j and K number-magnitude counts. The normalisation is adjusted $\pm 40\%$ away from $\phi^* = 1.5{\times}10^{-2}\,h^3\,\mathrm{Mpc}^{-3}$ at the bright end to compensate for the M^* variation.

prediction ($N \propto 10^{0.6m}$) given in section 5.3.1. This reduces the number of order of magnitudes covered by N from 6 to 3 and makes small variations easier to see, with no loss of information. The values of ϕ^* for the differing values of M^* are adjusted to normalise to the bright K-counts although ϕ^* is the same in b_j and K. Also shown on the figure is the prediction which results from increasing the faint end slope of the luminosity function from $\alpha = -1$ to $\alpha = -1.25$, which brackets different estimates in the literature. It can be seen that this is not enough to match the b_j counts or to allow the $\Omega_0 = 1$ model to match the K counts.

Another issue to be addressed is normalisation of the curves. ϕ^* can be derived from local redshift surveys along with the rest of the luminosity function, and Efstathiou *et al.* (1988) do this for five different surveys. They gave a mean ϕ^* of $(1.56 \pm 0.34) \times 10^{-2} h^3\,\mathrm{Mpc}^{-3}$ although the dispersion among estimates from the differing surveys amounts to a factor of two. An alternative approach is to choose a value of ϕ^* which normalises the prediction to the bright end of the counts. Note that the b_j and K normalisations are, in principle, not independent. Obviously we must see the same total number of galaxies if we integrate down to zero flux and so the *same* value of ϕ^* should be adopted for the models in b_j and K. A perfect model would fit the observed K and b_j counts at all magnitudes with the same value of ϕ^* and, of course, have the correct $b_j - \mathrm{K}$ colours.

If one were to normalise to the bright K counts ($K < 17$) then because of the $b_j - \mathrm{K}$ colours of the models this is equivalent to normalising in the optical at $b_j < 20$ *if* there was no optical evolution. In fact as can be seen from figure 5.12 there is already a factor of two excess at $b_j = 20$. It is possible to argue that the normalisation should be allowed to float independently in b_j and K because of the problem of field to field variations in the amplitude of the counts. This does not affect the no-evolution result – where relevant the effect of normalisation is discussed in the rest of this chapter.

5.4.2 Luminosity evolution

Historically the first and most obvious strategy to explain the blue count excess has been to simply say that galaxies were more luminous in the past. A galaxy must evolve simply through the ageing of its stellar populations even if no new stars are being formed. There has been two common approaches to modelling luminosity evolution:

1) Adopting a physical model for the evolution — this is the approach of evolutionary synthesis as detailed in section 5.3.3. An example of such an approach is GRVb. This has the advantage of also predicting the colours and hence counts in other bandpasses.

2) Parameterising the evolution via simple functions of redshift $L(z)$ or lookback time $L(t)$. This has the advantage of simplicity and fewer free parameters than physical models. An example is Shanks *et al.* 1984.

Physical luminosity evolution

The problem with any form of luminosity evolution is to reconcile it with the results of the deep redshift surveys of Broadhurst *et al.* (1988) to $b_j = 21.5$, and Colless *et al.* (1990) to $b_j = 22.5$. These give number-redshift distributions consistent with *no-evolution*, apart from the normalisation, and rule out any high-redshift tail from evolved luminous galaxies.

To some extent this problem can be alleviated by normalising at fainter magnitudes, $b_j = 19$–20, so that the amount of luminosity evolution to $b_j = 22.5$ is minimal. One is left with the problem of the overprediction at brighter b_j magnitudes which one has to attribute to very large-scale structure (i.e. that we are living in a hole in the galaxy distribution of size $\simeq 300h^{-1}\,\mathrm{Mpc}$).

Such models are plotted in figure 5.13 with a higher ϕ^* of $2.5\times10^{-2}\,h^3\,\mathrm{Mpc}^{-3}$ for different values of the redshift of formation. Since the star formation rates are fixed for each morphological type the only freedom left is to adjust H_0, Ω_0 and the redshift of formation. It can be seen that the $z_f = 30$ models provide the best fits to the b_j counts. However all the curves have a "bump" at some magnitude which is not seen in the data. The $z_f = 30$ model is the same as that plotted in figure 4 of GRVb, however the bump is not so apparent in their plots due to their more conventional method of plotting the counts. The bump is simply caused by the galaxies getting more luminous as the counts probe back in time to their formation redshift and then disappearing for $z > z_{max}$. Here z_{max} is set by the redshift of formation or, if it is very high, the appearance of the Lyman break (or heavy Lyman-α forest absorption) in the B band at $z \simeq 4$. Once the mean redshift starts to probe z_{max} we are no longer observing galaxies near L^* and the counts become dominated by sub-L^* galaxies on the flat part of the luminosity function. With $\alpha = -1$

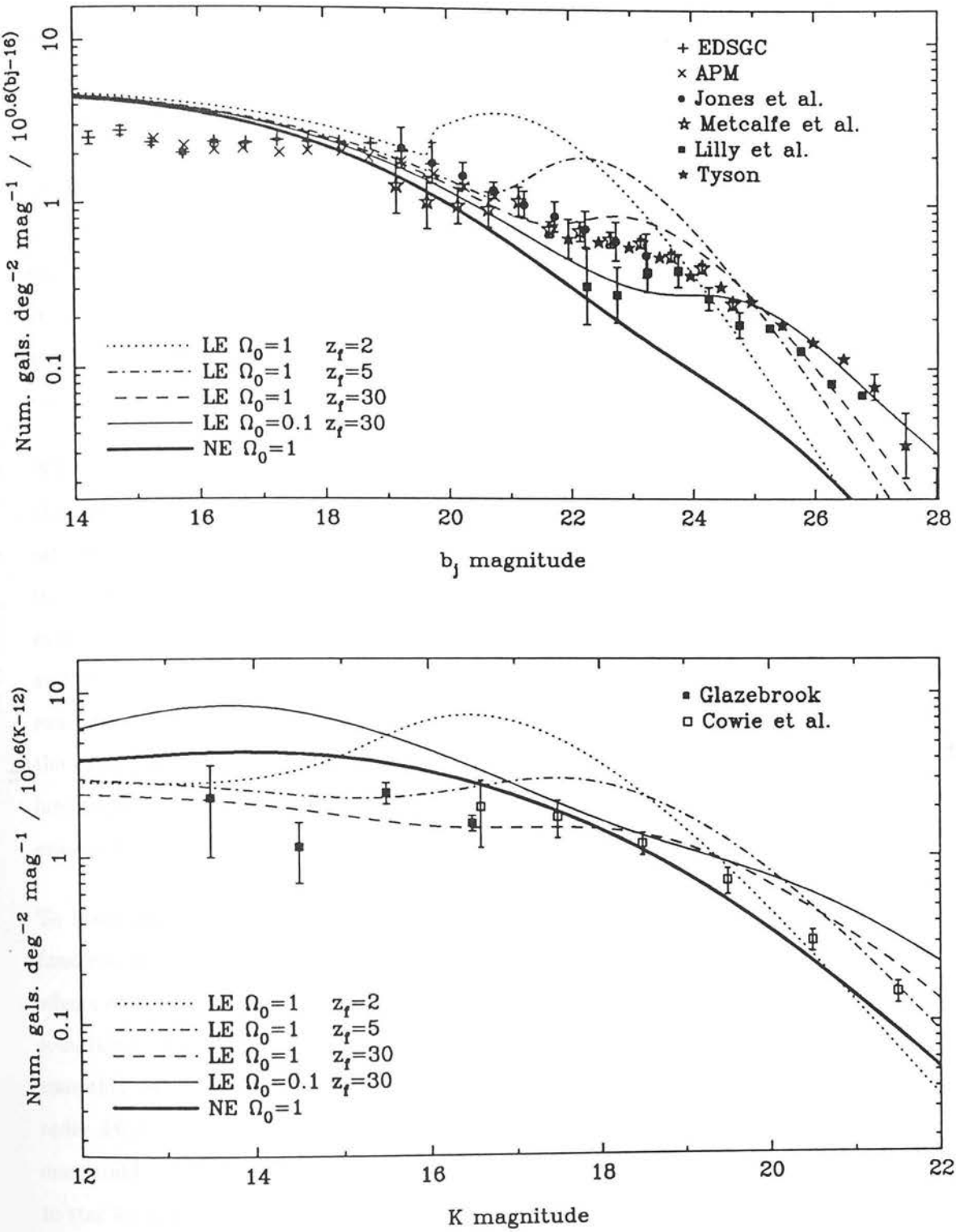

Fig. **5.13** Models of spectral evolution compared with no-evolution for the b_j and K number-magnitude counts. These are plotted with $H_0 = 50\,\mathrm{km\,s^{-1}\,Mpc^{-1}}$ and $\phi^* = 2.5{\times}10^{-2}\,h^3\,\mathrm{Mpc}^{-3}$.

then $N(m) \Rightarrow$ const. $\propto \phi^* V(z_{max})$, independent of the amount of luminosity evolution. Of course as one goes fainter then the behaviour depends on the slope of the luminosity function in unknown regimes. If one imposes a low luminosity cutoff then the model peaks and turns over.

Thus the sheer numbers of faint galaxies seen in Tyson's and Lilly *et al.*'s deep CCD counts require a very large volume, provided, of course, galaxy numbers are conserved. This then favours low Ω_0 cosmologies with very high redshifts of formation regardless of the details of the physical model. Such models are also marginally consistent with the deep b_j selected redshift surveys (see figure 5.14) in the low-Ω case, though this is critically dependent on the high normalisation as mentioned above.

What prediction does these models of spectral evolution make in the infrared? This is also shown in figure 5.13 for the same value of ϕ^*. As for the no-evolution model the infrared fluxes were computed using the new UV-hot K-correction. It can be seen at once that there is a puzzling discrepancy between the no-evolution model and the luminosity evolution model. The curves should match up with no-evolution at bright K magnitudes and they clearly do not, this indicates that there must be a large discrepancy at low redshifts between the resultant K and R corrections. These are plotted in figure 5.15 for the same models in b_j and K as in figure 5.13. It can be seen at once that, while the b_j luminosities evolve smoothly away from the K-correction, in K the curves are very different even at very low redshifts $z < 0.1$.

To investigate this further the b_j and K magnitudes of the models were plotted as a function of the age in Gyr. This was done in the rest frame so as to separate out the effects of the K-correction. The result is shown in figure 5.16. It is evident that there is something very wrong with the spectral-evolution models. While the b_j magnitudes vary smoothly with age, the K magnitudes seem to jump about discontinuously by factors of order ± 0.5 magnitudes at late epochs. This kind of behaviour is physically unrealistic as one would naively expect the b_j magnitudes to vary more due to their greater sensitivity to star formation.

The fault must lie in the extension of the models into the near-infrared. There was previous evidence that this set of models were unreliable. J.S. Dunlop (private communication, 1990) indicated that there were problems involving discontinuous change in the R – K

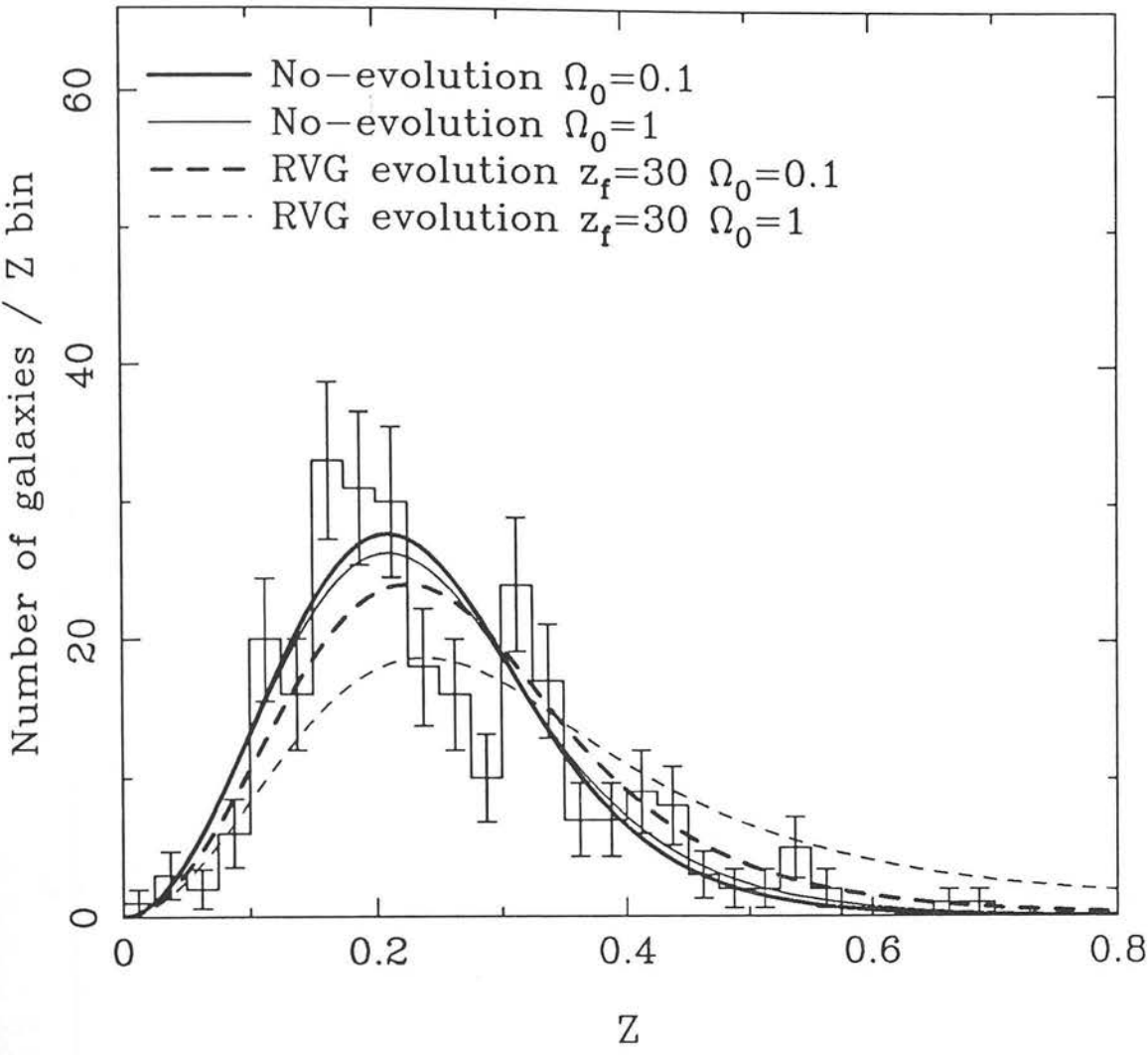

Fig. 5.14 The models of spectral evolution compared with the deep b_j selected redshift surveys of Broadhurst *et al.* (1988) and Colless *et al.* (1990). The Broadhurst and Colless datasets are simply combined and then binned. The curves are computed as a $20 < b_j < 21.5$ model normalised to the number of galaxies in the Broadhurst *et al.* sample plus a $21 < b_j < 22.5$ model normalised to the number of galaxies in the Colless *et al.* sample. This allows the redshift distributions to be compared directly regardless of any variations of absolute normalisation between the two samples in their magnitude overlap.

Note that at these magnitudes the redshift distribution is close to the no-evolution model, even though a model normalised at $b_j = 15$ predicts only a third of these galaxies. The RVG $z_f = 30$, $\Omega_0 = 0.1$ model marginally fits the redshift distribution, but this requires normalisation at $b_j = 19$ and only predicts 60% more galaxies than the no-evolution model. Any more luminosity evolution, such as in the $z_f = 30$, $\Omega_0 = 1$ RVG model, predicts an unobserved tail of high redshift galaxies.

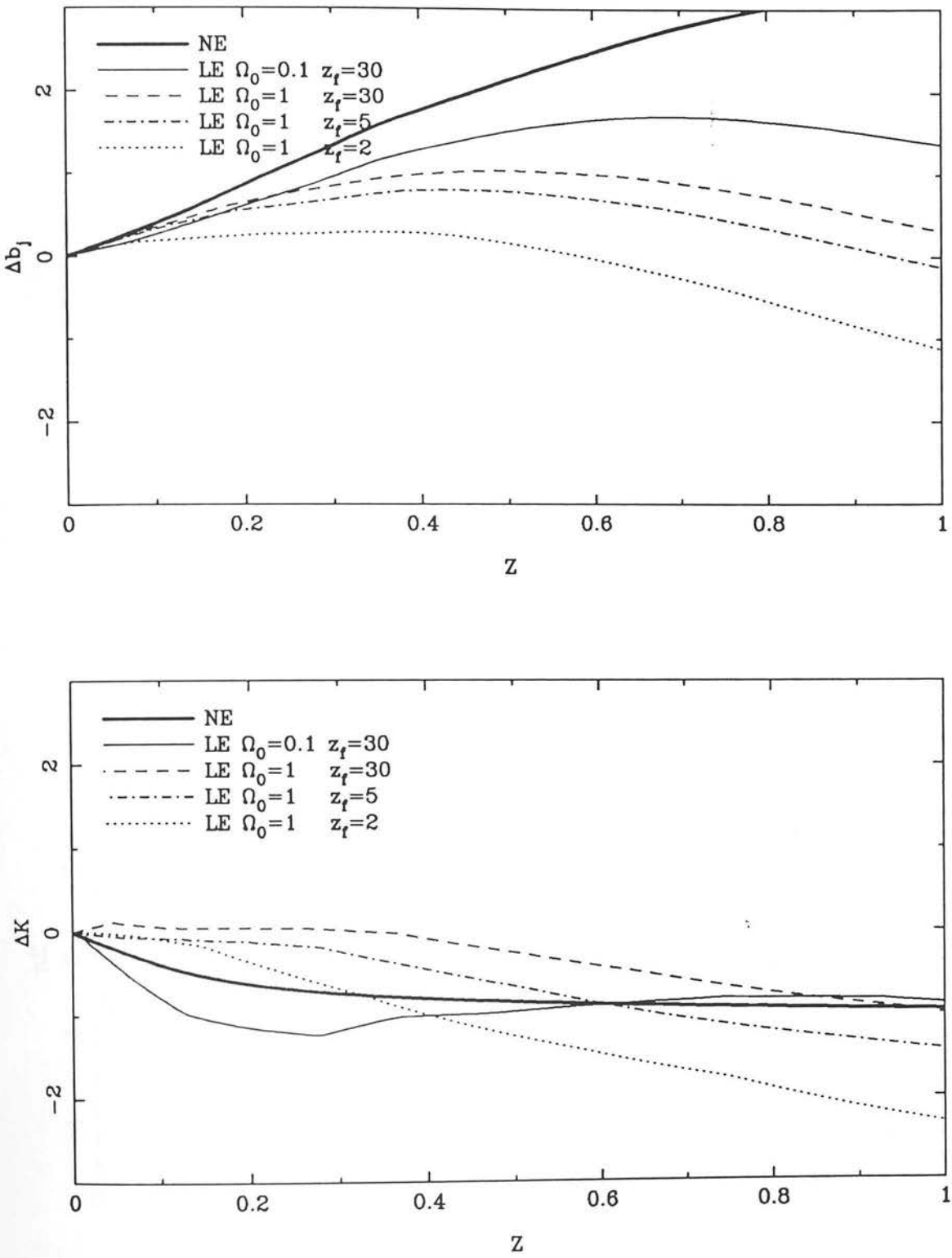

Fig. 5.15 The K/R-corrections corresponding to the models in figure 5.13 for the UV-hot elliptical type.

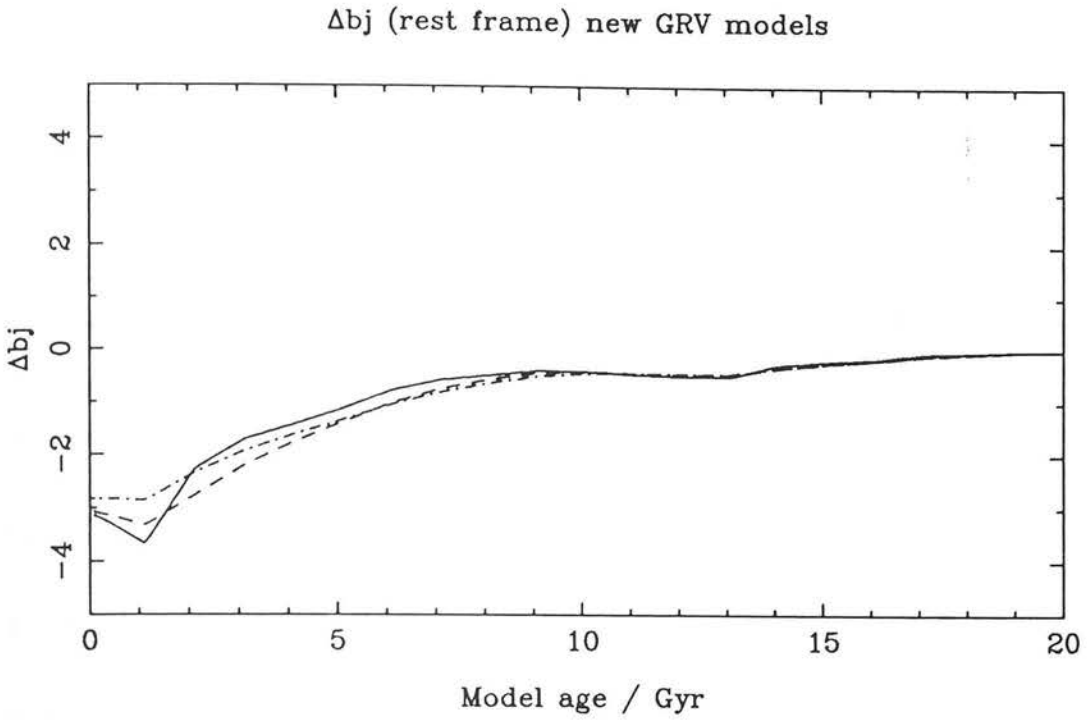

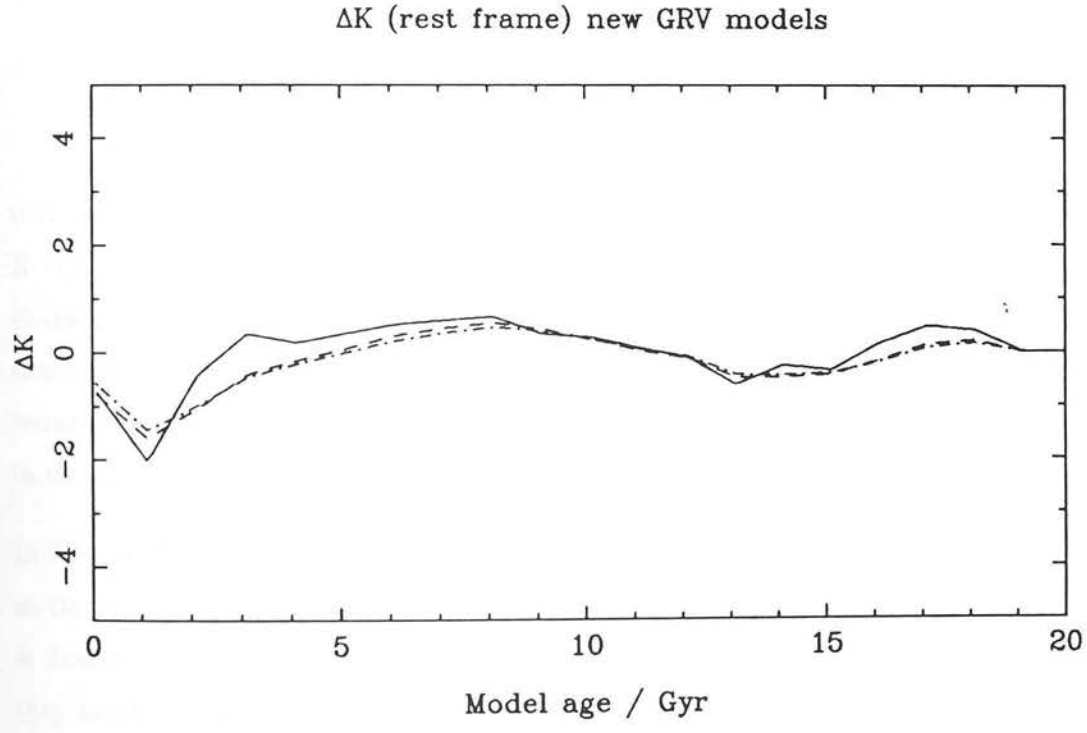

Fig. 5.16 The rest b_j and K magnitudes of the new RVG models (Burst, UV-cold and UV-hot) as a function of the model age in Gyr.

colour between 1 Gyr steps in the old (GRV) models. This was solved by smoothing with adjacent steps and the problem was absent in the new RVG models, however his sample was of radio galaxies at $z \gtrsim 1$ where rest frame $\simeq 1\,\mu$m is being observed in K. Here the differences between the new and old models are much less than they are at $2\,\mu$m.

The problem was associated with the fact that the model red light is dominated by the cool giant stars from the late stages of stellar evolution. While their rate of change with time is very small, the actual number of these stars in the evolutionary synthesis calculation is small and the jumps are almost certainly due to these stars entering and leaving the giant branch. Thus the problem boils down to a discretisation noise in the stellar evolution calculation. The JHK colours are not affected as all the giants have similar colours. Neither are the K-corrections for the non-evolving case.

Parametric luminosity evolution

Given these problems with the physical evolutionary models in K, is it possible to make any quantitative statement of the amount of luminosity evolution allowed by the K counts? By adopting a simple functional form for the luminosity evolution:

$$L^* \propto (1+z)^{\eta}$$

it is possible to obtain constraints for the amount of luminosity evolution allowed by the K counts. Note this can be regarded in two equivalent ways – either evolution of the characteristic Schechter luminosity by $(1+z)^{\eta}$ or brightening of the K-correction by the same amount. Such schemes can also be applied in b_j — $\eta \gtrsim 2$ is required to match the counts from $b_j = 16$ to 22. However, this results in a tail of high redshift galaxies not seen in the redshift distribution, as Broadhurst *et al.* discovered.

In K, how big a value of η is required to match *passive* evolution of the galaxy population, as the stars simply get younger with lookback time? From studies of radio galaxies Lilly & Longair (1984) estimate an increase in luminosity of 1 magnitude by $z = 1$ which they attribute to passive evolution. This can be regarded as an upper limit — the effect of increased star-formation in K is to *decrease* the mean luminosity with lookback time rather than increase it as in B. This may seem counter-intuitive but does make sense — the K light to first order is approximately proportional to the number of stars in the galaxy as the

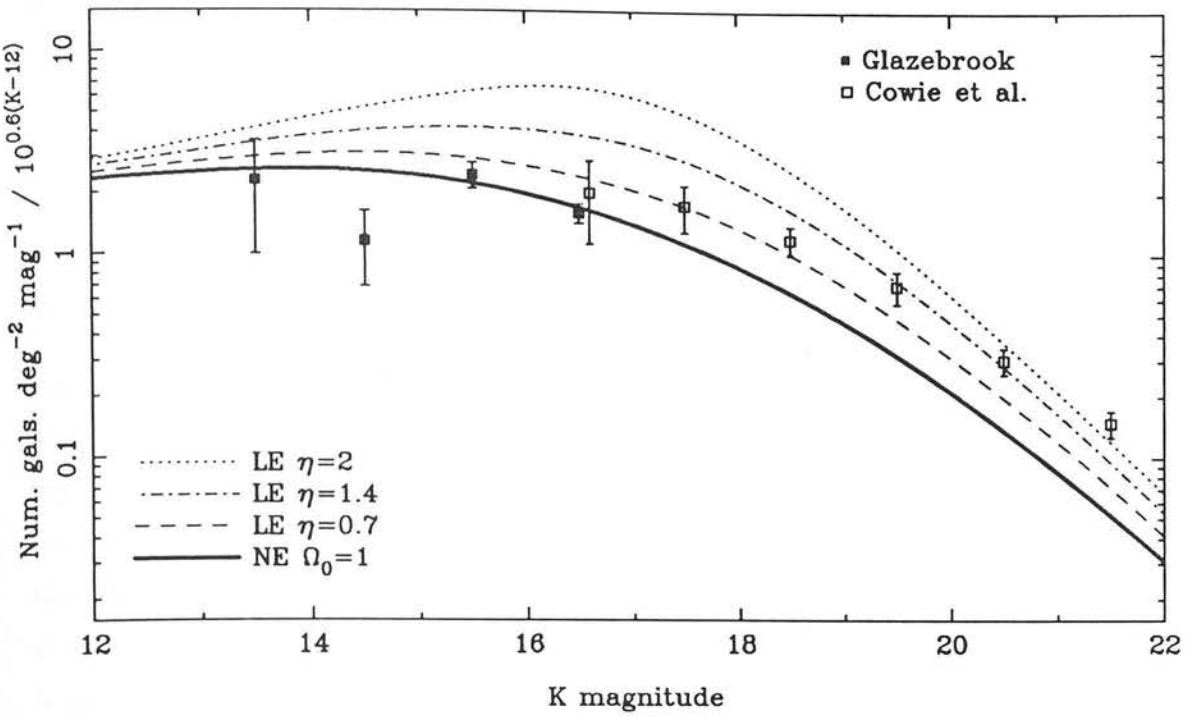

Fig. **5.17a** Parametric models of luminosity evolution compared with the data. $\phi^* = 1.5\times10^{-2}\,h^3\,\mathrm{Mpc}^{-3}$.

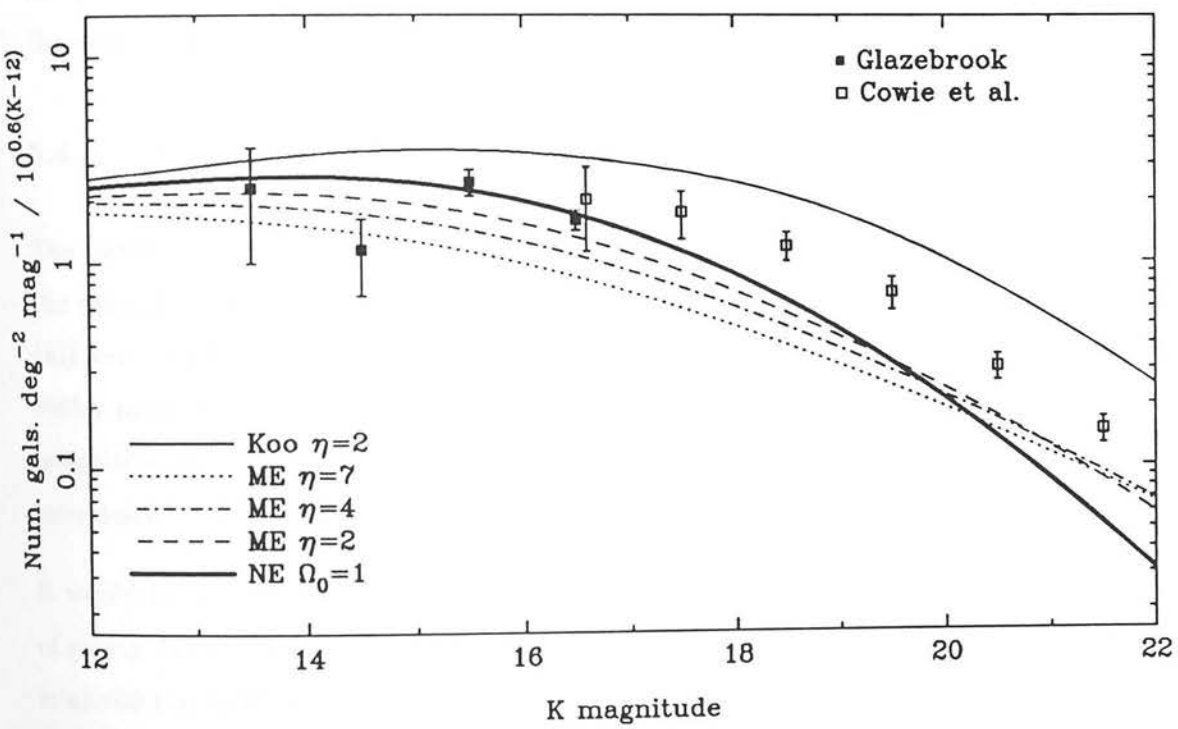

Fig. **5.17b** Parametric models of merger evolution compared with the data. $\phi^* = 1.5\times10^{-2}\,h^3\,\mathrm{Mpc}^{-3}$.

light is dominated by the old stellar population. Now passive evolution makes these stars younger and brighter in the past but the effect of star-formation is to reduce the *number* of stars in the past and hence make the galaxy dimmer. This was checked qualitatively by running some simple Bruzual models — an upper bound of $\simeq 1$ magnitude by $z = 1$ was found for a passively evolving model in an $\Omega_0 = 0.1$ cosmology. Increasing Ω_0 or the star-formation rate reduces this. This upper bound corresponds to $\eta = 1.4$, this is plotted in figure 5.17a along with $\eta = 0.7$ (0.5 magnitudes) and $\eta = 2$ (1.5 magnitudes).

Galaxies to $z \simeq 1$ are seen approximately to K $\simeq$ 18 in these models, so attention should be focused on this part of the counts. Such a simple function should not be extrapolated beyond this. It can be seen that mild amounts of luminosity evolution of 0.5–1 magnitude are consistent with the data only if normalisation is regarded as a free parameter, However the normalisation ($\phi^* = 1.5\times10^{-2}\,h^3\,\mathrm{Mpc}^{-3}$) is already at the bottom end of the range of values allowed by the optical data. It cannot be that the survey data are incomplete in galaxies: even if all the objects (stars and reference objects) in the $16 < \mathrm{K} < 17$ bin were added in this would only raise the point by 30%. Moreover, in this magnitude slice the mean redshift is 0.366 for no-evolution (see section 6.5.2 for a discussion on how to compute redshift distributions), which rises to 0.45 for $\eta = 1.4$, far too high to attribute the normalisation to large-scale structure.

5.4.3 Merging evolution

The beauty of the infrared counts is that they provide, in principle, an ideal measure of the mass function of galaxies. As the old stars which dominate the light should evolve only very slowly in the infrared to a good approximation K light should trace the galactic stellar mass and be insensitive to small amounts of star formation. The K light is also insensitive to dust extinction ($A_\mathrm{K} \simeq 0.1A_\mathrm{V}$) so all the light is being seen, even if the interstellar medium is heavily disrupted by a galaxy merger (e.g. Thronson *et al.* 1990).

It would be possible to model the history of galaxy merging with one's favourite theory of galaxy formation (e.g. Carlberg 1990), but as with luminosity evolution one desires to minimise the number of free parameters as a first step. In fact the analogy is quite apt as a simple parametric model will be adopted rather than a complex physical model.

Number-density evolution has been used to fit the optical counts using empirical functions

of the form $\phi^* \propto (1+z)^\eta$, e.g. Koo (1990) who found $\eta = 1.5$–2. This has the advantage of trivially explaining the deep redshift distributions, as most of the effect is simply to increase the normalisation of the no-evolution model. To demonstrate this the b_j counts and redshift distributions from such a model ($\Omega_0 = 1$) are shown in figure 5.18. Note $\eta = 2$ matches the redshift distribution and the count slope from $b_j = 18$ to 25. However it still requires a relatively high normalisation ($\phi^* = 2.5\times10^{-2}\,h^3\,\mathrm{Mpc}^{-3}$) and cannot explain the very bright Schmidt plate counts — this would require much stronger evolution. These models do, however, have the virtue that the asymptotic number density at the faint end is raised, as galaxies are no longer conserved. This means that $\Omega_0 = 1$ can now be consistent with the counts.

Such models are problematic since what they assume is merging plus a no-evolution K-correction. However it is simply not feasible that galaxies could merge and fail to form stars, which would change the luminosity, especially in b_j. And of course it is known that the faint galaxies are bluer, i.e. the excess is less in redder bands, and a proper model of number-density evolution should seek to account for this.

In principle the K counts provide a better test of such models as the effect on the K-correction from the associated star-formation is much less. However there is a problem as to the best way to translate such models into K. If such a form was to be interpreted as a pure change in the number density of galaxies then the same law would apply in K; as can be seen from figure 5.17b such a model ($\eta = 2$) quickly overpredicts the K counts. This is a general effect — if a particular model of pure density evolution, which fits the b_j data, is simply translated to K then it produces too many galaxies, simply because the large excess is not there in K.

It is possible to construct a more realistic model in K by requiring that the total amount of light in the K luminosity function be conserved. The assumption here is that because a small amount of star-formation has little effect in K, the combined K light from two systems before a merger is approximately the same as the K light afterwards. In other works K light is thought of as tracing stellar *mass*. Clearly this is not going to be true at some level, but it is a more natural starting point than pure number-density evolution as here it is effectively being assumed that the light *doubles*. For a Schechter function

$$L_{TOT} = \int_{-\infty}^{\infty} L\phi(L)dL \propto \phi^* L^*$$

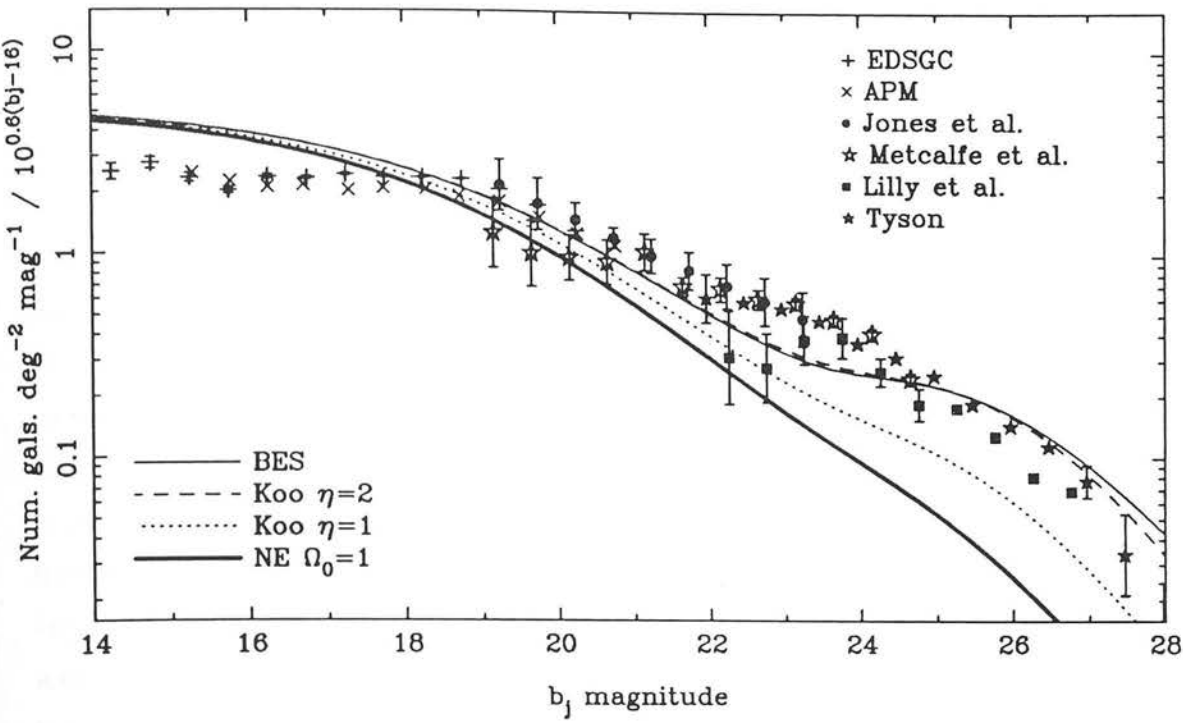

Fig. 5.18a The b_j counts with the Koo model of number-density evolution and the Broadhurst *et al.* model of luminosity function evolution. Note $\phi^* = 2.5\times10^{-2}\,h^3\,\mathrm{Mpc}^{-3}$.

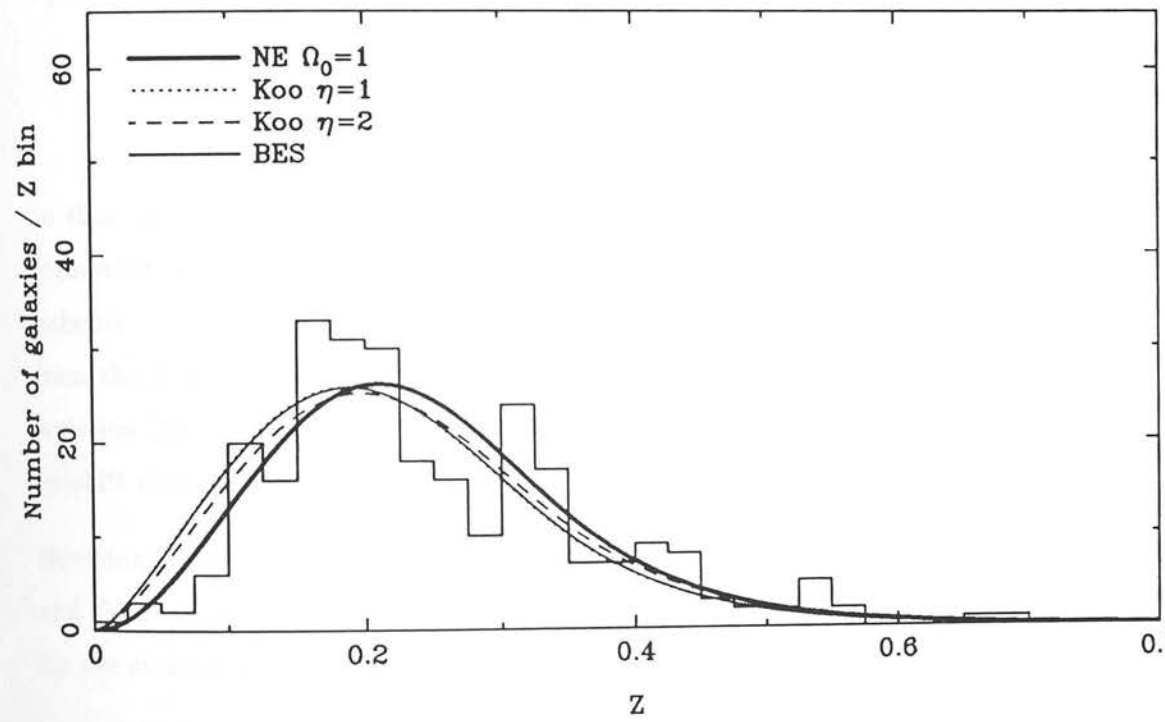

Fig. 5.18b The b_j redshift distributions and the Koo and Broadhurst *et al.* evolutionary models.

so any formalism which conserves $\phi^* L^*$ as a function of z will do. To investigate evolution in the number density the following parameterisation was adopted:

$$\phi^* \propto (1+z)^{\eta}$$
$$L^* \propto (1+z)^{-\eta}$$

Here η allows the amount of merging to be tuned. Note that this actually implements luminosity *devolution* as the galaxies break up into smaller bits at high-z. Figure 5.17b shows the results of such models with $\eta = 2$, 4 and 7 and $\phi^* = 1.5{\times}10^{-2}\,h^3\,\mathrm{Mpc}^{-3}$ which corresponds to the no-evolution normalisation to the K counts used before. Note that the effect is to bend up the faint end in such a way that the slope is a better match to the data. The normalisation is a little low, but this could be rectified as we do have some freedom to normalise *up*. Note also that the number-magnitude counts are *insensitive to large values of* η. This is because the effect of such merging is to stretch the model along a line of slope 0.4 in the $n-m$ plane — i.e. the surface brightness of the population on the sky is conserved.

What implications do these models have for the b_j counts? Koo's model is essentially equivalent to one of these merging models if one takes

$$\frac{L^*_{b_j}}{L^*_{\mathrm{K}}} \propto (1+z)^2$$

so that the net change in b_j luminosity is essentially 0 — the extra blue light from star formation making up for the decrease in galaxy size. It also implies that most of the galaxies in the blue excess would have been recently involved in mergers. It is known from the deep redshift surveys that for these galaxies $\simeq 80\%$ have strong [OII] and [OIII] emission lines, indicative of recent starburst activity. Thus it appears that while the redshift distribution may follow no-evolution the galaxies are evolved spectroscopically.

How does this relate to other methods of fitting the b_j data? In order to fit the counts and the redshift distribution in b_j Broadhurst *et al.* (1988) proposed an empirical form for the evolution of the luminosity function:

$$\phi(M)_z = \phi(M)_{z=0} \left[\left(\frac{\phi(M)}{\phi(M_0)} \right)_{z=0} \right]^{0.1z+0.2z^2}$$

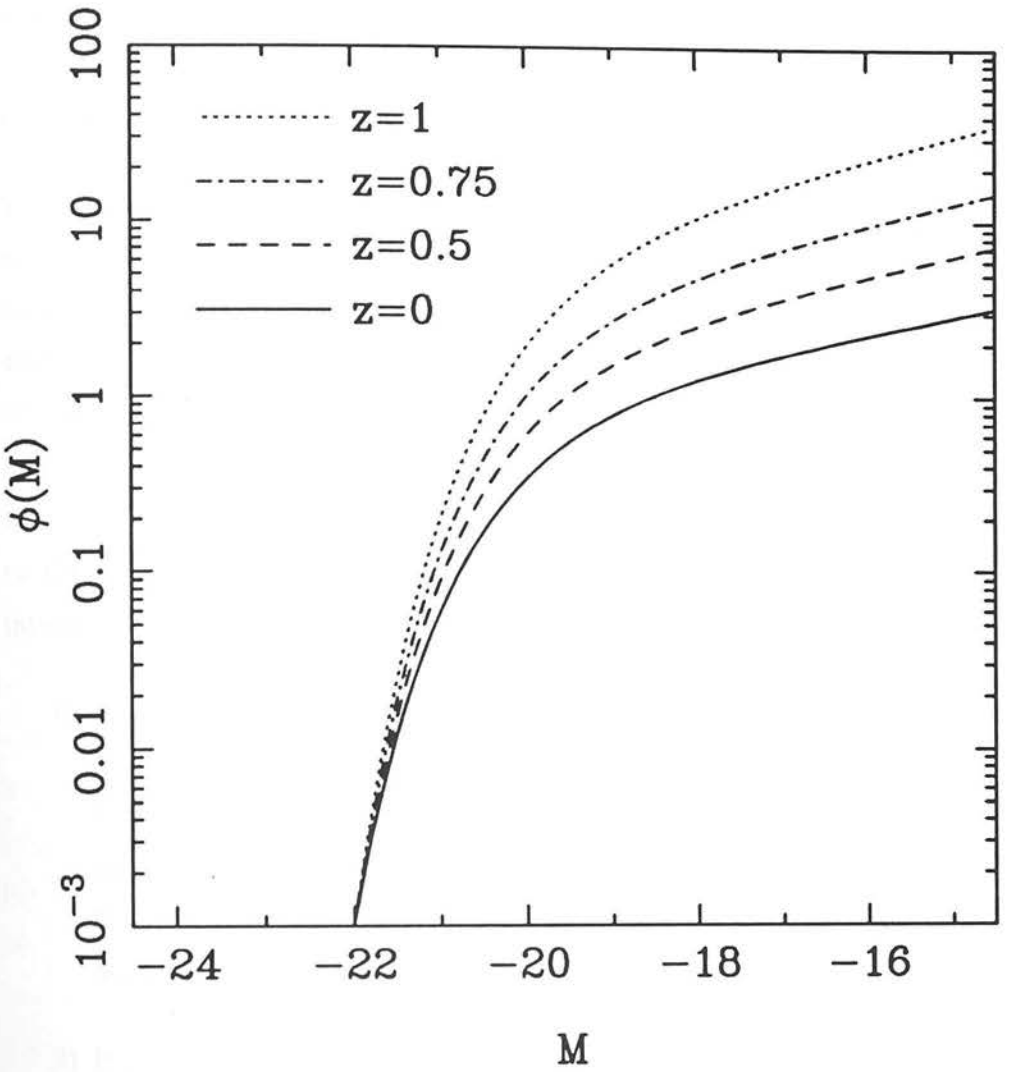

Fig. 5.19 The empirical form of b_j luminosity function evolution proposed by Broadhurst *et al.* (1988). In this plot $M^* = -20$ and $M_0 = M^* - 2$. It can be seen that the normalisation evolves by a factor of ~ 10 between $z = 0$ and $z = 1$.

where $\phi(M)$ is a Schechter function with $\alpha = -1.25$ and M_0 is set at $M_{b_j} = -23.5$, $\simeq 2$ magnitudes brighter than M^*. The evolution is taken to apply out to $z = 1$. This function is plotted in figure 5.19. It can be seen that this is slightly more complicated than pure number density or luminosity evolution — it is number density evolution, with a small amount of luminosity evolution, normalised to the same density at M_0. In practice the effect is similar to that of a pure number density model — steepening the b_j counts but keeping the mean redshift the same. The b_j predictions of this model are shown in figure 5.18; it can be seen that they are very similar to the Koo $\eta = 2$ model of number density evolution.

The interpretation of Broadhurst *et al.* was that this represented *differential* luminosity evolution with the faint galaxies evolving more than bright galaxies, giving an increase in normalisation due to the $\alpha = -1.25$ starting slope. Note however there is a big problem with this interpretation. Because the faint-end slope is relatively flat an enormous amount of horizontal luminosity evolution is required to simulate the effect of vertical density evolution, even with a value of α at the top-end of typical estimates. For example galaxies near M^* at $z = 1$ have to have evolved by $\simeq 4$ magnitudes since $z = 0$, and for galaxies on the faint end slope the evolution is up to 10 magnitudes. In K there are three possible interpretations:

1) If the function is regarded as pure density evolution it should be simply shifted along by a constant mean B − K colour. The same type-dependent K luminosity functions as before were used, with $M_0 = M^* - 2$. This is plotted against the counts in figure 5.20a and it can be seen that this overpredicts the number of faint K galaxies, as was expected. This is because the normalisation of the luminosity function has evolved by a factor of ~ 10 by $z = 1$.

2) If the function is regarded as a *differential* form of pure luminosity evolution, the then K band should be relatively unaffected and follow the no-evolution model, with $\alpha = -1.25$. However, as mentioned above, this would require very large amounts of evolution (4–10 magnitudes) in the B − K colours over $0 \leq z \leq 1$.

3) If the function is regarded as a merging model, then as above the natural application in K is to dim the characteristic luminosity with redshift so as to conserve mass. This was done by integrating the original function to give the scaling of total K

luminosity as a function of redshift. A fourth order polynomial was then fitted to this to give the empirical form, valid for $\alpha = -1.25$ and $z < 1$:

$$M(z) = 1 - 0.2046z + 7.1316z^2 - 11.871z^3 + 10.874z^4$$

The characteristic K luminosity thus changes by a factor of 7 since $z = 1$. This mass-conserving BES model is plotted in figure 5.20a. It can be seen that the result it gives is very similar to those of the $(1 + z)^\eta$ merging models, it corresponds to $\eta \simeq 2$–3. Such models would thus require evolution in the B − K colours by $\simeq 2$ magnitudes since $z = 1$.

Of course such models are extremely crude: we know that some L^* galaxies still exist at $z = 1$ from clusters and radio-galaxy data. However, as has been said above, it would be possible to construct a more sophisticated model in which, for example, big galaxies gobbled little ones or the merger rate depended on the clustering environment. But it does demonstrate an important point, namely that from the count slope alone it is not easy to tell whether galaxies at $z = 1$ exist in 2^4 subunits or even 2^7 subunits. The way to resolve this is to determine the redshift distribution. Such merging models will predict that the mean redshift of *K selected* samples will be *less* than the no-evolution prediction because galaxies become less luminous in the past. This is addressed in chapter 6.

K band luminosity evolution can be re-examined in the light of these models, by adding it in 'on top' of the luminosity devolution from merging. Any contribution from star-formation to the K light resulting from the merging can be thought of as being empirically included in this scheme. Figure 5.20b also shows $\eta = 2$ and 4 merging models with the L^* power raised by 1.4 and 2, an amount attributable to passive evolution. (Note the 2 + 2 model is the same as the "Koo" model in figure 5.17b). It can be seen that such models give a good match to the data in both slope *and* normalisation, the extra luminosity compensating for the merging.

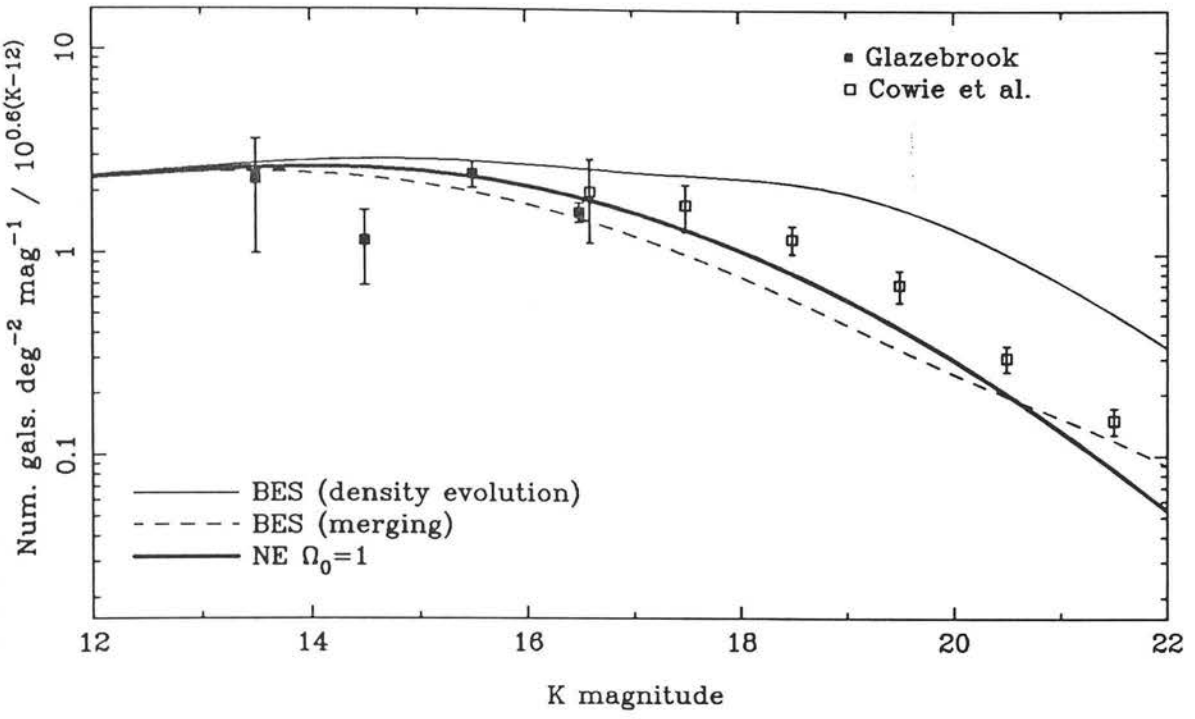

Fig. 5.20a K band predictions from the Broadhurst *et al.* luminosity function, interpreted in various ways. $\phi^* = 1.5\times10^{-2}\,h^3\,\mathrm{Mpc}^{-3}$, $\alpha = -1.25$.

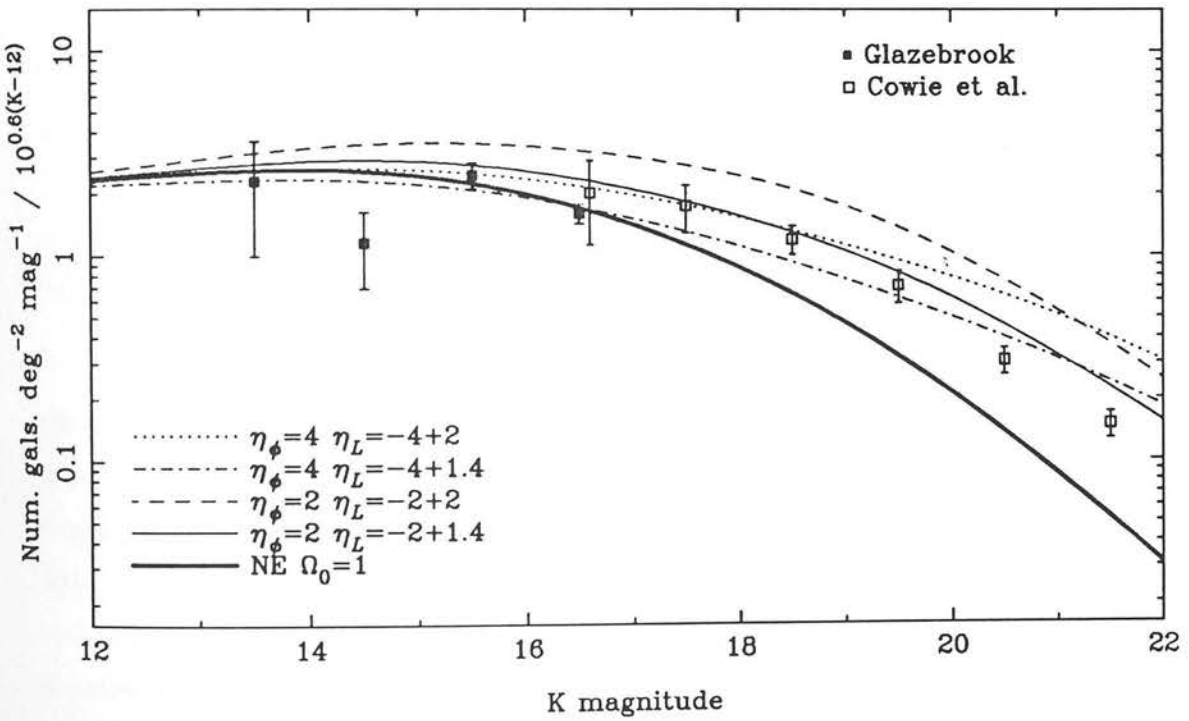

Fig. 5.20b Merging models with additional amounts of luminosity evolution added in "on top". $\phi^* = 1.5\times10^{-2}\,h^3\,\mathrm{Mpc}^{-3}$.

5.4.4 Non-standard world models

The expanding Robertson-Walker metric Big Bang universe is now the generally accepted cosmological model and the evidence for this is strong (see chapter 1). However it is worth examining the effect of non-standard cosmologies on the number-magnitude counts for the sake of completeness and because others have explored explaining the b_j count excess in this way (e.g. Lilly *et al.* 1991, Metcalfe *et al.* 1991). In addition the problem of reconciling globular cluster ages and H_0 can be solved by these cosmologies.

It is easy to see that changing the volume element, derived from the metric, will change the counts. For example if the universe were static and Euclidean the faint galaxy counts would be much steeper with a slope of 0.6, as they are at bright magnitudes.

One way of changing the volume element is by introducing the notorious cosmological constant. In a universe where the curvature is dominated by the cosmological constant ($\rho_{vac} >> \rho_m$) the volume element is $dV \propto z^2 dz$. The effect of this is shown in figure 5.21 using just K-corrections and no-evolution. The b_j counts undergo a mild steepening but not enough to explain the deep counts. In K the effect is, yet again, to over-predict the number of faint galaxies. If the curve was renormalised down then the mild steepening would be enough to match the K counts although the b_j counts would be too steep.

Another easy possibility to investigate is the steady-state theory. This has the same volume element but, to conserve the *proper* space density of galaxies $\phi^* \propto (1+z)^{-3}$. It is evident from the figure that this is ruled out as the under-prediction of faint galaxies is worse than a non-evolving Robertson-Walker prediction.

An even more regressive step would be to use a "Tired light" cosmology. In this scenario the universe is Euclidean and the redshift is caused by photons losing energy as they travel. The counts prediction differs from the Robertson-Walker metric in the volume element and a factor of $(1+z)$ from time-dilation at the source that is absent in the luminosity distance. The number-magnitude counts prediction is considerably steeper than any of the others and matches the b_j slope for $18 < b_j < 25$. However there are again too many predicted K galaxies. Even if the K normalisation is allowed to float, the faint slope is too steep.

There is one minor inconsistency in this treatment of non-standard cosmologies though. In principle the Schechter luminosity function parameters M^* and α should have been

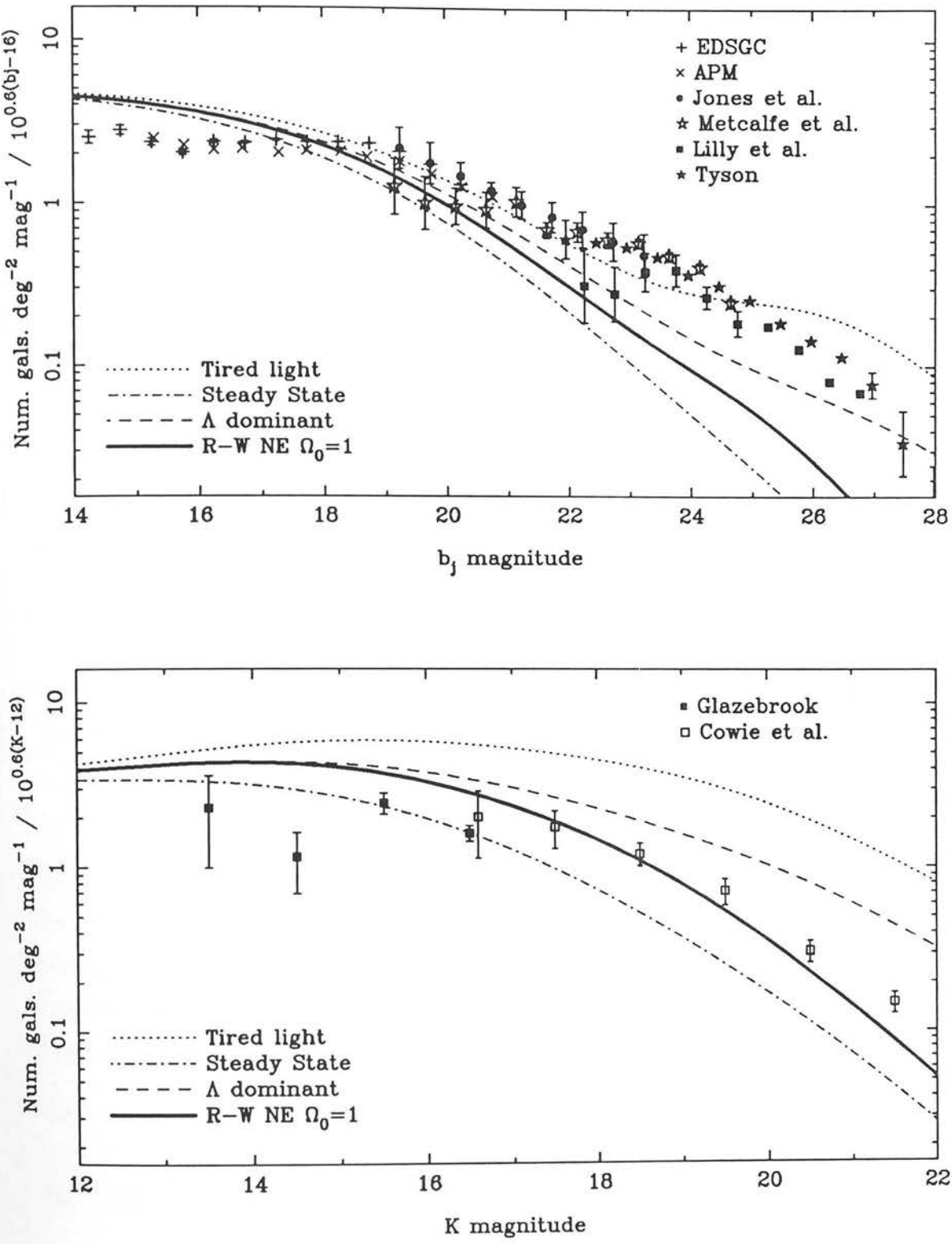

Fig. **5.21** Number-magnitude count predictions in non-standard world models (no-evolution, i.e. K-corrections only). Curves are for $\phi^* = 2.5\times10^{-2}\,h^3\,\mathrm{Mpc}^{-3}$.

redetermined self-consistently from the original datasets with the non-standard cosmological assumptions built in. However this is only a minor effect as the Schechter parameters are determined from bright data where the cosmological effects are small.

5.5 Summary

It is possible to explain the infrared number-magnitude galaxy counts in a model based upon optical galaxies. Unlike the b_j counts the K counts are well matched by a non-evolving galaxy model. If the data are normalised at bright magnitudes using the data presented here than the deep K counts of Cowie are only a factor of ~ 2 in excess of the non-evolving model, in contrast with the factor of ~ 10 excess seen in b_j. This follows the trend previously seen as number-magnitude counts were extended to redder optical bands.

There appears to be little evidence for pure luminosity evolution to $z = 1$, even the small amount predicted by passive evolution gives too many faint galaxies. Models of density evolution, and other models such as changing the volume element, which explain the b_j number counts and redshift distributions by increasing the number of galaxies generally overpredict the faint K counts. It is possible to match the slope by invoking a merging type evolutionary model, but only if the powerful assumption is made that merging conserves K light (i.e. $\simeq$ stellar mass). In this case the K counts are insensitive to the amount of merging. If passive evolution is added back in a satisfactory match can be obtained.

Such a merging model can naturally explain the b_j counts and redshift distributions if there is enough enhancement to the b_j light to compensate for the decrease in galaxy mass, thus keeping the mean redshift at the no-evolution value. This would have to be via some merger-driven starburst mechanism, which would also explain the galaxies in the b_j excess being spectroscopically evolved.

The principal uncertainty in modelling the counts is that the infrared luminosity function is taken by extrapolating the optical one with $b_j - \mathrm{K}$ colours of the models. If the colours are wrong then the predictions change. This will be explored in the next chapter.

6 COLOURS AND REDSHIFTS

6.1 Introduction

This chapter describes the optical-infrared colours of the galaxies in the infrared selected survey and discusses their relation to the redshifts determined from the spectroscopic survey (see chapter 4) and to the galaxy number-magnitude counts (see chapter 5).

One of the original aims of the survey (see chapter 1) was the search for primeval galaxies via unusually red optical-infrared colours. A red galaxy population is indeed found but its interpretation is not so clear cut. The colours of galaxies in the field at moderate redshifts ($z \lesssim 1$) are not well known. Most previous studies (e.g. Mobasher *et al.* 1986) have been based on optically selected samples, and thus biased against the detection of very red galaxies. It is only by using *infrared* selected samples of galaxies, such as the one presented here, that this bias can be countered.

The expected colours of normal galaxies are predicted using the models of spectral evolution introduced in chapter 5. The model colour-magnitude distributions and colour-redshift relations are derived and compared with the data. Also the spectra from the spectral evolution models are compared directly with those observed in the redshift survey.

The completeness of the redshift sample is checked and it appears that the sample is uniformly selected at bright K; and uniformly selected down to joint K and R limits for the objects fainter in K. The redshift distribution for the various samples is investigated and compared with the models use for the galaxy counts in chapter 5. The redshift distribution gives the ability to *deproject* the galaxy counts and can distinguish between different models of luminosity and number-density evolution which are not constrained by the number-magnitude counts.

6.2 The Colour Distributions of Survey Galaxies

The first item to be investigated is the colour magnitude relation. Figure 6.1 shows plots of R – K against K for the survey galaxies. These plots are for the galaxies as defined by the star-galaxy separation and are the same objects as used for the number-magnitude counts. They exclude the objects in the "reference star" position which turned out to be galaxies. They also exclude a few objects with highly anomalous colours which on detailed examination of the images proved to be spurious detector artifacts. Figure 6.2 shows the same plots for the field stars.

The redness of the galaxy population can be compared with the most expected, from the models of spectral evolution, by defining a "red envelope" below which galaxies should lie. This is done by plotting no-evolution (R – K, K) tracks as a function of redshift for a burst RVG model at age 16 Gyr with $M_K = -24.70$. This is 1.2 magnitudes brighter than M^* and is the approximate luminosity of a brightest cluster galaxy. The field galaxy population should lie fainter than this. The burst model forms all its stars in the first Gyr and then undergoes pure passive evolution of its stellar populations. This gives the reddest spectrum at 16 Gyr of all the models, thus the field population should also lie bluewards of this. This is shown in figure 6.3a. Also shown for comparison is that from a Bruzual c-model at the same age which also starts from a 1 Gyr burst. It can be seen that RVG model is about 1 magnitude redder at K = 16.5 than the Bruzual model and just about matches the red envelope of the galaxy distribution. The origin of this discrepancy is unclear, as the red and near-infrared light is dominated by giant branch stars then it almost certainly arises in the different treatment of the giant branch in the Bruzual models, in particular the neglect of the stages such as the Asymptotic Giant Branch.

Despite this range of uncertainty it is clear that only model spectra with old populations ($\sim$ 16 Gyr) and little luminosity evolution come close to matching the red end of the galaxy distribution. This appears paradoxical — we know from the optical B band count excess (see chapter 5) that the B – K colours *must* be getting bluer to some extent. To study this properly one needs to study the whole colour-magnitude distribution in more detail and not just the red end of it. For this it is necessary to calculate theoretical number-colour distributions from the spectral evolution models and compare them with the data.

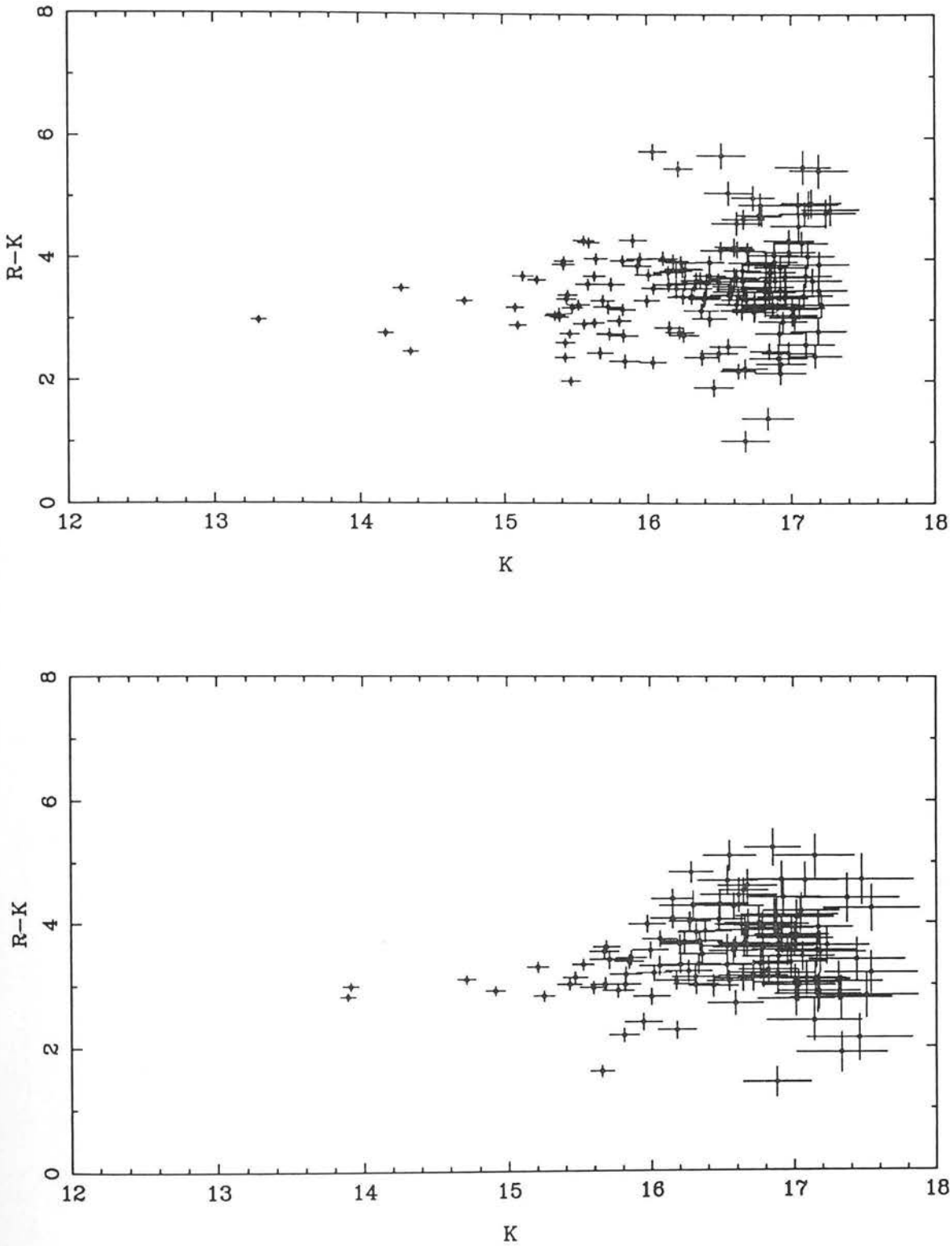

Fig. 6.1 The optical-infrared colour-magnitude diagrams for the survey galaxies in the October fields (top) and the March fields (bottom).

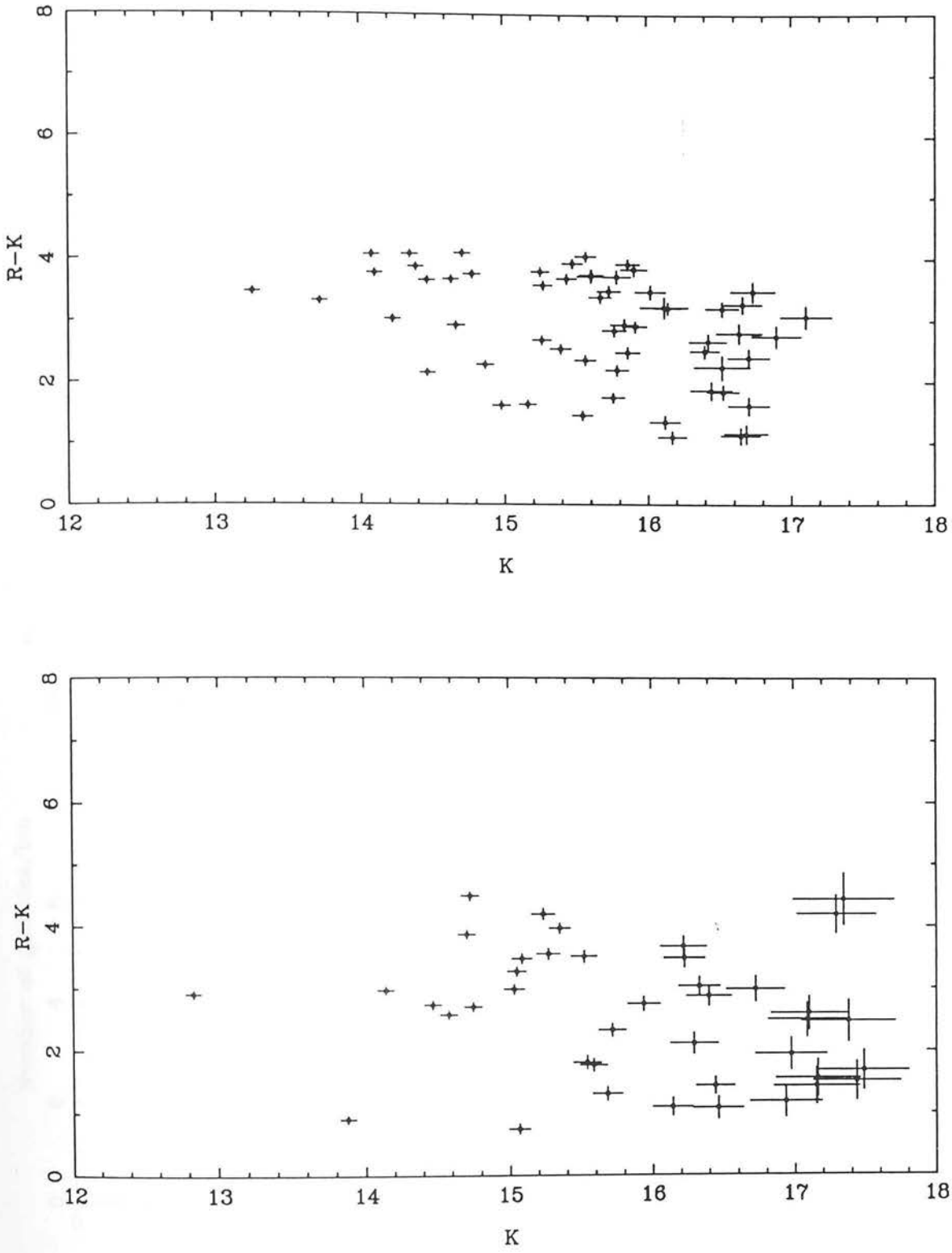

Fig. 6.2 The optical-infrared colour-magnitude diagrams for the survey stars in the October fields (top) and the March fields (bottom).

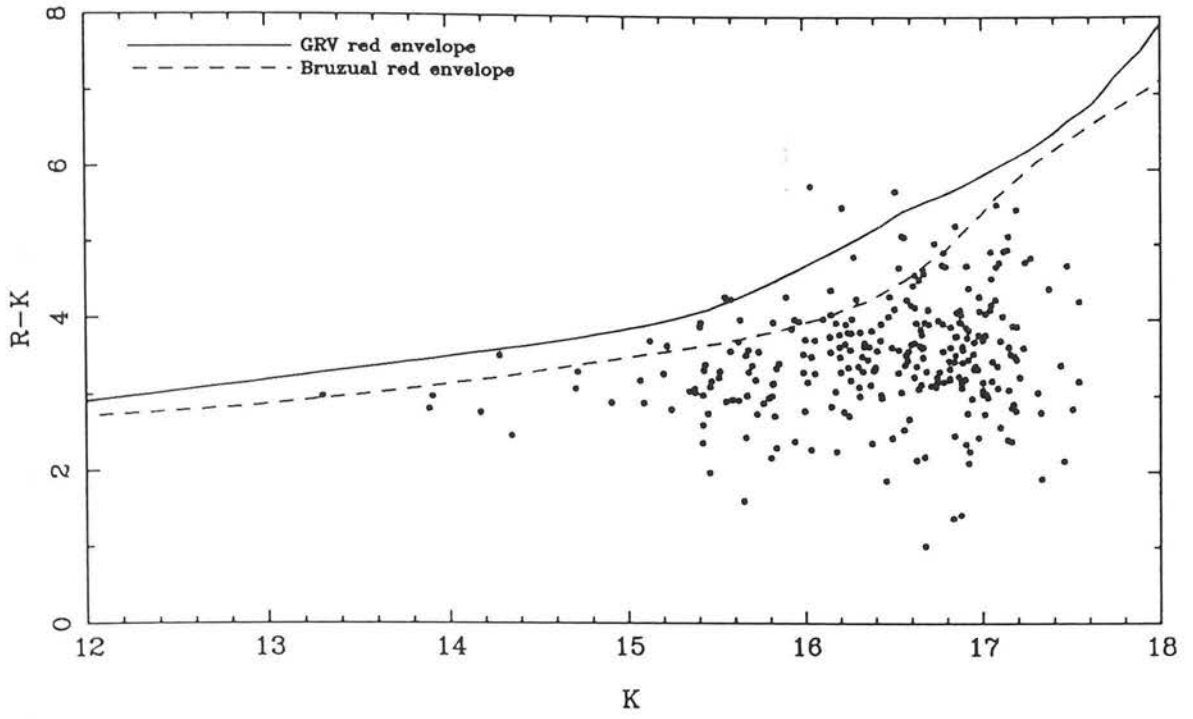

Fig. 6.3a Theoretical red galaxy envelopes from a RVG model and a Bruzual model.

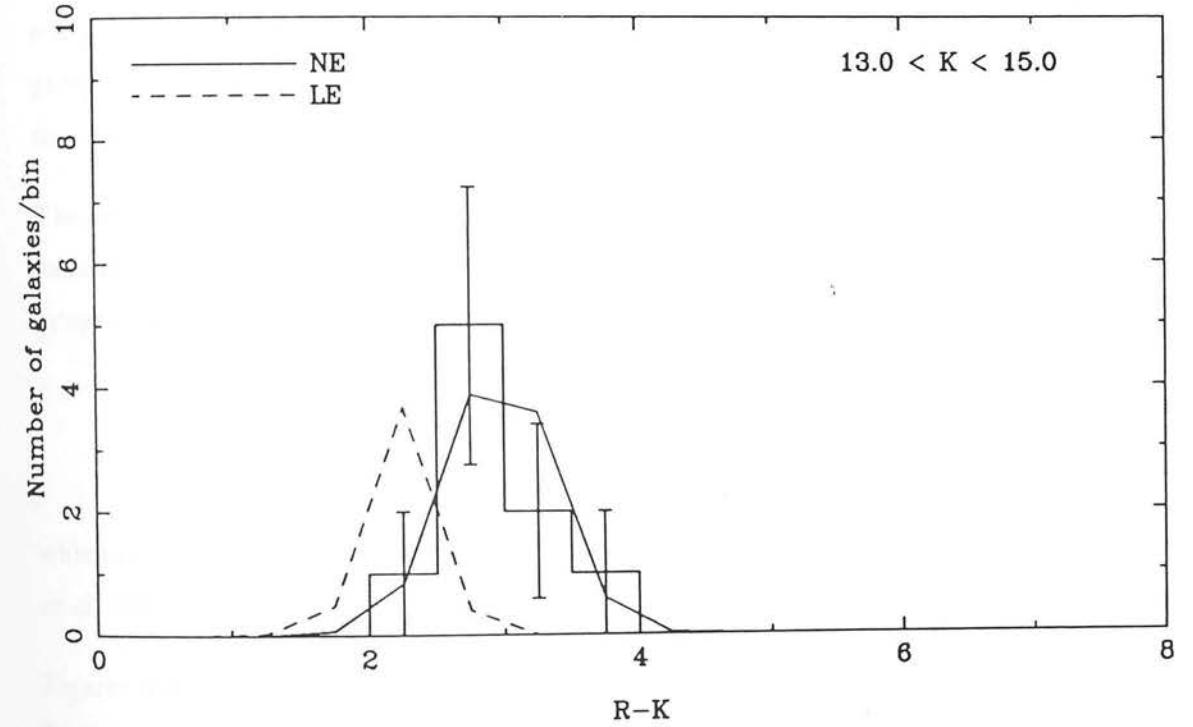

Fig. 6.3b The observed number-(R – K) colour distribution for $13 \leq K \leq 15$ compared with non-evolving and luminosity evolution predictions.

6.2.1 R – K colour-magnitude distributions

The approach adopted here for the comparison was first to bin the colours of the data between two magnitude limits $m_{min} \leq m \leq m_{max}$. For each model one has tabulated values of the colours, c, as a function of redshift z. At each redshift the number of galaxies with this colour is computed:

$$n_{gals} = \int_{M_{min}}^{M_{max}} \phi(M,z)\, dM \left(\frac{dV}{dz}\right) \Delta z$$

where $\phi(M,z)$ is the luminosity function expressed in magnitudes (see section 5.3.2) and

$$M_{min} = m_{min} - (m-M)(z)$$
$$M_{max} = m_{max} - (m-M)(z)$$

$(m-M)(z)$ is the distance modulus as defined in section 5.3.1, self-consistently including the K and E corrections from the model. Then the computed number of galaxies in each redshift interval is simply placed in the appropriate colour bin, using the same binning scheme as the data. The alternative approach of simply multiplying n_{gals} by dc/dz to generate number of galaxies per unit colour was tried, but not used as the insufficient time resolution in the models made the distribution curves noisy and irregular.

The integration over the luminosity function can be done rather easily provided it has the form of a Schechter function whose parameters depend on the redshift. In this case the integral, when re-expressed in luminosity, reduces to the incomplete gamma function:

$$\Gamma(a,x) = \int_x^{\infty} e^{-t} t^{a-1}\, dt$$

which can be efficiently calculated by means of a continued fraction approximation (Press *et al.* 1989, p.160).

Figures 6.3b, 6.4a and 6.4b show the data and predictions for the magnitude ranges $13 < K < 15$, $15 < K < 16$ and $16 < K < 17$. The non-evolving predictions are shown in each case normalised to the observed number of galaxies, this allows the colour distributions to be tested independently of the absolute normalisation which is already tested by the

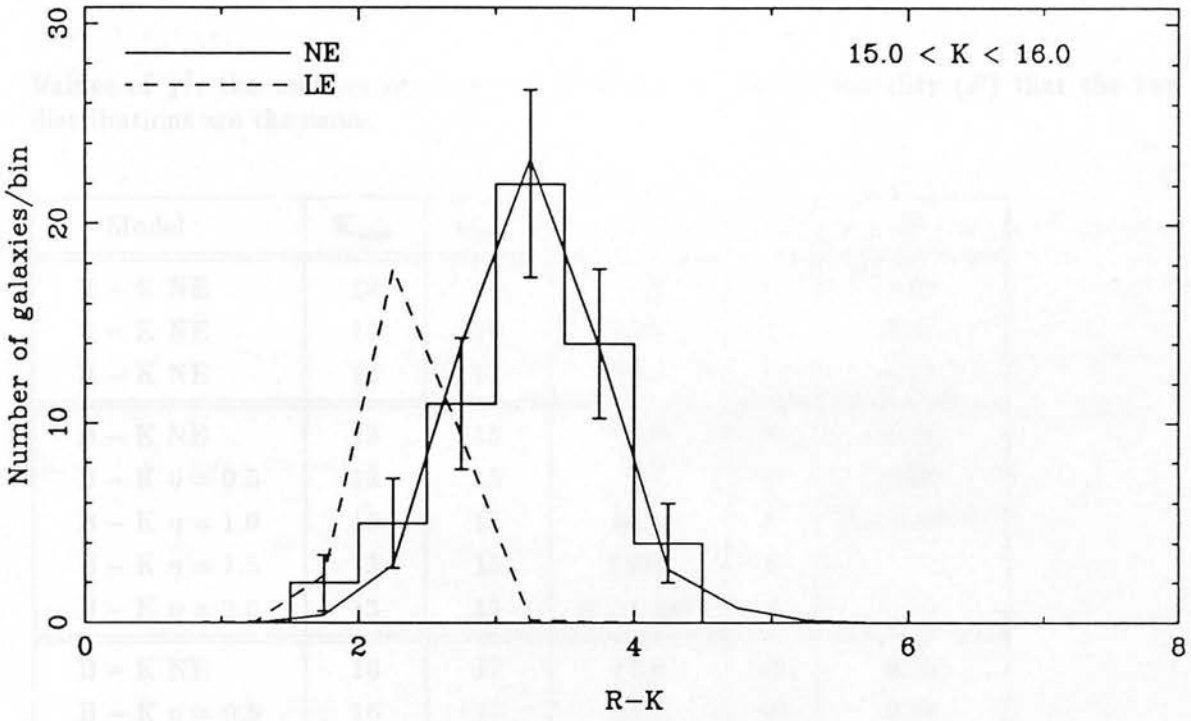

Fig. 6.4a The observed number-(R − K) colour distribution for $15 \leq K \leq 16$ compared with non-evolving and luminosity evolution predictions.

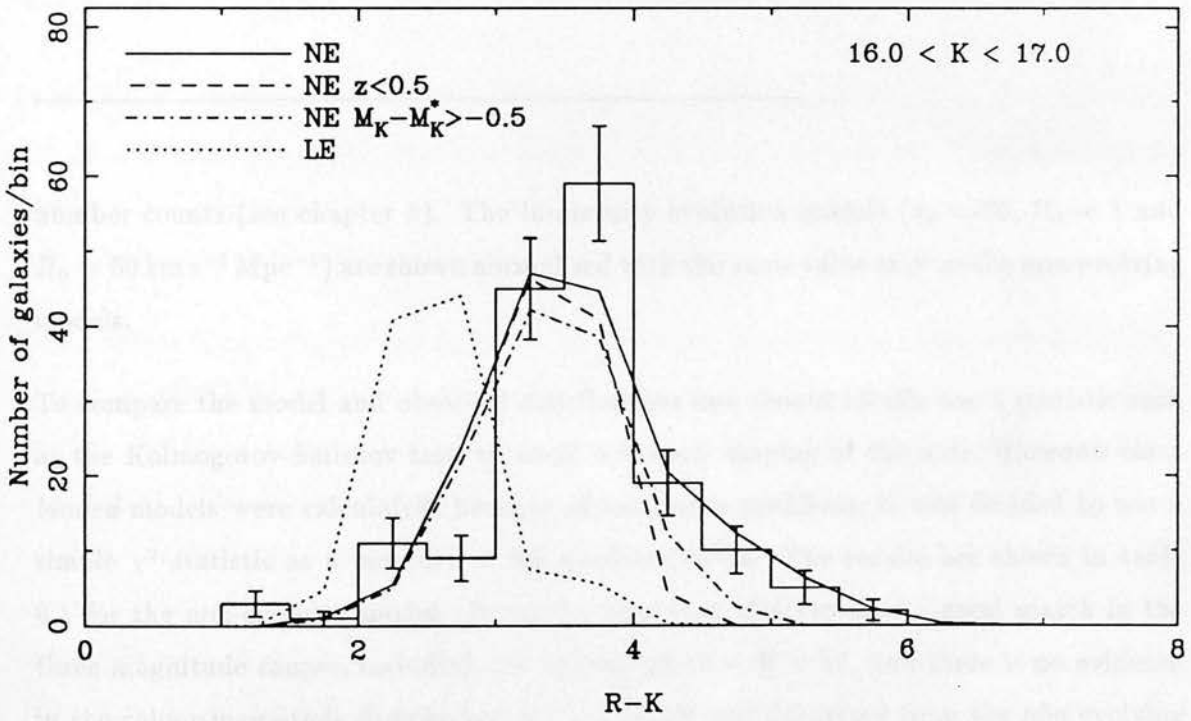

Fig. 6.4b The observed number-(R − K) colour distribution for $16 \leq K \leq 17$ compared with non-evolving and luminosity evolution predictions.

Table 6.1: Colour distribution fits

Values of χ^2, the number of degrees of freedom (ν) and probability (P) that the two distributions are the same.

Model	K_{min}	K_{max}	χ^2	ν	P
R – K NE	13	15	1.4	3	0.71
R – K NE	15	16	10.1	5	0.07
R – K NE	16	17	20.7	9	0.01
B – K NE	13	15	6.8	8	0.56
B – K $\eta = 0.5$	13	15	9.7	8	0.29
B – K $\eta = 1.0$	13	15	50.6	8	3.1×10^{-8}
B – K $\eta = 1.5$	13	15	1223	8	—
B – K $\eta = 2.0$	13	15	4.1×10^5	8	—
B – K NE	16	17	12.6	10	0.25
B – K $\eta = 0.5$	16	17	11.2	10	0.34
B – K $\eta = 1.0$	16	17	14.7	10	0.14
B – K $\eta = 1.5$	16	17	46.1	10	1.4×10^{-6}
B – K $\eta = 2.0$	16	17	706	10	—

number counts (see chapter 5). The luminosity evolution models ($z_f = 30$, $\Omega_0 = 1$ and $H_0 = 50\,\mathrm{km\,s^{-1}\,Mpc^{-1}}$) are shown normalised with the same value of ϕ^* as the non-evolving models.

To compare the model and observed distributions one should ideally use a statistic such as the Kolmogorov-Smirnov test, to avoid arbitrary binning of the data. However since *binned* models were calculated, because of resolution problems, it was decided to use a simple χ^2 statistic as a measure of the goodness of fit. The results are shown in table 6.1 for the non-evolving model. It can be seen that this provides a good match in the three magnitude ranges, including the red tail at $16 < K < 17$, and there is no evidence in the colour-magnitude distribution for any significant departure from the non-evolving model. However this is dependent on the form of the non-evolving model. The RVG models produce much redder colours than, for example, a Bruzual model as can be seen

from the red envelopes in figure 6.3. If one were to adopt Bruzual models then the entire model distribution would have to be shifted 1 magnitude bluewards; and then the red tail would be significant.

As for the luminosity evolution model, it can be seen from the figures that the colours are far too blue and the model is completely wrong. The formal χ^2 probabilities are vanishingly small. The other RVG luminosity evolution models are similar.

What are the redshifts and magnitudes of the galaxies in the red tail? This can be investigated by truncation of the integrations in terms of absolute magnitudes, or redshifts. Figure 6.4b shows the effect of

a) Truncating the integral at $z < 0.5$.

b) Truncating the integral at $M_K - M_K^* > -0.5$.

From this it can be seen that, according to the models, the galaxies in the red tail come from galaxies about a magnitude brighter than M^* at $z \geq 0.5$.

6.2.2 B – K colour-magnitude distributions

If the R – K colours are so red, and well match no-evolution, then how does this fit in with the optical number counts? There is known to be a large excess in the B counts which is not seen in K (see chapter 5) — this implies the galaxy population *must* be getting bluer and there ought to be consistency between the colours and the counts.

It is possible to investigate how much colour evolution is allowed by the observed colours, regardless of the defects of the spectral evolution models, by turning to the parametric models of chapter 5. For this it is better to use the B – K colour distribution rather than R – K as then like is being compared with like, even though the area being surveyed in B is smaller and the depth not quite enough to be complete for objects with the reddest B – K colours. The B limits vary from 23–24 depending on the field. Nevertheless a complete subsample with $B \leq 23$ can be defined and modelled with joint K and B limits. This is plotted in figure 6.5 for $13 < K < 16$ (note $B < 23$ has no effect for this sample) and $16 < K < 17$ samples. Model predictions for no-evolution ($\Omega_0 = 1$) are shown, normalised to the total number of galaxies. It can be seen that no-evolution provides quite a good fit.

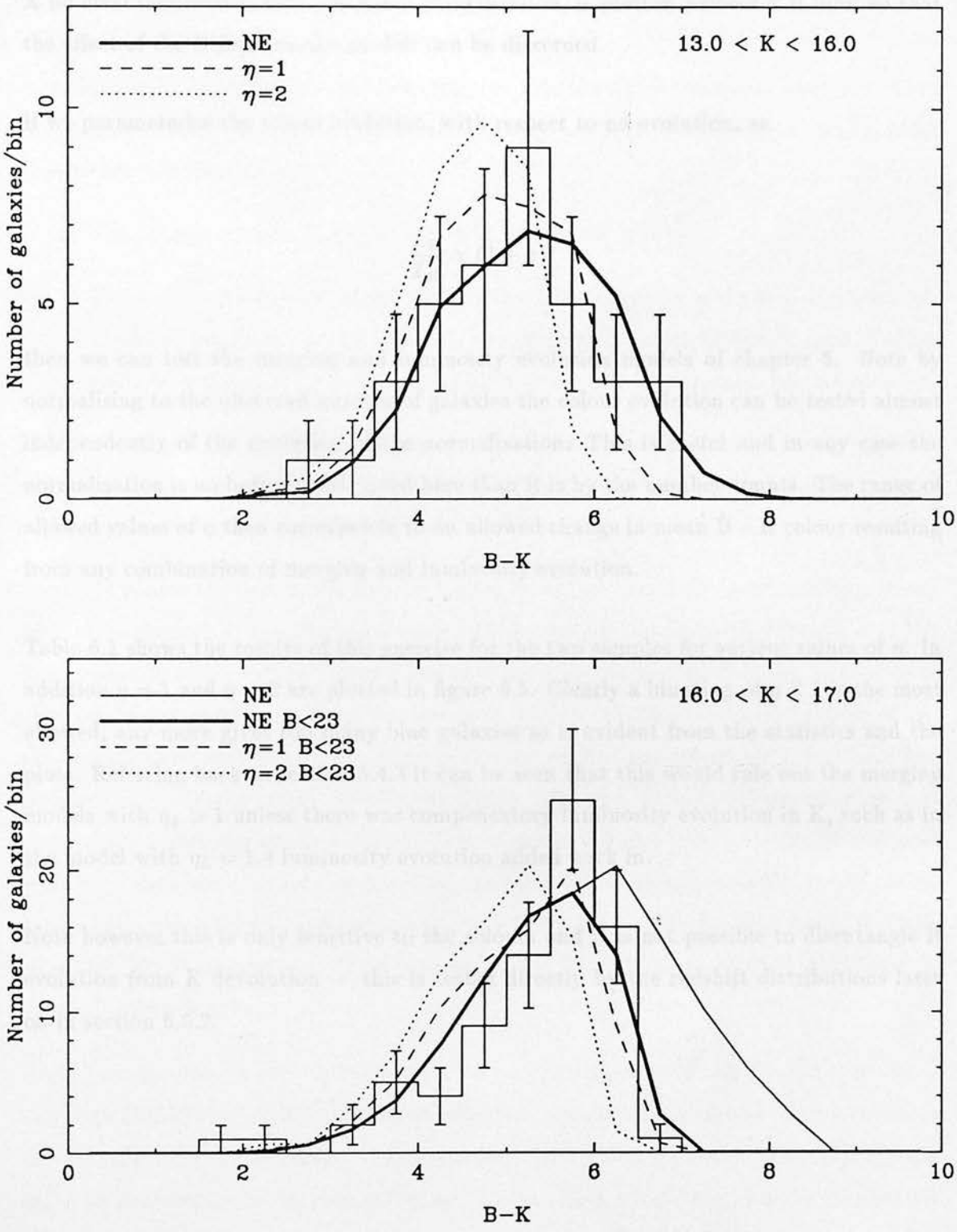

Fig. 6.5 B − K distributions for the $13 < K \leq 16$ sample (36 galaxies) and the $16 < K < 17$, $B < 23$ sample (78 galaxies). No-evolution and parametric colour evolution models are shown (computed with $\Omega_0 = 1$).

A no-evolution model, with the same normalisation, is plotted *without* a B limit so that the effect of the B limit on the models can be discerned.

If we parameterise the colour evolution, with respect to no-evolution, as

$$\frac{L_{\rm B}}{L_{\rm K}} \propto (1+z)^{\eta}$$

then we can test the merging and luminosity evolution models of chapter 5. Note by normalising to the observed number of galaxies the colour evolution can be tested almost independently of the evolution of the normalisation. This is useful and in any case the normalisation is no better constrained here than it is by the number-counts. The range of allowed values of η then corresponds to an allowed change in mean B – K colour resulting from any combination of merging and luminosity evolution.

Table 6.1 shows the results of this exercise for the two samples for various values of η. In addition $\eta = 1$ and $\eta = 2$ are plotted in figure 6.5. Clearly a bluening of $\eta \leq 1$ is the most allowed, any more gives too many blue galaxies as is evident from the statistics and the plots. Referring back to section 5.4.3 it can be seen that this would rule out the merging models with $\eta_\phi > 1$ unless there was compensatory luminosity evolution in K, such as in the model with $\eta_L = 1.4$ luminosity evolution added back in.

Note however this is only sensitive to the colours and it is not possible to disentangle B evolution from K devolution — this is tested directly by the redshift distributions later on in section 6.5.2.

6.3 JHK Observations of the Reddest Galaxies

In order to try and elucidate some further information on the reddest galaxies a short program of infrared photometry was embarked upon via service observation. The reddest objects full into two classes:

1) The reddest objects in $R - K \sim 5$ lying on the red envelope.
2) The objects which were present only in the K images at 5σ and which, if confirmed, would be extremely red ($R - K \gtrsim 6$) and of great interest. Although most of these could be accounted for (see sections 3.5.1 and 3.5.2) 32 remained unaccounted for.

The motivation for further observations was of course to see if these were a new population of objects. As discussed in chapter 1 the possibility exists that unusually red objects could be protogalaxies or brown dwarf stars.

Ideally of course the best follow-up observation would be to obtain spectra. The problem with this approach is the objects are interesting because they are *red*. With $R - K \gtrsim 5$ this implies $R > 21$, and as discussed in chapter 4 the deepest identifications that were obtained in the spectroscopic survey was at $R \lesssim 21$ in 20 000 s with LDSS. Some of the red objects were included, in the hope that they might have strong emission lines, but none of these were detected. A different attack might be via *infrared spectroscopy*, this time taking advantage of the redness. Unfortunately infrared spectrometers of sufficient sensitivity were not available at that time. Infrared array spectrometers, using the same detectors as the infrared cameras, are starting to become available. One example is the recent commissioning of the CGS4 instrument on UKIRT, so the future possibility of infrared spectra remains.

The follow-up observations that were decided on was a program of JHK infrared photometry with IRCAM on UKIRT. The most important observation is simply to try to confirm the "K-only" objects by further K observations. It is always possible that such objects could be detector artifacts, such as "ghost" images from bright stars nearby (several arcminutes) in the field. These are caused by light reflected off the internal surfaces in the camera optics and passing through the system twice to leave a spurious image. They are known to be a problem with IRCAM (I.S. McLean, 1989, private communication) and they are usually seen symmetrically on the other side of the optical axis (near the middle

of the chip) from the bright star, with an intensity a few percent of the star. In addition the ghost is commonly optically distorted and presents an unusual image, if it is bright enough. The way to test this is to take a second observation with the object position in a different part of the chip from the survey observations. If it is a real object it will still be there, while if it was a ghost it will not as the ghost will have moved to a different position with the change in location of its originator.

If the object is confirmed in K then J and H images can be taken. The $(J-H, H-K)$ colour-colour diagram allows the determination of the shape of the continuum in the near infrared. Objects with classical protogalactic colours (see section 1.2) should have continua, longwards of the Lyman break, dominated by hot blue OB stars ($T \sim 40\,000\,K$) and would be very blue in $J-H$ and $H-K$. Conversely, brown dwarves would have cool blackbody colours ($T \sim 1000$–$2000\,K$) and would consequently be very red in $J-H$ and $H-K$. Local galaxies all appear to have very similar near infrared continua, with $J-H = 0.75 \pm 0.15$ and $H-K = 0.25 \pm 0.15$, irrespective of morphological type, as is shown by the samples of Glass (1984) and Aaronson (1978).

Service observations were obtained in December 1989 on 4 K-only objects and 4 very red ($R-K \gtrsim 5$) paired K and R objects. These were 120 s exposures in K (and J and H where performed) and of sufficient depth to unambiguously confirm the K-only objects if they were real. None of the K-only objects were confirmed; all of them appear to be due to some kind of ghosting. In each case a bright star can be identified as the likely culprit. With the experience thus gained, the other K-only candidates were re-examined and another 10 identified as probable ghosts, leaving 18 K-only objects still unidentified. Subsequently 3 of these objects were re-observed by J.S. Dunlop to a detection limit of $K = 20.1$, and none were confirmed. Thus it seems we can almost definitely rule out the existence of an infrared only population down to the magnitude limit of this survey.

Regarding the red paired objects, one of these was not reconfirmed. Examination of the original survey K images reveals that the "object" appears to be some kind of noise artefact on *one* of the sub-mosaics making up the final K image. Another object was only reconfirmed in H. This is puzzling as the depth was sufficient to reach the required K limit. It does not seem likely that this is either a ghost or a noise artefact as it also appears in all the original sub-mosaics. However two red objects were reconfirmed; their colours are listed in table 6.2 and plotted, together with 1σ error ellipses in figure 6.6.

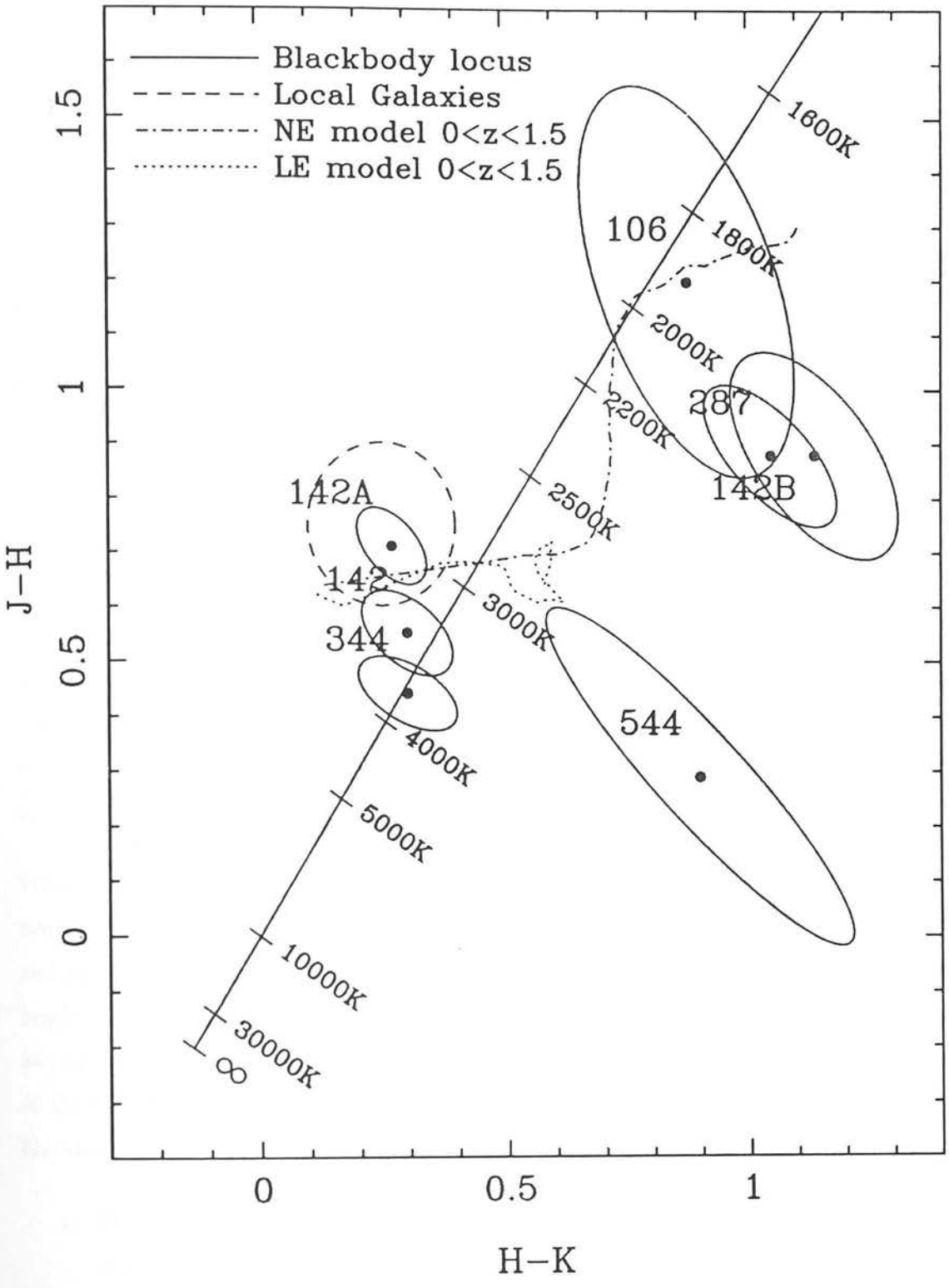

Fig. 6.6 The JHK colours, with 1σ error ellipses, for the red objects observed in service.

Table 6.2: Summary of red object JHK photometry

Object	K_{surv}	R_{surv}	J	H	K
OCTKR#544	16.96 ± 0.16	23.22 ± 0.27*	18.19 ± 0.07	17.90 ± 0.30	17.00 ± 0.10
OCTKR#106	16.22 ± 0.09	21.70 ± 0.09	18.30 ± 0.30	17.10 ± 0.20	16.20 ± 0.15
MAR#287	16.85 ± 0.19	22.09 ± 0.23†	18.99 ± 0.07	18.11 ± 0.11	17.06 ± 0.08
MAR#344	17.15 ± 0.27	22.25 ± 0.21	17.49 ± 0.03	17.05 ± 0.06	16.75 ± 0.08
MAR#142	16.28 ± 0.15	21.12 ± 0.09	16.82 ± 0.05	16.27 ± 0.06	15.97 ± 0.07
MAR#142A‡	—	—	17.46 ± 0.05	16.75 ± 0.05	16.48 ± 0.05
MAR#142B‡	—	—	20.29 ± 0.13	19.41 ± 0.14	18.27 ± 0.09

* $I = 20.16 \pm 0.13$.
† $I_{surv} = 20.28 \pm 0.10$
‡ 2″ apertures in 1″ seeing

In addition some extra JHK colours were kindly measured by J.S. Dunlop. One of these was a more accurate determination of the J – K colour of one of the service galaxies, and the others were observations of new red objects. One of these objects was clearly resolved into two separate components, each of these are shown separately in figure 6.6 and table 6.2.

What can be concluded from the colours of these objects? Figure 6.6 also shows the location of normal galaxies, the tracks of the new RVG models (both non-evolving K-correction and luminosity evolution) for $0 \leq z \leq 1$ and the blackbody locus for comparison. The bright component of object MAR#142 has colours consistent with it being a nearby galaxy or star. The fainter component of MAR#142, MAR#287 and the fainter component of OCTKR#106 both have very red J – H and H – K colours which correspond to a blackbody colour of 1900 ± 300K. This implies two very different explanations:

1) They could be galaxies at redshifts $z \gtrsim 1$. The R – K and JHK colours would then be consistent with the non-evolving models at these redshifts, and the colour-magnitude histograms show that this is where we would expect these objects to lie if they were just extreme examples of the red population. This would not be the case if one were to believe the luminosity evolution models — galaxies simply

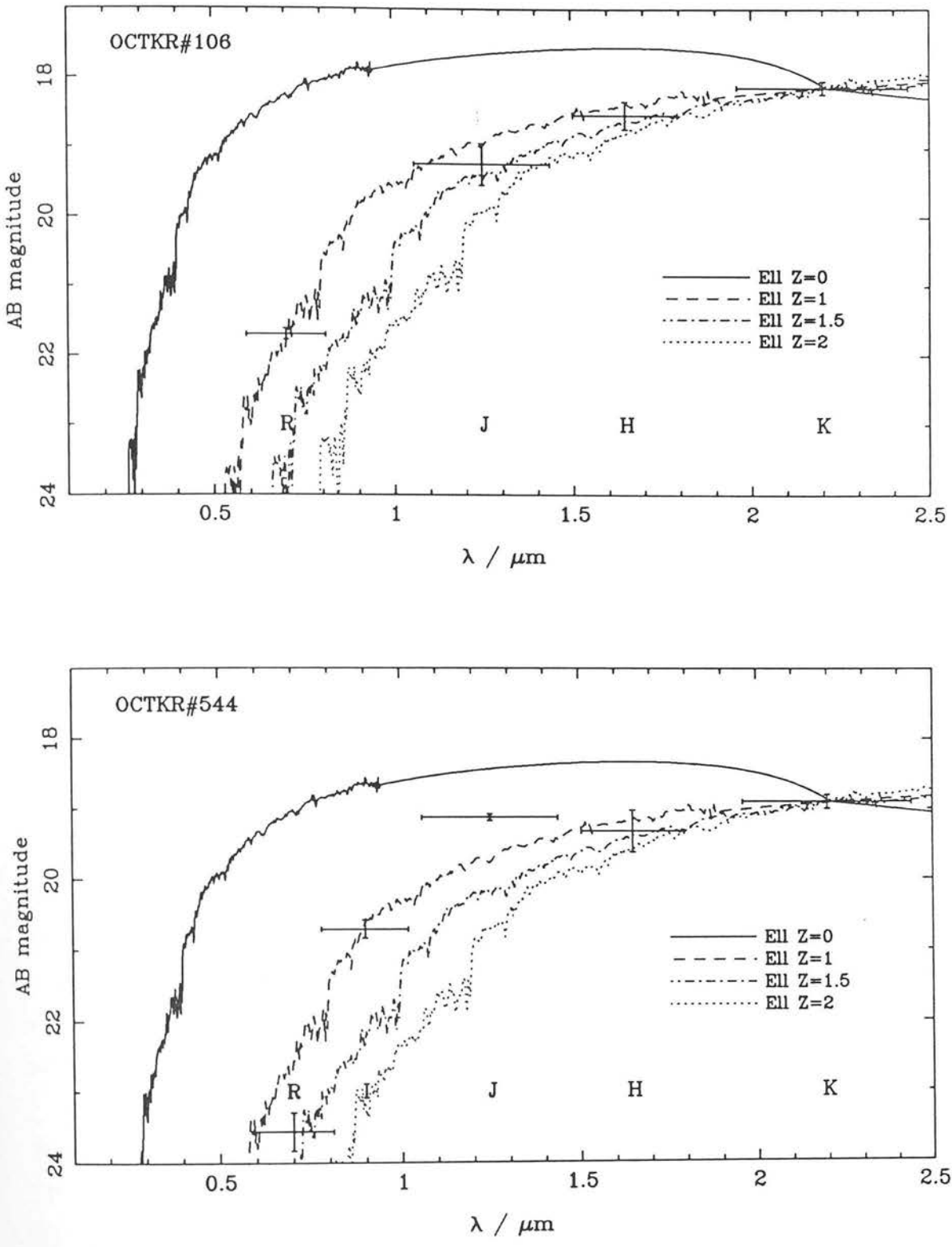

Fig. 6.7 Comparison of the spectral energy distribution of OCTKR#106 and OCTKR#544 with a redshifted elliptical galaxy template, normalised to the K band flux.

never get that red in JHK. However as can be seen from the rest of this chapter, and from chapter 5, the evidence from the bulk of the galaxy population is against these models. Figure 6.7 shows the RJHK spectral energy distribution for OCTKR#106 compared with the non-evolving elliptical templates. It can be seen that it is well matched by the template if $1 < z < 1.5$.

2) They could be very low mass M stars or brown dwarves. These objects are close to the R band limit so it is entirely feasible that the star-galaxy classification could be unreliable. Some support for this hypothesis is provided by their possible association with nearby objects. Object MAR#142 is only $\simeq 3''$ from its brighter component and object OCTKR#106 is $\simeq 18''$ from a bright star. It is not possible to distinguish between brown dwarves or M stars from the colours alone even if one had a distance estimate and hence a luminosity. Theoretical tracks for the zero age main sequence and contraction, deuterium burning and cooling of substellar objects only differ by 100–300 K at a given luminosity (Liebert, 1990). Of course brown dwarves have to be significantly younger — for objects at the critical ^{1}H burning mass ($0.08\,M_\odot$) the age for a temperature of 2000 K is $\simeq 1$ Gyr (Nelson *et al.*, 1986). Taking a radius of $\sim 0.05\,R_\odot$ for such an object implies $M_K \simeq 11$–12 (Becklin & Zuckerman, 1988) and distances of 50–100 pc for OCTKR#106 and 200–300 pc for MAR#142B. This would put MAR#142B $\sim$ 700 AU from MAR#142A if it were a binary star system.

There also appears to be a class of objects with bluer JHK colours in the survey. These include OCTKR#544 (the reddest object in the survey), MAR#344 and MAR#142A. It could be argued that the JHK colours are similar to low redshift galaxies, however the survey R magnitude and the I magnitude (where available) have to be considered too. The full RIJHK spectral energy distribution of OCTKR#544 is shown in figure 6.7. It can be seen that the main problem is in fact in the J magnitude, otherwise the SED would be consistent with a $z \sim 1$ galaxy as with the other two objects. It can be seen from figure 6.6 that it is about 1 magnitude too bright in J for this interpretation. The object has been observed in J *twice*, once in service ($J = 18.2 \pm 0.2$) and once by J.S. Dunlop ($J = 18.19 \pm 0.07$) so this is not in doubt. Could this be a high-redshift protogalaxy? If the Lyman-α forest were somewhere in the R–I bands then that would imply $z = 5$–8. The flat near-infrared continuum would then have a blackbody temperature of ~ 3000 K if

it was a classical protogalaxy (see section 1.2), which is indeed consistent with the errors.

However there is a more prosaic interpretation for objects with infrared colour temperatures of $\sim$ 3000 K and red R − K colours. These colours are entirely consistent with those of the coolest known M stars (see for example Hawkins & Bessell 1988). Though these objects would be of great intrinsic interest if they turn out to be galaxies this other possibility has to be checked, and the only way to do that is spectroscopically.

Some of these objects were observed with LDSS, however only one identification was secured. This was for MAR#533 (K = 15.4, R − K = 4.8) and it turned out to be an M star. Unfortunately this object was not observed in JHK so it is not known what its colour temperature is. However the R − K colour is consistent with the M stars of Hawkins & Bessell. The only other spectrum of one of these objects was obtained on 20/3/1991 using the Faint Object Spectrograph (FOS) on the INT.

A 4000 s exposure was taken in good seeing of the bright component of MAR#142 (the fainter component was not detected). This is shown in figure 6.8 together with an M star also observed in the same run for comparison. These spectra have not been fluxed, however it can be easily seen that there are enough spectral features in common to show that MAR#142A is some kind of M star. It is not possible to glean more information from such a spectrum as M star features are unreliable indicators of temperature compared to infrared colours. However, given that the primary is an M star does this make MAR#142B a cool brown dwarf? Its colours are 2σ from the black-body locus, although the actual temperature locus of real objects is poorly known from theory (M.R.S. Hawkins, 1991, private communication), and of course there are few known real objects much cooler than $\sim$ 3000K.

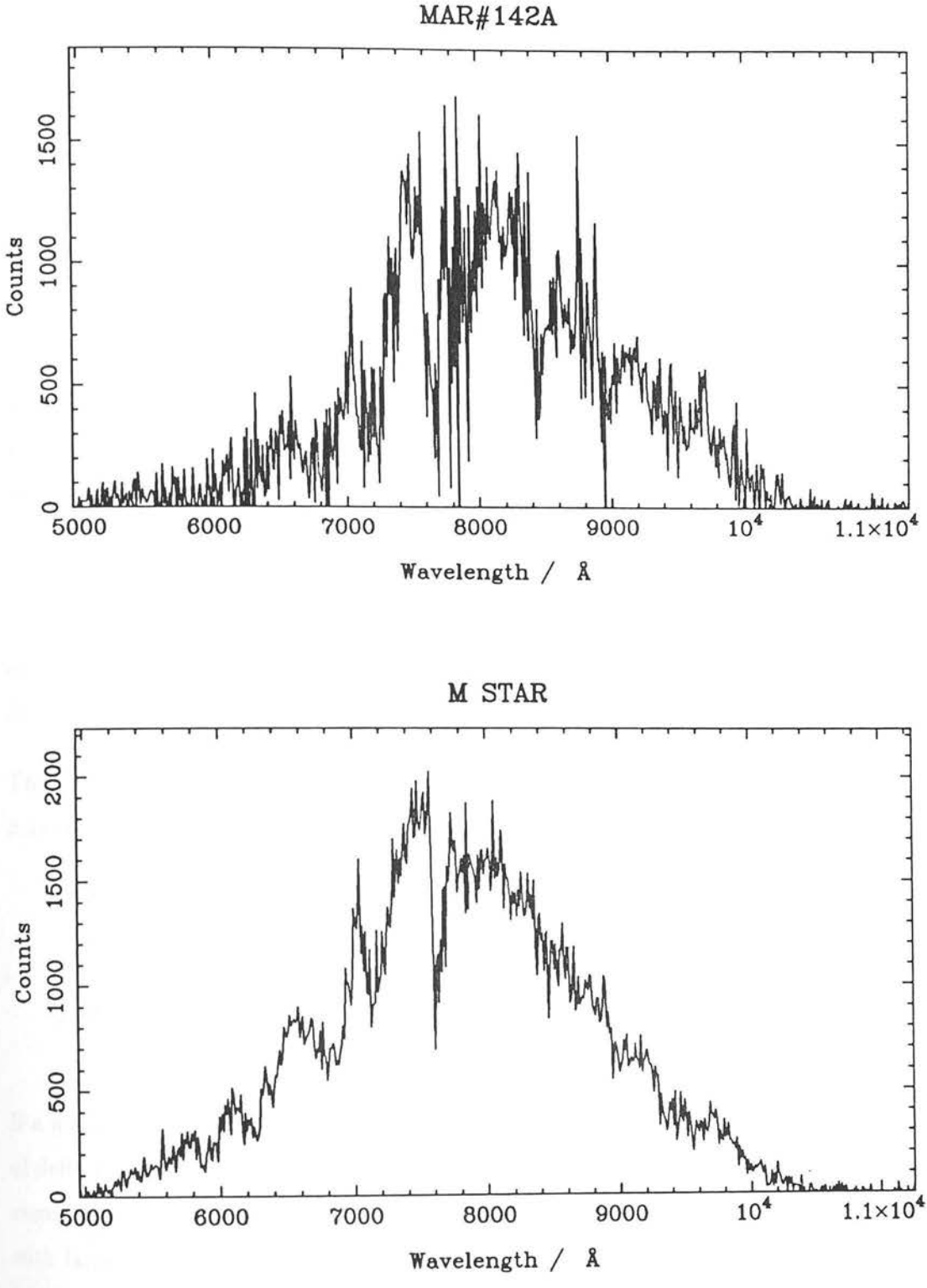

Fig. 6.8 A comparison of the FOS spectra of MAR#142A (top) and an M star (bottom). Note these spectra are unfluxed, the exposure times are 4000 s and 600 s respectively. The deep feature at $\simeq$ 7650 Å is the sky A band absorption.

6.4 The Colour-Redshift Relation

The colour-magnitude distributions of section 6.2 crudely show that the red tail of galaxies beyond R − K = 4 can be explained by unevolved galaxies at $z \gtrsim 0.5$.

It is possible to deproject this distribution and see what is happening directly with redshift in the galaxy population. The spectroscopic survey allows this to be done for a subset of the galaxies. Colour (in this case R − K) can be plotted against redshift and compared with the models.

This is done in figure 6.9a. The 53 redshifts derived in chapter 4 are plotted, galaxies with emission lines are plotted as a different symbol. The colours of the non-evolving RVG models are also shown. The spectral evolution models occur as lines in these plots, not distributions, as each model has only one, fixed spectral energy distribution at each epoch. No natural variations in colour among each type, as might be caused by a colour-luminosity relation (e.g. R.G. Bower, 1990), are built in. However the different models span the range of morphological types, and hence colours, so with knowledge of the number of galaxies in each type at each redshift it is possible to construct a approximate colour distribution. This allows the colour spread of the models to be compared with the data.

The number of *observed* galaxies in each type as a function of redshift depends on the K magnitude range of the survey. To calculate it it is necessary to:

1) Work out the absolute magnitude range corresponding to the observed K range from the distance modulus and R-correction at this redshift.

2) Integrate the luminosity function over this range (see section 6.2), scaling by the relative space density of the type.

If a number vs R − K plot is then made for a thin redshift slice the models appear as a set of delta functions containing the appropriate number of galaxies. If this is converted to a *cumulative* distribution, i.e. number< R − K then this appears as an increasing function with large steps at each type. It is then possible to assign colour confidence levels, i.e. the colours at which the cumulative distribution function increases past, for example, 5%, 25%, 50% and 95% of the total number of galaxies. Because of the stepwise nature of the function then these levels will lie at one of the model colours.

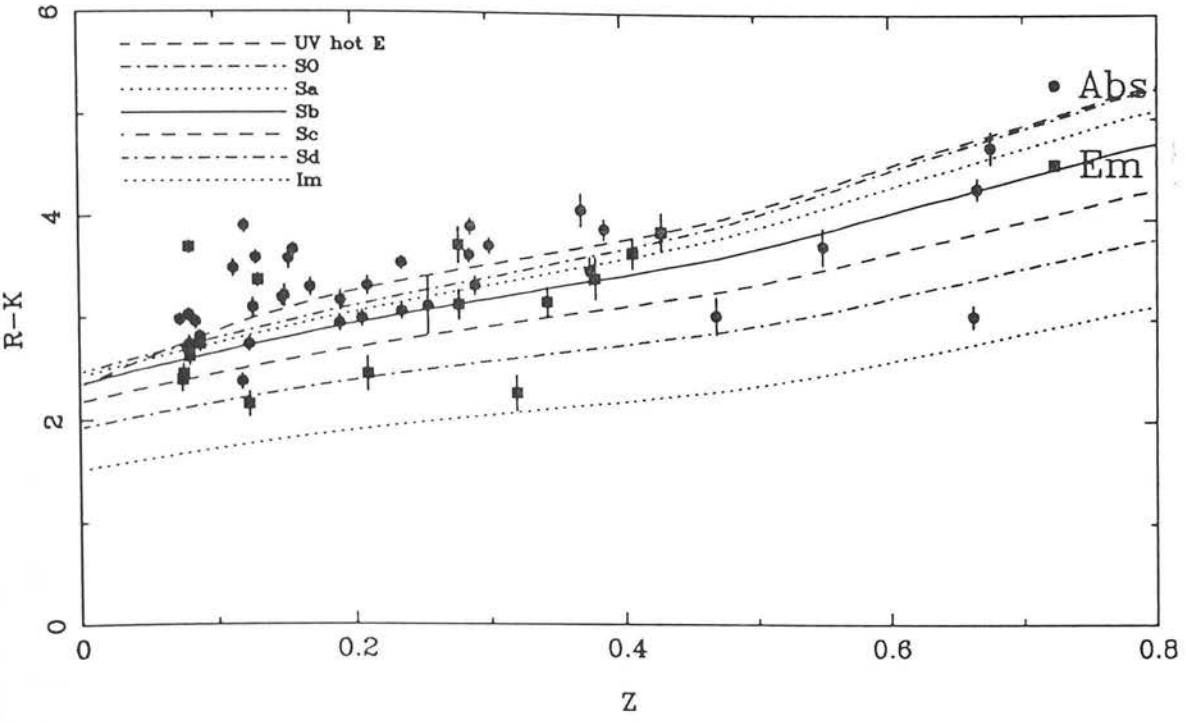

Fig. 6.9a The R – K colours of the non-evolving RVG models as a function of redshift compared with the data.

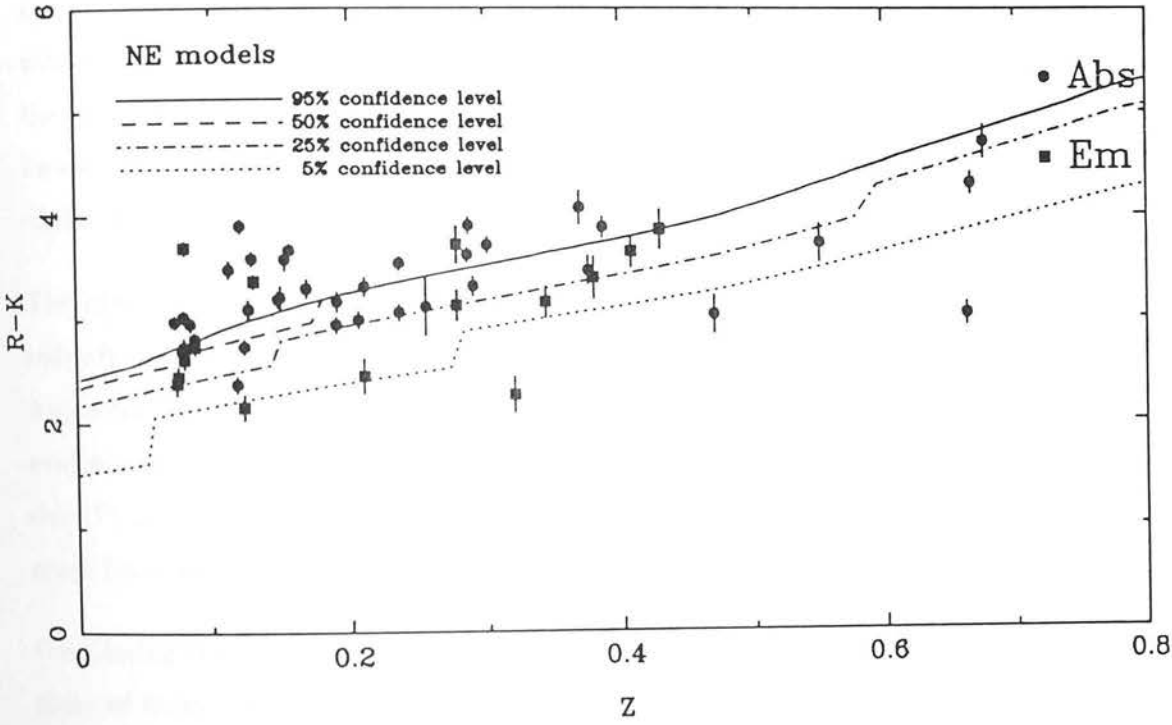

Fig. 6.9b The expected colour range as a function of redshift calculated for the non-evolving RVG models with a $13 < K < 17.5$ selected sample.

This is shown in figure 6.9b for comparison. It can be seen that the confidence levels follow the model tracks with jumps between them. It is easy to see why this happens. Initially the 5% contour might lie on one type, then as redshift increases the fraction of *observed* galaxies in the type drops below the 5% level and the 5% curve jumps to the next type. It is easy to interpolate by eye and see where these curves would lie if the model distributions were smooth rather than delta functions. These curves are for a K selection of $13 < K < 17.5$, changing the K limits around has only a very minor effect on the contours.

6.4.1 The bluest galaxies

How well do the colours of the real galaxies match the non-evolving prediction? Considering blue galaxies there are two galaxies whose colours are significantly bluer than the non-evolving model. One is an emission line object, OCTKR#323 ($z = 0.3205$, $R - K = 2.27$) (see Appendix B for plot) with an unambiguous redshift from strong Hβ, [OII] 3727 Å and [OII] 5007 Å lines. If we assume a value for $\Omega_0 = 1$ and take a K-correction from the RVG new UV-hot elliptical model an absolute K magnitude of -22.4 is obtained, about 1 magnitude fainter than M_K^*. So this would be consistent with a blue compact dwarf galaxy with a small amount of star formation blueing the $R - K$ colour. The $R - K$ colours of the new RVG models undergoing luminosity evolution are shown in figure 6.10a. It can be seen that this brings down the colours of the median of the galaxy population to those of this object.

The other blue object OCTKR#363 ($z = 0.663$, $R - K = 3.04$) has a more dubious redshift based largely on a 4000 Å break and possible H and K absorption lines (again see Appendix B). For an object this much bluer than the non-evolving prediction there is no evidence of any strong emission lines. Also the absolute magnitude (-24.5) and image size ($7'' \equiv 70h^{-1}$kpc) are rather large. It is quite plausible that this object could be at a much lower redshift with rather weak absorption features.

Considering the other galaxies on the blue envelope (5%–25% contour) it can be seen that many of them are emission line objects, as might be expected. Over the entire survey it

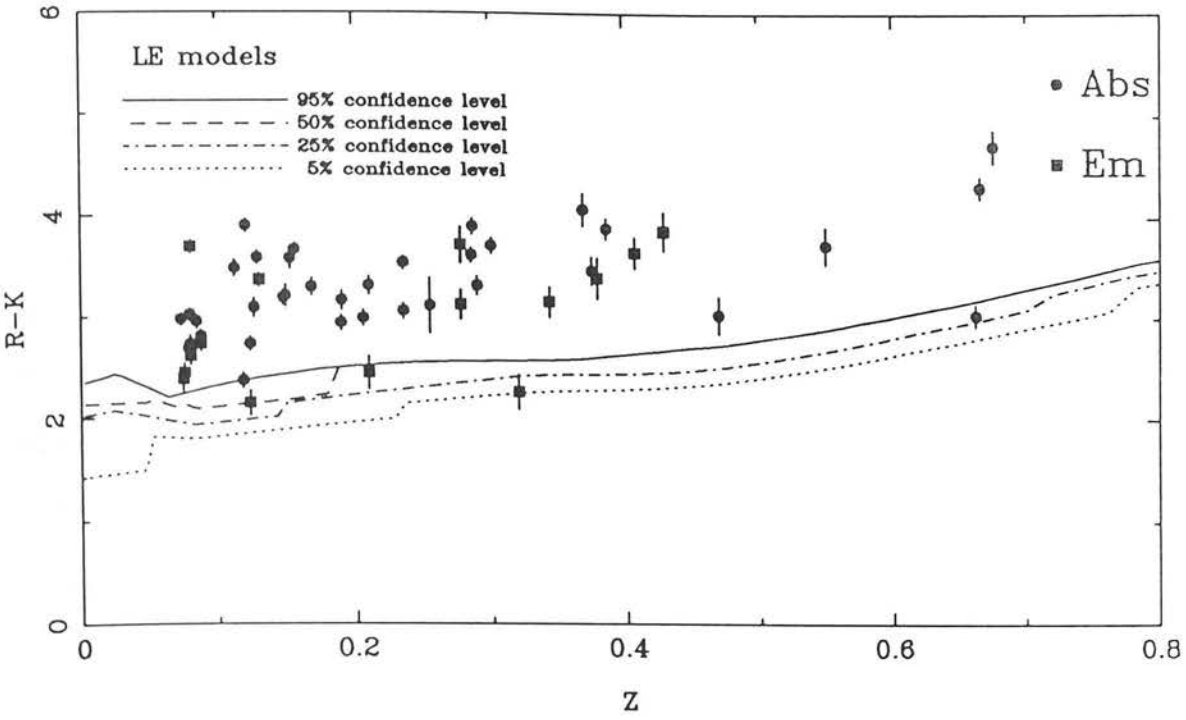

Fig. 6.10a The expected colour range for the evolving models of RVG (with $z_f = 30$, $H_0 = 50\,\mathrm{km\,s^{-1}\,Mpc^{-1}}$, $\Omega_0 = 1$) compared with the data.

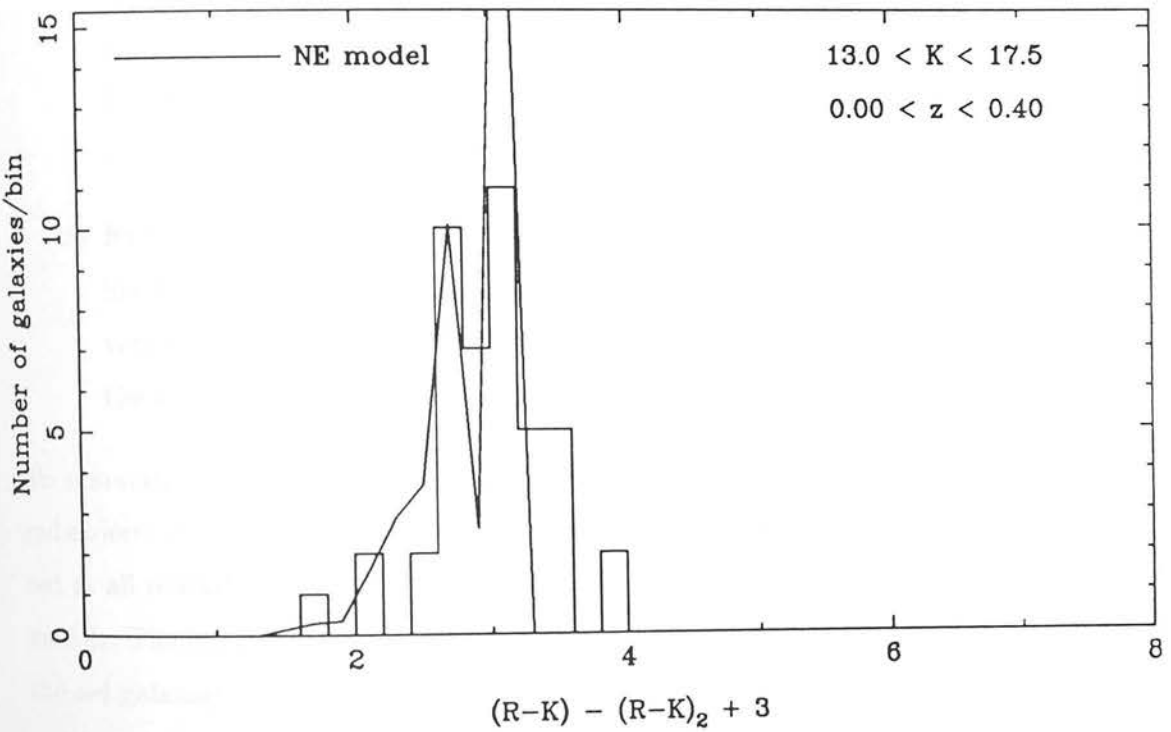

Fig. 6.10b The R – K colour (relative to UV-hot elliptical) distribution of the redshift data.

appears that 16 objects (30%) have emission lines of some kind.

6.4.2 The reddest galaxies

The other striking feature of figure 6.9b is the large number of red galaxies. This would be expected given the colour-magnitude distributions, however it appears that the excess is worse at *low redshift* by up to 1 magnitude in R – K. If one turns to luminosity evolution models such as in figure 6.10a then the discrepancy is even worse.

Could this effect have arisen from some kind of selection effect? There are several to be considered:

1) **R flux limit.** The redshift sample is limited to an R magnitude limit which varies from field to field (see section 4.5 for more details). However this has the wrong sign, it makes the data *blue-biased* as the reddest objects in each field remain unidentified.

2) **LDSS priority.** The LDSS selection was slightly biased in favour of very red objects by including at high priority objects with $R - K > 4$. However very few of these were identified, and the red excess at low redshift is actually in the range $3 < R - K < 4$ where this is inapplicable. In addition objects with $R < 21$ were given preference, this has the opposite effect and again blue-biases the sample.

3) **Redshift incompleteness** Are there redshift ranges in which objects are hard to identify in the spectral windows used? Certainly absorption line redshifts become very difficult at $z \gtrsim 0.8$ as the 4000 Å break, H and K lines get redshifted out of the window. But this does not apply at low redshifts.

To summarise most of the effects considered seem work in the wrong direction, removing red objects at *high* redshift. Of course it is possible that the entire galaxy population is too red at all redshifts, and that the entire galaxy population is too red for the non-evolving models. The issue of incompleteness is addressed further in 6.5.1. For now the problem of the red galaxies at $z < 0.4$ will be considered.

Figure 6.10b shows a comparison of the observed and model non-evolving distributions for $z < 0.4$. This time the cross-section is plotted, i.e. the R – K histogram for the galaxies

with redshifts. To make the red excess clearer at each redshift the R – K colour of the UV-hot elliptical is subtracted from the data and the models, with a constant of 3 added for convenience. Thus the ellipticals appear as a spike at $(R-K)_{rel} = 3$ and the other models are smeared out into a distribution. It can be seen that the blue tail and mode of the distribution is roughly correct, however there is a tail of *low redshift* red galaxies to be accounted for.

6.4.3 Reddening due to dust

An important question about the red galaxies is whether or not the redness in the R – K colour is correlated with any redness in the optical. This would be expected if the reddening arose from dust extinction. This is the only simple origin which is easy to model — the spectral evolution models were provided as data rather than programs so there is not the freedom to experiment with their parameters. Unfortunately, as most of the galaxies with redshifts are in the October fields, only 15/53 of the galaxies have B magnitudes and hence B – R colours. These define a complete sample, even though the multicolour survey is incomplete in B, because the spectroscopic sample is that much brighter, with a median K magnitude of $\sim$ 16. Those objects without B magnitudes lack them because they are in areas not surveyed in B, not because they are too red.

The (B – R, R – K) colour-colour diagram for the redshift sample is shown in figure 6.11a. Note there is an apparent correlation between redness in B – R and redness in R – K. However this correlation is misleading, as both are correlated with a third parameter, the redshift. Both B – R and R – K are expected to get redder with redshift in a non-evolving model.

One can do better than this by using the redshift information, rather than ignoring it. Figure 6.11b shows the same diagram, but this time plotted relative to a non-evolving burst model, from RVG, which supposedly defines a red envelope. Each galaxy has the colours of the model, at its redshift, subtracted from it and this *difference* is plotted. The extreme object at the lower left is OCTKR#363, which as mentioned in section 6.4.1 probably has an incorrect redshift. It can be seen that the burst model does indeed define a red envelope in B – R, although the number of points is small it is clear that the correlation between redness in B – R and R – K is reduced. Applying a simple Spearman Rank Correlation

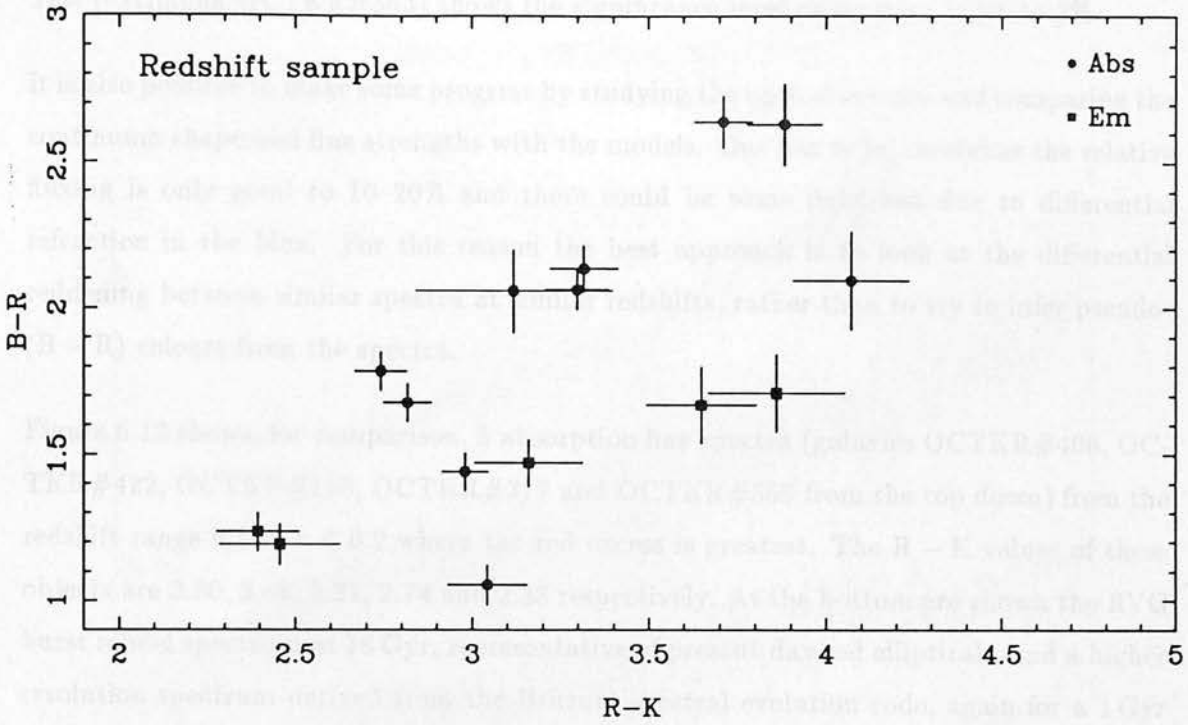

Fig. 6.11a The (B − R, R − K) colour-colour diagram for the 15 galaxies in the redshift sample with B magnitudes.

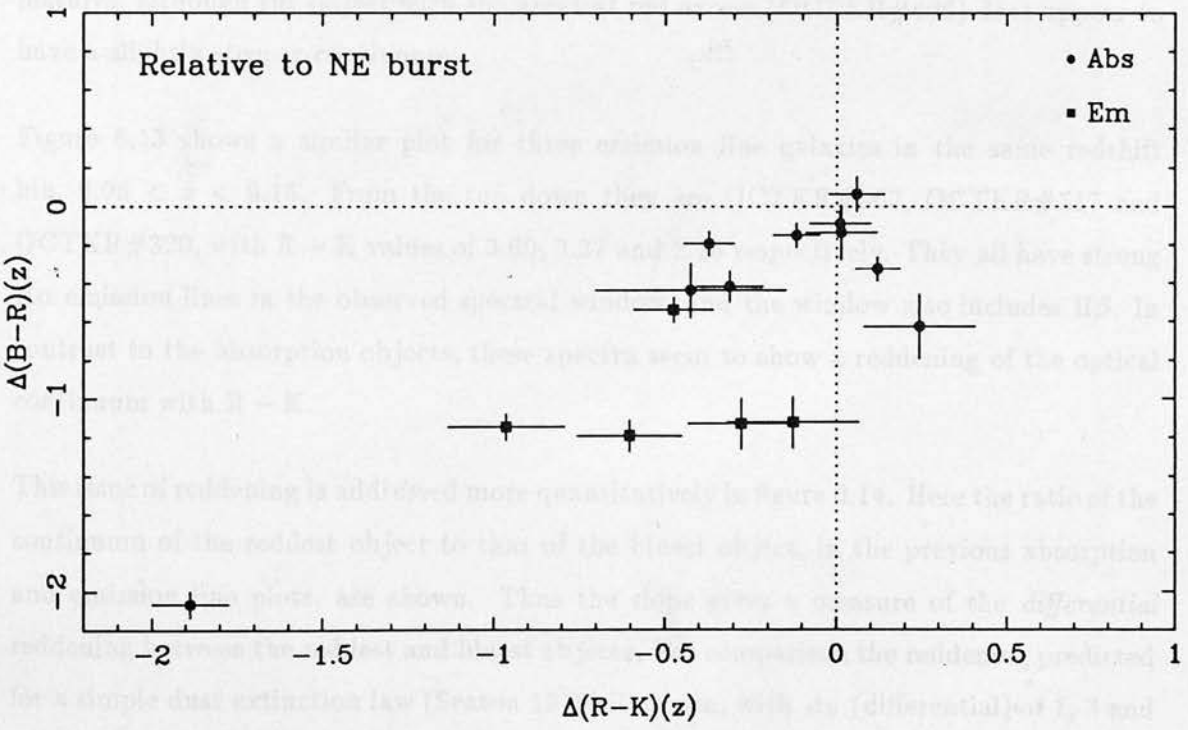

Fig. 6.11b As (a) but this time relative to the colours of a "red envelope".

Test (excluding OCTKR#363) shows the significance level drops from 0.5% to 3%.

It is also possible to make some progress by studying the optical spectra and comparing the continuum shape and line strengths with the models. One has to be careful as the relative fluxing is only good to 10–20% and there could be some light lost due to differential refraction in the blue. For this reason the best approach is to look at the differential reddening between similar spectra at similar redshifts, rather than to try to infer pseudo-(B – R) colours from the spectra.

Figure 6.12 shows, for comparison, 5 absorption line spectra (galaxies OCTKR#406, OCTKR#422, OCTKR#169, OCTKR#317 and OCTKR#558 from the top down) from the redshift range $0.1 < z < 0.2$ where the red excess is greatest. The R – K values of these objects are 3.90, 3.48, 3.21, 2.74 and 2.38 respectively. At the bottom are shown the RVG burst model spectrum at 16 Gyr, representative of present day red ellipticals, and a higher resolution spectrum derived from the Bruzual spectral evolution code, again for a 1 Gyr burst at 16 Gyr. These model spectra change little between 10 and 20 Gyr and have R – K colours of 2.46 and 2.42 respectively. It can be seen that despite the variation in R – K by 1.5 magnitudes all the spectra are remarkably similar in slope and strength of the spectral features, although the object with the greatest red excess (OCTKR#406) does appear to have a slightly steeper continuum.

Figure 6.13 shows a similar plot for three emission line galaxies in the same redshift bin, $0.05 < z < 0.15$. From the top down they are OCTKR#563, OCTKR#517 and OCTKR#320, with R – K values of 3.69, 3.37 and 2.16 respectively. They all have strong Hα emission lines in the observed spectral window, and the window also includes Hβ. In contrast to the absorption objects, these spectra seem to show a reddening of the optical continuum with R – K.

This issue of reddening is addressed more quantitatively in figure 6.14. Here the ratio of the continuum of the reddest object to that of the bluest object, in the previous absorption and emission line plots, are shown. Thus the slope gives a measure of the *differential* reddening between the reddest and bluest objects. For comparison the reddening predicted for a simple dust extinction law (Seaton 1979) is shown, with A_V (differential) of 1, 3 and 5 magnitudes. It can be seen that an $A_V \sim 1$ matches the reddest absorption line galaxies (relative to the bluest) while a much larger value of $A_V \sim 3$ is required for the emission

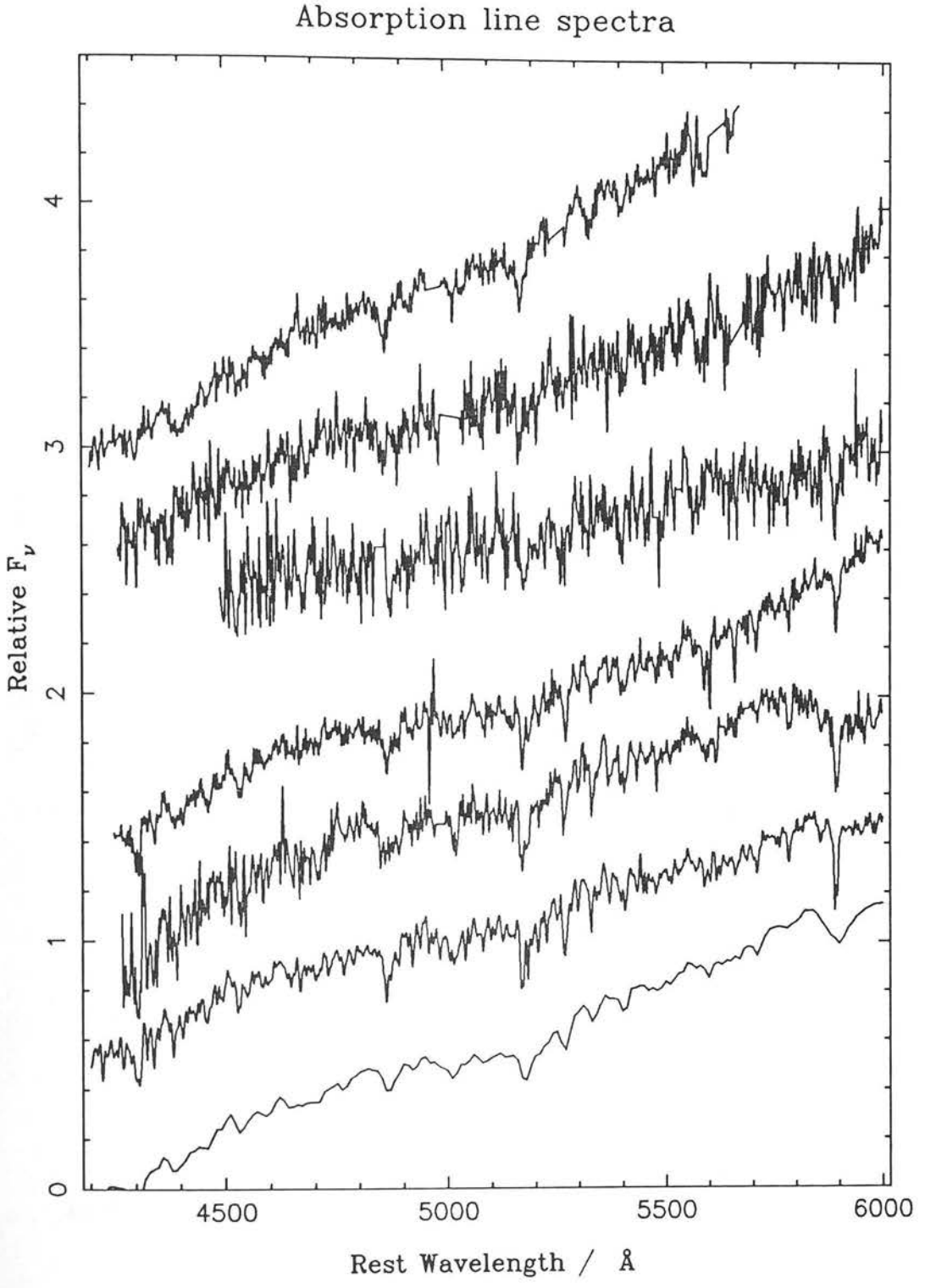

Fig. 6.12 Comparison of 5 absorption line spectra with $0.1 < z < 0.2$ and $3.90 > R - K > 2.38$ (from top down). The lowest spectrum is the RVG burst at 16 Gyr and the one immediately above is the equivalent Bruzual model spectrum.

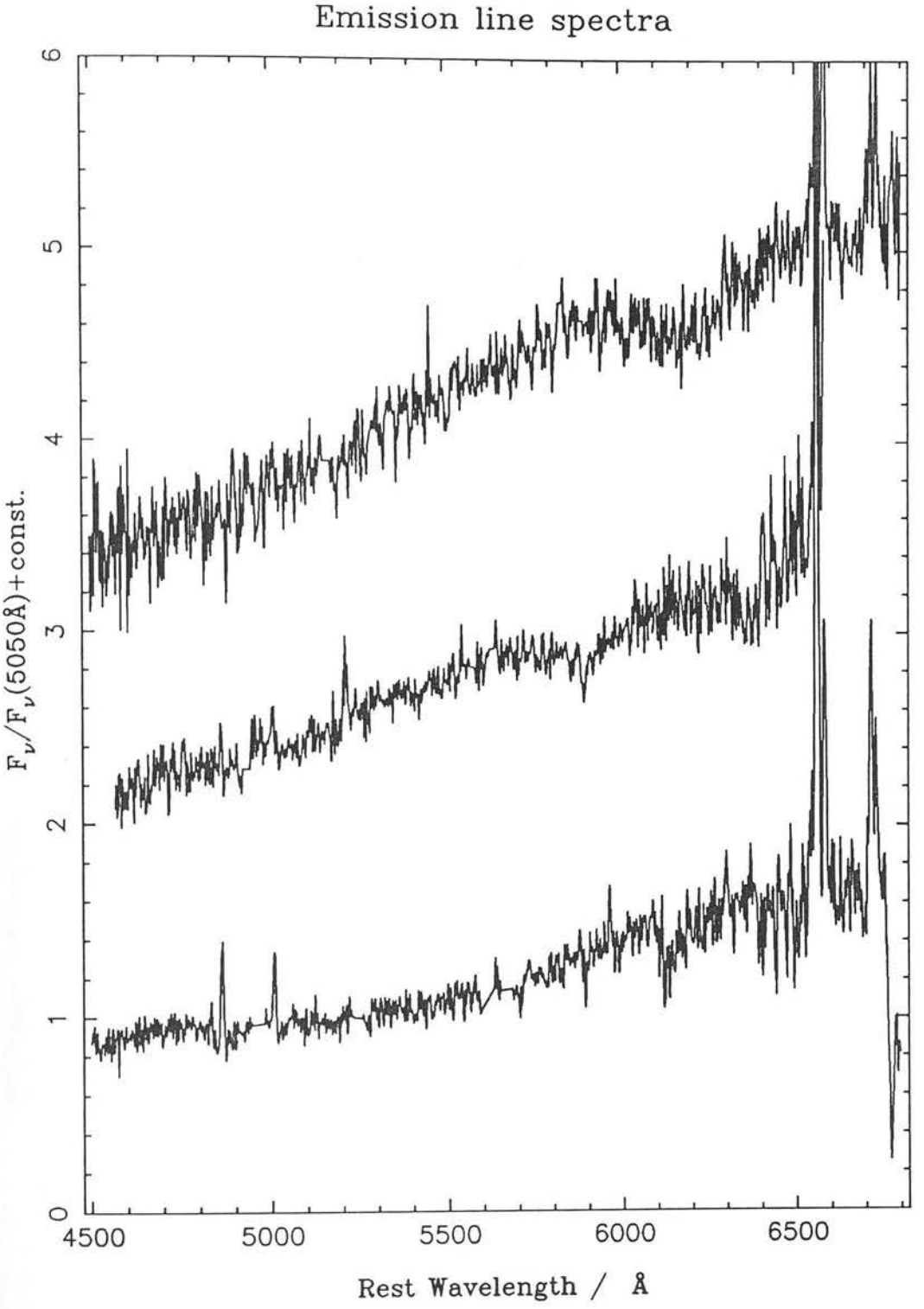

Fig. 6.13 Comparison of 3 emission line spectra with $0.05 < z < 0.15$ and and R − K of 3.69, 3.37 and 2.16 (from top down).

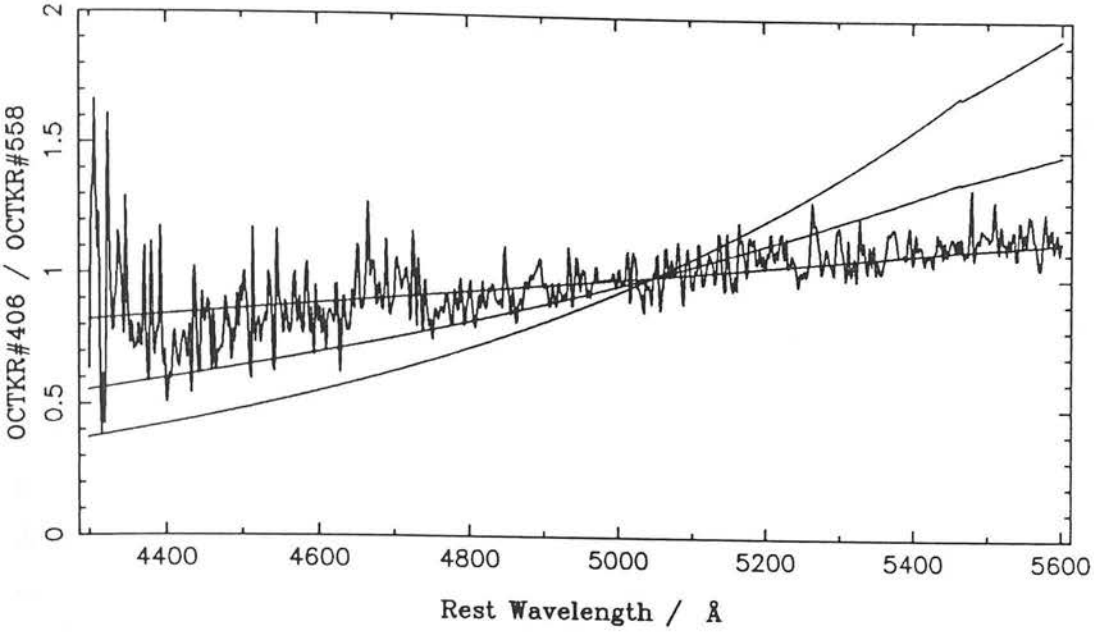

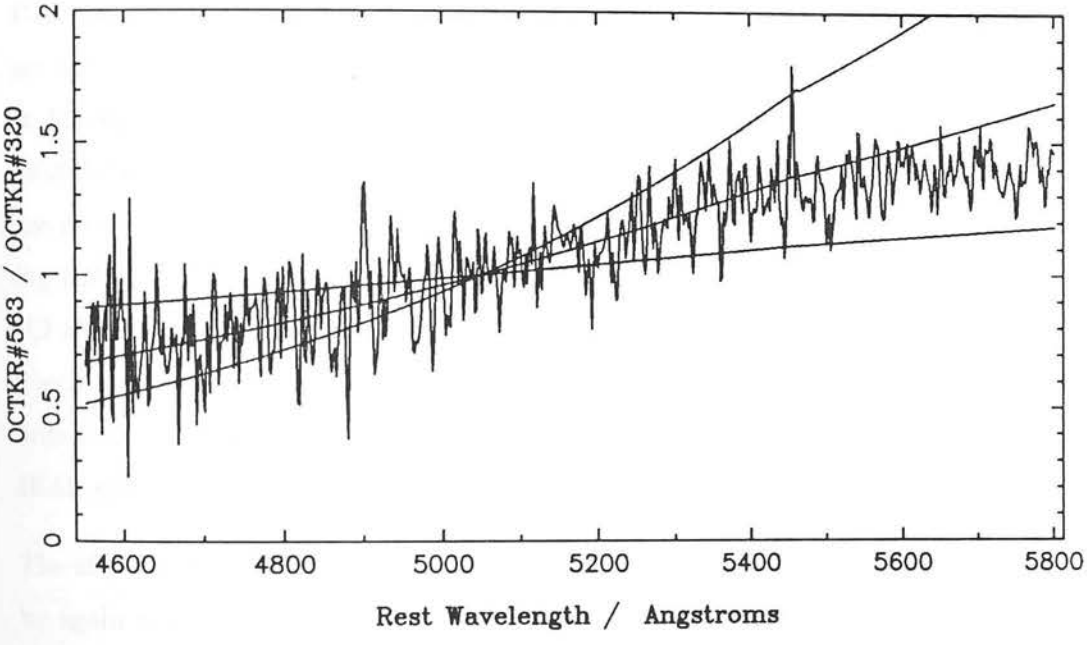

Fig. 6.14 Ratio of red and blue absorption (top) and emission line (bottom) galaxies compared with progressively steeper dust reddening laws with A_V of 1, 3 and 5 respectively.

Table 6.3: Extinction values for emission line galaxies in figure 6.13

Object	Hα/Hβ	A_V	A_V corr
OCTKR#563	> 14	> 4.6	> 2.7
OCTKR#517	31 ± 11	6.9 ± 0.3	4.9 ± 0.3
OCTKR#320	10 ± 2	3.8 ± 0.2	1.7 ± 0.2

line objects. Using the same model the corresponding differential extinction in the K and R bands can be computed, as $\Delta(R - K) = 0.64 A_V$. Thus for the absorption galaxies the difference in R – K extrapolated from the optical continuum reddening, if this was due to dust, comes to 0.64 magnitudes whereas 1.4 magnitudes is observed. Thus it appears unlikely that this reddening is due to dust alone. In contrast the optical reddening for the emission line galaxies predicts $\Delta(R - K) = 1.9$ magnitudes which is similar to the 1.5 magnitudes observed, given the uncertainties.

One can also try to estimate reddening by measuring the Hα/Hβ line ratios in these galaxies and comparing with the theoretical case-B values appropriate to HII regions (Hummer & Storey, 1987). This gives a value of 2.85 with standard conditions of 10 000 K and 10 000 $e^- m^{-3}$. For the galaxies shown in figure 6.13 the line ratios and extinction values are given in table 6.3. Hβ fluxes tend to be underestimated due to the effect of underlying Hβ absorption which is negligible for Hα. This is a *large* correction, taking a typical Hβ absorption equivalent width of 4 Å (for IRAS galaxies which have similar spectra, see Leech *et al.* 1989) the Hβ flux is doubled. The corrected A_V values are shown in the table, note that these are very approximate. They inhabit the upper end of the range found in IRAS galaxies (again, see Leech *et al.*).

The effect of this, and of differential refraction which has a similar effect, can be reduced by again just considering the *differential reddening* between spectra. For OCTKR#517 relative to OCTKR#320 a continuum value of $A_V \simeq 2$ is inferred in a similar way as in figure 6.14, this should be compared with the value $A_V = 3.1$ deduced from the line ratios. It is not unexpected that the reddening of the lines would be greater than that deduced from the continuum, this is commonly found in IRAS and starburst galaxies where the

star forming and line emitting regions are shrouded in dust.

To summarise there is little evidence to suggest that the optical-infrared redness observed in the bulk sample is correlated with optical redness. This rules out a simple model, such as dust absorption, which would redden both the B – R and R – K colours. However there are a few extreme emission line objects whose red R – K colours and optical continua can be explained by applying dust reddening to bluer examples.

This implies that the most likely answer is yet another problem with the spectral evolution models, this time in the optical-infrared colours. To resolve this issue spectrophotometry over a wide wavelength range is needed for comparison with the model spectra from the optical to the near infrared.

6.5 The Redshift Distribution

The redshift distribution of survey galaxies provide a complementary tool to the number-magnitude counts described in chapter 5. Galaxy counts alone provide a poor discriminant between cosmological models because the galaxies are seen in projection; no distinction can be directly made between bright galaxies faraway and nearby dwarf galaxies except via models. By measuring redshifts one obtains luminosities; the redshift distribution can then discriminate between models to which the galaxy counts are insensitive. For example, as has already been discussed, the Broadhurst *et al.* and Colless *et al.* redshift surveys have effectively ruled out simple models of luminosity evolution to explain the b_j count excess.

6.5.1 Completeness — the V/V_{max} test

Before discussing the modelling of the redshift distribution it is important to assess the completeness of the redshift survey in a more quantitative way. It is already apparent from section 4.4.4 that we already have a survey jointly limited, of necessity, in the K and R bands, with a R limit which varies from field to field. There is also the possibility of redshift limits imposed by the spectral windows used on each object.

A powerful method of assessing the completeness in flux limited surveys is the V/V_{max} test originally developed by Schmidt (1968) in conjunction with quasar surveys. In its simplest and extended by Rowan-Robinson (1968, 1969)

Table 6.4: V/V_{max} results with different options

No.	Type	n_{obj}	$< V/V_{max} >$	$\sqrt{12}\,\sigma$	K-S prob.
1	$10 < \mathrm{K} < 17.5$, applying R limits in each field, excluding K7 cluster and $\Omega_0 = 1$.	41	0.490	1.024	0.972
2	(1) with spectral window enabled.	41	0.517	1.050	0.739
3	(1) with K7 cluster included.	48	0.424	1.096	0.145†
4	(1) with $\Omega_0 = 0$.	41	0.485	1.019	0.946
5	(1) with no R limits applied.	41	0.199	0.672	1.7×10^{-9}
6	(1) with $10 < \mathrm{K} < 19$ selection.	41	0.482	1.041	0.968
7	(1) with $10 < \mathrm{K} < 16$ selection and no R limits applied.	29	0.445	0.964	0.514
8	(1) with RVG LE and $\Omega_0 = 1$, $H_0 = 50\,\mathrm{km\,s^{-1}\,Mpc^{-1}}$ and $z_f = 30$.	41	0.462	0.966	0.827

† On field K7 alone, $\langle V/V_{max} \rangle = 0.180$, K-S probability $= 2.5 \times 10^{-5}$.

---

form, one measures the flux and redshift z of an object and computes the maximum redshift z_{max} at which the object could have been placed and still be included in the survey, i.e. the redshift at which its flux falls below the survey limit. Then one calculates

$$\frac{V}{V_{max}} = \frac{vol(z)}{vol(z_{max})}$$

where $vol(z)$ gives the volume enclosed out to redshift z in a given cosmology. If the survey is truly unbiased, and the objects are not evolving, then the object could be randomly picked in the whole of the available volume. So if one computes the distribution of V/V_{max} for all the objects in the survey they should be uniformly distributed between 0 and 1, with average 1/2 and standard deviation $1/\sqrt{12}$. If there is any luminosity or number-density evolution in the sample then $V/V_{max} > 1/2$ as the objects are preferentially selected at the edge of the available volume.

The beauty of the V/V_{max} test is that it allows the inclusion of joint flux limits in a natural

way. The flux limit which is exceeded first is simply taken as defining the appropriate V_{max}. For this sample it also allows the possibility of testing the effect of the different spectral windows on the completeness. For each type of galaxy one can define a z_{max} at which spectral features usable to obtain a redshift are redshifted out of the observed window (note that these are different for each object).

Table 6.4 shows the V/V_{max} computations for differing options as to whether the field R flux limits, spectral windows, etc. are enabled. The mean and standard distribution are given for comparison with the expected values, the distribution is also compared with the theoretical uniform distribution using the Kolmogorov-Smirnov (K-S) test. This gives a probability that the data set was drawn from the theoretical distribution, based on the greatest difference between their respective cumulative distributions. Low values of the probability indicate that the data are unlikely to be uniformly distributed.

There are several important points to be drawn from the table, the numbers below correspond to those in the table (figure 6.15 shows graphically the V/V_{max} distributions in each field for (1) and (7)):

1) Applying the R limits in each field determined in section 4.4.4 gives a sensible result consistent with a uniform distribution. Note that this calculation excludes 5 objects in each field with $R > R_{lim}$, they cause the K-S probability to tend to asymptotically small values. A more complicated calculation would incorporate the identification function in a smooth way, but this would give similar results as only a few objects are affected. This method is a useful (and simple) approximation.

2) The spectral window was defined by classifying each galaxy and assigning a z_{max} according to type and *observed* wavelength range. For absorption line galaxies this was defined as redshifting the H and K lines out of the window, for galaxies with strong Hα lines and the bluer lines very weak this was defined by Hα, and for other emission line objects this was defined by Hβ as [OII]3727 Å was not relied on alone to deduce a redshift. In any case the effect of this extension can be seen to be negligible, this was expected as only a few galaxies were seen beyond $z = 0.6$.

3) There is an obvious cluster in field K7 at $z = 0.08 \pm 0.005$ accounting for 7/12 galaxies. This has little overall effect although the effect on K7 alone is large. Examination of the Schmidt plate for this field shows an obvious cD galaxy (catalogued

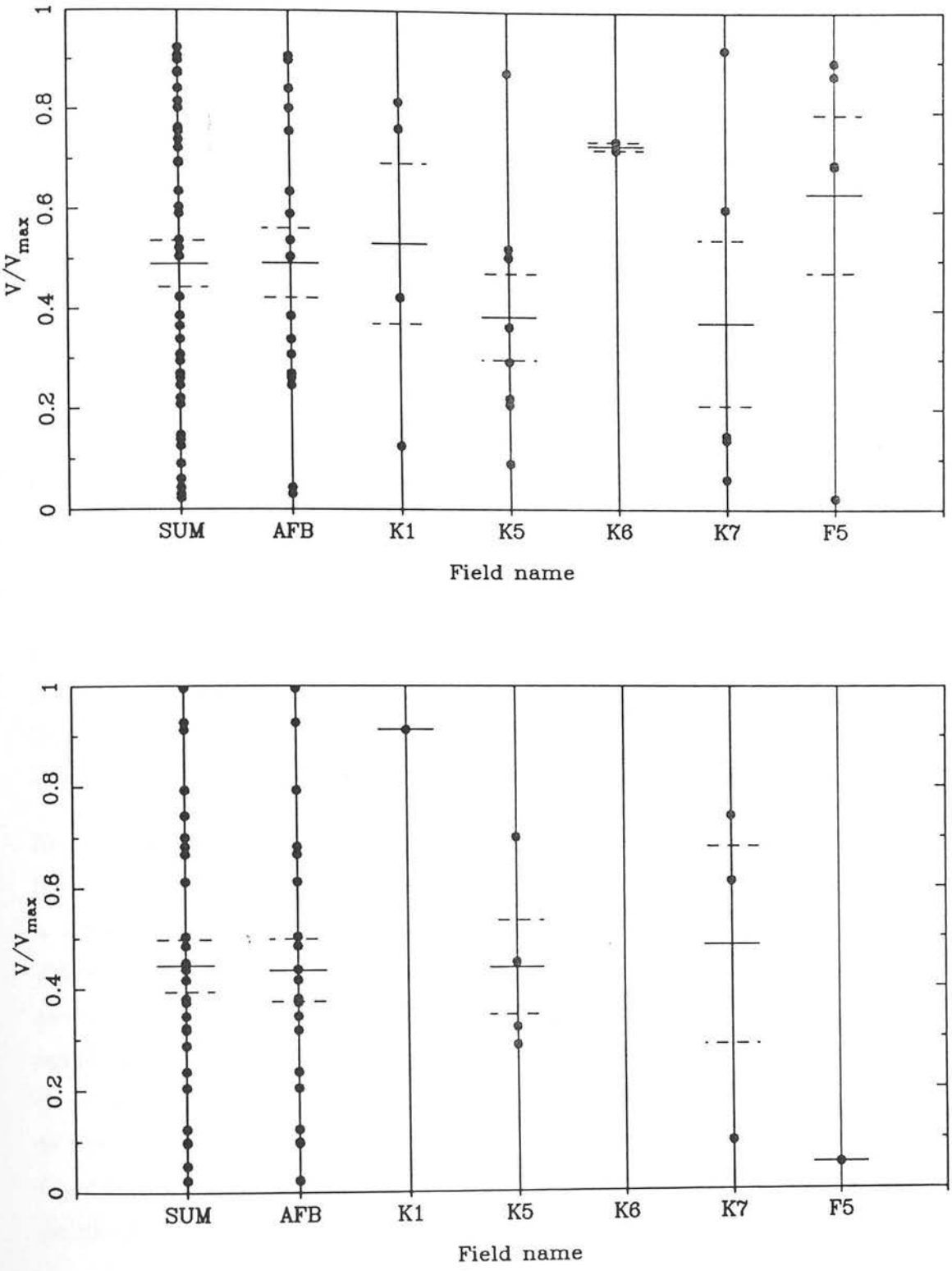

Fig. 6.15 The V/V_{max} distributions for each field computed according to options (1) (top) and (7) (bottom) in table 6.4. Mean values and errors on the mean are shown.

as MCG+00-06-002, $z = 0.0795$) a few arcminutes away.

4) At these low redshifts the effect of varying Ω_0 is negligible.

5) It is important to include the R limits correctly. If these are removed the V/V_{max} test is failed, showing that at K $\sim$ 17 the redshift survey is biased to blue objects.

6) At the faint end of the sample the actual choice of K limit has little effect: the V/V_{max} computation is dominated by the R band limits.

7) If a subsample is defined by K $<$ 16 then it is complete in R $-$ K colour; removal of the field R limits then has negligible effect.

There are some caveats to all this. Firstly the calculations depend on the spectral evolution models via the K and R band K-corrections. Note this *dependence* is differential in each band: it does not matter if the model R $-$ K colours are wrong, only $d(\mathrm{R}-\mathrm{K})/dz$ need be right. Secondly does the fact that the V/V_{max} test, using just the K-correction, gives sensible results rule out luminosity or number-density evolution? This can be tested by running the V/V_{max} test again, this time putting in a R-correction based on the spectral evolution models of RVG. These are known to have wrong colours, but as can be seen from the table (no. 8) this has little effect on V/V_{max}. This shows that although V/V_{max} is a good test for completeness, it is not necessarily the best test for evolution.

Nevertheless we can use the V/V_{max} to perform a simple test for luminosity evolution — it does have the advantage that it needs no knowledge of the luminosity function. V/V_{max} is actually a test for number-density evolution and luminosity evolution is regarded as *differential* number-density evolution, i.e. the number of low luminosity objects decreases and the number of high luminosity objects increases. What was done was to split the sample into two equal halves, separated by median absolute magnitude, use the K-S test as above to compare each with a uniform distribution, and use the two-sample K-S test to test the difference between the two data distributions. No significant difference was found between the two distributions, or between the two distributions and the uniform distribution.

6.5.2 Modelling of the redshift distribution

The two ingredients for the computation of the redshift distribution are basically the same as for the number-magnitude counts — the luminosity function and the K or R-correction. Using the results of section 5.3.1 we have

$$n(z) = \left(\frac{dV}{dz}\right) \int_{m_1}^{m_2} \phi(M(m,z))dm$$

for the number of objects per unit redshift at redshift z selected between observed magnitudes m_1 and m_2. $M(m,z)$ of course includes the distance modulus and K or R-corrections as defined in section 5.3.1. Also, as in the number-magnitude relation, $\phi(M)$ is a sum over differing luminosity functions for each galaxy type.

For a survey which is jointly limited in two magnitude ranges, such as K and R as we have here, the integrand can be simply modified to include a selection function which is 1 if $m_{\rm R} < {\rm R}_{\rm lim}$ and 0 otherwise. $m_{\rm R}$ is then computed from $m_{\rm K}$ by the model colours at a redshift z.

To deal with multiple flux limits in many fields $n(z)$ is calculated separately for each field and combined into a whole by weighting according to the number of *galaxies* in each field, this also ensures that the final $n(z)$ comes out normalised to the observed number of galaxies. The other alternative would be to weight by *area* in each field, which would have the advantage of testing the normalisation of the distribution as well. However the comparisons of the model distributions with the data presented here are only sensitive to the *shape* of the distributions and not their normalisations. In any case, the normalisation has already been tested by the number-magnitude counts models, the principal reason for having a redshift distribution is to measure its shape.

The approach taken here is to test the model distributions against the data using two very simple statistics. First the mean redshift is computed; here the fact that the mean is more sensitive to a high-redshift tail than the median is an advantage rather than a disadvantage as it was in the earlier data reduction chapters! Second the model is tested against the data using the Kolmogorov-Smirnov statistic which has already been introduced. This measures the maximum deviation between the model and data cumulative distributions; it has the advantage over the χ^2 statistic in that the data is not binned and is thus more sensitive.

The probability values derived from this should be treated cautiously, no allowance has been made in this calculation for the effect of clustering, large-scale structure, or even the controversial redshift spikes (Broadhurst *et al.* 1990). These are effectively convolved with the redshift distribution and make it lumpy, but the scale size of these are much less than that of the distribution width ($z \sim 0.2$ corresponds to $\sim 600\,h^{-1}\,\mathrm{Mpc}$). The effect will be to reduce the probabilities computed from K-S, however they will still be useful as a *relative* measure of the goodness of fit of different models. Finally, of course, there is no substitute for plotting out the data and comparing with the models by eye. No set of statistics can measure everything of interest in the data.

6.5.3 The no-evolution model

The no-evolution model is known to match the redshift distribution of optically selected samples down to $b_j = 22.5$ (see section 5.4.1), despite the large galaxy excess seen at this depth. How well does it match the K selected sample? The model is compared with the data in figure 6.16a. As for the number-magnitude models, the infrared K-correction is taken from the new RVG UV-hot model at 15 Gyr for all types. The data plotted is the sample shown to be complete in section 6.5.1 to K=17.5 and the field R band flux limits. Excluding the cluster in field K7, this consists of 41 galaxies. The data are shown binned in redshift intervals of $\Delta z = 0.025$, with minimal errors given by Poisson statistics. The model is calculated on a much finer grid. Two curves are plotted for $\Omega_0 = 1$ and $\Omega_0 = 0.1$. It can be seen that the effect of Ω_0 is minor; in the rest of this chapter Ω_0 is held fixed at 1. The statistical results are given in table 6.5, along with those from the rest of the models in this chapter. It can be seen that the no-evolution model is consistent with the data at the 5% level.

The effect of colour incompleteness must be considered. How sensitive is the no-evolution fit to the effect of the joint K,R limits? The R limits can be discarded by taking a colour complete sub-sample of 29 galaxies with $K < 16$. This is shown in figure 6.16b and compared with the corresponding no-evolution prediction without any R flux limits. It can be seen that this is as consistent with no-evolution as the deeper sample.

Another question to be addressed is what is the effect of the R – K colour excess described in section 6.4. This has an effect in the luminosity function as the M_K^* values are taken

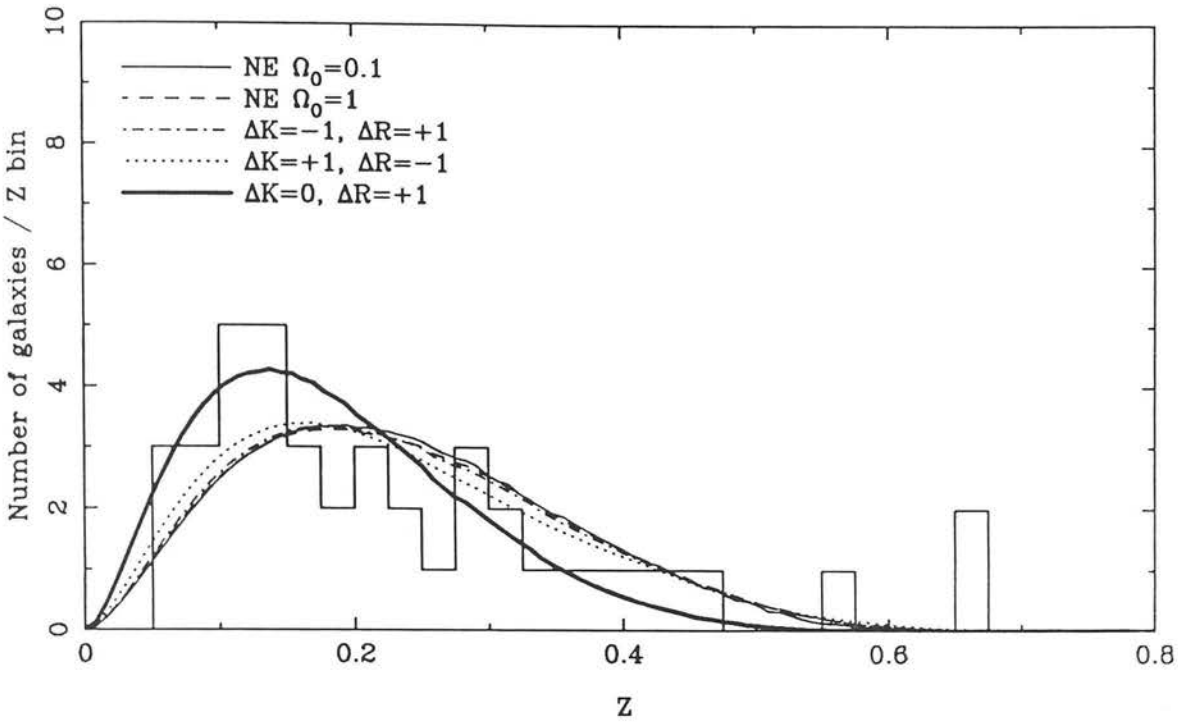

Fig. 6.16a No-evolution models and the $10 < K < 17.5$ K and R flux limited sample (41 galaxies).

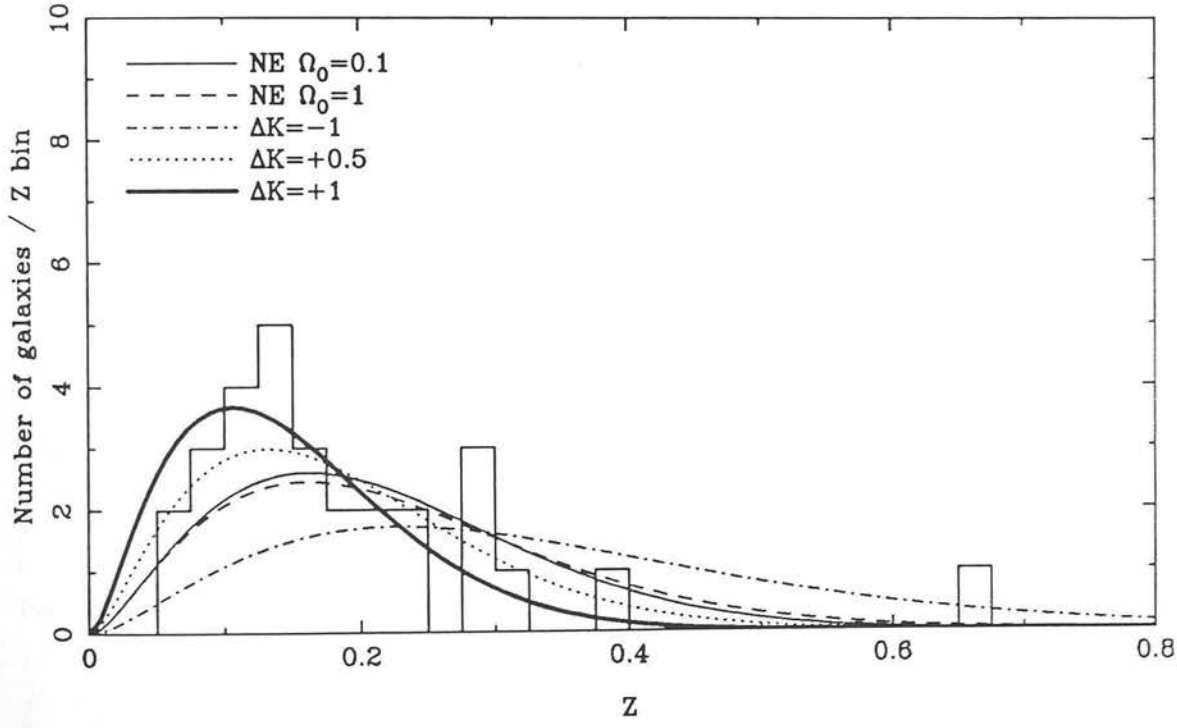

Fig. 6.16b No-evolution models and the $10 < K < 16$ colour complete sub-sample (29 galaxies).

Table 6.5: Comparison of number-redshift models with data

No.	Type	n_{obj}	$\overline{z}$	K-S prob.
1	$10 < \mathrm{K} < 17.5$, NE[1], K7 cluster excluded, $\Omega_0 = 1$ and field R limits.	41	0.241[4]	0.122
2	(1) with $\Omega_0 = 0.1$.	41	0.238	0.110
3	(1) with $\Delta\mathrm{K} = -1$, $\Delta\mathrm{R} = +1$.	41	0.238	0.153
4	(1) with $\Delta\mathrm{K} = +1$, $\Delta\mathrm{R} = -1$.	41	0.232	0.324
5	(1) with $\Delta\mathrm{K} = 0$, $\Delta\mathrm{R} = +1$.	41	0.187	0.355
6	$10 < \mathrm{K} < 16$, NE, K7 cluster excluded, $\Omega_0 = 1$ and no R limits.	29	0.228[5]	0.057
7	(6) with $\Omega_0 = 0.1$.	29	0.217	0.083
8	(6) with $\Delta\mathrm{K} = -1$.	29	0.322	1.6×10^{-5}
9	(6) with $\Delta\mathrm{K} = +0.5$.	29	0.187	0.661
10	(6) with $\Delta\mathrm{K} = +1$.	29	0.151	0.242
11	(1) with modified RVG R – K curves.	41	0.244	0.100
12	(11) with $\eta = 1.4$ LE[2]	41	0.287	0.007
13	(11) with $\eta = 2$ LE.	41	0.309	0.001
14	(6) with $\eta = 1.4$ LE.	29	0.312	1.1×10^{-4}
15	(6) with $\eta = 2$ LE.	29	0.357	1.2×10^{-6}
16	(11) with $\eta = 2$ ME[3]	41	0.214	0.379
17	(11) with $\eta = 4$ ME.	41	0.189	0.178
18	(11) with $\eta = 6$ ME.	41	0.169	0.015
19	(11) with $\eta = 7$ ME.	41	0.160	0.004
20	(6) with $\eta = 2$ ME.	29	0.181	0.597
21	(6) with $\eta = 4$ ME.	29	0.153	0.470
22	(6) with $\eta = 6$ ME.	29	0.134	0.081
23	(6) with $\eta = 7$ ME.	29	0.126	0.021

Notes

1) No-evolution.
2) Luminosity evolution with $L^* \propto (1+z)^{\eta}$.
3) Merging evolution with $\phi^* \propto (1+z)^{\eta}$, $L^* \propto (1+z)^{-\eta}$.
4) For sample data with this criterion $\overline{z} = 0.237 \pm 0.024$
5) For sample data with this criterion $\overline{z} = 0.191 \pm 0.022$

as the optical $M^*_{b_j}$ values minus a model $b_j - K$ colour. If the colours are wrong, then so are the M^*_K values and so is the count prediction. Is it possible to investigate the effects of this on the $n(z)$ modelling regardless of the actual cause of the redness?

There are two orthogonal possibilities. Firstly the K magnitudes of the objects could be too bright, with the R magnitudes unchanged. This is investigated in figure 6.16 by changing M^*_K. To do this self-consistently for the joint K and R limited sample one must simultaneously brighten K and redden R – K by the same amount. It can be seen that the effect of a K brightening is almost exactly cancelled by the effect of the R limit which biases the model distribution to bluer low redshift objects. This holds even if the brightening is extended to extreme values of $\Delta M^*_K = -5$. In contrast dimming by 1 magnitude does alter the distribution to lower redshifts, but not significantly.

So there is a problem that the effect of the joint K and R limit in the deep sample renders it rather insensitive to the exact value of M^*_K. It is possible to resolve this by considering the $K < 16$ sample which is effectively unbiased in R, resulting in the sample being more sensitive to changes in the K luminosity. Curves are shown in figure 6.16b for $\Delta M^*_K = -1$, 0.5 and 1 magnitude, it is evident that the trend in the data is to *fainter* K luminosities and *lower* redshifts with an effect of order $\sim$ 0.5–1 magnitude. It would be possible to vary ΔM^*_K and find the minimum value of the K-S probability, however this is strictly an invalid use of this statistic and formal errors on the best fit values could not be obtained. The use of the statistic here is merely to serve as a guide to the range of consistent models.

It seems that the tendency in K is in the wrong sense to explain the discrepancy in R – K, which makes the situation even more puzzling. The other possibility is that the R magnitudes of the models are incorrect. Obviously this can not be tested by the R unbiased $K < 16$ sample, but examining the $K < 17.5$ sample shows that adding 1 magnitude to the model R magnitudes does make the distribution more consistent with the data. Making the models redder means they have to be biased to lower redshifts to make the colours blue enough to fit within the R limits.

6.5.4 Towards an empirical colour picture

It is possible to see how much reddening of R is allowed by casting a look at the colour-magnitude distribution (figure 6.17) again. Just reddening R shifts the model colour distributions to the right from no-evolution, if we take reduced $\Delta\chi^2 \lesssim 1$ then this corresponds to $\Delta R \lesssim 0.2$ magnitudes, in all K magnitude ranges. A similar argument applies to ΔM_K^*: the effect is not just a simple shift because the luminosity function is being changed. The same criterion on $\Delta\chi^2$ gives $\Delta M_K^* \lesssim 0.3$ magnitudes, the limit being strongest in the $16 < K < 17$ bin.

It is also evident that the predicted distribution is much more sensitive to M_K^* than to R, so the preferred method of fixing the colours is to tinker with the R magnitudes of the models. In addition we know from the redshift distribution to $K < 16$ (section 6.5.3) that the observed M_K^* distribution indicates that M_K^* should not be brighter.

The effect that is needed to make the $R - K - z$ colours match is of order 1 magnitude (see figure 6.9). However, if we apply this naively the colour-magnitude distribution is completely wrong. But we need some *sensible* model for the $R - K$ colours in order to use the deep $K < 17.5$ redshift distribution to test evolution in the K band. Is it possible to compute the joint (K, R) limited $n(z)$ using the *observed* $R - K$ colours of the data?

A solution was found to this problem by applying an *empirical* fix to the model colours. If figure 6.9 is examined it can be seen that the discrepancy is greatest in the red envelope at *low* redshift ($z < 0.2$), at higher redshifts the model colours well match no-evolution. If an adjustment is made to redden the low redshift colours *only* this will have little effect on the colour-magnitude distribution as only a fraction of the galaxies are affected. The adjustment was done with an exponential functional form:

$$\Delta(R - K) = \Delta_i \, e^{-z/z_0}$$

The parameter z_0 was chosen so that the excess is reduced by half at $z = 0.1$ and Δ_i varied linearly with galaxy type i from 0, for Irregulars, to 1 magnitude for ellipticals. This has the effect of "bending up" the red envelope of the models to match the data at low redshifts, as can be seen in figure 6.17b. Figure 6.18a shows the resultant colour-magnitude distribution, the effect is minor and the χ^2 values are similar to those for the

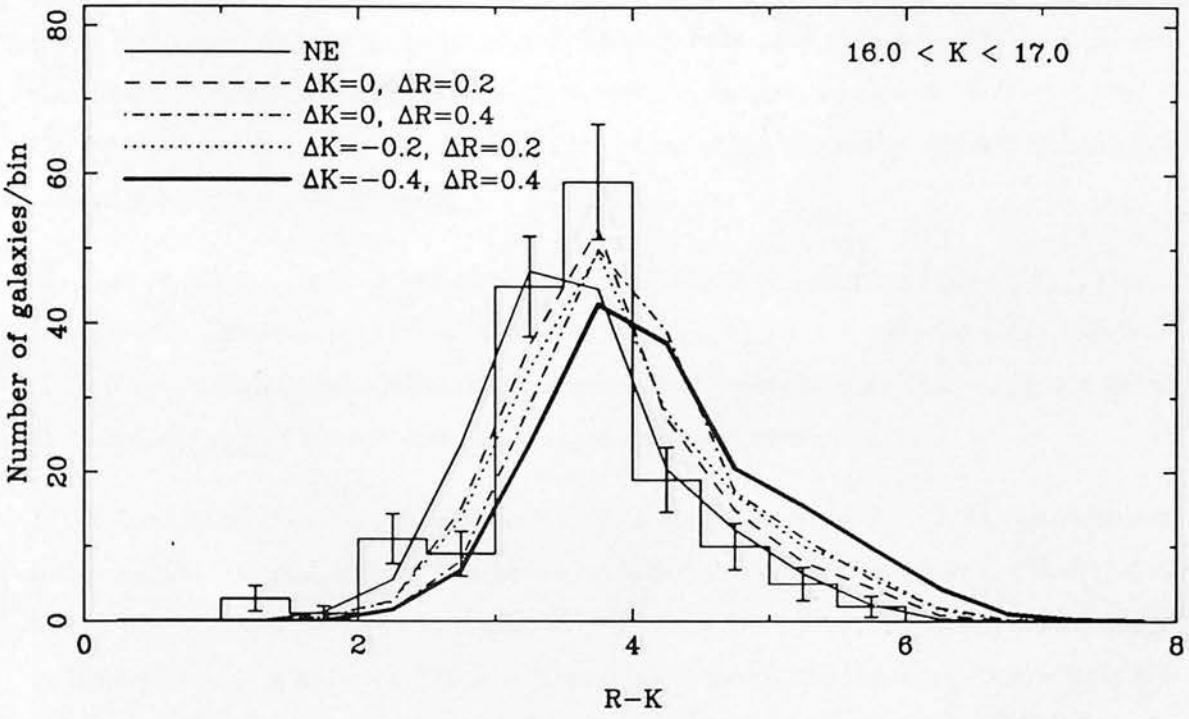

Fig. 6.17a The effect of varying the K and R magnitudes on the model fits to the colour-magnitude distribution.

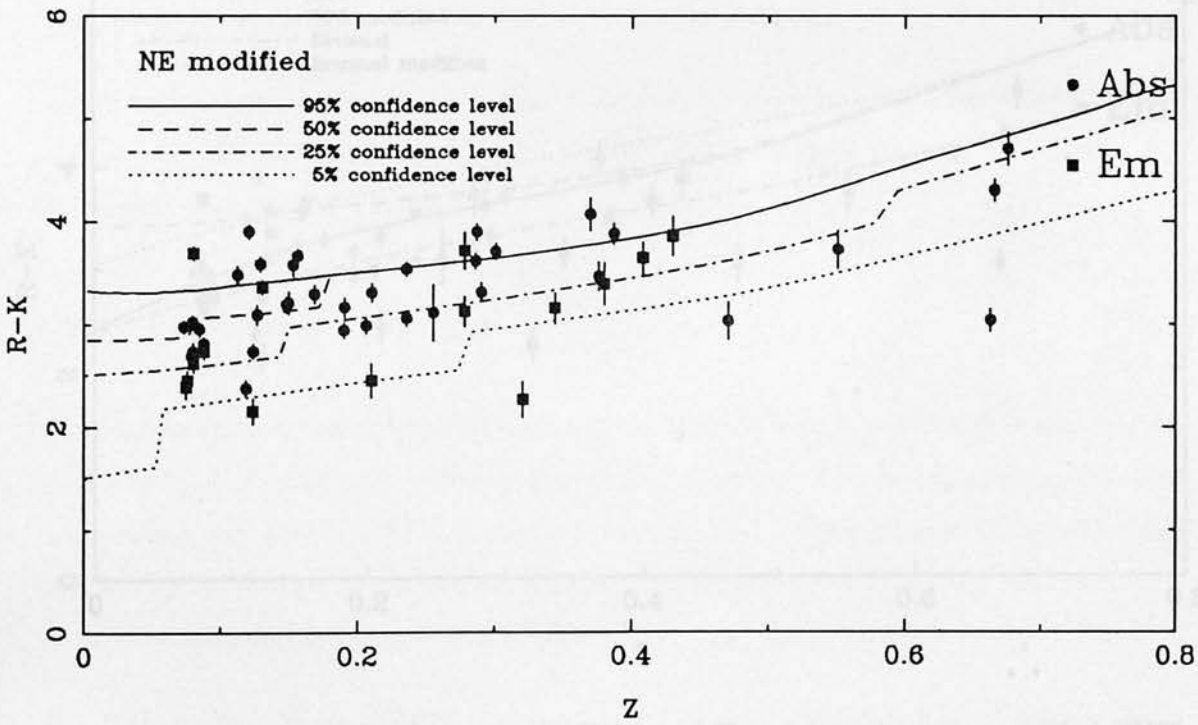

Fig. 6.17b The modified RVG models.

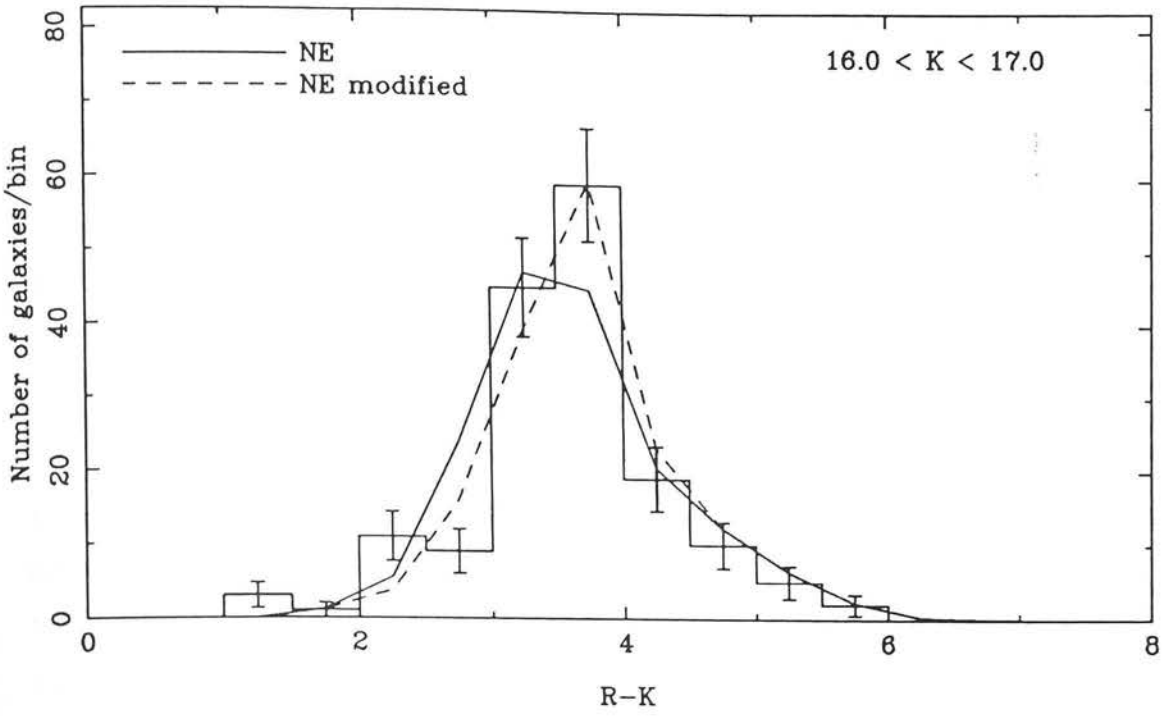

Fig. 6.18a A comparison of the colour-magnitude model distribution from the modified RVG no-evolution model with the old one.

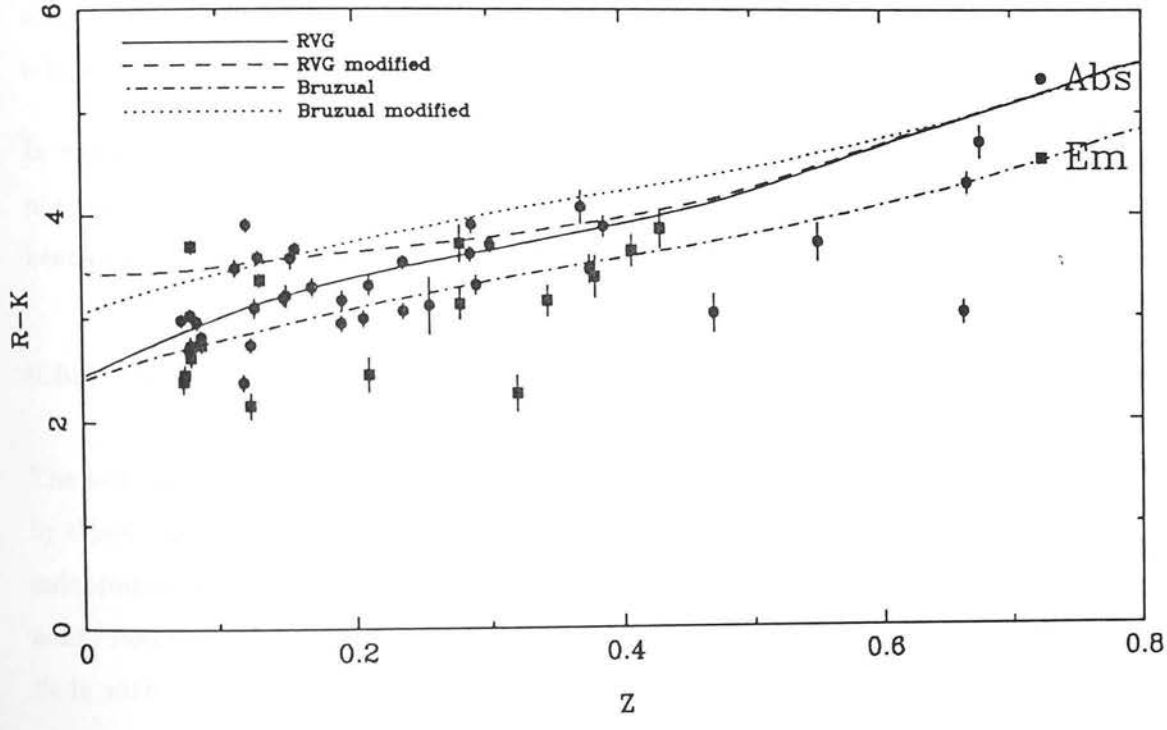

Fig. 6.18b A comparison between the RVG and Bruzual models, the modified RVG model has a similar slope to the reddened Bruzual model.

standard no-evolution model. The actual offset is taken as being in the R band rather than the K band, for the reasons given above. Thus it only affects the K = 17.5 sample and the effect is to lower the mean no-evolution redshift, the curve is shown in figure 6.19a. It can be seen that the actual effect of this modification on the model redshift distribution is negligible, despite the R limits.

Another important check is whether or not this affects the results of the V/V_{max} test of section 6.5.1. Repeating (1) from table 6.4 gives $\langle V/V_{max} \rangle = 0.490$, the same as before. Thus it appears that the modifications required to the standard RVG no-evolution model to match the $z \lesssim 0.2$ colours have little effect on model predictions.

Is this kind of modification within the plausible range of uncertainty of the spectral evolution models? In this scheme an elliptical galaxy has a similar colour at $z = 0$ as it does at $z = 0.3$, whilst in the old scheme the R − K colour has blued by about a magnitude. A Bruzual model is not as red in R − K as a RVG model and the slope of R − K vs z is less steep. This is shown in figure 6.18b which shows a raw RVG model, a RVG model reddened using the above scheme, a raw Bruzual model and a Bruzual model reddened by 0.65 magnitudes. The modified RVG model roughly matches a reddened Bruzual model, so it it reasonable to conclude that such a scheme is within the uncertainties. In fact this scheme can be regarded as a hybrid between the two models.

In any case the important thing is that this gives an empirical basis for computing the $n(z)$ in joint (K, R) limited samples. In the rest of this chapter this will be taken as the benchmark no-evolution model.

6.5.5 Luminosity evolution

The next issue to be considered is luminosity evolution, and how much it is constrained by this dataset. Luminosity evolution has already been tested for in a luminosity function independent way with the V/V_{max} test (see section 6.5.1). By folding in the model luminosity function though we do get an extra constraint (if only to reject it!) and we have a tie in with the number-magnitude counts.

The RVG models of luminosity evolution were not used because as has already been pointed out in section 5.4.2 there isn't any in the infrared. Instead the same parametric

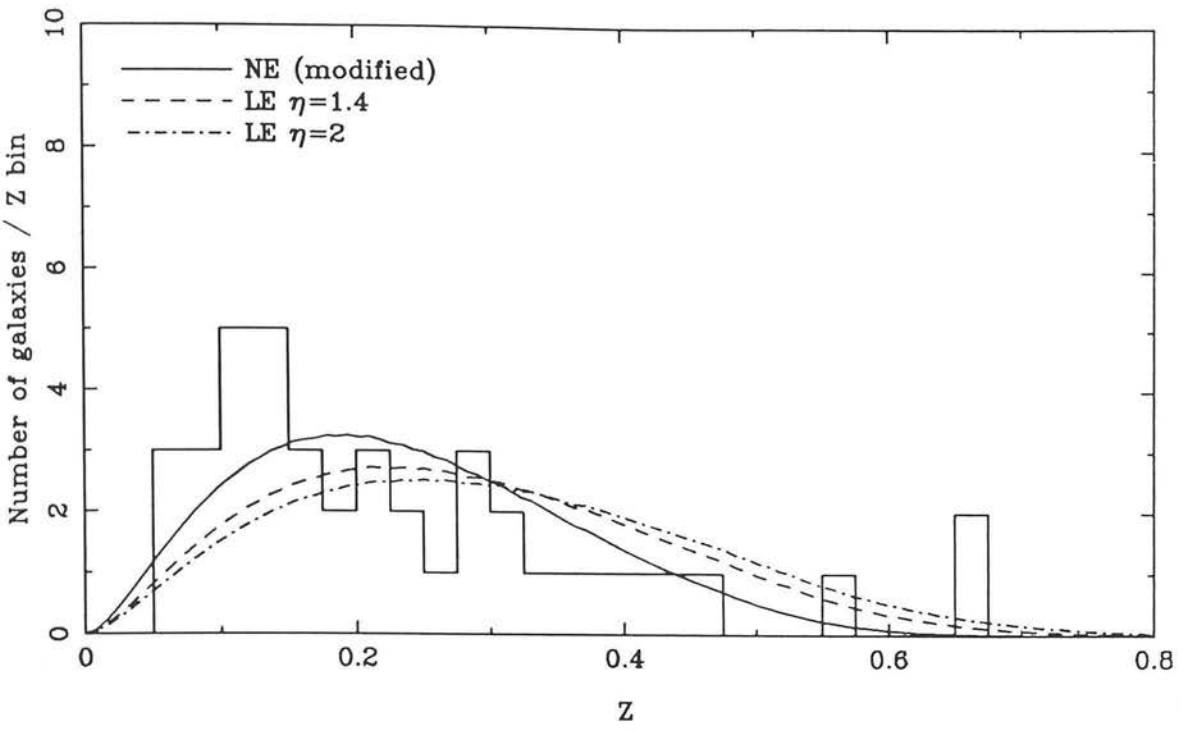

Fig. 6.19a Luminosity evolution models and the $10 < K < 17.5$ K and R flux limited sample (41 galaxies).

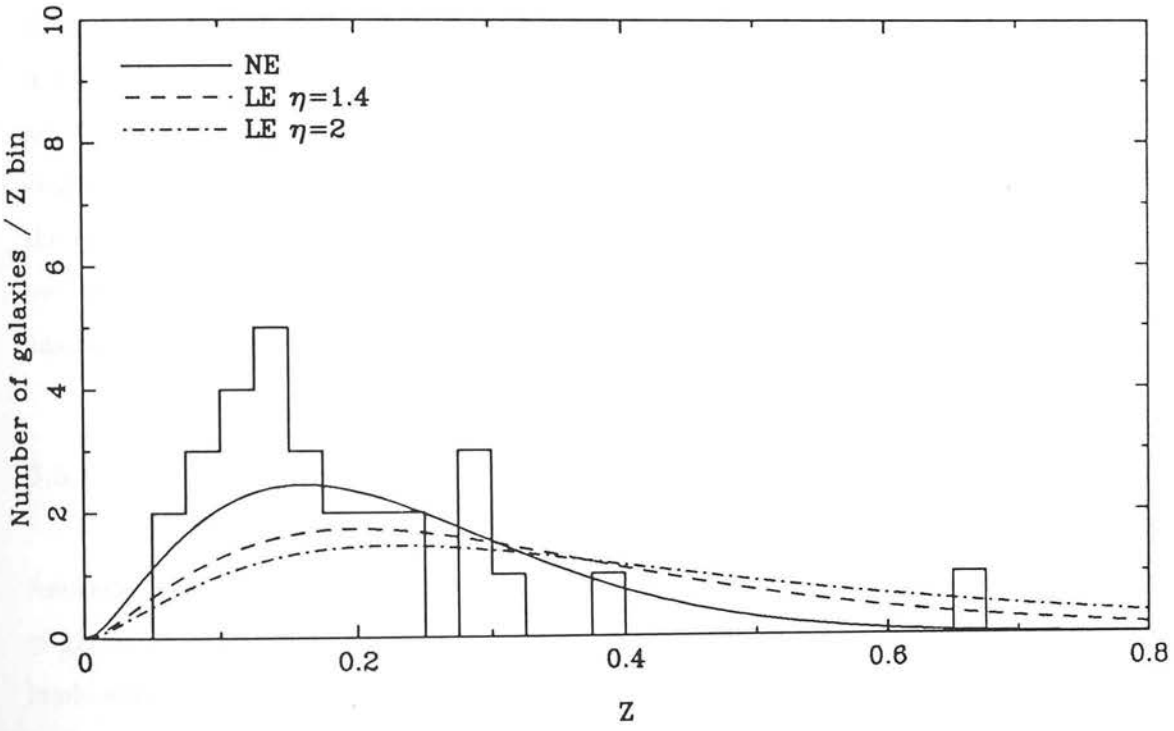

Fig. 6.19b Luminosity evolution models and the $10 < K < 16$ colour complete subsample (29 galaxies).

model of section 5.4.2 :

$$L^* \propto (1+z)^{\eta}$$

was tested for various values of η. The results are shown in figure 6.19 and table 6.5 for the $K < 16$ and $K < 17.5$ samples with $\eta = 1.4$ and 2 which produce 1 and 1.5 magnitudes of luminosity evolution by $z = 1$ respectively. As has already been discussed in section 5.4.2 evidence from the radio-galaxy population (Lilly & Longair 1984) shows a 1 magnitude K brightening by $z = 1$ which is attributed to passive evolution in their stellar populations, such an amount of luminosity evolution appears inconsistent with the K number counts (see section 5.4.2).

It is already apparent however from the results with no-evolution that the data favour slightly lower values of L^* and so we would expect luminosity evolution models to be even more strongly rejected, and this is indeed the case as can be seen from table 6.5. Also the rejection is *stronger* for the $K = 16$ sample than the deeper sample. Again this is because of the field R limits bringing the mean redshift down as the faint objects are biased towards the blue, this time the effect is *amplified* by the luminosity evolution.

Note these models only incorporate K band luminosity evolution without any *colour* evolution. Is this reasonable? Firstly for the $K < 16$ subsample this is irrelevant as there are no R limits. Secondly there is no evidence from the colour-redshift diagram for any colour evolution with respect to the models at the deepest redshifts. Although an empirical fix to the colours has been applied at low-redshift, the fact that after the fix the colours of the models match those of the data implies that the $n(z)$ for the joint (K, R) limited sample has been computed correctly.

6.5.6 Merging evolution

Another issue to be addressed is what is the effect of changes in the number density of galaxies with redshift? A model was developed (section 5.4.3) where the integral K luminosity was conserved with redshift on the basis that we could expect the K light to trace the mass:

$$\phi^* \propto (1+z)^{\eta}$$

$$L^* \propto (1+z)^{-\eta}$$

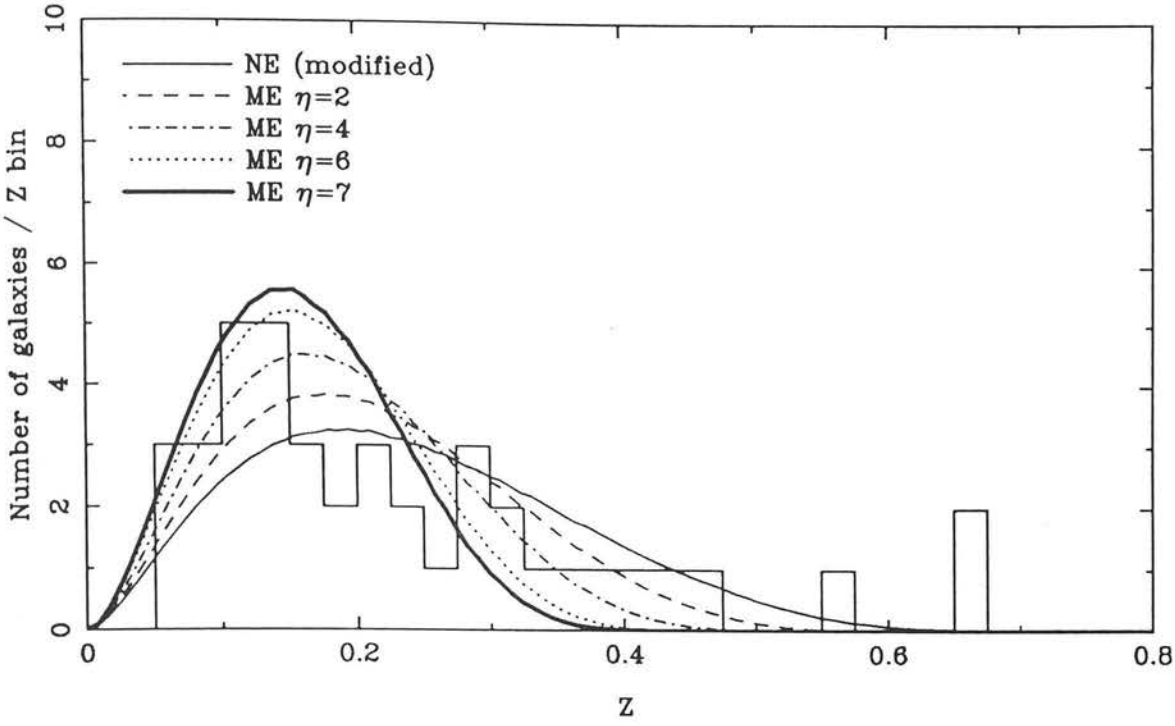

Fig. 6.20a Merging evolution models and the $10 < K < 17.5$ K and R flux limited sample (41 galaxies).

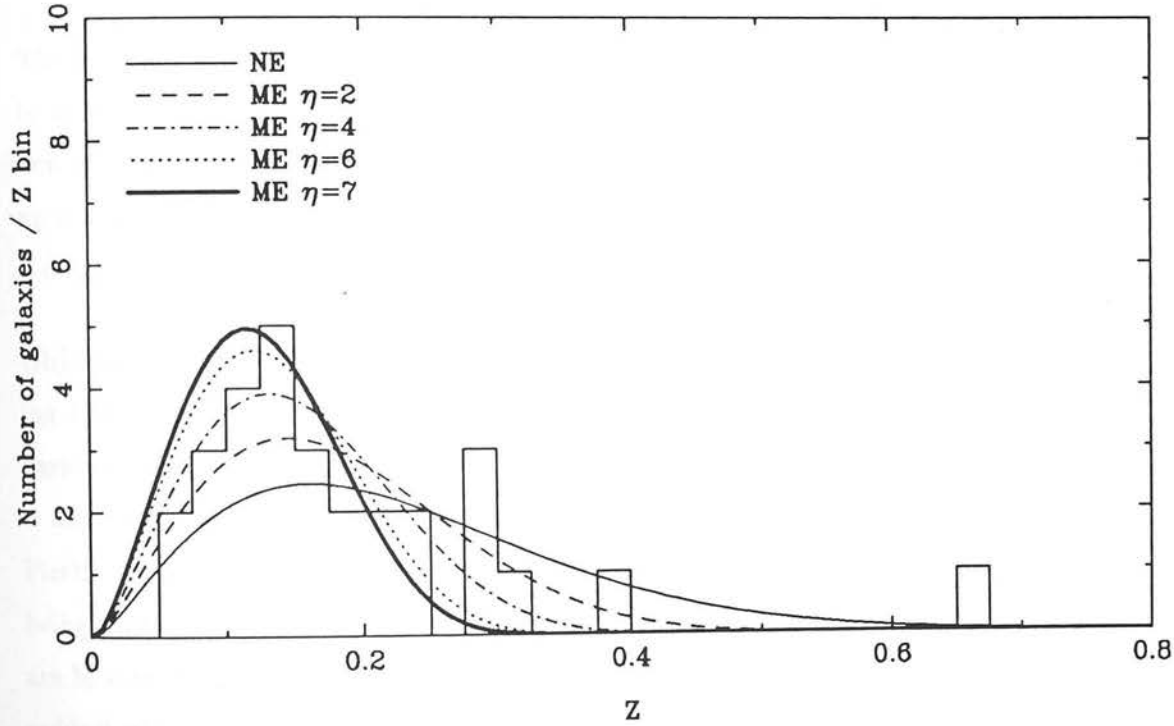

Fig. 6.20b Merging evolution models and the $10 < K < 16$ colour complete sub-sample (29 galaxies).

This actually requires luminosity *devolution* in order to allow the number of galaxies to increase with redshift. The results of these models for the redshift distribution is shown in figure 6.20 for rates of evolution given by $\eta = 2$, 4, 6 and 7. Table 6.5 shows that this gives an improved fit to the data relative to no-evolution as the mean redshift is lowered. The most favoured model is $\eta \simeq 2$–3, at 2% confidence we can reject $\eta > 6$ from the K < 17.5 sample and $\eta > 7$ from the K < 16 sample. Note that because the models are normalised to the data it is mainly the devolution in the luminosity which is being tested rather than the evolution in the normalisation.

Of course conserving K light is a bit too simple. At least passive evolution must be going on simply from the ageing of the stars. This is not inconsistent with the merging picture provided the results is still a net luminosity devolution (see section 5.4.3). If a power law L^* evolution of 1.4–2 is added on on top of the the merging then the results are still consistent if higher values of η are chosen.

6.6 Summary

The colour-magnitude diagram for infrared selected galaxies reveals that the population is very *red* in R − K colour — the distribution can only be fitted by the very reddest non-evolving spectral evolution models. A large number of the less extreme red objects now have spectra which reveal them to be galaxies in the field at $z < 1$; and their R − K vs z diagram confirms that their colours are similar to or redder than non-evolving models.

Objects with even redder R − K colours, or not detected in R, were investigated by obtaining JHK colours. This showed that all the non-detections re-observed were attributable to various kinds of detector and object-detection artifacts, and it appears unlikely that there is any population of "K-only" objects. The other objects appear to fall into two classes. Firstly there are objects with blue JHK colours which present the exciting possibility of being protogalaxies at very high redshift. However a more prosaic explanation is that they are M stars contaminating the sample as the star-galaxy separation is less reliable for the reddest objects. Secondly there are objects with red JHK colours which could be either unevolved galaxies at $z > 1$ or even cooler stars — candidate brown dwarves. Thus it appears that the very reddest objects have distances somewhere between 5×10^1 pc and

$5 \times 10^9 \, h^{-1}$ pc, with a heavily excluded middle. Only future spectroscopy can distinguish between these possibilities.

For the objects with redshifts, examination of the spectra and B – R colours shows that the redness in R – K appears to be uncorrelated with redness in the optical ruling out a simple model such as dust extinction to explain this. The number-redshift distribution of the galaxies was investigated for a $K < 16$ colour-complete sample and a $K < 17.5$ blue-biased sample, modelled using the *observed* R – K colours. This appears to show that the origin of the redness does not lie in a K band excess — indeed the complete $K < 16$ sample has a mean redshift *less than the no-evolution prediction* at the 5% level which makes the galaxies fainter and bluer. It seems likely that the problem must arise in the R band and is some sort of problem with the spectral evolution models possibly associated with the giant branch.

Because of the low mean redshift, the number-redshift distribution appears to be consistent with the simple merging models of section 5.4.3 where galaxies get fainter in K with lookback time. In terms of the models of section 5.4.3 the constraint is $0 < \eta < 6$ with $\eta = 2$–3 favoured. Any net amount of luminosity evolution appears to be ruled out, although luminosity evolution could be included in the merging scenario.

7 CONCLUDING REMARKS

It is a worthwhile exercise to review the aims of this thesis to see which of these have been achieved, and which will repay further study in the future.

One of the main aims of this study was to survey the 2 μm universe and to reveal any new classes of object which might be discovered there. Such objects could include protogalaxies at very high redshift and cool low-mass brown dwarf stars. The survey is essentially complete to K = 17 over 575$\Box'$, though objects are seen down to the 5 σ detection limit of K $\simeq$ 17.3. It appears conclusive that no new populations of *infrared only* objects are seen, that is objects detected only in the K band and not in any optical bands, despite a large number of spurious K detections generated by the noise characteristics of the detector. The typical R limit of the survey is $\simeq$ 23.8 — this corresponds to a limiting R – K colour of 6–7.

What does this imply for protogalaxies? The expectation is that protogalaxies will reveal themselves in very large numbers when they are first detected. The surface density on the sky of such objects can be estimated at $\gtrsim 5/\Box'$ simply on the basis that there should be at least one protogalaxy for every galaxy that exists today (Collins & Joseph, 1988). Mergers, of course, would make them more numerous but fainter. The exact magnitude at which this population comes in, however, depends on the luminosity of the objects, about which there is considerable controversy. The K band is sensitive to such objects out to $z \sim 20$ where the Lyman limit gets redshifted out of it. There is no evidence in the counts of galaxies for any such substantial new population — the number of objects is fully consistent with that expected from redshifting the local galaxy population with little or no luminosity evolution (see chapter 5). A large fraction of these galaxies now have spectroscopic identifications showing them to have the expected redshift distribution for normal galaxies with $z < 1$. Thus we can rule out detection of the bulk protogalactic population to K = 17.3, confirming the earlier work of Collins & Joseph (1988) with the single element detector UKT9.

Of course a large-area survey is not ideal for detecting such a high surface density population — ideally it would be better to spend integration time going fainter. However, as has

been discussed in previous chapters, the problem with this lies in performing the follow-up observations to confirm the nature of the primeval galaxies. The luminosity function for such objects is of course unknown, but if they had a tail to high luminosities then it is possible to trade survey area for depth. Could luminous, rare protogalaxies be hiding among the reddest objects in this survey? To check this near-infrared colours have been measured for samples of the reddest objects with mixed results. The problem is that the RJHK colours of such objects are almost indistinguishable from cool M stars. Down here near the R band CCD limit star-galaxy classification is unreliable, only spectroscopy can resolve this issue.

The other kind of red object which might have been picked up by this survey were cool brown dwarf stars. Indeed it appears (see section 6.3) that a handful of promising candidates have been found. These have very red R − K, J − H and H − K colours which indicate that if they were stars they would have to be very cool at $\sim 2000\,\mathrm{K}$. This time the confusion is inverted — they have the same colours as unevolved galaxies at $z > 1$ and spectroscopy is needed to distinguish the alternatives.

Although the objects are faint this need not be too difficult, integrations of 4000–10 000 s in excellent conditions are needed on a 2 m class telescope with a high performance red spectrograph to reach $\sim$5–10 σ on the continuum. Once this is achieved distinction is easy: cool stars have deep and jagged molecular bands while classical protogalaxies would have strong Lyman-α lines with the shortwards ultraviolet continuum eaten away by the Lyman-α forest. Of course a protogalactic spectrum is not *necessarily* like that, though Lyman-α forest absorption seems most probable because it has already been observed in $z \sim 4$ quasars. However it should be possible to rule in or out a stellar interpretation.

Another possibility is infrared spectroscopy. The new generation of 2 μm array spectrometers such as CGS4 on UKIRT have comparable sensitivity to the infrared array cameras. Because of the redness of the objects this is competitive in terms of signal/noise and integration time with optical spectroscopy. The possibilities are similar: classical protogalaxies at $z \lesssim 5$ would have strong Hα and Hβ lines in the near-infrared windows, while cool stars would again have deep molecular features.

Thus it seems that in a few nights of telescope time a good sample of 10–20 such objects could be observed and this issue resolved. Also once the stars are distinguished it will

be possible to quantify the numbers of stars in the red tail of the distribution. This will make it possible to determine more accurately the luminosity function (or upper limits thereof) for red low-mass stars which are poorly constrained by optical surveys. In addition the temperatures of such objects can be determined — not from spectroscopy as the line strengths are poorly correlated with temperature but from the JHK colours once it is known which objects are stars. Such numbers are of course important for an understanding of the star-formation process and the resultant initial mass function would have implications for the galaxy spectral evolution models discussed in chapter 5. It would also give new limits on the amount of dark matter in the solar neighbourhood in the form of cool stars and brown dwarves.

The other main aim of this survey was to study galaxy evolution in the infrared. What we have in fact is rather a remarkable null result — this is the first time that counts of galaxies in *any* waveband have come within a factor of two of matching the prediction of a standard Robertson-Walker cosmology. The constraint is not just from the number-magnitude counts; by choosing to cover a large area rather than going very deep in K it has been possible to construct a K selected redshift survey with a well-defined completeness. This is extremely valuable in deprojecting the counts and again indicates little evolution.

The colours too appear to indicate little evolution, though this is more problematic. They appear to be so red in R – K that only the reddest non-evolving spectral evolution models can match them. Even then when the colour-redshift relation is examined there appear to be objects considerably redder than the models. Is it possible that galaxies have hitherto undiscovered infrared excesses? The contrary appears to be indicated by the redshift distribution which has a mean redshift *less* than the no-evolution prediction at the 5% significance level, indicating that, if anything, the galaxies are fainter in K than expected.

This no-evolution model was constructed by taking the B luminosity function together with model B – K colours. This of course raises the question as to how does this fit in with the deep B band number-magnitude counts? These show a much larger excess over the no-evolution model than the K counts so surely the B – K colours *must* be getting bluer? It appears that the most likely solution to these difficulties lies in the R band portions of the model spectra, and is some unknown difficulty with the spectral evolution models. The red to near-infrared portion of a galaxies spectrum is dominated by giant branch stars whose treatment is probably the most controversial aspect of the spectral-evolution

codes, especially on short time-scales (e.g. Charlot & Bruzual, 1991). It certainly appears possible to construct models, involving merging, which can fit the B counts, K counts, redshift distributions and B – K colours (see chapters 5 and 6). If, as seems plausible, the B – K evolution arose as the average of short starburst events it might be possible to construct a stellar evolution model where B – R got bluer while R – K got redder with redshift.

One way to resolve this would be to look at the B – R and R – K colours of the galaxies with redshift, together with the spectra, to assess the importance of star-formation. Unfortunately due to the vagaries of telescope time scheduling the deep redshift survey has been constructed principally in the October fields where there is the least optical data: mainly just R band coverage. However it would only take a few hours of telescope time to obtain B magnitudes for just the galaxies with redshifts, and this would greatly clarify the matter.

Returning to the number-magnitude counts, when this bright K sample is combined with the deeper data of other workers it appears that there is still a small excess at the faint end over the prediction of the no-evolution model. There are two main ways this can be explained. Firstly it is possible to invoke pure luminosity evolution, however this has to switch on *after* $z = 1$ otherwise it violates the bright K count and redshift data. An alternative scenario can be constructed in which the galaxy population *devolves* in K luminosity via merging. The redshift data favours this more strongly than no-evolution as the redshifts indicate lower luminosities than those predicted. If the expected K luminosity evolution from passive evolution is then added back in we can then obtain a result consistent with the redshift distribution and the deeper counts. Such a model can also naturally explain the b_j excess as being due to merger driven starbursts. The low redshifts of the galaxies in the Broadhurst *et al.* and Colless *et al.* surveys are explained, despite their bluer colours, because they have lower masses and hence are nearer.

Such modelling is at a very simple level and subject to a number of uncertainties. However it does make two predictions which are eminently testable:

1) As K surveys are pushed deeper the mean redshift will not increase substantially and should be less than the no-evolution prediction. This can be tested by deeper K selected redshift surveys (see below).

2) There should be an increase in the number of faint merging/interacting pairs with redshift. Deep high quality imaging (as will be available from the *Hubble Space Telescope* in a few years)* will test this.

How feasible are deeper K selected samples? Firstly the present redshift sample is only complete to K = 16, with the data to K = 17 being blue biased. Chapter 6 demonstrates the importance of having a complete sample with no optical-infrared colour bias to probe mass-function evolution. There is almost no increase in sensitivity to the various models in the deeper sample because of the effect of the bias. The bias introduces a dependency on the optical part of the model, which as we have seen is rather an uncertain component. Additionally as the blue galaxies are preferentially included then the models are forced to put them at low redshift, mimicking the merging effect and hence reducing the signal. Any optical spectroscopic sample will of course have an effective optical limit, however if one has a complete sample unbiased by colour then the R band limits in the modelling can be discarded.

What are the prospects for completing this survey and future deeper K selected redshift surveys? To be complete to K = 17 another magnitude is needed — effectively it is necessary to reach R $\simeq$ 22 in $\simeq$ 20 000 seconds. The best faint object spectrographs have this kind of performance but a multislit device is preferable to observe a greater number of galaxies. The LDSS multislit instrument used to reach the faintest limits on the AAT is marginally less sensitive than this, and it is on a poor site with mediocre seeing. Although the required performance is available in the best conditions these are rather rare.

The development of LDSS2 for the William Herschel Telescope promises to give FOS level performance with a multislit capability. This is on a much better site with better seeing, this is an ideal instrument with which to complete this and future surveys. It will have an on-site mask manufacturing capability, in particular it will be possible to make masks from direct images taken with the same instrument on the same night. This might not seem so important given that the positions are already known from the infrared data. However for deep slit spectroscopy accurate positions are vital and the difference between 0.5″ and 0.1″ RMS accuracy might make more than a factor of two difference in integration time. Note, however, that the multiplex advantage is greatly reduced for a K selected galaxy

* Hopefully!

sample simply because of the wider variation in their optical fluxes. While one galaxy might take 10 000 s for enough light to be collected to secure a redshift its neighbour might require only 1000 s, in which case the other 9000 s is wasted. Of course, if the surface density of objects is high enough, this could be got round by observing a series of masks for progressively redder classes of objects. Thus all objects on any particular mask would have similar optical magnitudes and hence require similar exposures. However this would introduce an obvious colour bias unless the whole program was successfully completed.

The coming of bigger and bigger CCDs means that more large telescopes are acquiring multi-object capabilities: the prospects for future, deeper, surveys are good. How far can this go? The colours of the galaxies seem to be getting rapidly redder at K = 17; at K = 18–19 spectra at R = 25 may be necessary to achieve completeness. However it is also possible that the average colours may start to get bluer in such a way that a plateau is reached (maybe B will be a better region for spectroscopy than R?) as one goes fainter in K.

On the other hand if this does not happen things become more problematic. One has to face up to accurate modelling of the B – K colours to deduce anything at all. If merger-driven starbursts play an important role this would be a daunting task astrophysically. However such an approach does have the advantage of being able to turn the problem on its head — one could take a B selected redshift sample (e.g. the Colless *et al.* data) and measure K magnitudes for all of them. This is very feasible — K $\simeq$ 20 can be achieved in 15 minutes with IRCAM using current sensitivities.

Alternatively there is infrared spectroscopy. The sensitivity of instruments such as CGS4 allow a 10 σ continuum detection to be achieved for a K = 17 object in 3 hours. Although this has no multislit capability it could be used to get redshifts for a handful of the reddest objects in an otherwise complete survey.

Infrared arrays too are getting bigger, in the distant future (5–10 years) instruments such as NICMOS on the HST will have a near-infrared wide field imaging and multiobject spectroscopic capability (not necessarily multislit though — the performance of fibres is much better in the infrared). Near-infrared astronomy will be greatly benefitted by space based instruments. In principle this band is ideal for cosmological studies because the

K-corrections are negative and objects can be seen to greater distances. However what prevents this is the enormously high background — working above the atmosphere will all but eliminate this.

Finally such multiobject surveys will allow the follow up of brown dwarf and protogalaxy candidates without risking scarce telescope time. Obviously if there are very red objects then to be complete it is necessary to identify them: there is always the possibility that they could be "normal" galaxies (and I will not attempt to define that term!).

BIBLIOGRAPHY

Aaronson, M., 1978. *Astrophys. J.*, **221**, L103.

Bahcall, J.N. & Soneira, R.M., 1980. *Astrophys. J. Suppl.*, **44**, 73.

Bahcall, J.N., 1984. *Astrophys. J.*, **287**, 926.

Baron, E. & White, S.D.M., 1987. *Astrophys. J.*, **322**, 585.

Becklin, E.E. & Zuckerman, B., 1988. *Nature*, **336**, 656.

Black, D.C., 1985. In: *Astrophysics of Brown Dwarfs*, ed. Kafatos, M.C., Harrington, R.S. and Maran, S.P., Cambridge University Press, Cambridge, p. 139.

Blumenthal, G.R., Faber, S.M., Primack, J.R. and Rees, M.J., 1984. *Nature*, **311**, 517.

Bond, J.R., Szalay, A.S. and Turner, M.S., 1982. *Phys. Rev. Letters*, **48**, 1636.

Bower, R.G., 1990. *The Stellar Populations of Early-Type Galaxies in Groups and Clusters*, Ph.D. Thesis, University of Durham.

Broadhurst, T.J., Ellis, R.S. & Shanks, T., 1988. *Mon. Not. R. Astr. Soc.*, **235**, 827.

Broadhurst, T.J., Ellis, R.S., Koo, D.C. and Szalay A.S., 1990. *Nature*, **343**, 726.

Brown, G.S. & Tinsley, B.M., 1974. *Astrophys. J.*, **194**, 555.

Bruzual, G., 1983a. *Astrophys. J.*, **273**, 105.

Bruzual, G., 1983b. *Rev. Mex. Astr. Astrofis.*, **8**, 29.

Bruzual, G., 1983c. *Rev. Mex. Astr. Astrofis.*, **8**, 63.

Butcher, H. & Oemler, A., 1978. *Astrophys. J.*, **219**, 18.

Carlberg, R.G., 1990. *Astrophys. J.*, **359**, L1.

Casali, M.M., Aspin, C.A., McLean, I.S., 1987. *IRCAM users guide.*

Chambers, K.C. & Charlot, S., 1990. *Astrophys. J.*, **348**, L1.

Charlot, S. & Bruzual, G., 1991. *Astrophys. J.*, 367, 126.

Colless, M., Ellis, R.S., Taylor, K. and Hook, R.N., 1990. *Mon. Not. R. Astr. Soc.*, **244**, 408.

Collins, C.A., 1986. *Infrared Studies of Galaxy Formation and the Hubble Flow*, Ph.D. Thesis, University of London.

Collins, C.A., and Joseph, R.D., 1988. *Mon. Not. R. Astr. Soc.*, **235**, 209.

Collins, C.A. & Nichol, R.C., 1991. *Mon. Not. R. Astr. Soc.*, submitted.

Collins, C.A., Nichol, R.C. and Lumsden, S.L., 1991. *Mon. Not. R. Astr. Soc.*, submitted.

Corwin, H.G. & Emerson, D., 1982. *Mon. Not. R. Astr. Soc.*, **200**, 621.

Costero, R. & Osterbrook, D.E., 1977. *Astrophys. J.*, **211**, 675.

Couch, W.J. & Sharples, R.M. 1987. *Mon. Not. R. Astr. Soc.*, **229**, 423.

Couchman, H.M.P. & Carlberg, R.G., 1991. *Astrophys. J.*, in press.

Cowie, L.L., Gardner, J.P., Lilly, S.J. and McLean, I.S., 1990. *Astrophys. J.*, **360**, L1.

Cowie, L. L., 1991. In: *Observational Tests of Inflation*, ed. Shanks, T. , Kluwer, Dordrecht, in press.

Davies, R.D., Lasenby, A.N., Watson, R.A., Daintree, E.J., Hopkins, J., Beckman, J., Sanchez-Almeida, J. and Rebolo, R., 1987. *Nature*, **326**, 462.

Dressler, A. & Gunn, J.E., 1982. *Astrophys. J.*, **263**, 533.

Dressler, A. & Gunn, J.E., 1990. In: *The Evolution of the Universe of Galaxies: The Edwin Hubble Centennial Symposium, Astronomical Soc. of the Pacific Conference Series Vol. 10*, ed. Kron, R.G., p. 200.

Dunlop, J.S., 1987. *The High-Redshift Evolution of Radio Galaxies and Quasars*, Ph.D. Thesis, Univ. of Edinburgh.

Dunlop, J.S., Guideroni, B., Rocca-Volmerange, B., Peacock, J.A. and Longair, M.S., 1989. *Mon. Not. R. Astr. Soc.*, **240**, 257.

Efstathiou, G. & Silk, J., 1983. *Fundam. Cosmic. Phys.*, **9**, 1.

Efstathiou, G., Ellis, R.S. and Peterson, B.A., 1988. *Mon. Not. R. Astr. Soc.*, **232**, 431.

Engels, D., Sherwood, W.A., Wamsteker, W. & Schultz, G.V., 1981. *Astr. Astrophys. Suppl. Ser.*, **45**, 5.

Evrard, A., 1989. In: *The Interstellar Medium in External Galaxies*, ed. Shull, J.M. and Thronson, H.A., Kluwer, Dordrecht, in press.

Frogel, J.A., Persson, S.E., Aaronson, M. & Matthews, K., 1978. *Astrophys. J.*, **220**, 75.

Gamow, G., 1948. *Nature*, **162**, 680.

Glass, I.S., 1984. *Mon. Not. R. Astr. Soc.*, **211**, 461.

Guideroni, B. & Rocca-Volmerange, B.,1987 (GRV). *Astr. Astrophys.*, **186**, 1.

Guideroni, B. & Rocca-Volmerange, B.,1990 (GRVb). *Astr. Astrophys.*, **227**, 362.

Gunn, J.E., Longair, M.S., Rees, M.J., 1978. In: *Observational Cosmology, Eighth Advanced Course of the Swiss Society of Astronomy and Astrophysics*, ed. Maeder, A., Martinet, L. and Tammann, G.

Guth, A.H., 1981. *Phys. Rev. D.*, **23**, 347.

Hall, P., & Mackay, C.D, 1984. *Mon. Not. R. Astr. Soc.*, **210**, 979.

Hawkins, M.R.S. & Bessell, M.S., 1988. *Mon. Not. R. Astr. Soc.*, **234**, 177.

Hayes, D.S. & Latham, D.W., 1975. *Astrophys. J.*, **197**, 593.

Henry, J.P. & Lavery, R.J., 1987. *Astrophys. J.*, **323**, 473.

Heydon-Dumbleton, N.H, Collins, C.A. and MacGillivray, H.T, 1989. *Mon. Not. R. Astr. Soc.*, **238**, 379.

Hubble, E.P. & Tolman, R.C., 1935. *Astrophys. J.*, **82**, 302.

Hummer, D.G. & Storey, P.J., 1987. *Mon. Not. R. Astr. Soc.*, **224**, 801.

Jarvis, J.F. & Tyson, J.A., 1980. *Astr. J.*, **86**, 476.

Jenkins, C.R. & Reid, I.N., 1991. *Astr. J.*, **101**, 1595.

Johnson, H.L., 1966. *Ann. Rev. Astr. Astrophys.*, **4**, 193.

Jones, L.R., Fong, R., Shanks, T., Ellis, R.S. & Peterson, B.A., 1991. *Mon. Not. R. Astr. Soc.*, **249**, 481.

Kapteyn, J.C, 1906. *Plan of Selected Areas.*

King C.R. & Ellis, R.S., 1985. *Astrophys. J.*, **288**, 456.

Kolb, E.W. & Turner, M.S., 1990. *The Early Universe*, Addison-Wesley.

Koo, D.C., 1986. In: *Proceedings of the Erice Workshop on The Spectral Evolution of Galaxies*, ed. Chiosi, C. and Renzini, A., Reidel, Dordrecht, p. 419.

Koo, D.C., 1990. In: *The Evolution of the Universe of Galaxies: The Edwin Hubble Centennial Symposium, Astronomical Soc. of the Pacific Conference Series Vol. 10*, ed. Kron, R.G., p. 268.

Kron, R.G., 1978. Ph.D. Thesis, University of California at Berkeley.

Kron, R.G.,, 1980. *Astrophys. J. Suppl.*, **43**, 305.

Kron, R., 1982. *Vistas Astr.*, **26**, 37.

Landolt, A.U., 1983. *Astr. J.*, **88**, 439.

Larson, R. B. & Tinsley, B.M., 1974. *Astrophys. J.*, **192**, 293.
Lavery, R.J., & Henry, J.P., 1987. Astrophys. J., 323, 473.
Lavery, R.J. & Henry, J.P., 1988. *Astrophys. J.*, **330**, 596.

Lee, T.A., 1970. *Astrophys. J.*, **162**, 217.

Leech, K.J., Penston, M.V., Terlevich, R., Lawrence, A., Rowan-Robinson, M. and Crawford, J., 1989. *Mon. Not. R. Astr. Soc.*, **240**, 349.

Leggett, S.K. & Hawkins, M.R.S., 1988. *Mon. Not. R. Astr. Soc.*, **234**, 1065.

Liebert, J., 1990. *Very Low Mass Stars and Brown Dwarfs, McDonald Observatory 50th Anniversary Symposium.*

Lilly, S.J., 1988. *Astrophys. J.*, **333**, 161.

Lilly, S.J., Cowie, L.L. and Gardner, J.P., 1991. *Astrophys. J.*, **369**, 79.

Lilly, S.J. & Longair, M.S., 1984. *Mon. Not. R. Astr. Soc.*, **211**, 833.

Maddox, S.J., Efstathiou, G., Sutherland, W.J. and Loveday, J., 1990. *Mon. Not. R. Astr. Soc.*, **242**, 43P.

Maddox, S.J., Sutherland, W.J., Efstathiou, G., Loveday, J. and Peterson, B.A., 1990. *Mon. Not. R. Astr. Soc.*, **247**, 1P.

McCarthy, D.W., Probst, R.G. and Low, F.J., 1985. *Astrophys. J.*, **290**, L9.

Metcalfe, N., Shanks, T., Fong, R. & Jones L.R., 1991. *Mon. Not. R. Astr. Soc.*, **249**, 498.

Mobasher, B., Ellis, R.S. and Sharples R.M., 1986. *Mon. Not. R. Astr. Soc.*, **223**, 11.

Nelson, L.A., Rappaport, S.A. and Joss, P.C., 1986. *Astrophys. J.*, **311**, 226.

Parry, I.R. & Sharples, R.M., 1988. In: *Fibres Optics in Astronomy, Astronomical Soc. of the Pacific Conference Series Vol. 3*, ed. S.C. Barden, p. 93.

Partridge, R. B. and Peebles, P.J.E., 1967. *Astrophys. J.*, **147**, 868.

Peacock, J.A., 1987. In: *Astrophysical Jets and their engines*, ed. Kundt, W., NATO ASI C208, Reidel, Dordrecht, p. 171.

Penzias, A.A., Wilson, R.W., 1965. *Astrophys. J.*, **142**, 419.

Peterson, B.A., Ellis, R.S., Kibblewhite, E.J., Bridgeland, M., Hooley, T. and Horne, D., 1979. *Astrophys. J.*, **233**, L109.

Press, W.H., Flannery, B.P., Teukolsky, S.A. and Vetterling, W.T., 1989. *Numerical Recipes (FORTRAN version)*, Cambridge University Press.

Reid, N. and Gilmore, G., 1982. *Mon. Not. R. Astr. Soc.*, **201**, 73.

Readhead, A.C.S., Lawrence, C.R., Myers, S.T., Sargent, W.L.W., Hardebeck, H.E., and Moffet, A.T., 1989. *Astrophys. J.*, **346**, 566.

Rocca-Volmerange, B. & Guideroni, B., 1988 (RVG). *Astr. Astrophys. Suppl. Ser.*, **75**, 93.

*
Rowan-Robinson, M., 1986. *The Cosmological Distance Ladder*, Freeman.

Salpeter, E.E., 1955. *Astrophys. J.*, **121**, 161.

Sancisi, R. & van Albada, T.S., 1987. In: *Dark Matter in the Universe*, ed. Kormendy, J. and Knapp, G.R.

* Rowan-Robinson, M., 1968. Mon. Not. R. Astr. Soc., 138, 445.
Rowan-Robinson, M., 1969. Nature, 224, 1094.

Saunders, W., Frenk, C., Rowan-Robinson, M., Efstathiou, G., Lawrence, A., Kaiser, N., Ellis, R., Crawford, J., Xiao-Yang, X. and Parry, I., 1991. *Nature*, **349**, 32.

Scalo, J.M., 1986. *Fundam. Cosmic. Phys.*, **11**, 1.

Schechter, P.L., 1976. *Astrophys. J.*, **203**, 297.

Schmidt, M., 1968. *Astrophys. J.*, **151**, 393.

Schmidt, M. & Green, R.F., 1983. *Astrophys. J.*, **269**, 352.

Seaton, M.J., 1979. *Mon. Not. R. Astr. Soc.*, **187**, 785.

Shanks, T.S., Stevenson, P.R., Fong, R., MacGillivray, H.T., 1984. *Mon. Not. R. Astr. Soc.*, **206**, 767.

Smoot, G.F., Bennett, C.L., Kogut, A., Aymon, J., Backus, C., De Amici, G., Galuk, K., Jackson, P.D., Keegstra, P., Rokke, L., Tenorio, L., Torres, S., Gulkis, S., Hauser, M.G., Janssen, M., Mather, J.C., Weiss, R., Wilkinson, D.T., Wright, E.L., Boggess, N.W., Cheng, E.S., Kelsall, T., Lubin, P., Meyer, S., Moseley, S.H., Murdock, T.L., Shafer, R.A. and Silverberg, R.F., 1991. *Astrophys. J.*, **371**, L1.

Stetson, P.B., 1990. *The Technique of Least Squares.*

Stone, R.P.S., 1977. *Astrophys. J.*, **218**, 767.

Stone, R.P.S. & Baldwin, J.A., 1983. *Mon. Not. R. Astr. Soc.*, **204**, 347.

Terrell, J., 1977. *Am. J. Phys.*, **45**, 869.

Thronson, H.A., Jr., Majewski, S., Descartes, L. and Hereld M., 1990. *Astrophys. J.*, **364**, 456.

Tinsley, B.M. & Gunn, J.E., 1976. *Astrophys. J.*, **203**, 52.

Tinsley, B.M., 1977. *Astrophys. J.*, **211**, 621.

Tokunaga, A.T., 1986. *NASA Infrared Telescope Facility Photometry Manual.*

Tolkien, J.R.R., 1937. *The Hobbit.*

Tonry, J. & Davis, M., 1979. *Astr. J.*, **84**, 1511.

Tyson, J.A., 1988. *Astr. J.*, **96**, 1.

Wall, J.V. & Laing, R.A., 1986. *Users' Guide to the Prime Focus CCD Camera on the Isaac Newton Telescope.*

Warren, S.J., Hewett, P.C., Irwin, M.J., McMahon, R.G., Bridgeland, M.T., Bunclark, P.S. and Kibblewhite, E.J., 1987. *Nature*, **325**, 131.

Weinberg, S., 1972. *Gravitation & Cosmology*, (New York: Wiley).

White, S.D.M., Frenk, C.S.F. and Davis, M., 1983. *Astrophys. J.*, **274**, L1.

White, S.D.M., 1986. In: *Inner Space/Outer Space*, ed. Kolb E.W., Turner, M.S., Lindley, D., Olive, K. and Seckel, D., University of Chicago Press, p. 228.

White, S.D.M., 1989. In: *Physics of the Early Universe, Proceedings of the 36th Scottish Universities Summer School in Physics*, ed. Peacock, J.A., Heavens, A.F. and Davies, A.T.

Wynn, C.G. & Worswick, S.P., 1988. *Observatory*, **108**, 161.

Yang, J., Turner, M.S., Steigman, G., Schramm, D.N. and Olive K.A., 1984. *Astrophys. J.*, **281**, 493.

Yee H.K.C. & Green, R.F., 1987. *Astrophys. J.*, **319**, 28.

Yoshii, Y. & Takahara, F., 1988. *Astrophys. J.*, **326**, 1.

Zuckerman, B. & Becklin E.E., 1987. *Nature*, **330**, 138.

A POSITIONS AND MAGNITUDES

This appendix lists the positions and magnitudes of all the objects in the October and March K band catalogues. The catalogues are KRBPAIR3 (also referred to in the text for brevity as OCTKR) for the October fields, described in section 3.5.1, and KBVRIPAIR2 (or MAR) for the March fields, described in section 3.5.2.

The RA and DEC are given for the K position in 1950.0 coordinates. The RMS accuracy is $\simeq 0.5''$ (see section 2.6.1). All objects down to the catalogue limit are listed for the sake of completeness. Note however that the evidence is that the objects only detected in the K band are detector artifacts (see section 6.3), apart from a few fields which escaped optical coverage.

The column "G" refers to whether or not the object was classified as a galaxy or a star, based on the R band CCD image (see section 3.6). Similarly the column "R" refers to whether or not the object was one of the original reference objects included in for the photometric cross-calibration.

The optical magnitudes are in the CCD systems described in section 3.3.1. The infrared magnitudes are for the UKIRT K filter, though at this level of photometric accuracy the colour terms needed to convert to other K filters are negligible. The magnitude errors are the random photometric errors, as determined from the background noise, added in quadrature to the estimated systematic error in the zeropoints, as determined from the cross-calibration.

There were a few *paired* objects ($\lesssim 15$) in each catalogue with very extreme R – K colours which turned out, on visual inspection, to be various pairing artifacts (e.g. caused by diffraction spikes). These are marked by setting the "G" and "R" columns to "–".

ID	RA	DEC	K	R	B	G	R
1	22 39 9·43	00 34 59·26	17·16±0·20	—	—	–	–
2	22 39 8·45	00 35 12·90	16·05±0·09	—	—	–	–
3	22 39 2·97	00 35 16·83	16·76±0·15	—	—	–	–
4	22 39 3·26	00 35 22·55	16·82±0·15	—	—	–	–
5	22 39 6·36	00 35 22·79	14·39±0·05	16·88±0·04	—	N	Y
6	22 39 8·40	00 35 26·82	15·47±0·07	17·45±0·04	—	Y	N
7	22 39 9·17	00 36 13·75	17·18±0·19	—	—	–	–
8	22 39 7·53	00 36 15·47	17·10±0·20	—	—	–	–
9	22 39 0·31	00 36 43·87	15·84±0·10	18·16±0·04	—	Y	N
10	22 39 1·02	00 37 0·99	15·11±0·07	—	—	–	–
11	22 38 59·55	00 37 38·27	14·25±0·05	17·84±0·04	—	Y	Y
12	22 38 58·72	00 37 45·03	14·67±0·06	17·59±0·04	—	N	N
13	22 38 56·20	00 37 55·02	15·22±0·07	—	—	–	–
14	22 38 42·61	00 30 29·10	17·34±0·20	—	—	–	–
15	22 38 38·65	00 30 53·92	16·68±0·12	—	—	–	–
16	22 38 39·90	00 31 23·21	14·97±0·06	17·19±0·04	19·22±0·04	Y	Y
17	22 38 40·40	00 31 41·06	11·49±0·05	Saturated	Saturated	N	N
18	22 38 41·69	00 31 49·68	16·43±0·10	20·39±0·05	—	Y	N
19	22 38 40·79	00 32 50·94	16·75±0·20	20·00±0·04	22·55±0·16	Y	N
20	22 38 41·43	00 32 54·72	14·24±0·05	Saturated	18·50±0·04	N	N
21	22 38 39·41	00 32 58·58	16·02±0·10	19·50±0·04	22·27±0·12	N	N
22	22 38 34·02	00 33 16·66	16·46±0·14	18·34±0·04	20·21±0·04	Y	N
23	22 38 38·75	00 33 19·17	15·61±0·08	19·36±0·04	21·97±0·10	N	N
24	22 38 37·94	00 33 18·39	16·08±0·11	18·48±0·04	19·71±0·04	Y	Y
25	22 38 39·59	00 33 56·50	15·59±0·08	19·17±0·04	—	Y	N
26	22 38 43·08	00 32 39·46	16·58±0·14	—	—	–	–
27	22 38 46·79	00 32 59·82	16·73±0·15	20·22±0·04	22·73±0·17	N	N
28	22 38 43·60	00 32 59·89	17·05±0·18	21·95±0·10	—	Y	N
29	22 38 43·68	00 33 29·90	14·77±0·06	Saturated	17·93±0·04	N	Y
30	22 38 45·58	00 33 52·90	16·41±0·11	—	—	–	–
31	22 38 43·84	00 33 55·83	15·90±0·09	20·20±0·05	—	Y	N
32	22 38 41·09	00 34 10·28	16·71±0·15	—	—	–	–
33	22 38 45·45	00 34 14·14	12·46±0·05	Saturated	—	N	N
34	22 38 39·36	00 37 11·35	11·09±0·05	Saturated	—	N	N
35	22 38 42·13	00 37 33·29	13·50±0·05	Saturated	—	N	Y
36	22 38 38·47	00 38 7·80	14·20±0·06	Saturated	—	N	N
37	22 38 42·64	00 38 23·07	15·83±0·14	19·89±0·04	—	–	–
38	22 38 44·10	00 40 9·32	15·44±0·06	18·85±0·05	—	Y	N
39	22 38 42·96	00 40 9·69	17·11±0·18	—	—	–	–
40	22 38 43·58	00 40 42·65	16·39±0·11	19·74±0·07	—	Y	N
41	22 38 48·36	00 40 54·03	16·34±0·11	19·99±0·09	—	Y	N
42	22 38 45·83	00 40 55·65	12·95±0·05	Saturated	—	N	Y
43	22 38 43·29	00 41 14·42	15·44±0·07	18·77±0·05	—	Y	N
44	22 38 48·15	00 41 16·83	17·04±0·17	—	—	–	–
45	22 38 45·45	00 41 44·28	15·89±0·08	—	—	–	–
46	22 38 39·16	00 40 19·45	14·98±0·06	16·60±0·04	—	N	N
47	22 38 37·47	00 40 38·06	16·83±0·16	20·74±0·14	—	Y	N

ID	RA	DEC	K	R	B	G	R
48	22 38 40·37	00 41 2·50	14·93±0·06	16·91±0·04	—	N	Y
49	22 38 38·53	00 41 10·37	17·00±0·19	—	—	–	–
50	22 38 38·88	00 41 24·01	16·50±0·13	18·95±0·05	—	Y	N
51	22 38 43·12	00 41 54·54	13·72±0·05	17·04±0·04	—	N	N
52	22 38 33·59	00 34 43·47	16·92±0·17	—	—	–	–
53	22 38 38·93	00 34 44·34	17·24±0·21	—	—	–	–
54	22 38 38·45	00 34 51·21	16·96±0·17	20·68±0·06	—	Y	N
55	22 38 34·85	00 34 50·88	13·70±0·05	Saturated	—	N	N
56	22 38 34·54	00 35 28·69	16·74±0·15	19·87±0·05	—	Y	N
57	22 38 36·89	00 35 34·04	15·16±0·06	17·45±0·04	—	N	Y
58	22 38 40·14	00 35 40·22	15·58±0·07	—	—	–	–
59	22 38 39·64	00 35 49·40	16·79±0·15	—	—	–	–
60	22 38 35·90	00 35 50·83	13·89±0·05	Saturated	—	N	N
61	22 38 38·86	00 35 55·59	16·66±0·13	19·94±0·05	—	N	N
62	22 38 33·19	00 36 2·97	16·74±0·15	21·74±0·14	—	Y	N
63	22 38 39·45	00 36 10·78	16·61±0·13	—	—	–	–
64	22 38 38·90	00 36 24·13	16·81±0·15	—	—	–	–
65	22 38 40·78	00 36 26·20	14·57±0·05	—	—	–	–
66	22 40 30·26	00 25 56·63	16·92±0·18	20·79±0·05	—	Y	N
67	22 40 29·63	00 26 1·91	16·98±0·18	—	—	–	–
68	22 40 31·98	00 26 12·71	16·25±0·10	19·00±0·04	—	Y	N
69	22 40 28·53	00 26 37·21	13·72±0·05	Saturated	—	N	Y
70	22 40 26·40	00 26 44·79	16·20±0·10	—	—	–	–
71	22 40 30·66	00 26 51·57	16·01±0·09	19·75±0·04	—	Y	N
72	22 40 30·54	00 26 54·94	16·58±0·14	—	—	–	–
73	22 40 27·78	00 27 11·34	15·48±0·07	18·67±0·04	—	Y	N
74	22 40 30·69	00 27 20·31	15·26±0·06	—	—	–	–
75	22 39 59·64	00 20 42·90	13·62±0·05	Saturated	—	N	N
76	22 39 59·15	00 20 57·83	13·93±0·05	Saturated	—	N	Y
77	22 40 2·69	00 21 34·23	16·31±0·12	19·70±0·04	—	Y	N
78	22 40 28·91	00 20 23·44	13·02±0·05	Saturated	—	N	N
79	22 40 25·22	00 20 31·31	11·52±0·05	Saturated	—	N	N
80	22 40 27·21	00 20 54·81	16·70±0·14	19·11±0·04	—	N	N
81	22 40 25·74	00 21 16·52	14·59±0·05	Saturated	—	N	Y
82	22 40 28·71	00 21 18·40	16·07±0·10	—	—	–	–
83	22 40 19·12	00 27 19·50	12·31±0·05	Saturated	—	N	N
84	22 40 18·59	00 27 36·18	16·65±0·16	—	—	–	–
85	22 40 22·67	00 27 56·95	15·15±0·06	—	—	–	–
86	22 40 20·66	00 28 10·50	14·62±0·06	Saturated	—	N	Y
87	22 40 21·70	00 28 14·40	16·58±0·14	—	—	–	–
88	22 40 19·37	00 28 30·56	16·64±0·16	19·44±0·04	—	N	N
89	22 40 17·67	00 28 35·92	14·50±0·05	Saturated	—	N	N
90	22 40 12·72	00 21 29·73	16·84±0·18	18·22±0·04	—	Y	N
91	22 40 9·02	00 21 37·83	15·83±0·09	19·00±0·04	—	Y	N
92	22 40 12·52	00 22 7·27	13·63±0·05	Saturated	—	N	Y
93	22 40 8·88	00 22 13·41	17·04±0·20	—	—	–	–
94	22 40 14·20	00 22 15·96	14·78±0·06	18·54±0·04	—	N	N

ID	RA	DEC	K	R	B	G	R
95	22 40 11·48	00 22 26·00	16·33±0·12	19·85±0·04	—	Y	N
96	22 40 13·93	00 22 32·01	16·04±0·10	21·81±0·10	—	Y	N
97	22 40 10·95	00 22 55·33	16·86±0·17	—	—	–	–
98	22 40 14·67	00 23 12·06	12·56±0·05	Saturated	—	N	N
99	22 40 17·67	00 23 53·24	16·42±0·13	19·09±0·04	—	N	N
100	22 40 14·89	00 23 54·02	14·46±0·05	Saturated	—	N	Y
101	22 40 15·37	00 24 2·76	16·27±0·12	20·10±0·04	—	Y	N
102	22 40 18·41	00 24 4·29	17·12±0·20	22·03±0·10	—	Y	N
103	22 40 16·07	00 24 9·02	17·17±0·20	—	—	–	–
104	22 40 18·20	00 24 30·77	17·14±0·20	22·07±0·11	—	Y	N
105	22 40 17·65	00 24 50·61	12·81±0·05	Saturated	—	N	Y
106	22 40 18·74	00 24 58·85	16·22±0·10	21·70±0·09	—	Y	N
107	22 40 15·16	00 24 59·87	14·22±0·05	Saturated	—	N	N
108	22 40 18·36	00 25 32·06	17·15±0·20	—	—	–	–
109	22 40 20·59	00 25 39·50	15·42±0·06	19·38±0·04	—	Y	N
110	22 40 20·19	00 25 39·53	16·85±0·16	20·40±0·05	—	Y	N
111	22 40 9·74	00 28 40·49	13·88±0·05	Saturated	—	N	Y
112	22 40 10·57	00 29 2·60	12·86±0·05	Saturated	—	N	N
113	22 40 14·49	00 29 22·74	16·15±0·10	19·03±0·04	—	Y	N
114	22 40 16·50	00 29 42·72	16·62±0·14	—	—	–	–
115	22 40 14·40	00 29 40·86	10·94±0·05	Saturated	—	N	N
116	22 40 16·90	00 29 58·62	13·84±0·05	Saturated	—	N	Y
117	22 40 18·59	00 30 4·06	15·45±0·07	—	—	–	–
118	22 40 15·23	00 30 4·37	16·67±0·15	21·33±0·07	—	Y	N
119	22 40 19·10	00 30 12·30	16·62±0·15	19·88±0·08	—	Y	N
120	22 40 19·71	00 30 14·37	15·69±0·08	19·00±0·05	—	Y	N
121	22 40 16·51	00 30 18·37	15·95±0·09	19·95±0·04	—	Y	N
122	22 40 13·24	00 30 23·93	15·91±0·09	—	—	–	–
123	22 40 13·96	00 30 37·83	16·28±0·11	—	—	–	–
124	22 40 14·59	00 30 39·76	16·51±0·14	20·66±0·05	—	Y	N
125	22 40 1·64	00 23 49·49	16·85±0·15	—	—	–	–
126	22 39 59·79	00 23 48·58	11·43±0·05	Saturated	—	N	N
127	22 40 4·05	00 23 54·34	16·32±0·10	—	—	–	–
128	22 40 1·87	00 23 55·20	14·89±0·06	17·02±0·04	—	N	Y
129	22 40 5·60	00 23 57·96	17·19±0·19	20·00±0·05	—	Y	N
130	22 40 5·75	00 24 15·68	14·71±0·05	18·81±0·04	—	N	N
131	22 40 0·39	00 24 24·58	17·17±0·19	—	—	–	–
132	22 39 58·28	00 24 46·24	16·82±0·15	20·04±0·05	—	Y	N
133	22 39 30·93	00 20 56·76	16·59±0·14	22·49±0·19	—	–	–
134	22 39 32·41	00 20 57·16	17·05±0·21	—	—	–	–
135	22 39 31·74	00 20 59·03	16·56±0·14	—	—	–	–
136	22 39 31·38	00 21 9·52	15·15±0·06	21·48±0·09	22·51±0·17	–	–
137	22 39 38·42	00 21 26·36	16·18±0·10	20·15±0·05	22·36±0·12	Y	N
138	22 39 37·84	00 21 26·98	16·11±0·10	20·12±0·05	—	Y	N
139	22 39 32·14	00 21 40·79	16·39±0·12	—	—	–	–
140	22 39 31·83	00 21 41·13	16·72±0·15	—	—	–	–
141	22 39 31·39	00 21 41·63	16·43±0·13	—	—	–	–

ID	RA	DEC	K	R	B	G	R
142	22 39 30·96	00 21 41·56	16·43±0·13	—	—	–	–
143	22 39 35·21	00 21 45·40	16·65±0·14	—	—	–	–
144	22 39 32·77	00 21 45·58	15·64±0·08	19·64±0·04	22·20±0·11	Y	N
145	22 39 34·89	00 21 44·89	15·03±0·06	17·50±0·04	19·17±0·04	N	Y
146	22 39 38·01	00 21 50·51	16·75±0·15	19·93±0·05	21·40±0·06	Y	N
147	22 39 31·88	00 22 23·58	12·79±0·05	Saturated	Saturated	N	N
148	22 39 37·96	00 22 27·49	17·03±0·19	—	—	–	–
149	22 39 33·89	00 22 29·13	15·03±0·06	—	—	–	–
150	22 39 40·25	00 24 7·27	15·79±0·08	—	—	–	–
151	22 39 40·14	00 24 16·61	15·56±0·07	18·49±0·04	19·86±0·04	Y	N
152	22 39 35·56	00 24 44·44	14·87±0·06	17·15±0·04	18·96±0·04	N	N
153	22 39 37·95	00 24 44·58	14·47±0·05	16·62±0·04	18·25±0·04	N	N
154	22 39 36·72	00 24 51·06	13·26±0·05	16·72±0·04	18·92±0·04	N	N
155	22 39 36·60	00 24 58·69	15·77±0·08	18·62±0·04	20·83±0·05	N	N
156	22 39 37·57	00 25 1·29	13·44±0·05	16·45±0·04	18·65±0·04	N	Y
157	22 39 35·76	00 25 31·00	16·87±0·18	—	—	–	–
158	22 39 35·05	00 25 40·21	16·59±0·14	—	—	–	–
159	22 39 37·16	00 25 44·39	13·30±0·05	16·28±0·04	17·73±0·04	Y	N
160	22 39 36·20	00 25 48·17	17·12±0·20	—	—	–	–
161	22 39 39·28	00 27 33·02	17·16±0·20	—	—	–	–
162	22 39 38·26	00 27 45·19	16·26±0·10	—	—	–	–
163	22 39 39·29	00 28 21·42	15·89±0·08	17·39±0·04	—	N	Y
164	22 39 38·59	00 28 33·25	16·88±0·17	20·95±0·16	—	Y	N
165	22 39 42·65	00 28 31·97	10·65±0·05	Saturated	—	N	N
166	22 39 38·87	00 29 0·92	17·01±0·20	—	—	–	–
167	22 39 33·70	00 31 1·39	15·15±0·07	17·52±0·04	—	N	Y
168	22 39 32·73	00 31 13·99	13·56±0·05	Saturated	—	N	N
169	22 39 32·42	00 31 27·18	15·73±0·10	18·94±0·04	—	Y	N
170	22 39 35·14	00 31 31·19	15·78±0·11	—	—	–	–
171	22 39 34·70	00 31 29·63	16·52±0·19	18·76±0·04	—	N	N
172	22 39 30·14	00 31 46·79	16·59±0·19	20·60±0·06	—	–	–
173	22 39 34·22	00 31 53·23	15·39±0·09	18·48±0·04	—	Y	N
174	22 39 22·17	00 21 46·16	12·83±0·05	Saturated	Saturated	N	N
175	22 39 23·80	00 22 6·27	14·68±0·06	17·53±0·04	19·52±0·04	N	Y
176	22 39 27·16	00 22 43·66	15·48±0·07	19·42±0·04	21·84±0·08	N	N
177	22 39 34·11	00 22 43·32	13·43±0·05	Saturated	Saturated	N	N
178	22 39 29·92	00 24 36·04	13·30±0·05	Saturated	—	N	N
179	22 39 27·58	00 24 45·69	14·68±0·05	Saturated	—	N	Y
180	22 39 27·16	00 25 0·35	15·57±0·07	17·93±0·04	—	N	N
181	22 39 31·48	00 25 0·98	16·98±0·18	19·43±0·04	21·40±0·06	Y	N
182	22 39 30·89	00 25 19·64	17·13±0·20	—	—	–	–
183	22 39 24·38	00 25 24·90	15·08±0·06	—	—	–	–
184	22 39 30·47	00 25 29·30	14·38±0·05	—	—	–	–
185	22 39 15·90	00 25 28·72	16·12±0·16	19·35±0·04	—	N	N
186	22 39 15·70	00 25 41·47	12·68±0·05	Saturated	—	N	N
187	22 39 17·36	00 26 11·27	13·46±0·05	Saturated	—	N	Y
188	22 39 15·03	00 26 34·66	11·78±0·05	Saturated	—	N	N

ID	RA	DEC	K	R	B	G	R
189	22 39 4·09	00 22 54·61	16·69±0·17	20·02±0·04	22·41±0·13	Y	N
190	22 39 5·99	00 22 58·60	15·93±0·09	19·82±0·04	22·44±0·13	Y	N
191	22 39 6·69	00 23 4·77	14·34±0·05	Saturated	17·49±0·04	N	N
192	22 39 7·82	00 23 41·61	13·18±0·05	Saturated	18·17±0·04	N	Y
193	22 39 9·07	00 24 23·74	16·74±0·17	—	—	–	–
194	22 39 9·78	00 24 24·97	15·91±0·09	19·75±0·04	—	N	N
195	22 38 52·49	00 23 40·98	17·05±0·18	—	—	–	–
196	22 38 58·81	00 23 43·79	16·99±0·18	—	22·32±0·14	–	–
197	22 38 57·30	00 23 50·31	15·93±0·09	—	—	–	–
198	22 38 55·21	00 24 3·35	16·00±0·09	19·31±0·04	21·45±0·06	Y	N
199	22 38 56·90	00 24 14·64	16·89±0·17	20·54±0·05	—	Y	N
200	22 38 52·32	00 24 16·34	17·00±0·18	20·09±0·05	—	Y	N
201	22 38 58·03	00 24 19·10	15·44±0·07	19·13±0·04	—	N	N
202	22 38 56·20	00 24 26·83	15·89±0·08	17·37±0·04	—	N	Y
203	22 38 58·67	00 24 29·99	10·54±0·05	Saturated	—	N	N
204	22 38 57·19	00 25 11·02	16·07±0·09	—	—	–	–
205	22 38 57·01	00 25 20·68	15·76±0·08	17·51±0·04	—	N	N
206	22 38 56·35	00 25 21·87	17·02±0·17	—	—	–	–
207	22 38 58·29	00 25 54·14	12·67±0·05	Saturated	—	N	Y
208	22 38 58·53	00 26 7·80	17·13±0·18	22·00±0·15	—	–	–
209	22 38 55·65	00 26 40·97	16·96±0·16	—	—	–	–
210	22 38 58·49	00 29 32·18	13·01±0·05	Saturated	—	N	N
211	22 38 58·41	00 29 42·84	16·86±0·16	—	—	–	–
212	22 39 0·35	00 29 45·16	16·91±0·18	20·13±0·07	—	Y	N
213	22 38 57·59	00 29 46·09	16·68±0·15	17·84±0·04	—	N	N
214	22 39 3·70	00 30 0·94	16·14±0·10	—	—	–	–
215	22 39 1·02	00 30 5·54	13·69±0·05	Saturated	—	N	Y
216	22 39 0·34	00 30 34·62	15·27±0·06	18·85±0·04	—	N	N
217	22 38 48·11	00 25 37·35	15·35±0·06	—	—	–	–
218	22 38 47·76	00 25 43·57	12·68±0·05	Saturated	—	N	N
219	22 38 51·05	00 26 1·83	13·02±0·05	Saturated	—	N	Y
220	22 38 47·57	00 26 21·46	16·78±0·15	21·50±0·08	—	Y	N
221	22 38 48·39	00 26 51·88	15·12±0·06	—	—	–	–
222	22 38 40·67	00 26 5·12	15·55±0·07	17·00±0·04	—	N	N
223	22 38 41·18	00 26 14·78	14·63±0·05	18·31±0·04	—	N	N
224	22 38 39·84	00 26 19·33	16·20±0·11	20·01±0·04	—	Y	N
225	22 38 38·87	00 26 31·70	14·76±0·06	Saturated	—	N	N
226	22 38 39·41	00 26 32·98	17·15±0·20	20·80±0·06	—	Y	N
227	22 38 45·33	00 26 43·38	15·97±0·08	—	—	–	–
228	22 38 42·33	00 26 49·36	14·43±0·05	Saturated	—	N	Y
229	22 38 39·37	00 27 32·27	16·62±0·13	20·33±0·05	—	Y	N
230	22 38 38·41	00 27 37·82	16·79±0·15	21·68±0·13	—	Y	N
231	22 38 42·44	00 28 59·67	15·86±0·08	18·35±0·04	—	N	N
232	22 38 47·67	00 29 7·48	14·50±0·05	Saturated	—	N	N
233	22 38 44·56	00 29 12·65	15·83±0·08	17·36±0·04	—	N	Y
234	22 38 42·07	00 29 41·65	16·82±0·16	—	—	–	–
235	22 38 46·42	00 29 50·08	16·96±0·18	20·67±0·05	22·98±0·20	Y	N

ID	RA	DEC	K	R	B	G	R
236	22 39 15·76	00 22 35·53	12·98±0·05	Saturated	16·63±0·04	N	Y
237	22 39 19·23	00 22 35·67	15·62±0·08	—	—	–	–
238	22 38 44·41	00 21 0·75	16·89±0·19	—	—	–	–
239	22 38 45·17	00 21 22·18	14·25±0·05	Saturated	16·59±0·04	N	Y
240	22 38 37·50	00 24 41·12	13·23±0·05	Saturated	—	N	Y
241	22 38 38·86	00 24 47·73	16·47±0·13	—	—	–	–
242	22 38 38·60	00 29 40·71	15·48±0·08	—	—	–	–
243	22 38 37·67	00 29 49·00	16·83±0·20	—	—	–	–
244	22 38 37·48	00 29 50·20	16·61±0·18	20·29±0·05	—	Y	N
245	22 39 14·25	00 30 20·50	13·49±0·05	16·60±0·04	—	Y	Y
246	22 39 10·88	00 25 41·10	13·78±0·05	17·67±0·04	—	N	Y
247	22 39 12·33	00 26 7·48	14·10±0·05	17·87±0·04	—	N	N
248	22 39 10·53	00 26 17·35	16·85±0·18	20·31±0·05	—	Y	N
249	22 38 54·43	00 20 48·00	16·41±0·17	20·01±0·04	22·50±0·12	Y	N
250	22 38 53·87	00 20 58·55	16·52±0·17	22·22±0·12	—	Y	N
251	22 38 57·24	00 21 19·40	14·36±0·06	Saturated	19·06±0·04	N	Y
252	22 39 0·62	00 22 23·30	13·83±0·05	Saturated	16·50±0·04	N	Y
253	22 39 3·52	00 22 30·43	15·13±0·07	18·85±0·04	21·48±0·07	Y	N
254	22 39 1·07	00 23 5·30	14·90±0·06	22·24±0·18	22·60±0·18	–	–
255	22 39 3·88	00 26 40·89	14·46±0·06	17·56±0·04	—	N	Y
256	22 38 50·01	00 22 34·47	13·49±0·05	Saturated	17·58±0·04	N	Y
257	22 38 52·95	00 22 47·91	14·24±0·05	—	—	–	–
258	22 38 52·38	00 29 3·59	14·55±0·06	16·54±0·04	—	N	Y
259	22 38 50·30	00 29 11·81	16·20±0·14	19·72±0·05	—	Y	N
260	22 38 56·12	00 30 35·30	16·25±0·12	20·09±0·05	22·62±0·16	Y	N
261	22 38 55·28	00 30 43·82	14·03±0·05	16·74±0·04	18·81±0·04	N	Y
262	22 38 56·39	00 30 44·39	14·66±0·06	19·04±0·04	21·83±0·09	–	–
263	22 38 56·85	00 30 53·56	16·68±0·16	17·70±0·04	18·67±0·04	Y	N
264	00 52 6·68	00 15 33·98	13·63±0·05	Saturated	—	N	Y
265	00 52 10·66	00 15 35·34	14·73±0·05	18·03±0·04	—	Y	N
266	00 52 10·07	00 15 39·59	16·90±0·17	19·65±0·04	—	N	N
267	00 52 6·99	00 15 54·34	15·80±0·08	18·79±0·04	—	Y	N
268	00 52 9·92	00 15 57·50	17·05±0·19	21·60±0·10	—	Y	N
269	00 52 7·09	00 16 7·61	13·53±0·05	Saturated	—	N	N
270	00 52 36·28	00 18 4·65	16·55±0·12	—	—	–	–
271	00 52 36·55	00 18 9·82	16·23±0·10	19·02±0·04	20·09±0·04	Y	N
272	00 52 31·83	00 18 37·65	16·76±0·14	—	—	–	–
273	00 52 32·69	00 18 39·61	17·14±0·19	—	—	–	–
274	00 52 34·06	00 18 42·19	15·79±0·08	17·86±0·04	19·52±0·04	N	Y
275	00 52 31·39	00 19 2·46	11·62±0·05	Saturated	Saturated	N	N
276	00 52 34·44	00 19 6·12	15·87±0·08	19·79±0·04	22·16±0·09	N	N
277	00 52 33·75	00 19 8·60	17·23±0·20	—	—	–	–
278	00 52 30·32	00 19 27·93	16·65±0·13	—	—	–	–
279	00 52 34·51	00 19 27·23	14·88±0·06	Saturated	17·21±0·04	N	N
280	00 52 27·76	00 16 17·83	16·14±0·09	19·36±0·04	22·12±0·09	N	N
281	00 52 29·84	00 16 48·97	16·97±0·16	19·42±0·04	20·62±0·05	Y	Y
282	00 52 38·84	00 23 20·96	15·35±0·07	—	—	–	–

ID	RA	DEC	K	R	B	G	R
283	00 52 37·41	00 23 55·91	14·25±0·05	18·36±0·04	—	Y	Y
284	00 52 35·16	00 24 45·68	16·82±0·19	20·18±0·05	—	Y	N
285	00 52 34·76	00 20 19·43	15·56±0·08	18·14±0·04	19·46±0·04	Y	Y
286	00 52 40·63	00 14 57·24	16·06±0·09	—	—	–	–
287	00 52 33·94	00 15 28·97	17·16±0·20	—	—	–	–
288	00 52 37·75	00 15 38·02	15·57±0·07	18·60±0·04	19·94±0·04	Y	Y
289	00 52 36·87	00 15 47·36	16·70±0·14	18·32±0·04	19·20±0·04	N	N
290	00 52 13·34	00 23 10·03	13·37±0·05	Saturated	—	N	N
291	00 52 13·80	00 23 32·68	16·96±0·20	20·36±0·05	—	Y	N
292	00 52 11·17	00 23 48·42	14·61±0·06	18·58±0·04	—	N	Y
293	00 52 15·23	00 23 49·49	15·52±0·08	18·76±0·04	—	Y	N
294	00 52 9·19	00 23 56·33	15·31±0·07	—	—	–	–
295	00 52 14·31	00 23 56·77	15·36±0·07	18·42±0·04	—	Y	N
296	00 52 7·87	00 24 24·73	16·66±0·16	20·30±0·05	—	Y	N
297	00 52 4·75	00 20 52·75	15·43±0·07	18·05±0·04	—	Y	N
298	00 52 5·38	00 21 26·35	16·60±0·13	20·80±0·07	—	Y	N
299	00 52 8·28	00 21 28·60	14·73±0·06	17·62±0·04	—	N	Y
300	00 52 9·76	00 21 30·25	16·04±0·09	18·34±0·04	—	Y	N
301	00 52 9·01	00 21 40·36	17·09±0·20	—	—	–	–
302	00 52 8·35	00 21 48·30	14·18±0·05	16·95±0·04	—	Y	N
303	00 52 13·18	00 17 0·61	16·87±0·17	20·14±0·05	—	Y	N
304	00 52 12·15	00 17 13·21	16·83±0·16	19·17±0·04	—	N	Y
305	00 52 10·33	00 17 20·39	17·16±0·21	—	—	–	–
306	00 52 15·91	00 17 22·13	15·16±0·06	—	—	–	–
307	00 52 12·75	00 17 25·90	15·73±0·08	19·22±0·04	—	N	N
308	00 52 19·77	00 23 25·78	16·95±0·17	—	—	–	–
309	00 52 18·95	00 23 32·65	15·64±0·07	—	—	–	–
310	00 52 19·98	00 23 47·07	16·43±0·11	—	—	–	–
311	00 52 17·39	00 24 5·44	11·10±0·05	Saturated	—	N	N
312	00 52 20·15	00 24 14·74	14·97±0·06	18·51±0·04	—	Y	Y
313	00 52 17·60	00 24 20·68	16·25±0·10	19·63±0·05	—	Y	N
314	00 52 21·87	00 24 29·16	17·02±0·18	20·06±0·05	—	Y	N
315	00 52 21·10	00 25 1·65	17·14±0·20	—	—	–	–
316	00 52 25·49	00 20 11·44	16·80±0·13	21·50±0·09	—	Y	N
317	00 52 24·21	00 20 29·08	15·20±0·06	17·94±0·04	19·73±0·04	Y	Y
318	00 52 22·30	00 20 37·49	16·98±0·16	—	—	–	–
319	00 52 25·52	00 20 39·10	16·92±0·16	20·41±0·06	22·14±0·09	Y	N
320	00 52 24·81	00 20 45·78	16·63±0·12	18·79±0·04	—	Y	N
321	00 52 16·03	00 18 58·77	16·50±0·13	20·14±0·05	—	Y	N
322	00 52 16·89	00 19 14·99	14·10±0·05	17·40±0·04	—	N	Y
323	00 52 17·10	00 19 55·94	16·93±0·17	19·20±0·04	—	Y	N
324	00 52 27·09	00 24 30·20	15·79±0·10	19·51±0·04	—	N	N
325	00 52 27·31	00 24 38·29	14·62±0·06	18·29±0·04	—	N	Y
326	00 52 23·33	00 24 40·86	15·86±0·10	—	—	–	–
327	00 52 25·67	00 24 51·40	15·83±0·10	18·57±0·04	—	Y	N
328	00 52 27·41	00 21 1·12	14·35±0·06	18·43±0·04	—	N	N
329	00 52 27·57	00 21 23·25	15·75±0·10	19·33±0·04	—	Y	N

ID	RA	DEC	K	R	B	G	R
330	00 52 29·06	00 21 36·10	14·81±0·06	—	—	–	–
331	00 52 30·44	00 21 47·98	15·22±0·07	18·68±0·04	—	N	Y
332	00 52 44·19	00 10 37·28	12·64±0·05	Saturated	Saturated	N	N
333	00 52 46·55	00 10 49·16	16·86±0·17	20·65±0·05	—	Y	N
334	00 52 47·79	00 10 52·72	15·83±0·08	19·80±0·04	21·15±0·06	Y	N
335	00 52 47·46	00 10 57·31	16·85±0·17	—	22·62±0·16	–	–
336	00 52 48·07	00 11 11·93	16·57±0·13	19·99±0·04	21·40±0·06	Y	N
337	00 52 48·86	00 11 18·85	16·38±0·12	19·53±0·04	20·90±0·05	Y	N
338	00 52 48·20	00 11 33·02	15·57±0·07	19·62±0·04	21·84±0·09	N	N
339	00 52 47·08	00 11 32·76	15·68±0·08	17·71±0·04	19·09±0·04	N	Y
340	00 52 48·71	00 11 51·46	15·59±0·07	19·86±0·04	21·98±0·09	Y	N
341	00 52 42·98	00 12 12·43	16·66±0·14	19·82±0·04	21·29±0·06	Y	N
342	00 53 10·93	00 10 9·29	17·08±0·19	—	—	–	–
343	00 53 10·32	00 10 17·94	15·58±0·07	—	—	–	–
344	00 53 16·37	00 10 20·11	15·52±0·07	—	—	–	–
345	00 53 10·70	00 10 23·13	16·65±0·13	17·77±0·04	18·44±0·04	N	N
346	00 53 10·28	00 10 42·10	16·59±0·13	20·06±0·05	21·82±0·09	Y	N
347	00 53 12·76	00 10 47·93	15·99±0·09	17·28±0·04	18·22±0·04	N	Y
348	00 53 9·79	00 11 0·20	14·47±0·05	18·12±0·04	20·36±0·05	N	N
349	00 53 11·74	00 11 38·97	16·56±0·12	19·13±0·04	20·65±0·05	Y	N
350	00 53 12·73	00 11 41·53	15·79±0·08	17·99±0·04	19·89±0·04	N	N
351	00 53 13·53	00 5 9·21	16·44±0·13	—	—	–	–
352	00 53 11·53	00 5 22·41	16·33±0·13	—	—	–	–
353	00 53 12·83	00 5 30·51	13·70±0·05	Saturated	Saturated	N	Y
354	00 53 12·64	00 5 48·91	14·29±0·05	17·80±0·04	19·86±0·04	Y	N
355	00 53 8·76	00 5 55·12	16·68±0·15	18·88±0·04	19·76±0·04	Y	N
356	00 53 9·54	00 6 5·00	15·08±0·06	18·27±0·04	20·46±0·04	Y	N
357	00 53 11·05	00 6 6·58	13·37±0·05	Saturated	Saturated	N	N
358	00 53 16·43	00 6 8·82	16·15±0·10	19·73±0·04	22·67±0·14	Y	N
359	00 53 16·69	00 6 21·49	15·69±0·08	—	—	–	–
360	00 52 48·99	00 9 26·06	17·24±0·21	22·00±0·11	—	Y	N
361	00 52 44·93	00 9 40·96	15·12±0·06	—	—	–	–
362	00 52 47·71	00 9 43·32	17·10±0·18	20·18±0·04	22·03±0·10	N	N
363	00 52 46·35	00 10 4·23	16·32±0·10	19·36±0·04	20·42±0·05	Y	Y
364	00 52 47·10	00 10 19·78	16·58±0·12	20·14±0·04	22·33±0·12	Y	N
365	00 52 42·74	00 10 29·49	17·10±0·17	21·85±0·10	—	Y	N
366	00 52 44·58	00 7 30·30	17·08±0·19	22·60±0·19	—	Y	N
367	00 52 45·06	00 7 38·01	13·32±0·05	Saturated	16·97±0·04	N	Y
368	00 52 48·77	00 7 43·42	12·28±0·05	Saturated	Saturated	N	N
369	00 52 54·23	00 5 7·63	13·47±0·05	Saturated	18·09±0·04	N	N
370	00 52 49·01	00 5 12·80	17·18±0·20	—	—	–	–
371	00 52 51·06	00 5 14·37	14·81±0·06	Saturated	17·46±0·04	N	N
372	00 52 49·95	00 5 27·87	15·44±0·07	—	—	–	–
373	00 52 54·09	00 5 27·37	16·38±0·12	18·77±0·04	20·17±0·04	Y	N
374	00 52 51·40	00 5 29·65	16·92±0·18	19·04±0·04	20·22±0·04	Y	N
375	00 52 51·17	00 5 45·83	14·82±0·06	18·27±0·04	20·38±0·05	N	Y
376	00 52 58·93	00 9 38·61	16·62±0·15	—	22·08±0·14	–	–

ID	RA	DEC	K	R	B	G	R
377	00 52 50·41	00 7 26·42	15·45±0·07	—	—	–	–
378	00 52 51·47	00 7 28·52	17·10±0·20	19·70±0·04	20·74±0·05	Y	N
379	00 52 54·99	00 7 38·15	17·03±0·19	—	—	–	–
380	00 52 52·22	00 7 45·79	17·19±0·20	22·65±0·19	—	Y	N
381	00 52 54·22	00 7 47·12	14·03±0·05	Saturated	18·12±0·04	N	Y
382	00 52 55·13	00 7 59·47	15·00±0·06	Saturated	16·93±0·04	N	N
383	00 52 55·23	00 8 13·40	17·09±0·20	—	—	–	–
384	00 53 3·55	00 9 40·12	17·17±0·19	—	—	–	–
385	00 52 59·56	00 9 44·62	14·35±0·05	16·82±0·04	18·28±0·04	Y	N
386	00 53 5·20	00 9 46·14	17·20±0·20	—	—	–	–
387	00 53 2·15	00 9 46·91	16·88±0·16	20·85±0·13	—	Y	N
388	00 52 59·51	00 9 56·84	15·09±0·06	—	—	–	–
389	00 53 7·11	00 10 26·41	15·94±0·08	—	18·73±0·04	–	–
390	00 53 3·43	00 10 37·53	15·33±0·06	18·21±0·04	20·20±0·04	N	Y
391	00 53 10·42	00 6 37·83	15·23±0·06	Saturated	19·52±0·04	N	N
392	00 53 7·44	00 7 15·48	16·24±0·10	20·18±0·05	21·61±0·06	Y	N
393	00 53 8·49	00 7 13·16	12·94±0·05	Saturated	18·89±0·04	N	Y
394	00 53 4·49	00 8 2·77	16·26±0·11	19·87±0·05	22·15±0·10	Y	N
395	00 53 11·83	00 11 54·04	16·40±0·11	19·76±0·05	22·03±0·10	Y	N
396	00 53 12·35	00 12 12·19	16·92±0·15	—	—	–	–
397	00 53 16·03	00 12 45·61	14·80±0·05	17·85±0·04	20·02±0·04	N	Y
398	00 53 15·66	00 12 46·22	17·19±0·19	20·68±0·07	22·82±0·19	Y	N
399	00 53 16·55	00 12 50·32	17·13±0·17	21·71±0·15	22·16±0·12	–	–
400	00 53 11·97	00 13 25·19	17·21±0·19	20·46±0·06	22·32±0·13	Y	N
401	00 53 14·93	00 13 25·96	15·39±0·06	18·43±0·04	18·99±0·04	Y	N
402	01 53 10·82	00 49 1·11	13·89±0·05	Saturated	—	N	Y
403	01 53 12·93	00 49 3·22	16·81±0·19	—	—	–	–
404	01 53 10·78	00 49 46·84	16·80±0·18	—	—	–	–
405	01 53 1·29	00 41 51·41	15·73±0·09	18·50±0·04	—	Y	N
406	01 53 5·36	00 42 32·46	14·28±0·05	18·18±0·04	—	Y	Y
407	01 53 14·14	00 47 37·45	15·75±0·09	17·54±0·04	—	N	Y
408	01 53 15·70	00 42 55·02	16·37±0·13	20·02±0·05	—	Y	N
409	01 53 16·87	00 43 8·04	16·57±0·16	21·66±0·11	—	Y	N
410	01 53 18·80	00 43 11·24	12·60±0·05	Saturated	—	N	Y
411	01 53 28·63	00 46 32·36	14·43±0·06	17·39±0·04	—	Y	Y
412	01 53 19·85	00 39 45·70	16·62±0·17	21·22±0·08	—	Y	N
413	01 53 32·10	00 49 51·29	15·18±0·07	—	—	–	–
414	01 53 32·74	00 49 54·56	15·07±0·06	17·95±0·04	—	N	Y
415	01 53 35·28	00 49 55·79	16·91±0·20	19·28±0·04	—	Y	N
416	01 53 33·83	00 50 2·06	15·98±0·10	—	—	–	–
417	01 53 32·47	00 48 9·46	12·90±0·05	Saturated	—	N	Y
418	01 53 31·84	00 45 49·69	15·05±0·07	17·74±0·04	—	Y	Y
419	01 53 0·01	00 41 7·52	15·84±0·09	18·78±0·04	—	N	N
420	01 53 0·51	00 42 2·55	15·40±0·07	17·94±0·04	—	N	N
421	01 53 0·63	00 42 21·93	16·44±0·14	18·31±0·04	—	N	N
422	01 53 21·37	00 46 21·86	15·66±0·07	19·15±0·04	—	Y	Y
423	01 53 20·49	00 46 52·46	15·27±0·06	17·95±0·04	—	N	N

ID	RA	DEC	K	R	B	G	R
424	01 53 27·81	00 44 32·64	17·15±0·20	—	—	–	–
425	01 53 24·68	00 44 39·93	14·68±0·05	17·51±0·04	—	Y	Y
426	01 53 27·88	00 45 1·18	17·15±0·19	22·29±0·17	—	–	–
427	01 53 26·57	00 45 8·68	16·81±0·16	21·92±0·13	—	–	–
428	01 53 28·37	00 45 9·80	16·83±0·15	20·47±0·05	—	Y	N
429	01 53 26·57	00 45 18·19	17·09±0·19	—	—	–	–
430	01 53 27·95	00 45 25·69	17·14±0·19	—	—	–	–
431	01 53 21·72	00 41 17·11	15·67±0·09	18·13±0·04	—	Y	N
432	01 53 20·86	00 41 57·87	15·42±0·08	18·04±0·04	—	Y	Y
433	01 53 19·41	00 42 32·47	15·54±0·08	—	—	–	–
434	01 53 31·18	00 43 20·30	14·23±0·05	17·25±0·04	—	N	N
435	01 53 34·71	00 41 18·60	17·03±0·17	—	—	–	–
436	01 53 31·22	00 41 19·00	17·20±0·20	—	—	–	–
437	01 53 3·69	00 48 41·69	17·19±0·20	21·11±0·07	—	Y	N
438	01 53 3·80	00 49 23·65	17·12±0·18	21·17±0·07	—	Y	N
439	01 53 2·82	00 49 26·34	15·33±0·06	16·93±0·04	—	N	Y
440	01 53 0·80	00 50 8·55	16·99±0·17	21·29±0·08	—	Y	N
441	01 53 1·29	00 50 13·51	16·70±0·13	20·65±0·06	—	Y	N
442	01 53 6·30	00 47 37·15	16·94±0·17	19·12±0·04	—	Y	Y
443	01 53 5·62	00 47 44·12	16·43±0·11	20·17±0·05	—	Y	N
444	01 53 4·30	00 47 48·24	17·08±0·18	21·34±0·09	—	Y	N
445	01 53 6·35	00 48 17·98	15·46±0·06	18·23±0·04	—	Y	N
446	01 53 10·12	00 45 52·91	15·42±0·07	—	—	–	–
447	01 53 6·26	00 46 2·88	16·18±0·11	—	—	–	–
448	01 53 9·71	00 46 11·14	14·78±0·06	—	—	–	–
449	01 53 10·68	00 46 19·45	16·94±0·18	—	—	–	–
450	01 53 10·07	00 46 40·77	16·91±0·18	—	—	–	–
451	01 53 4·59	00 45 34·78	15·35±0·07	—	—	–	–
452	01 53 20·01	00 48 42·15	17·17±0·18	19·57±0·04	—	Y	N
453	01 53 22·62	00 49 11·69	16·85±0·14	20·64±0·05	—	Y	N
454	01 53 13·88	00 43 58·12	16·82±0·13	20·28±0·05	—	Y	N
455	01 53 13·50	00 44 41·53	15·77±0·07	18·77±0·04	—	Y	Y
456	01 53 11·14	00 44 45·71	15·95±0·08	—	—	–	–
457	01 53 14·85	00 45 1·44	17·10±0·17	20·83±0·06	—	Y	N
458	01 53 14·12	00 45 13·19	17·27±0·20	22·09±0·16	—	Y	N
459	01 53 13·79	00 45 36·08	17·16±0·18	—	—	–	–
460	01 53 15·11	00 39 43·33	9·72±0·05	—	—	–	–
461	01 53 13·83	00 39 59·46	16·00±0·13	—	—	–	–
462	01 53 12·42	00 40 35·81	15·22±0·08	17·95±0·04	—	Y	Y
463	01 53 26·20	00 48 15·25	16·54±0·15	19·41±0·04	—	Y	Y
464	01 52 23·77	00 39 7·05	14·61±0·05	Saturated	—	N	Y
465	01 52 25·36	00 39 58·41	17·07±0·18	—	—	–	–
466	01 52 40·14	00 32 45·31	16·69±0·18	—	—	–	–
467	01 52 40·19	00 32 49·07	16·70±0·15	19·42±0·04	—	Y	Y
468	01 52 39·76	00 30 19·28	14·84±0·06	Saturated	—	N	Y
469	01 52 48·85	00 39 51·71	15·57±0·09	18·50±0·04	19·74±0·04	Y	Y
470	01 52 45·83	00 40 17·39	15·61±0·09	19·34±0·04	21·64±0·07	N	N

ID	RA	DEC	K	R	B	G	R
471	01 52 45·35	00 35 42·42	14·81±0·06	Saturated	—	N	Y
472	01 52 57·60	00 33 11·27	15·12±0·07	19·32±0·04	—	–	–
473	01 52 54·99	00 33 52·20	13·25±0·05	Saturated	—	N	Y
474	01 52 19·70	00 34 27·38	16·85±0·13	19·33±0·04	—	Y	N
475	01 52 20·22	00 34 52·79	16·40±0·10	18·91±0·04	—	N	N
476	01 52 20·67	00 35 1·30	14·99±0·05	18·50±0·04	—	N	Y
477	01 52 32·33	00 37 10·16	16·63±0·12	20·79±0·06	—	Y	N
478	01 52 28·29	00 37 17·30	16·70±0·12	20·83±0·06	—	Y	N
479	01 52 31·61	00 37 41·77	16·04±0·08	19·56±0·04	—	Y	N
480	01 52 30·11	00 35 9·20	12·98±0·05	Saturated	—	N	Y
481	01 52 31·18	00 35 17·38	16·29±0·12	—	—	–	–
482	01 52 32·02	00 35 28·09	15·39±0·07	—	—	–	–
483	01 52 27·29	00 32 51·21	16·43±0·12	—	—	–	–
484	01 52 28·00	00 33 29·75	14·54±0·05	Saturated	—	N	Y
485	01 52 31·03	00 31 1·47	10·38±0·05	Saturated	—	N	N
486	01 52 27·31	00 31 11·25	15·72±0·08	—	—	–	–
487	01 52 26·98	00 31 14·50	16·85±0·16	—	—	–	–
488	01 52 31·08	00 31 18·47	17·19±0·20	—	—	–	–
489	01 52 30·68	00 31 24·02	16·66±0·14	19·39±0·05	—	Y	Y
490	01 52 38·62	00 36 26·20	16·06±0·09	Saturated	—	N	Y
491	01 52 35·55	00 36 27·18	15·63±0·07	19·34±0·04	—	Y	N
492	01 52 34·91	00 36 29·24	14·76±0·06	—	—	–	–
493	01 52 37·15	00 36 32·51	16·12±0·10	17·47±0·04	—	N	N
494	01 52 38·30	00 36 52·30	16·39±0·12	—	20·93±0·05	–	–
495	01 52 38·83	00 36 54·83	13·59±0·05	Saturated	Saturated	N	N
496	01 52 37·04	00 37 18·30	17·05±0·20	21·74±0·09	—	–	–
497	01 52 37·97	00 34 32·34	13·80±0·05	Saturated	—	N	Y
498	01 52 40·47	00 34 57·58	11·68±0·05	Saturated	—	N	N
499	01 52 19·67	00 28 0·01	15·23±0·06	18·88±0·04	—	Y	N
500	01 52 22·96	00 28 52·36	14·97±0·06	18·22±0·04	—	N	Y
501	01 52 24·06	00 29 13·69	15·10±0·06	18·00±0·04	—	Y	N
502	01 52 45·28	00 22 33·32	16·15±0·10	19·93±0·04	—	Y	N
503	01 52 43·23	00 23 1·31	16·37±0·11	18·93±0·04	—	Y	Y
504	01 52 41·62	00 23 3·42	16·16±0·10	—	—	–	–
505	01 52 40·43	00 23 8·48	11·65±0·05	Saturated	—	N	N
506	01 52 44·12	00 23 21·20	16·43±0·12	19·46±0·04	—	Y	N
507	01 52 36·97	00 20 11·86	16·95±0·16	20·32±0·05	—	Y	N
508	01 52 52·69	00 28 53·35	16·52±0·11	18·37±0·04	—	N	N
509	01 52 52·77	00 29 45·23	16·06±0·08	—	—	–	–
510	01 52 52·08	00 29 46·18	15·23±0·06	17·96±0·04	—	Y	Y
511	01 52 49·82	00 29 47·50	16·66±0·12	20·48±0·05	—	Y	N
512	01 52 49·91	00 29 54·93	16·94±0·15	—	—	–	–
513	01 52 52·01	00 30 10·03	16·40±0·10	19·79±0·04	—	Y	N
514	01 52 41·70	00 26 57·49	16·40±0·10	—	—	–	–
515	01 52 45·70	00 27 30·45	16·02±0·08	—	—	–	–
516	01 52 48·99	00 27 44·30	14·21±0·05	Saturated	—	N	N
517	01 52 45·72	00 27 46·09	14·85±0·05	18·22±0·04	—	Y	Y

ID	RA	DEC	K	R	B	G	R
518	01 52 48·66	00 28 11·50	15·26±0·06	19·06±0·04	—	N	N
519	01 52 45·62	00 28 23·17	17·16±0·18	—	—	–	–
520	01 52 51·65	00 26 7·60	16·63±0·12	20·03±0·05	—	Y	N
521	01 52 50·02	00 26 30·46	16·68±0·12	18·97±0·04	—	Y	Y
522	01 52 53·92	00 26 35·22	15·39±0·06	—	—	–	–
523	01 52 50·56	00 26 47·42	15·52±0·07	—	—	–	–
524	01 52 47·77	00 27 6·86	15·22±0·06	Saturated	—	N	N
525	01 52 55·08	00 25 7·90	17·00±0·18	20·19±0·05	—	Y	N
526	01 52 56·16	00 25 58·24	14·39±0·05	18·26±0·04	—	N	N
527	01 52 55·18	00 26 1·51	14·89±0·06	18·53±0·04	—	Y	Y
528	01 52 52·04	00 26 9·38	15·17±0·06	—	—	–	–
529	01 52 54·69	00 26 11·49	17·09±0·20	20·49±0·05	—	Y	N
530	01 52 58·88	00 26 53·42	15·98±0·09	—	—	–	–
531	01 52 55·49	00 20 42·16	16·71±0·15	—	—	–	–
532	01 52 54·89	00 20 45·05	15·24±0·06	18·00±0·04	—	Y	Y
533	01 52 54·30	00 21 25·08	17·10±0·19	21·94±0·10	—	–	–
534	01 52 20·07	00 25 30·40	15·57±0·07	—	—	–	–
535	01 52 20·70	00 26 2·32	16·78±0·15	18·26±0·04	—	Y	Y
536	01 52 17·82	00 26 24·69	12·57±0·05	Saturated	—	N	N
537	01 52 22·61	00 22 53·37	13·52±0·05	Saturated	—	N	N
538	01 52 23·55	00 23 22·30	17·06±0·18	20·26±0·04	—	Y	N
539	01 52 24·92	00 23 43·42	14·05±0·05	Saturated	—	N	Y
540	01 52 27·74	00 24 32·90	15·63±0·07	18·58±0·04	—	Y	N
541	01 52 27·74	00 21 49·88	15·92±0·08	18·83±0·04	—	N	N
542	01 52 23·24	00 22 2·71	17·14±0·18	22·03±0·11	—	–	–
543	01 52 21·42	00 22 16·06	16·94±0·17	19·92±0·04	—	Y	N
544	01 52 20·59	00 22 28·13	16·96±0·16	—	—	–	–
545	01 52 20·10	00 19 49·20	16·52±0·11	19·73±0·05	—	N	N
546	01 52 26·54	00 20 15·16	15·63±0·07	—	—	–	–
547	01 52 24·16	00 20 20·22	16·75±0·14	19·00±0·04	—	N	Y
548	01 52 23·74	00 20 23·22	16·56±0·12	—	—	–	–
549	01 52 25·48	00 21 3·85	15·16±0·06	16·80±0·04	—	N	N
550	01 52 31·99	00 28 57·55	16·87±0·17	18·98±0·04	—	Y	Y
551	01 52 33·57	00 29 1·92	16·99±0·18	21·10±0·07	—	Y	N
552	01 52 30·38	00 29 10·95	15·67±0·08	19·06±0·04	—	N	N
553	01 52 30·94	00 29 36·74	14·08±0·05	18·15±0·04	—	N	N
554	01 52 31·59	00 29 50·40	16·31±0·11	—	—	–	–
555	01 52 31·69	00 27 1·28	16·97±0·18	19·81±0·04	—	Y	Y
556	01 52 35·11	00 27 23·60	14·82±0·06	—	—	–	–
557	01 52 32·91	00 27 30·36	16·17±0·10	17·28±0·04	—	N	N
558	01 52 41·29	00 28 27·72	15·43±0·07	17·80±0·04	—	Y	N
559	01 52 36·83	00 28 55·47	12·92±0·05	Saturated	—	N	N
560	01 52 43·18	00 29 0·94	15·49±0·07	—	—	–	–
561	01 52 39·81	00 29 5·68	16·27±0·10	18·78±0·04	—	Y	Y
562	01 52 34·21	00 25 10·99	16·67±0·16	—	—	–	–
563	01 52 36·76	00 25 14·35	14·40±0·05	18·09±0·04	—	Y	Y
564	01 52 37·05	00 25 30·23	16·92±0·16	19·70±0·04	—	Y	N

ID	RA	DEC	K	R	B	G	R
565	01 52 36·50	00 25 49·43	15·56±0·07	19·85±0·05	—	Y	N
566	01 52 19·21	00 38 30·48	16·67±0·17	—	—	–	–
567	01 52 26·65	00 31 9·48	14·50±0·06	—	—	–	–
568	01 52 24·55	00 31 17·28	14·38±0·05	18·04±0·04	—	N	Y
569	01 52 32·38	00 32 40·97	13·37±0·05	Saturated	—	N	Y
570	01 52 41·66	00 39 34·10	16·67±0·19	20·18±0·04	22·30±0·10	Y	N
571	01 52 38·20	00 39 55·06	15·20±0·08	18·50±0·04	20·56±0·05	Y	Y
572	01 52 49·19	00 34 26·93	14·96±0·06	17·74±0·04	—	N	Y
573	01 52 47·83	00 34 42·11	16·79±0·20	—	—	–	–
574	01 52 46·01	00 32 37·12	15·16±0·06	18·78±0·04	—	Y	Y
575	01 52 46·53	00 31 14·41	14·90±0·06	18·20±0·04	—	N	Y
576	01 52 44·69	00 31 30·01	15·42±0·08	19·32±0·04	—	Y	N

ID	RA	DEC	K	R	B	V	I	G	R
1	09 18 5·54	−00 20 14·09	17·30±0·33	—	—	—	—	–	–
2	09 18 9·15	−00 20 13·04	16·81±0·23	—	—	—	—	–	–
3	09 18 3·52	−00 20 5·49	17·10±0·28	—	—	—	—	–	–
4	09 18 8·76	−00 19 34·74	16·85±0·22	—	—	—	—	–	–
5	09 18 7·83	−00 19 34·93	17·07±0·28	22·13±0·21	—	—	—	Y	N
6	09 18 6·78	−00 19 29·34	17·00±0·26	20·74±0·07	22·94±0·29	—	—	Y	N
7	09 18 8·96	−00 19 27·89	16·37±0·16	—	—	—	—	–	–
8	09 18 3·96	−00 19 25·24	13·87±0·05	Saturated	19·04±0·04	—	—	N	N
9	09 18 5·36	−00 19 24·83	13·66±0·05	Saturated	Saturated	—	—	N	Y
10	09 18 4·33	−00 19 14·08	16·88±0·24	18·31±0·03	19·29±0·04	—	—	Y	N
11	09 18 7·37	−00 19 10·74	17·16±0·30	18·72±0·03	20·13±0·05	—	—	N	N
12	09 18 2·05	−00 18 33·41	17·20±0·31	—	—	—	—	–	–
13	09 18 30·49	−00 24 51·37	14·14±0·05	17·11±0·03	19·34±0·04	—	—	N	N
14	09 18 33·60	−00 24 47·49	17·09±0·27	19·58±0·04	21·40±0·08	—	—	N	N
15	09 18 30·36	−00 24 37·16	16·90±0·24	—	—	—	—	–	–
16	09 18 29·19	−00 24 36·60	16·69±0·20	—	—	—	—	–	–
17	09 18 34·17	−00 24 34·11	15·85±0·10	19·21±0·03	21·64±0·09	—	—	Y	N
18	09 18 28·01	−00 24 30·94	15·69±0·09	19·29±0·03	21·39±0·08	—	—	Y	N
19	09 18 29·22	−00 24 24·18	17·38±0·33	19·85±0·04	22·23±0·15	—	—	N	N
20	09 18 30·32	−00 24 15·37	15·09±0·07	Saturated	16·84±0·04	—	—	N	Y
21	09 18 32·58	−00 23 58·37	16·62±0·19	—	—	—	—	–	–
22	09 18 31·83	−00 23 56·13	16·51±0·17	—	—	—	—	–	–
23	09 18 34·03	−00 23 53·35	16·23±0·14	—	—	—	—	–	–
24	09 18 33·64	−00 23 51·97	16·48±0·17	—	—	—	—	–	–
25	09 18 31·61	−00 23 24·96	17·30±0·32	—	—	—	—	–	–
26	09 18 41·98	−00 23 3·26	15·72±0·09	18·05±0·03	20·17±0·05	—	—	N	N
27	09 18 43·50	−00 22 55·08	17·33±0·32	19·24±0·03	21·26±0·07	—	—	Y	N
28	09 18 40·40	−00 22 47·69	17·51±0·36	20·34±0·05	21·83±0·11	—	—	Y	N
29	09 18 42·23	−00 22 43·33	17·52±0·36	—	—	—	—	–	–
30	09 18 37·08	−00 22 30·90	14·75±0·06	17·45±0·03	19·56±0·04	—	—	N	N
31	09 18 38·10	−00 22 23·50	16·75±0·20	—	—	—	—	–	–
32	09 18 39·62	−00 22 15·33	13·33±0·05	Saturated	Saturated	—	—	N	Y
33	09 18 40·47	−00 21 57·21	15·09±0·07	18·56±0·03	20·73±0·06	—	—	N	N
34	09 18 38·21	−00 21 26·82	14·08±0·05	Saturated	17·36±0·04	—	—	N	N
35	09 18 41·51	−00 19 11·36	15·62±0·09	20·52±0·06	22·59±0·21	—	—	–	–
36	09 18 42·11	−00 19 10·89	16·20±0·14	—	—	—	—	–	–
37	09 18 40·77	−00 19 10·80	15·96±0·12	—	—	—	—	–	–
38	09 18 44·34	−00 19 6·01	17·17±0·30	20·02±0·04	22·59±0·22	—	—	Y	N
39	09 18 40·43	−00 18 54·19	16·89±0·24	—	—	—	—	–	–
40	09 18 44·05	−00 18 53·80	16·23±0·14	19·71±0·04	22·20±0·16	—	—	N	N
41	09 18 41·75	−00 18 53·71	15·21±0·07	18·49±0·03	19·61±0·04	—	—	Y	N
42	09 18 39·51	−00 18 43·11	16·98±0·25	18·92±0·03	20·18±0·05	—	—	N	N
43	09 18 43·42	−00 18 44·21	16·44±0·17	19·42±0·04	21·84±0·12	—	—	Y	N
44	09 18 41·86	−00 18 39·41	16·34±0·16	20·04±0·04	22·54±0·21	—	—	Y	N
45	09 18 39·96	−00 18 36·69	16·60±0·20	—	—	—	—	–	–
46	09 18 41·06	−00 18 35·62	17·27±0·33	—	—	—	—	–	–
47	09 18 44·44	−00 18 33·04	16·81±0·23	—	—	—	—	–	–

ID	RA	DEC	K	R	B	V	I	G	R
48	09 18 45·71	−00 18 30·29	16·86±0·23	—	—	—	—	–	–
49	09 18 40·78	−00 18 26·24	17·01±0·27	19·78±0·04	21·36±0·08	—	—	Y	N
50	09 18 44·89	−00 18 26·62	16·94±0·25	18·13±0·03	19·15±0·04	—	—	N	N
51	09 18 43·27	−00 18 22·79	15·12±0·07	Saturated	16·96±0·04	—	—	N	Y
52	09 18 41·40	−00 18 12·83	16·32±0·16	19·32±0·03	21·26±0·08	—	—	Y	N
53	09 18 45·56	−00 18 16·46	14·77±0·06	—	—	—	—	–	–
54	09 18 45·52	−00 18 1·26	17·13±0·29	—	—	—	—	–	–
55	09 18 39·40	−00 17 39·26	16·63±0·20	Saturated	—	—	—	N	N
56	09 18 44·17	−00 17 40·84	9·39±0·05	—	—	—	—	–	–
57	09 18 45·68	−00 17 32·43	17·02±0·27	—	—	—	—	–	–
58	09 18 38·56	−00 20 19·74	16·82±0·24	—	—	—	—	–	–
59	09 18 38·15	−00 20 18·61	16·45±0·18	21·56±0·13	—	—	—	–	–
60	09 18 45·25	−00 20 19·01	13·29±0·05	Saturated	17·26±0·04	—	—	N	N
61	09 18 42·21	−00 20 11·94	16·97±0·27	—	—	—	—	–	–
62	09 18 45·34	−00 20 7·78	15·73±0·10	—	—	—	—	–	–
63	09 18 42·81	−00 20 6·96	16·66±0·21	20·83±0·07	—	—	—	–	–
64	09 18 40·80	−00 19 53·90	15·43±0·09	—	20·95±0·06	—	—	–	–
65	09 18 40·76	−00 19 50·12	15·04±0·07	18·02±0·03	20·15±0·05	—	—	N	N
66	09 18 39·21	−00 19 48·39	17·21±0·33	—	—	—	—	–	–
67	09 18 43·96	−00 19 44·76	16·90±0·26	—	—	—	—	–	–
68	09 18 44·57	−00 19 30·53	17·15±0·30	—	—	—	—	–	–
69	09 18 38·84	−00 19 29·16	17·04±0·29	—	—	—	—	–	–
70	09 18 41·78	−00 19 29·91	13·92±0·05	Saturated	Saturated	—	—	N	Y
71	09 18 38·56	−00 19 21·18	16·02±0·12	19·21±0·03	21·70±0·11	—	—	Y	N
72	09 18 38·19	−00 19 13·84	17·01±0·27	—	—	—	—	–	–
73	09 18 38·93	−00 19 10·12	17·05±0·28	—	—	—	—	–	–
74	09 18 39·66	−00 19 4·39	16·92±0·25	—	—	—	—	–	–
75	09 18 42·94	−00 18 51·64	16·92±0·26	21·34±0·11	—	—	—	Y	N
76	09 18 39·45	−00 18 47·38	16·55±0·19	—	—	—	—	–	–
77	09 18 8·61	−00 20 18·26	15·94±0·11	18·69±0·03	21·11±0·11	—	—	N	N
78	09 18 8·05	−00 20 19·34	12·83±0·05	15·74±0·03	17·95±0·04	—	—	N	N
79	09 18 12·29	−00 20 16·54	17·42±0·34	—	—	—	—	–	–
80	09 18 13·50	−00 20 14·33	16·18±0·13	18·45±0·04	20·53±0·05	—	—	Y	N
81	09 18 11·09	−00 20 14·79	16·10±0·12	—	—	—	—	–	–
82	09 18 9·89	−00 20 13·22	16·91±0·23	—	—	—	—	–	–
83	09 18 11·57	−00 19 57·40	14·26±0·05	—	20·25±0·11	—	—	–	–
84	09 18 12·94	−00 19 58·86	10·36±0·05	Saturated	Saturated	—	—	N	N
85	09 18 13·04	−00 19 36·78	16·71±0·20	—	—	—	—	–	–
86	09 18 11·10	−00 19 35·78	17·22±0·30	—	—	—	—	–	–
87	09 18 13·61	−00 19 36·04	16·65±0·19	—	—	—	—	–	–
88	09 18 10·04	−00 19 30·77	14·26±0·05	—	—	—	—	–	–
89	09 18 13·36	−00 19 28·86	15·77±0·10	Saturated	Saturated	—	—	N	N
90	09 18 11·71	−00 19 28·35	16·40±0·16	19·27±0·03	21·63±0·10	—	—	N	N
91	09 18 10·66	−00 19 25·30	14·60±0·06	—	—	—	—	–	–
92	09 18 10·26	−00 21 3·19	16·24±0·14	—	—	—	—	–	–
93	09 18 10·54	−00 21 1·80	15·85±0·10	—	—	—	—	–	–
94	09 18 9·88	−00 20 35·44	15·52±0·09	—	—	—	—	–	–

ID	RA	DEC	K	R	B	V	I	G	R
95	09 18 10·49	−00 20 32·80	16·88±0·22	—	22·26±0·17	—	—	—	—
96	09 18 4·79	−00 20 30·28	17·51±0·36	—	—	—	—	—	—
97	09 18 6·51	−00 20 22·86	17·30±0·31	—	—	—	—	—	—
98	09 18 10·28	−00 19 53·32	17·18±0·29	20·07±0·05	21·57±0·10	—	—	Y	N
99	09 18 10·61	−00 19 28·59	16·82±0·21	—	—	—	—	—	—
100	09 18 8·70	−00 26 10·35	16·67±0·21	—	—	—	—	—	—
101	09 18 8·48	−00 26 9·58	16·68±0·21	—	—	—	—	—	—
102	09 18 8·31	−00 25 58·39	17·28±0·34	—	—	—	—	—	—
103	09 18 12·07	−00 25 46·14	15·74±0·11	—	—	—	—	—	—
104	09 18 11·66	−00 25 28·00	14·47±0·06	—	20·17±0·05	—	—	—	—
105	09 18 11·85	−00 25 13·55	15·07±0·07	15·82±0·03	16·79±0·04	—	—	N	N
106	09 18 10·18	−00 25 7·96	17·14±0·30	—	—	—	—	—	—
107	09 18 8·93	−00 24 55·94	15·60±0·10	—	20·74±0·06	—	—	—	—
108	09 18 11·53	−00 24 54·85	16·78±0·24	19·98±0·04	22·44±0·18	—	—	Y	N
109	09 18 10·40	−00 24 47·64	11·93±0·05	—	Saturated	—	—	—	—
110	09 18 13·55	−00 24 44·67	16·00±0·13	18·81±0·03	21·05±0·08	—	—	Y	N
111	09 18 12·05	−00 24 34·33	16·46±0·17	17·55±0·03	19·81±0·05	—	—	N	N
112	09 18 20·11	−00 19 22·56	15·52±0·09	—	—	—	—	—	—
113	09 18 17·31	−00 19 7·85	16·35±0·17	—	—	—	—	—	—
114	09 18 20·23	−00 19 4·30	15·24±0·08	19·44±0·04	21·95±0·13	—	—	N	N
115	09 18 19·57	−00 18 44·79	16·91±0·26	—	—	—	—	—	—
116	09 18 16·20	−00 18 39·41	12·56±0·05	Saturated	Saturated	—	—	N	N
117	09 18 17·03	−00 18 30·51	13·32±0·05	Saturated	Saturated	—	—	N	Y
118	09 18 15·57	−00 18 10·74	17·01±0·28	20·04±0·05	21·91±0·13	—	—	Y	N
119	09 18 17·39	−00 18 11·49	15·68±0·10	18·69±0·03	21·17±0·08	—	—	Y	N
120	09 18 16·74	−00 24 20·17	16·78±0·20	20·73±0·06	22·60±0·25	—	—	Y	N
121	09 18 17·31	−00 23 52·72	15·25±0·07	18·07±0·03	19·90±0·05	—	—	Y	N
122	09 18 15·45	−00 23 42·00	14·34±0·06	15·96±0·03	17·34±0·04	—	—	N	Y
123	09 18 18·09	−00 23 0·11	16·87±0·23	20·85±0·07	—	—	—	Y	N
124	09 18 18·28	−00 26 21·08	17·34±0·31	—	—	—	—	—	—
125	09 18 19·60	−00 25 52·58	17·50±0·35	—	—	—	—	—	—
126	09 18 20·21	−00 25 51·33	17·32±0·30	—	—	—	—	—	—
127	09 18 16·83	−00 25 34·81	13·46±0·05	—	17·14±0·04	—	—	—	—
128	09 18 17·06	−00 24 58·61	14·71±0·06	18·58±0·03	21·06±0·08	—	—	N	N
129	09 18 18·88	−00 26 54·63	17·17±0·29	—	—	—	—	—	—
130	09 18 19·75	−00 26 46·49	17·39±0·34	—	—	—	—	—	—
131	09 18 21·90	−00 26 16·63	13·27±0·05	—	—	—	—	—	—
132	09 18 25·27	−00 26 1·90	17·33±0·32	—	—	—	—	—	—
133	09 18 23·96	−00 25 59·09	16·56±0·17	—	20·00±0·05	—	—	—	—
134	09 18 21·59	−00 23 22·38	17·38±0·36	—	—	—	—	—	—
135	09 18 24·21	−00 23 17·17	15·82±0·11	—	—	—	—	—	—
136	09 18 22·79	−00 23 12·07	17·15±0·30	—	—	—	—	—	—
137	09 18 21·96	−00 23 8·05	16·72±0·21	—	21·26±0·24	—	—	—	—
138	09 18 21·56	−00 23 8·16	16·26±0·15	—	21·10±0·20	—	—	—	—
139	09 18 27·46	−00 23 7·59	16·74±0·22	—	—	—	—	—	—
140	09 18 27·50	−00 23 3·35	16·47±0·17	—	—	—	—	—	—
141	09 18 26·38	−00 23 2·30	14·58±0·06	17·15±0·03	18·70±0·04	—	—	N	N

ID	RA	DEC	K	R	B	V	I	G	R
142	09 18 25·37	−00 23 1·65	16·28±0·15	21·12±0·08	—	—	—	Y	N
143	09 18 23·55	−00 22 47·77	15·95±0·12	—	—	—	—	–	–
144	09 18 24·90	−00 22 37·40	12·98±0·05	Saturated	Saturated	—	—	N	Y
145	09 18 23·07	−00 22 31·88	16·61±0·20	—	—	—	—	–	–
146	09 18 23·98	−00 22 23·33	16·67±0·20	21·28±0·16	—	—	—	Y	N
147	09 18 26·21	−00 22 10·16	16·89±0·25	20·34±0·05	22·42±0·17	—	—	Y	N
148	09 18 24·52	−00 21 54·84	11·72±0·05	Saturated	16·06±0·04	—	—	N	N
149	09 18 28·07	−00 0 35·97	16·46±0·19	—	—	—	—	–	–
150	09 18 31·67	−00 0 30·89	9·99±0·05	—	—	—	—	–	–
151	09 18 33·80	00 0 10·52	16·78±0·25	—	—	—	—	–	–
152	09 18 33·13	00 0 11·52	17·05±0·31	—	—	—	—	–	–
153	09 18 31·06	00 0 13·25	13·29±0·05	—	—	—	—	–	–
154	09 18 28·19	00 0 23·88	17·11±0·33	—	—	—	—	–	–
155	09 18 32·00	00 0 28·71	15·80±0·11	—	—	—	—	–	–
156	09 18 33·56	00 0 45·40	16·82±0·26	—	—	—	—	–	–
157	09 18 31·65	00 0 45·80	14·74±0·07	—	—	—	—	–	–
158	09 18 33·58	00 0 57·07	16·75±0·25	—	—	—	—	–	–
159	09 18 27·49	−00 7 32·89	16·08±0·13	—	—	—	—	–	–
160	09 18 27·82	−00 7 27·00	14·43±0·06	—	—	—	—	–	–
161	09 18 28·18	−00 7 23·18	17·26±0·31	—	—	—	—	–	–
162	09 18 25·58	−00 7 17·61	16·88±0·23	—	—	—	—	–	–
163	09 18 27·95	−00 6 55·11	16·09±0·12	—	—	—	—	–	–
164	09 18 24·79	−00 6 54·72	13·24±0·05	—	—	—	—	–	–
165	09 18 25·80	−00 6 41·82	12·86±0·05	—	—	—	—	–	–
166	09 18 28·54	−00 6 36·60	17·29±0·32	—	—	—	—	–	–
167	09 18 40·68	00 0 3·18	15·72±0·10	—	—	—	—	–	–
168	09 18 38·75	00 0 14·23	17·15±0·29	—	—	—	—	–	–
169	09 18 38·36	00 0 16·79	16·92±0·24	—	—	—	—	–	–
170	09 18 42·94	00 0 17·91	17·38±0·35	—	—	—	—	–	–
171	09 18 40·53	00 0 20·73	14·62±0·06	—	—	—	—	–	–
172	09 18 37·70	00 0 26·26	16·92±0·24	—	—	—	—	–	–
173	09 18 42·52	00 0 29·85	17·10±0·27	—	—	—	—	–	–
174	09 18 42·82	00 0 37·61	16·20±0·14	—	—	—	—	–	–
175	09 18 42·21	00 0 37·32	17·20±0·30	—	—	—	—	–	–
176	09 18 44·41	00 0 56·97	17·31±0·33	—	—	—	—	–	–
177	09 18 43·03	00 0 58·20	17·26±0·30	—	—	—	—	–	–
178	09 18 41·01	−00 1 30·70	16·63±0·22	—	—	—	—	–	–
179	09 18 42·00	−00 1 1·45	16·45±0·20	—	—	—	—	–	–
180	09 18 40·04	−00 1 2·29	13·91±0·05	—	—	—	—	–	–
181	09 18 39·18	−00 0 56·19	16·37±0·18	—	—	—	—	–	–
182	09 18 36·97	−00 0 50·34	16·78±0·25	—	—	—	—	–	–
183	09 18 38·31	−00 0 51·13	14·50±0·06	—	—	—	—	–	–
184	09 18 34·72	−00 0 46·98	16·08±0·14	—	—	—	—	–	–
185	09 18 35·72	−00 0 43·72	17·23±0·36	—	—	—	—	–	–
186	09 18 35·85	−00 0 4·57	17·24±0·35	—	—	—	—	–	–
187	09 18 37·13	−00 3 21·81	12·13±0·05	—	—	—	—	–	–
188	09 18 37·14	−00 3 12·30	15·79±0·13	—	—	—	—	–	–

ID	RA	DEC	K	R	B	V	I	G	R
189	09 18 39·02	−00 3 3·58	12·83±0·05	—	—	—	—	–	–
190	09 18 39·74	−00 2 52·82	15·74±0·12	—	—	—	—	–	–
191	09 18 37·44	−00 4 53·70	17·35±0·36	—	—	—	—	–	–
192	09 18 37·49	−00 4 34·64	10·75±0·05	—	—	—	—	–	–
193	09 18 35·42	−00 4 20·49	17·01±0·28	—	—	—	—	–	–
194	09 18 32·55	−00 4 11·82	17·06±0·27	—	—	—	—	–	–
195	09 18 31·32	−00 4 10·72	13·75±0·05	—	—	—	—	–	–
196	09 18 34·24	−00 4 10·84	15·23±0·08	—	—	—	—	–	–
197	09 18 33·99	−00 4 5·26	15·90±0·11	—	—	—	—	–	–
198	09 18 34·45	−00 3 48·81	17·06±0·28	—	—	—	—	–	–
199	09 18 44·10	−00 1 25·95	15·53±0·08	—	—	—	—	–	–
200	09 18 43·63	−00 1 9·42	14·61±0·06	—	—	—	—	–	–
201	09 18 43·26	−00 0 54·01	15·90±0·10	—	—	—	—	–	–
202	09 18 47·71	−00 0 50·12	16·85±0·21	—	—	—	—	–	–
203	09 18 44·45	−00 0 47·30	13·62±0·05	—	—	—	—	–	–
204	09 18 47·83	−00 0 43·44	17·29±0·31	—	—	—	—	–	–
205	09 18 46·90	−00 0 40·05	16·52±0·16	—	—	—	—	–	–
206	09 18 45·46	−00 0 32·36	17·31±0·31	—	—	—	—	–	–
207	09 18 46·95	−00 0 3·75	16·95±0·24	—	—	—	—	–	–
208	09 18 44·64	00 0 3·71	16·96±0·22	—	—	—	—	–	–
209	09 18 45·82	−00 2 46·81	12·51±0·05	—	—	—	—	–	–
210	09 18 47·02	−00 2 25·89	16·55±0·17	—	—	—	—	–	–
211	09 18 44·03	−00 2 12·15	13·94±0·05	—	—	—	—	–	–
212	09 18 42·58	−00 2 10·12	15·10±0·07	—	—	—	—	–	–
213	09 18 58·30	−00 6 33·61	15·85±0·11	—	—	—	—	–	–
214	09 18 58·65	−00 5 58·36	14·12±0·05	—	—	—	—	–	–
215	09 19 2·24	−00 5 51·35	16·58±0·18	—	—	—	—	–	–
216	09 19 0·25	−00 5 35·62	17·01±0·26	—	—	—	—	–	–
217	09 19 2·33	−00 5 21·43	17·12±0·29	—	—	—	—	–	–
218	10 43 34·92	00 5 35·00	17·44±0·33	20·84±0·07	22·78±0·24	—	—	Y	N
219	10 43 34·17	00 5 37·36	16·58±0·17	20·12±0·05	22·27±0·16	—	—	Y	N
220	10 43 39·38	00 5 45·75	12·95±0·05	Saturated	17·30±0·04	—	—	N	N
221	10 43 35·82	00 5 55·52	16·82±0·21	20·06±0·04	22·62±0·20	—	—	Y	N
222	10 43 36·25	00 6 13·52	14·65±0·06	17·95±0·03	19·77±0·04	—	—	Y	Y
223	10 43 35·67	00 6 45·53	17·16±0·27	20·71±0·06	23·07±0·28	21·82±0·19	18·74±0·03	Y	N
224	10 43 36·91	00 9 34·33	17·54±0·34	21·78±0·18	—	—	21·09±0·15	Y	N
225	10 43 38·64	00 9 40·99	15·81±0·09	—	21·55±0·09	20·23±0·05	—	–	–
226	10 43 39·27	00 9 42·38	15·66±0·08	17·27±0·03	18·48±0·04	17·72±0·03	Saturated	Y	N
227	10 43 38·99	00 9 46·12	15·89±0·09	—	—	—	—	–	–
228	10 43 39·90	00 9 52·49	15·35±0·07	19·32±0·04	21·90±0·11	20·36±0·06	17·52±0·02	N	N
229	10 43 36·59	00 9 55·16	17·06±0·22	20·52±0·07	22·48±0·17	21·69±0·17	19·60±0·04	Y	N
230	10 43 38·33	00 10 8·45	16·59±0·16	20·19±0·05	22·61±0·19	21·10±0·10	19·21±0·03	Y	N
231	10 43 40·33	00 10 13·50	17·67±0·36	—	—	—	—	–	–
232	10 43 37·17	00 10 35·40	17·57±0·33	—	—	—	—	–	–
233	10 43 42·23	00 2 30·92	17·19±0·24	—	—	—	21·16±0·25	–	–
234	10 43 36·47	00 2 33·88	17·38±0·29	—	—	—	—	–	–
235	10 43 41·19	00 2 40·06	17·19±0·25	—	—	—	—	–	–

ID	RA	DEC	K	R	B	V	I	G	R
236	10 43 42·01	00 2 42·02	13·17±0·05	Saturated	Saturated	Saturated	Saturated	N	N
237	10 43 36·66	00 2 47·97	17·46±0·30	—	—	—	—	–	–
238	10 43 37·86	00 2 54·28	16·36±0·13	—	—	—	—	–	–
239	10 43 40·00	00 3 3·29	15·53±0·08	18·85±0·03	20·71±0·08	19·59±0·04	18·14±0·03	Y	N
240	10 43 36·71	00 3 16·24	12·31±0·05	Saturated	Saturated	Saturated	Saturated	N	N
241	10 43 41·62	00 3 18·17	17·17±0·24	21·09±0·10	23·23±0·31	22·12±0·22	19·82±0·09	Y	N
242	10 43 38·64	00 3 21·23	15·33±0·07	17·36±0·03	18·75±0·04	17·94±0·03	Saturated	Y	Y
243	10 43 42·20	00 3 29·67	17·54±0·32	20·73±0·08	22·54±0·18	21·50±0·13	19·49±0·05	Y	N
244	10 43 38·04	00 3 31·01	16·44±0·13	17·88±0·03	19·11±0·04	18·37±0·03	Saturated	N	N
245	10 43 35·67	00 3 55·12	15·40±0·07	—	—	—	—	–	–
246	10 43 37·01	00 4 11·42	17·20±0·25	—	—	—	—	–	–
247	10 43 36·71	00 4 13·20	17·23±0·25	—	—	—	—	–	–
248	10 43 42·37	00 1 15·82	17·20±0·26	—	—	—	—	–	–
249	10 43 44·89	00 1 41·43	16·60±0·16	—	—	—	—	–	–
250	10 43 45·26	00 1 57·58	17·05±0·24	—	—	—	—	–	–
251	10 43 42·69	00 2 4·24	13·03±0·05	15·71±0·03	17·75±0·04	16·57±0·03	Saturated	N	Y
252	10 43 45·32	00 2 20·01	17·22±0·26	—	—	—	—	–	–
253	10 43 45·25	00 2 33·86	17·63±0·37	—	—	—	—	–	–
254	10 43 45·99	00 2 48·79	17·41±0·30	—	—	—	—	–	–
255	10 43 46·03	00 2 52·96	17·13±0·25	—	—	—	—	–	–
256	10 43 39·63	00 2 57·11	17·35±0·30	—	—	—	—	–	–
257	10 43 46·27	00 6 35·69	16·95±0·24	22·61±0·30	—	—	—	–	–
258	10 43 43·88	00 6 39·48	15·58±0·09	21·25±0·10	—	—	20·05±0·06	–	–
259	10 43 46·78	00 6 40·51	17·24±0·30	—	—	—	—	–	–
260	10 43 44·45	00 6 58·98	16·48±0·17	20·53±0·07	—	21·49±0·14	18·67±0·03	Y	N
261	10 43 44·82	00 7 10·22	17·51±0·37	—	—	—	—	–	–
262	10 43 44·97	00 7 16·83	16·95±0·25	20·51±0·07	22·02±0·12	21·32±0·12	19·55±0·07	Y	N
263	10 43 47·74	00 7 27·06	15·82±0·10	16·84±0·03	17·49±0·04	17·08±0·03	16·50±0·02	N	Y
264	10 43 45·53	00 7 38·24	16·91±0·24	—	—	—	—	–	–
265	10 43 51·10	00 7 42·80	17·35±0·33	—	—	—	—	–	–
266	10 43 50·15	00 7 45·61	15·85±0·11	—	—	—	—	–	–
267	10 43 45·48	00 7 52·25	16·06±0·12	19·80±0·05	21·91±0·11	20·71±0·07	18·03±0·02	Y	N
268	10 43 48·85	00 7 53·08	17·12±0·28	—	—	—	—	–	–
269	10 43 49·35	00 8 11·71	16·65±0·18	20·32±0·06	21·80±0·10	21·11±0·11	19·55±0·04	Y	N
270	10 43 46·69	00 8 16·62	17·50±0·37	—	—	—	—	–	–
271	10 43 56·91	00 3 36·51	16·21±0·13	19·53±0·04	22·14±0·15	20·96±0·09	18·71±0·02	Y	N
272	10 43 54·04	00 3 40·05	16·61±0·18	—	—	—	—	–	–
273	10 43 55·91	00 3 56·98	16·86±0·21	—	—	—	—	–	–
274	10 43 55·33	00 3 59·78	16·45±0·15	—	—	—	—	–	–
275	10 43 57·03	00 4 26·23	14·39±0·06	Saturated	17·36±0·04	16·58±0·03	Saturated	N	Y
276	10 43 54·36	00 4 27·93	17·32±0·31	—	—	—	—	–	–
277	10 43 57·63	00 5 19·40	17·57±0·36	—	—	—	—	–	–
278	10 44 4·44	00 8 5·99	17·68±0·36	—	—	—	—	–	–
279	10 44 9·21	00 8 7·75	17·58±0·34	—	—	—	—	–	–
280	10 44 8·46	00 8 14·48	17·44±0·31	18·95±0·03	20·74±0·05	19·72±0·04	18·23±0·03	N	N
281	10 44 7·24	00 8 20·55	17·57±0·34	—	—	—	—	–	–
282	10 44 6·64	00 8 39·22	17·15±0·24	20·24±0·05	22·23±0·27	21·07±0·10	19·45±0·05	Y	N

ID	RA	DEC	K	R	B	V	I	G	R
283	10 44 9·37	00 8 41·23	16·54±0·15	—	—	—	—	–	–
284	10 44 8·17	00 8 52·99	16·32±0·13	20·16±0·05	22·62±0·19	21·35±0·12	19·11±0·05	Y	N
285	10 44 6·89	00 8 54·23	13·82±0·05	Saturated	18·46±0·04	17·25±0·03	Saturated	N	Y
286	10 44 3·19	00 9 2·05	17·08±0·23	21·78±0·18	—	22·39±0·29	20·37±0·11	Y	N
287	10 44 9·55	00 9 16·21	16·85±0·19	22·09±0·24	—	—	20·28±0·10	Y	N
288	10 44 8·60	00 9 20·53	17·02±0·22	20·82±0·08	—	21·98±0·20	19·77±0·06	Y	N
289	10 44 5·25	00 3 35·55	16·63±0·17	20·60±0·07	22·77±0·24	21·77±0·17	18·85±0·03	Y	N
290	10 44 4·57	00 3 36·31	17·54±0·34	—	—	—	—	–	–
291	10 44 3·76	00 3 42·06	16·62±0·16	—	—	—	—	–	–
292	10 44 3·37	00 3 50·97	16·55±0·16	19·61±0·04	21·96±0·11	20·55±0·07	18·77±0·02	Y	N
293	10 44 6·82	00 4 8·52	17·49±0·31	19·18±0·03	20·64±0·05	19·76±0·04	18·67±0·03	N	N
294	10 44 6·09	00 4 11·98	17·30±0·28	21·49±0·14	—	22·46±0·30	20·72±0·15	N	N
295	10 44 5·83	00 4 16·72	14·44±0·06	Saturated	17·83±0·04	16·98±0·03	Saturated	N	Y
296	10 44 5·84	00 4 22·78	17·19±0·26	—	—	—	—	–	–
297	10 44 9·55	00 4 41·97	16·65±0·17	21·18±0·11	22·33±0·15	21·80±0·18	20·82±0·15	Y	N
298	10 44 7·10	00 4 47·06	16·90±0·20	—	—	—	—	–	–
299	10 44 6·18	00 4 47·23	15·05±0·06	18·32±0·03	20·60±0·05	19·20±0·03	16·84±0·02	N	N
300	10 44 8·81	00 5 7·71	17·23±0·27	—	—	—	—	–	–
301	10 44 12·07	00 5 17·80	17·02±0·26	21·10±0·10	23·21±0·30	22·09±0·24	20·33±0·10	Y	N
302	10 44 14·19	00 5 43·99	15·08±0·07	—	17·83±0·04	17·11±0·03	—	–	–
303	10 44 14·74	00 5 46·41	15·29±0·08	—	—	—	—	–	–
304	10 44 14·93	00 5 52·63	14·67±0·06	—	—	—	—	–	–
305	10 44 14·65	00 5 56·02	15·53±0·08	—	—	—	—	–	–
306	10 44 17·25	00 6 6·78	17·37±0·33	—	—	—	—	–	–
307	10 44 12·55	00 6 12·45	15·65±0·09	—	—	—	—	–	–
308	10 44 17·44	00 6 19·58	15·88±0·11	—	—	—	—	–	–
309	10 44 11·42	00 6 28·14	16·93±0·23	—	—	—	—	–	–
310	10 44 16·80	00 6 29·22	9·46±0·05	—	—	—	—	–	–
311	10 44 11·76	00 6 35·08	17·03±0·26	—	—	—	—	–	–
312	10 44 10·78	00 6 34·30	16·91±0·23	20·82±0·08	22·31±0·15	21·09±0·10	20·23±0·09	Y	N
313	10 42 46·12	−00 11 36·27	16·95±0·27	—	—	—	—	–	–
314	10 42 47·95	−00 11 35·59	17·38±0·37	—	—	—	—	–	–
315	10 42 48·54	−00 11 33·60	16·92±0·26	20·69±0·07	22·67±0·20	—	—	Y	N
316	10 42 46·10	−00 11 19·67	17·33±0·36	—	—	—	—	–	–
317	10 42 50·90	−00 11 18·63	16·94±0·27	—	—	—	—	–	–
318	10 42 49·21	−00 11 9·26	15·54±0·09	17·29±0·03	18·55±0·04	—	—	N	Y
319	10 42 47·97	−00 11 8·11	16·94±0·26	—	—	—	—	–	–
320	10 42 49·98	−00 11 0·19	15·46±0·09	—	—	—	—	–	–
321	10 42 49·74	−00 10 55·69	16·33±0·16	—	—	—	—	–	–
322	10 42 49·60	−00 10 50·37	16·15±0·14	20·55±0·06	22·34±0·15	—	—	Y	N
323	10 42 48·71	−00 10 40·15	15·43±0·08	18·44±0·03	20·13±0·09	—	—	Y	N
324	10 42 50·91	−00 10 34·24	17·19±0·32	—	22·75±0·21	—	—	–	–
325	10 42 49·03	−00 10 25·74	16·53±0·19	19·85±0·04	21·48±0·27	—	—	Y	N
326	10 42 51·58	−00 10 28·45	10·25±0·05	Saturated	Saturated	—	—	N	N
327	10 42 57·45	−00 7 2·02	17·15±0·29	—	—	—	—	–	–
328	10 43 0·36	−00 6 41·26	15·35±0·08	—	—	—	—	–	–
329	10 42 57·69	−00 6 16·45	14·68±0·06	17·86±0·03	19·97±0·04	—	—	Y	Y

ID	RA	DEC	K	R	B	V	I	G	R
330	10 42 54·17	−00 5 36·39	13·88±0·05	14·79±0·03	Saturated	—	—	N	N
331	10 42 53·11	−00 10 32·62	17·45±0·35	—	—	—	—	–	–
332	10 42 56·33	−00 10 17·83	17·05±0·27	21·25±0·10	23·20±0·30	—	—	Y	N
333	10 42 53·31	−00 9 50·67	16·33±0·14	19·36±0·03	21·69±0·09	—	—	N	N
334	10 42 56·90	−00 9 45·72	13·22±0·05	Saturated	18·96±0·04	—	—	N	Y
335	10 42 54·06	−00 9 45·01	17·06±0·25	—	—	—	—	–	–
336	10 43 0·13	−00 9 9·13	17·45±0·35	—	—	—	—	–	–
337	10 42 58·90	−00 9 6·28	17·09±0·27	20·20±0·05	22·83±0·23	—	—	Y	N
338	10 43 0·66	−00 9 1·55	16·60±0·19	—	—	—	—	–	–
339	10 42 58·12	−00 8 56·80	17·35±0·32	—	—	—	—	–	–
340	10 43 20·63	−00 4 5·71	17·22±0·30	—	—	—	—	–	–
341	10 43 18·92	−00 4 3·10	17·09±0·27	—	—	—	—	–	–
342	10 43 17·80	−00 4 0·57	14·93±0·06	16·95±0·03	18·75±0·05	—	—	N	Y
343	10 43 18·16	−00 3 55·25	16·98±0·25	20·79±0·19	—	—	—	Y	N
344	10 43 14·52	−00 3 42·20	17·15±0·28	22·25±0·21	—	—	—	Y	N
345	10 43 14·02	−00 3 9·61	14·64±0·06	—	—	—	—	–	–
346	10 43 8·58	−00 9 59·18	17·06±0·29	—	—	—	—	–	–
347	10 43 11·17	−00 9 54·65	16·80±0·23	—	—	—	—	–	–
348	10 43 12·91	−00 9 54·66	17·19±0·33	—	—	—	—	–	–
349	10 43 10·50	−00 9 43·63	17·17±0·32	—	—	—	—	–	–
350	10 43 13·02	−00 9 40·97	17·16±0·31	21·83±0·19	22·92±0·26	22·30±0·27	21·41±0·21	–	–
351	10 43 11·54	−00 9 38·94	15·77±0·11	18·68±0·03	20·84±0·06	19·28±0·04	17·92±0·02	Y	N
352	10 43 9·63	−00 9 33·60	16·84±0·25	—	—	—	—	–	–
353	10 43 13·11	−00 9 24·62	15·67±0·10	19·20±0·04	21·28±0·12	19·82±0·05	18·35±0·03	Y	N
354	10 43 10·11	−00 9 19·63	16·83±0·24	—	—	—	—	–	–
355	10 43 10·27	−00 9 14·91	17·08±0·29	—	—	—	—	–	–
356	10 43 12·36	−00 9 11·02	13·95±0·05	—	—	—	—	–	–
357	10 43 10·03	−00 9 6·51	16·32±0·16	—	—	—	—	–	–
358	10 43 13·19	−00 12 49·85	16·65±0·20	19·75±0·04	22·21±0·15	20·67±0·08	18·31±0·03	Y	N
359	10 43 14·24	−00 12 42·45	17·46±0·37	19·60±0·04	21·59±0·09	20·32±0·06	18·87±0·03	Y	N
360	10 43 11·57	−00 12 31·61	16·98±0·26	20·34±0·06	22·99±0·28	21·59±0·17	19·50±0·04	Y	N
361	10 43 10·53	−00 12 17·60	15·02±0·07	17·26±0·03	19·14±0·04	17·98±0·03	Saturated	Y	Y
362	10 43 7·77	−00 12 5·24	16·90±0·24	—	—	—	—	–	–
363	10 43 7·30	−00 11 54·76	16·27±0·15	20·29±0·06	22·60±0·21	21·24±0·11	18·35±0·03	Y	N
364	10 43 9·61	−00 11 49·76	15·82±0·11	18·82±0·03	20·72±0·06	19·55±0·04	17·86±0·02	Y	N
365	10 43 8·44	−00 11 42·97	17·12±0·28	—	—	—	—	–	–
366	10 43 8·05	−00 11 34·00	16·84±0·22	—	—	—	—	–	–
367	10 43 7·68	−00 11 33·97	17·30±0·33	21·64±0·20	—	—	20·05±0·07	–	–
368	10 43 9·51	−00 11 31·66	16·18±0·14	19·25±0·04	21·07±0·11	19·82±0·04	18·54±0·03	Y	N
369	10 43 10·42	−00 11 30·21	17·19±0·31	—	—	—	—	–	–
370	10 43 7·91	−00 11 27·22	16·55±0·18	21·66±0·16	—	22·26±0·26	21·12±0·16	Y	N
371	10 43 23·99	−00 7 32·43	17·37±0·34	—	—	—	—	–	–
372	10 43 20·41	−00 7 20·58	17·22±0·30	—	—	—	—	–	–
373	10 43 21·50	−00 7 7·83	17·20±0·29	—	—	—	—	–	–
374	10 43 20·43	−00 6 50·46	14·56±0·06	—	—	—	—	–	–
375	10 43 24·10	−00 6 45·58	14·69±0·06	Saturated	18·32±0·04	—	—	N	Y
376	10 43 21·32	−00 6 39·53	17·48±0·36	22·19±0·20	—	—	—	Y	N

ID	RA	DEC	K	R	B	V	I	G	R
377	10 43 27·86	−00 6 23·56	16·76±0·21	20·09±0·11	22·12±0·12	—	—	Y	N
378	10 43 21·81	−00 10 44·76	15·47±0·08	18·59±0·03	20·95±0·06	19·42±0·04	17·75±0·02	Y	N
379	10 43 19·84	−00 10 11·70	17·00±0·26	—	—	—	—	–	–
380	10 43 21·04	−00 10 5·68	14·92±0·06	17·26±0·03	19·17±0·04	17·97±0·03	Saturated	Y	Y
381	10 43 19·49	−00 9 36·82	17·21±0·31	—	—	—	—	–	–
382	10 43 24·80	−00 12 33·01	16·48±0·16	—	—	21·69±0·18	19·93±0·06	–	–
383	10 43 25·06	−00 12 28·53	13·44±0·05	16·72±0·03	18·96±0·04	17·59±0·03	Saturated	N	Y
384	10 43 45·14	−00 16 51·37	14·47±0·06	—	—	—	—	–	–
385	10 43 45·79	−00 16 41·86	14·49±0·06	—	—	—	—	–	–
386	10 43 46·86	−00 16 37·81	14·03±0·05	—	—	—	—	–	–
387	10 44 23·53	−00 22 37·39	16·24±0·16	—	—	—	—	–	–
388	10 44 23·73	−00 22 27·81	16·78±0·24	—	—	—	—	–	–
389	10 44 22·02	−00 22 21·96	16·58±0·20	20·85±0·09	—	22·35±0·26	19·73±0·05	Y	N
390	10 44 23·54	−00 22 16·15	16·82±0·24	—	—	—	—	–	–
391	10 44 22·71	−00 22 13·74	16·36±0·16	19·85±0·05	21·91±0·11	20·58±0·06	19·15±0·04	Y	N
392	10 44 21·68	−00 21 53·85	17·07±0·30	—	—	—	—	–	–
393	10 44 20·56	−00 21 52·37	14·96±0·07	Saturated	17·94±0·04	17·22±0·03	Saturated	N	Y
394	10 44 22·70	−00 21 49·51	17·20±0·33	—	—	—	—	–	–
395	10 44 21·72	−00 21 48·55	17·31±0·36	—	—	—	20·59±0·11	–	–
396	10 44 23·43	−00 21 41·53	16·68±0·22	—	—	—	—	–	–
397	10 43 55·31	−00 18 51·86	13·85±0·05	Saturated	17·04±0·04	16·09±0·03	Saturated	N	N
398	10 43 52·35	−00 18 35·78	15·75±0·10	16·94±0·03	17·75±0·04	17·23±0·03	16·58±0·02	N	Y
399	10 43 48·25	−00 22 47·88	16·50±0·25	—	—	—	—	–	–
400	10 43 49·42	−00 22 45·64	16·61±0·26	21·07±0·10	22·43±0·15	21·62±0·15	20·39±0·10	Y	N
401	10 43 49·99	−00 22 44·82	16·78±0·31	—	—	—	—	–	–
402	10 43 49·75	−00 22 44·79	16·74±0·30	22·10±0·23	—	—	—	–	–
403	10 43 49·94	−00 22 4·26	15·71±0·14	19·11±0·04	20·74±0·06	19·69±0·04	18·45±0·03	Y	N
404	10 43 49·57	−00 21 54·66	13·64±0·05	Saturated	17·46±0·04	16·51±0·03	Saturated	N	Y
405	10 44 4·61	−00 19 52·44	15·30±0·08	16·73±0·03	17·67±0·04	17·09±0·03	16·32±0·02	N	Y
406	10 44 2·56	−00 19 49·44	15·54±0·10	17·36±0·03	18·33±0·04	17·72±0·03	16·96±0·02	N	N
407	10 44 4·62	−00 19 29·49	16·91±0·26	—	—	—	—	–	–
408	10 44 4·94	−00 19 27·28	16·97±0·27	—	—	—	—	–	–
409	10 44 4·68	−00 19 22·85	17·10±0·30	—	—	—	—	–	–
410	10 44 3·66	−00 19 21·99	16·71±0·22	—	—	—	Saturated	–	–
411	10 44 1·82	−00 19 7·25	16·23±0·16	19·92±0·06	22·36±0·15	20·96±0·09	18·50±0·03	Y	N
412	10 43 57·47	−00 21 40·94	15·05±0·07	17·44±0·03	19·21±0·04	18·13±0·03	16·76±0·02	N	Y
413	10 43 58·91	−00 21 35·51	17·35±0·35	21·78±0·23	—	—	21·42±0·25	N	N
414	10 43 58·10	−00 21 20·04	16·78±0·21	—	—	—	—	–	–
415	10 43 59·48	−00 21 16·97	16·53±0·18	20·14±0·06	22·32±0·27	20·97±0·10	19·27±0·04	Y	N
416	10 44 8·47	−00 18 50·99	17·14±0·33	19·57±0·05	21·89±0·19	20·49±0·07	18·28±0·03	Y	N
417	10 44 5·32	−00 18 4·93	14·13±0·06	16·73±0·03	18·81±0·04	17·54±0·03	15·84±0·02	N	Y
418	10 44 8·95	−00 18 0·99	16·86±0·26	20·96±0·09	22·99±0·31	—	19·23±0·03	Y	N
419	10 44 11·55	−00 23 16·77	17·31±0·30	20·36±0·06	21·91±0·11	20·92±0·08	19·63±0·05	Y	N
420	10 44 10·40	−00 23 0·65	17·17±0·26	—	—	—	—	–	–
421	10 44 10·67	−00 22 55·48	17·23±0·29	20·87±0·09	23·18±0·30	21·84±0·17	19·57±0·05	Y	N
422	10 44 10·32	−00 22 48·90	17·31±0·30	—	—	—	—	–	–
423	10 44 10·96	−00 22 37·85	17·30±0·29	—	—	—	—	–	–

ID	RA	DEC	K	R	B	V	I	G	R
424	10 44 11·52	−00 22 26·66	13·13±0·05	Saturated	18·30±0·04	17·10±0·03	Saturated	N	Y
425	10 44 8·74	−00 22 22·19	17·07±0·25	—	—	—	—	–	–
426	10 44 22·95	−00 15 54·33	16·00±0·12	17·27±0·03	18·05±0·04	17·59±0·03	Saturated	N	Y
427	10 44 20·21	−00 15 34·32	16·30±0·14	—	21·90±0·12	—	—	–	–
428	10 44 22·26	−00 15 34·04	12·87±0·05	—	—	—	—	–	–
429	10 44 17·40	−00 18 49·22	14·00±0·05	Saturated	18·45±0·04	17·39±0·03	Saturated	N	Y
430	10 44 18·28	−00 18 26·29	15·60±0·09	18·55±0·03	19·85±0·04	18·94±0·03	17·92±0·02	Y	N
431	10 44 18·97	−00 18 12·59	16·88±0·24	21·01±0·10	23·01±0·29	21·70±0·17	20·09±0·06	Y	N
432	10 44 17·79	−00 18 8·46	17·16±0·31	—	—	—	—	–	–
433	10 44 16·89	−00 18 5·13	16·91±0·25	21·63±0·16	—	—	19·98±0·06	Y	N
434	10 44 20·28	−00 18 2·74	16·59±0·19	19·29±0·04	20·28±0·05	19·65±0·04	18·71±0·03	Y	N
435	13 41 47·02	00 10 4·61	16·72±0·24	19·86±0·04	21·87±0·11	20·59±0·07	19·04±0·03	Y	N
436	13 41 48·11	00 10 7·58	16·90±0·27	—	—	—	—	–	–
437	13 41 48·73	00 10 15·51	16·25±0·17	—	—	—	—	–	–
438	13 41 50·27	00 10 36·82	15·95±0·13	17·65±0·03	18·91±0·04	18·17±0·03	17·11±0·02	N	Y
439	13 41 46·47	00 10 39·79	15·95±0·13	18·35±0·03	19·91±0·04	18·94±0·03	17·70±0·02	Y	N
440	13 41 48·05	00 10 47·44	16·20±0·16	—	—	—	—	–	–
441	13 41 51·61	00 11 0·90	16·74±0·25	—	—	—	—	–	–
442	13 41 51·03	00 11 4·96	16·44±0·19	—	—	—	20·49±0·10	–	–
443	13 41 51·54	00 11 10·92	16·68±0·23	20·65±0·07	23·14±0·30	22·03±0·22	18·61±0·03	Y	N
444	13 41 53·42	00 11 13·66	16·48±0·20	20·79±0·08	—	22·29±0·28	19·48±0·04	Y	N
445	13 42 5·07	00 9 32·74	16·89±0·27	20·00±0·05	22·06±0·13	20·56±0·06	19·23±0·03	Y	N
446	13 42 8·32	00 9 56·45	16·15±0·15	20·22±0·05	22·32±0·15	21·23±0·12	19·39±0·04	Y	N
447	13 42 5·40	00 10 8·76	14·28±0·06	17·73±0·03	20·09±0·05	18·76±0·03	Saturated	N	Y
448	13 42 7·24	00 10 14·31	17·16±0·34	—	—	—	—	–	–
449	13 42 7·72	00 10 19·00	17·05±0·31	—	—	—	—	–	–
450	13 42 5·43	00 10 26·78	16·38±0·18	20·24±0·05	21·95±0·11	21·00±0·09	19·37±0·04	Y	N
451	13 42 5·18	00 7 49·07	16·35±0·16	19·14±0·04	21·09±0·10	19·88±0·04	18·14±0·03	Y	Y
452	13 42 3·16	00 7 49·83	15·82±0·11	18·99±0·04	21·04±0·08	19·82±0·04	18·10±0·03	Y	N
453	13 42 7·17	00 8 1·70	13·51±0·05	Saturated	Saturated	Saturated	Saturated	N	N
454	13 42 2·39	00 4 56·55	16·73±0·20	19·71±0·05	21·89±0·15	20·70±0·08	18·22±0·03	N	N
455	13 42 5·23	00 4 56·00	17·04±0·27	—	—	—	—	–	–
456	13 42 6·03	00 5 2·00	17·18±0·30	—	—	—	—	–	–
457	13 42 5·95	00 5 24·77	17·14±0·29	—	—	—	—	–	–
458	13 42 3·15	00 5 30·50	17·36±0·35	—	—	—	—	–	–
459	13 42 3·58	00 5 40·13	16·20±0·14	19·85±0·05	21·52±0·11	20·69±0·07	19·01±0·04	Y	N
460	13 42 5·72	00 5 39·95	16·86±0·24	—	—	—	—	–	–
461	13 42 0·94	00 5 46·42	17·04±0·27	—	—	—	—	–	–
462	13 42 −0·02	00 5 47·05	16·60±0·19	—	—	—	—	–	–
463	13 41 58·60	00 5 47·40	17·04±0·27	—	—	22·41±0·28	—	–	–
464	13 42 2·15	00 5 45·62	15·49±0·08	16·62±0·03	17·44±0·04	16·91±0·03	16·24±0·02	N	Y
465	13 42 3·74	00 5 52·17	16·89±0·24	20·51±0·08	21·28±0·09	20·63±0·07	19·97±0·08	Y	N
466	13 42 8·43	00 0 41·07	14·41±0·06	—	—	—	—	–	–
467	13 42 5·71	00 0 43·88	15·94±0·12	—	—	—	—	–	–
468	13 42 6·61	00 0 55·90	11·86±0·05	—	—	—	—	–	–
469	13 42 10·00	00 0 59·01	16·93±0·26	—	—	—	—	–	–
470	13 42 6·87	00 1 18·81	15·68±0·10	17·00±0·03	17·85±0·04	17·31±0·03	Saturated	N	N

ID	RA	DEC	K	R	B	V	I	G	R
471	13 42 9·41	00 1 31·67	14·99±0·07	17·15±0·03	18·57±0·04	17·68±0·03	Saturated	N	Y
472	13 42 12·90	00 2 0·01	16·68±0·21	—	—	—	—	–	–
473	13 42 12·48	00 2 2·84	17·08±0·29	—	—	—	—	–	–
474	13 42 12·83	00 2 4·45	17·24±0·34	—	—	—	—	–	–
475	13 42 13·08	00 2 6·21	17·30±0·36	—	—	—	—	–	–
476	13 42 11·99	00 2 7·18	16·66±0·20	20·53±0·08	22·56±0·26	21·20±0·13	—	Y	N
477	13 42 11·24	00 2 11·77	17·03±0·28	—	—	—	—	–	–
478	13 42 12·04	00 2 22·79	17·18±0·32	—	—	—	—	–	–
479	13 42 10·69	00 2 24·01	15·86±0·11	—	21·45±0·10	20·47±0·07	18·82±0·04	–	–
480	13 42 13·47	00 8 4·32	17·21±0·31	—	—	—	—	–	–
481	13 42 13·72	00 8 4·38	17·14±0·30	—	—	—	—	–	–
482	13 42 9·50	00 8 47·91	16·90±0·25	—	—	—	—	–	–
483	13 42 11·78	00 9 24·30	17·19±0·31	—	—	—	—	–	–
484	13 42 8·09	00 3 3·51	17·10±0·31	—	—	—	—	–	–
485	13 42 10·50	00 3 24·10	15·87±0·12	18·29±0·03	20·10±0·05	19·02±0·03	17·53±0·02	N	Y
486	13 41 45·96	00 8 12·96	17·11±0·29	—	—	—	—	–	–
487	13 41 45·64	00 8 15·01	17·37±0·35	—	—	—	—	–	–
488	13 41 45·28	00 8 18·19	16·97±0·26	—	—	—	—	–	–
489	13 41 44·59	00 8 19·91	17·31±0·34	—	—	—	—	–	–
490	13 41 41·70	00 8 35·02	17·24±0·32	—	—	—	—	–	–
491	13 41 39·33	00 8 43·51	17·14±0·29	—	—	—	—	–	–
492	13 41 39·04	00 8 50·33	17·42±0·36	—	—	—	—	–	–
493	13 41 40·56	00 8 52·09	17·21±0·30	—	—	—	—	–	–
494	13 41 42·78	00 8 58·70	17·37±0·36	21·78±0·18	22·88±0·26	22·33±0·28	21·14±0·16	Y	N
495	13 41 39·03	00 8 59·21	16·94±0·26	—	—	—	—	–	–
496	13 41 42·01	00 9 0·39	16·00±0·12	19·55±0·04	21·80±0·11	20·34±0·06	18·64±0·03	Y	N
497	13 41 39·15	00 9 5·18	16·97±0·26	—	—	—	—	–	–
498	13 41 39·30	00 9 8·46	16·79±0·22	—	—	—	—	–	–
499	13 41 39·84	00 9 9·68	16·78±0·22	—	—	—	—	–	–
500	13 41 39·46	00 9 11·09	16·99±0·27	—	—	—	—	–	–
501	13 41 47·41	00 8 0·66	14·95±0·07	17·54±0·03	19·55±0·05	18·39±0·03	Saturated	Y	Y
502	13 41 51·16	00 8 17·33	17·42±0·36	—	—	—	—	–	–
503	13 41 53·73	00 4 1·71	17·14±0·30	—	—	—	—	–	–
504	13 41 46·77	00 4 20·06	16·76±0·23	—	—	21·64±0·21	—	–	–
505	13 41 49·86	00 4 23·79	15·88±0·11	19·36±0·04	21·68±0·17	20·23±0·06	18·55±0·03	Y	Y
506	13 41 46·24	00 4 47·46	17·00±0·28	—	—	—	—	–	–
507	13 41 49·17	00 5 2·81	16·70±0·22	—	—	—	—	–	–
508	13 41 47·30	00 5 12·23	17·17±0·31	—	—	—	—	–	–
509	13 41 49·63	00 1 50·15	17·26±0·34	—	—	—	—	–	–
510	13 41 49·08	00 1 50·57	16·96±0·27	—	—	—	—	–	–
511	13 41 50·78	00 1 57·15	17·18±0·33	—	—	21·67±0·20	—	–	–
512	13 41 50·64	00 2 8·41	17·13±0·33	—	—	—	—	–	–
513	13 41 50·41	00 2 12·30	16·92±0·28	—	—	—	—	–	–
514	13 41 48·38	00 2 15·79	16·63±0·21	—	—	—	21·27±0·26	–	–
515	13 41 50·20	00 2 29·18	15·38±0·09	16·72±0·03	17·66±0·04	17·08±0·03	Saturated	N	Y
516	13 41 46·82	00 2 31·24	17·07±0·30	—	—	—	—	–	–
517	13 41 51·18	00 2 30·90	17·19±0·33	—	—	—	—	–	–

ID	RA	DEC	K	R	B	V	I	G	R
518	13 41 51·29	00 2 34·08	17·06±0·31	—	—	—	—	–	–
519	13 41 50·06	00 2 45·04	17·19±0·35	—	—	—	—	–	–
520	13 41 50·80	00 2 48·65	16·29±0·17	18·41±0·03	19·77±0·04	18·90±0·04	17·91±0·02	N	N
521	13 41 50·73	00 2 53·24	16·76±0·24	—	—	—	—	–	–
522	13 41 50·08	00 2 58·07	16·82±0·25	—	—	—	—	–	–
523	13 41 50·26	00 3 6·88	17·17±0·33	—	—	—	—	–	–
524	13 41 50·53	00 3 21·05	16·61±0·21	—	—	—	—	–	–
525	13 41 50·29	00 3 21·54	16·83±0·25	—	—	—	—	–	–
526	13 41 58·67	00 10 32·01	14·37±0·06	Saturated	17·26±0·04	16·53±0·03	Saturated	N	Y
527	13 41 55·80	00 10 37·07	17·33±0·36	—	—	—	—	–	–
528	13 41 59·82	00 10 42·35	16·14±0·14	17·25±0·03	18·11±0·04	17·64±0·03	Saturated	N	N
529	13 41 55·13	00 11 13·39	17·28±0·35	—	—	—	—	–	–
530	13 41 55·64	00 11 20·53	16·90±0·25	—	—	—	—	–	–
531	13 41 56·08	00 7 23·41	17·00±0·26	—	—	—	—	–	–
532	13 41 56·94	00 7 40·36	17·37±0·35	—	—	—	—	–	–
533	13 41 56·10	00 7 47·38	15·37±0·08	20·24±0·07	22·84±0·24	21·36±0·12	18·04±0·03	Y	N
534	13 41 58·53	00 8 5·53	15·18±0·07	17·95±0·03	20·09±0·05	18·87±0·03	16·97±0·02	N	Y
535	13 42 2·16	00 8 22·61	17·05±0·28	—	—	—	—	–	–
536	13 42 0·04	00 3 35·78	17·40±0·36	21·42±0·16	—	—	20·54±0·14	–	–
537	13 41 56·79	00 3 43·30	17·39±0·35	—	—	—	—	–	–
538	13 42 −0·01	00 3 44·42	17·15±0·30	18·59±0·03	19·47±0·05	18·92±0·03	18·24±0·03	N	N
539	13 41 59·88	00 3 47·58	16·89±0·23	—	20·62±0·06	—	—	–	–
540	13 41 59·51	00 3 48·31	17·01±0·26	—	—	—	—	–	–
541	13 41 58·10	00 3 52·05	13·61±0·05	Saturated	Saturated	Saturated	Saturated	N	N
542	13 42 0·09	00 3 52·10	16·99±0·26	—	—	—	—	–	–
543	13 41 59·12	00 4 3·05	17·35±0·34	—	—	—	—	–	–
544	13 41 58·64	00 4 5·16	15·10±0·07	—	—	—	—	–	–
545	13 41 59·09	00 4 11·44	16·67±0·19	20·32±0·07	22·38±0·20	20·91±0·10	19·55±0·05	Y	N
546	13 41 58·07	00 4 25·50	16·73±0·21	—	—	—	—	–	–
547	13 41 56·51	00 4 28·64	16·17±0·14	18·49±0·03	20·10±0·05	19·14±0·04	17·78±0·02	N	Y
548	13 41 57·93	00 4 31·94	17·17±0·29	—	—	—	—	–	–
549	13 41 58·86	00 4 33·89	17·17±0·30	—	—	—	—	–	–
550	13 41 54·03	00 5 2·38	13·89±0·05	16·71±0·03	18·39±0·04	17·26±0·03	16·03±0·02	Y	N
551	13 41 56·34	00 5 15·51	14·47±0·06	17·20±0·03	19·13±0·04	17·98±0·03	Saturated	N	N
552	13 41 58·18	00 3 2·56	14·49±0·06	Saturated	17·49±0·04	16·74±0·03	Saturated	N	Y
553	13 40 55·34	00 3 5·79	17·24±0·33	—	—	—	—	–	–
554	13 40 53·51	00 3 30·67	17·22±0·32	—	—	—	—	–	–
555	13 40 53·05	00 3 36·25	17·33±0·37	—	—	—	—	–	–
556	13 41 23·20	−00 3 7·76	15·97±0·13	19·95±0·05	22·62±0·22	—	—	Y	N
557	13 41 23·36	−00 2 42·28	16·84±0·25	—	—	—	—	–	–
558	13 41 21·46	−00 2 39·26	15·21±0·08	Saturated	17·82±0·04	—	—	N	Y
559	13 41 15·37	−00 5 45·58	16·89±0·26	20·55±0·08	21·77±0·12	—	—	Y	N
560	13 41 15·21	−00 5 9·83	16·73±0·22	—	—	—	—	–	–
561	13 41 13·35	−00 5 5·49	17·06±0·30	—	—	—	—	–	–
562	13 41 12·80	−00 5 0·88	17·33±0·36	—	—	—	—	–	–
563	13 41 14·96	−00 4 57·47	15·30±0·08	17·91±0·03	19·84±0·04	—	—	N	Y
564	13 41 13·26	−00 4 53·49	17·30±0·36	—	—	—	—	–	–

ID	RA	DEC	K	R	B	V	I	G	R
565	13 41 27·62	00 1 4·74	15·49±0·09	17·16±0·03	18·20±0·04	—	—	N	Y
566	13 41 24·09	00 1 15·70	17·17±0·31	—	—	—	—	–	–
567	13 41 24·18	00 1 25·09	17·34±0·36	—	—	—	—	–	–
568	13 41 25·44	00 1 44·10	17·10±0·30	—	—	—	—	–	–
569	13 41 25·97	00 1 58·06	16·75±0·24	20·75±0·08	23·06±0·30	—	—	Y	N
570	13 41 26·62	−00 3 26·00	16·22±0·16	19·89±0·04	20·63±0·06	—	—	N	N
571	13 41 28·95	−00 3 23·13	17·19±0·34	—	—	—	—	–	–
572	13 41 25·89	−00 3 16·57	16·87±0·25	—	—	—	—	–	–
573	13 41 25·82	−00 3 3·64	16·42±0·19	—	—	—	—	–	–
574	13 40 53·29	−00 4 24·33	14·91±0·07	17·82±0·03	19·79±0·04	—	—	Y	N
575	13 40 57·14	−00 4 13·12	15·52±0·09	19·03±0·03	21·50±0·08	—	—	N	N
576	13 40 56·59	−00 4 13·26	15·59±0·09	17·36±0·03	18·77±0·04	—	—	N	N
577	13 40 53·61	−00 4 11·13	14·15±0·05	Saturated	Saturated	—	—	N	N
578	13 40 53·48	−00 3 40·85	15·89±0·12	19·05±0·03	21·09±0·06	—	—	Y	Y
579	13 40 55·25	−00 3 33·14	15·21±0·08	—	—	—	—	–	–
580	13 41 0·81	00 1 11·24	17·10±0·27	19·70±0·04	21·62±0·09	—	—	N	N
581	13 41 0·84	00 1 20·41	17·16±0·27	22·57±0·28	—	—	—	–	–
582	13 40 58·05	00 1 44·83	17·19±0·28	—	—	—	—	–	–
583	13 41 0·55	00 1 59·47	15·07±0·07	Saturated	18·29±0·04	—	—	N	Y
584	13 40 57·57	00 2 3·07	17·39±0·33	—	—	—	—	–	–
585	13 40 58·85	00 2 10·43	17·28±0·30	21·75±0·14	22·84±0·23	—	—	–	–
586	13 40 59·14	−00 1 45·76	16·10±0·13	Saturated	17·78±0·04	—	—	N	Y
587	13 40 58·18	−00 1 36·11	17·24±0·33	—	—	—	—	–	–
588	13 40 56·61	−00 1 10·90	17·15±0·31	—	—	—	—	–	–
589	13 41 4·94	−00 3 23·54	14·99±0·07	17·94±0·03	20·04±0·04	—	—	N	Y
590	13 41 7·13	−00 3 7·68	17·19±0·33	22·07±0·26	—	—	—	–	–
591	13 41 6·52	−00 2 44·34	16·90±0·26	—	—	—	—	–	–
592	13 41 7·64	−00 2 40·91	17·26±0·35	—	—	—	—	–	–
593	13 41 7·59	−00 2 37·73	16·74±0·23	—	—	—	—	–	–
594	13 41 7·45	−00 2 32·63	16·51±0·20	—	—	—	—	–	–
595	13 41 6·12	−00 2 30·79	17·10±0·31	—	—	—	—	–	–
596	13 41 12·35	00 3 1·31	16·30±0·23	20·57±0·06	22·73±0·22	—	—	Y	N
597	13 41 14·77	00 3 20·79	9·80±0·05	Saturated	Saturated	—	—	N	N
598	13 41 14·78	00 3 28·73	14·37±0·06	—	—	—	—	–	–
599	13 41 12·79	00 3 25·72	14·28±0·06	—	—	—	—	–	–
600	13 41 12·54	00 3 28·99	14·88±0·08	—	—	—	—	–	–
601	13 41 12·29	00 3 38·79	14·47±0·07	Saturated	Saturated	—	—	N	Y
602	13 41 11·70	−00 0 31·21	17·35±0·32	—	—	—	—	–	–
603	13 41 8·56	−00 0 31·50	17·38±0·33	—	—	—	—	–	–
604	13 41 10·41	−00 0 30·22	17·21±0·30	—	—	—	—	–	–
605	13 41 9·38	−00 0 26·63	17·05±0·26	21·17±0·11	22·93±0·25	—	—	Y	N
606	13 41 11·09	−00 0 27·57	17·26±0·31	—	—	—	—	–	–
607	13 41 8·85	−00 0 20·32	16·39±0·16	—	—	—	—	–	–
608	13 41 10·15	−00 0 16·48	16·88±0·23	—	—	—	—	–	–
609	13 41 8·71	−00 0 12·92	13·91±0·05	16·89±0·03	18·77±0·04	—	—	Y	N
610	13 41 12·21	−00 0 0·57	16·33±0·15	19·66±0·04	21·99±0·13	—	—	Y	N
611	13 41 9·56	00 0 5·38	17·03±0·26	20·02±0·04	21·92±0·12	—	—	Y	N

ID	RA	DEC	K	R	B	V	I	G	R
612	13 41 11·83	00 0 13·09	16·11±0·13	18·84±0·03	20·83±0·06	—	—	N	Y
613	13 41 8·96	00 0 12·39	15·86±0·11	19·29±0·04	22·02±0·12	—	—	Y	N
614	13 41 10·31	00 0 16·52	17·02±0·26	—	—	—	—	–	–
615	13 41 8·62	−00 4 10·92	16·79±0·24	—	—	—	—	–	–
616	13 41 10·21	−00 4 2·61	14·95±0·07	18·73±0·03	21·19±0·08	—	—	N	Y
617	13 41 6·83	−00 4 0·12	17·18±0·32	—	—	—	—	–	–
618	13 41 9·08	−00 3 54·93	17·04±0·28	—	—	—	—	–	–
619	13 41 7·60	−00 3 46·75	16·31±0·16	19·44±0·04	20·96±0·06	—	—	Y	N
620	13 41 9·83	−00 3 44·27	17·33±0·36	20·12±0·05	21·55±0·09	—	—	Y	N
621	13 41 6·86	−00 3 33·73	14·72±0·06	17·80±0·03	19·39±0·04	—	—	Y	N
622	13 41 9·60	−00 3 22·16	17·28±0·34	—	—	—	—	–	–
623	13 41 9·99	−00 3 20·60	16·70±0·22	—	—	—	—	–	–
624	13 41 9·97	−00 3 9·61	16·84±0·24	—	—	—	—	–	–
625	13 41 8·20	−00 3 8·86	17·07±0·29	—	—	—	—	–	–
626	13 41 21·30	00 1 46·83	15·85±0·12	17·82±0·03	19·66±0·04	—	—	Y	Y
627	13 41 20·80	00 2 11·02	16·26±0·16	19·48±0·04	22·26±0·16	—	—	Y	N
628	13 41 22·70	00 2 25·15	15·13±0·08	—	—	—	—	–	–
629	13 40 53·87	00 9 51·69	15·00±0·07	17·12±0·03	18·83±0·04	—	—	N	Y
630	13 40 53·86	00 10 1·23	15·27±0·08	18·83±0·03	21·33±0·08	—	—	N	N
631	13 40 55·25	00 10 33·47	16·87±0·26	—	—	—	—	–	–
632	13 40 54·48	00 10 37·68	17·17±0·32	—	—	—	—	–	–
633	13 41 7·31	00 14 5·03	17·20±0·32	—	—	—	—	–	–
634	13 41 6·66	00 14 9·35	17·31±0·36	—	—	—	—	–	–
635	13 41 8·07	00 14 18·93	16·89±0·25	20·07±0·06	22·23±0·22	—	—	Y	N
636	13 41 8·12	00 14 28·58	17·18±0·31	20·71±0·11	—	—	—	Y	N
637	13 41 4·26	00 14 39·73	14·91±0·07	16·64±0·03	17·92±0·04	—	—	Y	Y
638	13 41 5·32	00 14 46·50	16·84±0·23	—	—	—	—	–	–
639	13 40 55·21	00 12 26·70	15·81±0·10	18·00±0·03	19·28±0·04	—	—	Y	N
640	13 40 53·83	00 13 9·31	17·08±0·27	—	—	—	—	–	–
641	13 40 57·07	00 13 8·22	14·39±0·06	18·26±0·03	20·55±0·05	—	—	N	Y
642	13 40 53·30	00 13 10·07	17·08±0·28	—	—	—	—	–	–
643	13 40 59·71	00 9 42·93	16·54±0·19	18·60±0·03	20·65±0·05	—	—	N	Y
644	13 40 58·42	00 9 54·21	17·02±0·28	—	—	—	—	–	–
645	13 41 2·82	00 8 13·86	15·14±0·07	17·82±0·03	20·00±0·04	—	—	N	Y
646	13 41 3·14	00 5 56·14	17·36±0·33	—	—	—	—	–	–
647	13 41 1·58	00 5 59·00	17·30±0·32	—	—	—	—	–	–
648	13 41 2·35	00 6 2·39	14·90±0·06	—	—	—	—	–	–
649	13 41 0·67	00 6 0·44	14·73±0·06	19·22±0·03	21·81±0·12	—	—	N	N
650	13 41 0·20	00 6 8·32	16·78±0·21	20·38±0·05	—	—	—	Y	N
651	13 41 0·06	00 6 18·41	16·45±0·16	18·57±0·03	20·14±0·05	—	—	N	Y
652	13 41 9·64	00 11 7·07	16·06±0·14	19·36±0·04	19·84±0·05	—	—	Y	N
653	13 41 11·59	00 11 21·35	17·27±0·34	—	—	—	—	–	–
654	13 41 10·20	00 11 27·25	16·54±0·21	21·23±0·13	22·91±0·27	—	—	Y	N
655	13 41 9·79	00 11 29·96	16·57±0·21	—	—	—	—	–	–
656	13 41 10·07	00 11 31·69	16·68±0·22	—	—	—	—	–	–
657	13 41 13·30	00 11 34·57	16·81±0·25	—	—	—	—	–	–
658	13 41 12·46	00 11 43·35	15·23±0·08	—	—	—	—	–	–

ID	RA	DEC	K	R	B	V	I	G	R
659	13 41 10·10	00 11 47·22	16·98±0·27	—	—	—	—	–	–
660	13 41 10·03	00 11 50·13	16·62±0·21	—	—	—	—	–	–
661	13 41 13·19	00 11 53·14	14·75±0·06	18·91±0·03	21·38±0·08	—	—	N	Y
662	13 41 9·93	00 12 0·74	16·79±0·25	—	—	—	—	–	–
663	13 41 12·09	00 12 2·89	15·07±0·07	—	—	—	—	–	–

B REDSHIFTS AND SPECTRA

This appendix lists the redshifts measured in the spectroscopic survey and presents plots of all the galaxy spectra.

The table overleaf lists for each galaxy the ID, K magnitude, R magnitude, redshift, type (whether emission line or absorption line or both) and spectral features. These features include the principle ones used to determine the redshift (see section 4.4.1), as well as weaker ones thought to be present when the spectra were smoothed and examined carefully. Doubtful features are marked with a question mark. Where only a few features were present, and the redshift was backed up by a significant cross-correlation peak, this is indicated. Note all the spectra with strong features features had large CCF peaks (see section 4.4.2). The errors on the redshifts are omitted to save space. This was because they were all similar, with typical $\Delta z \simeq 0.0005$ and the maximum being $\Delta z \simeq 0.001$ for the fainter spectra (again see sections 4.4.1 and 4.4.2).

Following the table the IDs of all the stellar spectra are listed, followed by plots (9 pages) of all the galaxy spectra listed in the table. For ease of reference the galaxy spectra are sorted into ID order. This was done regardless of whether the galaxy ID referred to the October or March catalogue as, coincidentally, the subset of galaxy spectra have no overlapping IDs.

Each spectra is labelled with catalogue, ID number and redshift. The X axis is *observed* wavelength rather than rest wavelength — it was felt that this was more appropriate bearing in mind that one or two of the redshifts could be wrong. Also this ensures that the sky features appear at the same wavelengths in all the spectra. Note while the *AUTOFIB* spectra have the sky absorption bands divided out the LDSS spectra do not (see chapter 4 for reasons). It can also be seen from the residual sky *emission* lines that the sky-subtraction is much less accurate with *AUTOFIB* than with LDSS, because of the use of fibres rather than slits. Note also that some of the *AUTOFIB* spectra consist of different wavelength ranges, observed on different nights with different exposure times. These were joined together, hence the noise level can be discontinuous across the spectra.

Mask	ID	K	R	Redshift	Ty	Spectral Features
AFB	11	14.25 ± 0.05	17.84 ± 0.04	0.1291	A	Mg b, Na D.
	73	15.48 ± 0.07	18.67 ± 0.04	0.1480	A	Hβ, Mg b, 5268 Å, Na D.
	91	15.83 ± 0.09	19.00 ± 0.04	0.1905	A	Mg b, 5268 Å, X^{n}*.
	120	15.69 ± 0.08	19.00 ± 0.05	0.2103	A	Mg b, 5268 Å, X^{n}.
	149	15.03 ± 0.06	— †	0.0738	E	Hα, [NII], [SII].
	159	13.30 ± 0.05	16.28 ± 0.04	0.0732	A	Mg b, 5268 Å, Na D.
	169	15.73 ± 0.10	18.94 ± 0.04	0.1496	A	Hβ, Mg b, 5268 Å, Na D.
	173	15.39 ± 0.09	18.48 ± 0.04	0.1267	A	Hβ, Mg b, Na D.
	190	15.93 ± 0.09	19.82 ± 0.04	0.3870	A	K, H, Hβ, Mg b, 5268 Å.
	198	16.00 ± 0.09	19.31 ± 0.04	0.2902	A	Hβ, G?, Mg b, 5268 Å, X^{n}.
	253	15.13 ± 0.07	18.84 ± 0.04	0.3008	A	4000 Å break, G, Hβ, Mg b, 5268 Å.
	510	15.23 ± 0.06	17.96 ± 0.04	0.0880	E	Na D (abs), Hα, [NII], [SII].
	517	14.85 ± 0.05	18.22 ± 0.04	0.1305	E	Hβ, [OIII] 5007 Å, Na D (abs), Hα.
	540	15.63 ± 0.07	18.58 ± 0.04	0.1900	A	Hβ, Mg b, X^{n}.
	558	15.43 ± 0.07	17.80 ± 0.04	0.1186	A	G, Mg b, 5268 Å, Na D.
	563	14.40 ± 0.05	18.09 ± 0.04	0.0803	E	Hα, [NII], [SII].
	568	14.38 ± 0.05	18.04 ± 0.04	0.1563	A	G, Hβ, Mg b, 5268 Å, Na D.
	571	15.20 ± 0.08	18.50 ± 0.04	0.1686	A	G, Hβ, Mg b, Na D.
	574	15.16 ± 0.06	18.78 ± 0.04	0.2860	A	4000 Å break, G, Hβ, Mg b, 5268 Å.
	576	15.42 ± 0.08	19.32 ± 0.04	0.2870	A	4000 Å break, G, Hβ, Mg b.
K1	24	16.08 ± 0.11	18.48 ± 0.04	0.0749	E	Hβ, [OIII] 4959 Å, [OIII] 5007 Å, Hα, [NII], [SII].
	31	15.90 ± 0.09	20.20 ± 0.05	0.6660	A	4000 Å break, K, H.
	54	16.96 ± 0.17	20.68 ± 0.06	0.2780	EA	[OII] 3727 Å (em), Hη, K, H, Hδ, Hβ (em), Mg b.
	56	16.74 ± 0.15	19.87 ± 0.05	0.2780	EA	[OII] 3727 Å (em), Hη, K, H, Hδ, G, Hβ (abs/em), [OIII] 5007 Å (em), Mg b, 5268 Å.

* "X^{n}" is short for "significant cross-correlation peak".

† This field not covered in R.

Mask	ID	K	R	Redshift	Ty	Spectral Features
K5	281	16.97 ± 0.16	19.42 ± 0.04	0.2100	E	Hα (very strong).
	323	16.93 ± 0.17	19.20 ± 0.04	0.3205	E	[OII] 3727 Å, Hγ, Hβ, [OIII] 4959 Å, [OIII] 5007 Å.
	316	16.80 ± 0.13	21.50 ± 0.09	0.6760	A	K, H, 4000 Å break, Hδ.
	317	15.20 ± 0.06	17.94 ± 0.04	0.1237	A	Hβ, G, Mg b, 5268 Å, Na D.
	320	16.63 ± 0.12	18.79 ± 0.04	0.1236	E	Hβ, [OIII] 5007 Å, Hα, [NII], [SII].
	329	15.75 ± 0.10	19.33 ± 0.04	0.1530	A	Hβ, Mg b, 5268 Å, Na D.
	291	16.96 ± 0.20	20.36 ± 0.05	0.3800	E	NeV 3426 Å?, [OII] 3727 Å, Hβ.
	295	15.36 ± 0.07	18.42 ± 0.04	0.2356	A	K, H, 4000 Å break, G, Hβ, Mg b, 5268 Å.
	312	14.97 ± 0.06	18.51 ± 0.04	0.2356	A	K, H, 4000 Å break, Hδ, G, Hβ, Mg b, 5268 Å, Na D.
	314	17.02 ± 0.18	20.06 ± 0.05	0.4706	A	K, H, 4000 Å break, G, 4384 Å.
K6	363	16.32 ± 0.10	19.36 ± 0.04	0.6630	A	K, H, 4000 Å break, Hδ.
	341	16.66 ± 0.14	19.82 ± 0.04	0.3440	EA	Hζ?, K, 4000 Å break, Hδ?, Hβ (em), G.
K7	462	15.22 ± 0.08	17.95 ± 0.04	0.0801	A	K, H, Mg b?, 5268 Å, Na D.
	431	15.67 ± 0.09	18.13 ± 0.04	0.0760	E	Hα, [NII], [SII].
	432	15.42 ± 0.08	18.04 ± 0.04	0.0804	E	[OIII] 5007 Å?, Hα, [NII], [SII].
	406	14.28 ± 0.05	18.18 ± 0.04	0.1206	A	K, H, G, Hβ.
	434	14.23 ± 0.05	17.25 ± 0.04	0.0797	A	Na D, Hα.
	454	16.82 ± 0.13	20.28 ± 0.05	0.3760	A	K, H, G, Hβ.
	455	15.77 ± 0.07	18.77 ± 0.04	0.2062	A	K, H, G, Hβ, Mg b, 5268 Å.
	457	17.10 ± 0.17	20.83 ± 0.06	0.5510	A	Hη, K, H, 4000 Å break.
	418	15.05 ± 0.07	17.74 ± 0.04	0.0789	A	Na D, Hα.
	422	15.66 ± 0.07	19.15 ± 0.04	0.1125	A	Hβ, Mg b, Na D, 5268 Å, X^n.
	411	14.43 ± 0.06	17.39 ± 0.04	0.0846	A	Mg b, Na D, 5268 Å, Hα.
	423	15.27 ± 0.06	17.95 ± 0.04	0.0800	A	Hβ, Mg b?, 5268 Å.

Mask	ID	K	R	Redshift	Ty	Spectral Features
F5	550	13.89 ± 0.05	16.71 ± 0.03	0.0877	A	K, H, G, Mg b, 5268 Å, Na D.
	459	16.20 ± 0.14	19.85 ± 0.05	0.4082	EA	[OII] 3727 Å (em), Hη, 3879 Å+Hζ, K, H?, G, Hβ (em).
	445	16.89 ± 0.27	20.00 ± 0.05	0.2551	A	K, H, G, Hβ, Mg b, 5268 Å.
	446	16.15 ± 0.15	20.22 ± 0.05	0.3698	A	K, H, G?, Mg b.
	450	16.38 ± 0.18	20.24 ± 0.05	0.4299	E	[OII] 3727 Å, Hβ, [OIII] 5007 Å.

The following objects in the individual fields were identified as stars spectroscopically. Their ID's, only, are listed for brevity. The full list of positions and magnitudes can be obtained by cross-referencing the IDs with the table in Appendix A.

AFB: 5, 6, 12, 16, 20, 23, 25, 29, 35, 36, 37, 38, 41, 51, 75, 89, 92, 94, 107, 145, 152, 163, 167, 172, 175, 176, 179, 187, 191, 194, 201, 210, 215, 216, 217, 218, 225, 228, 233, 236, 240, 242, 245, 246, 247, 251, 252, 255, 258, 261, 262, 402, 439, 448, 464, 468, 470, 471, 472, 473, 476, 484, 495, 497, 500, 532, 534, 549, 556, 569, 572, 575.

K1: 29, 33, 34, 35, 36, 37, 38, 41, 46, 60.

K5: 274, 290, 303, 307, 322, 328, 331.

K6: 338, 371, 375, 381, 382.

K7: 407, 408.

F5: 515, 528, 533, 547.

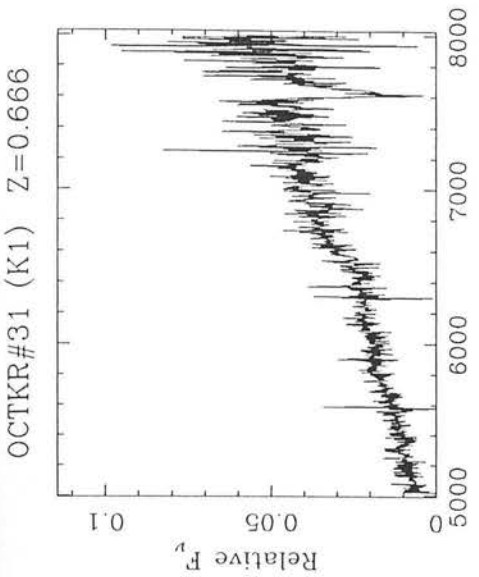
OCTKR#31 (K1) Z=0.666
Relative F_ν
Wavelength / Å

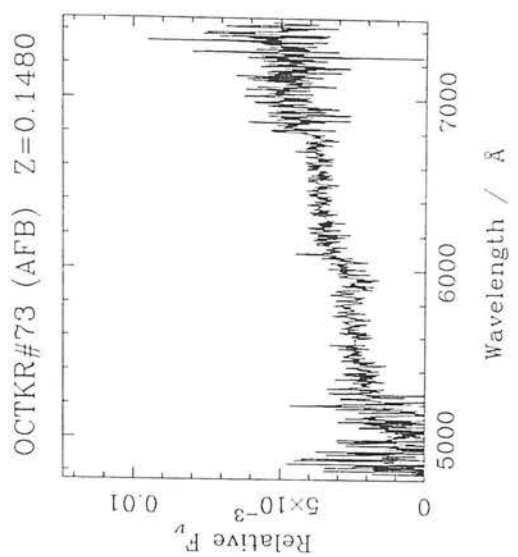
OCTKR#73 (AFB) Z=0.1480
Relative F_ν
Wavelength / Å

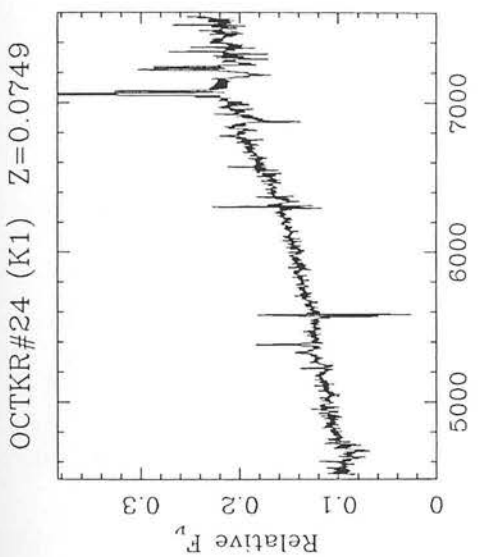
OCTKR#24 (K1) Z=0.0749
Relative F_ν
Wavelength / Å

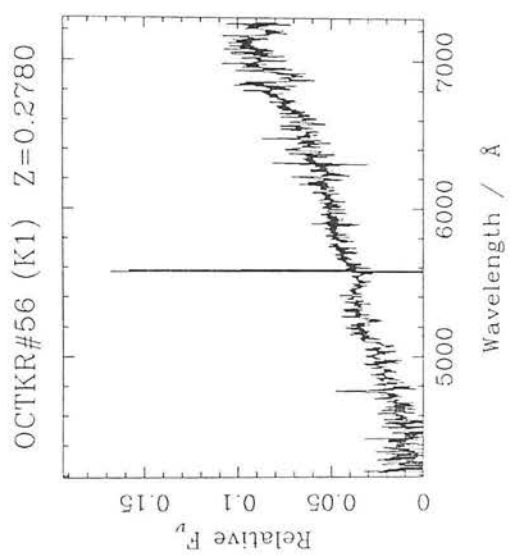
OCTKR#56 (K1) Z=0.2780
Relative F_ν
Wavelength / Å

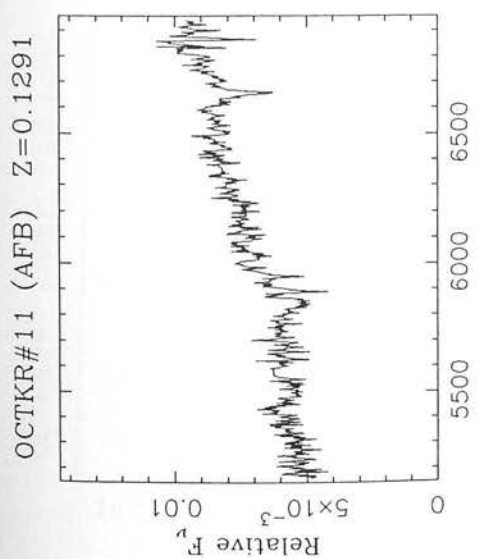
OCTKR#11 (AFB) Z=0.1291
Relative F_ν
Wavelength / Å

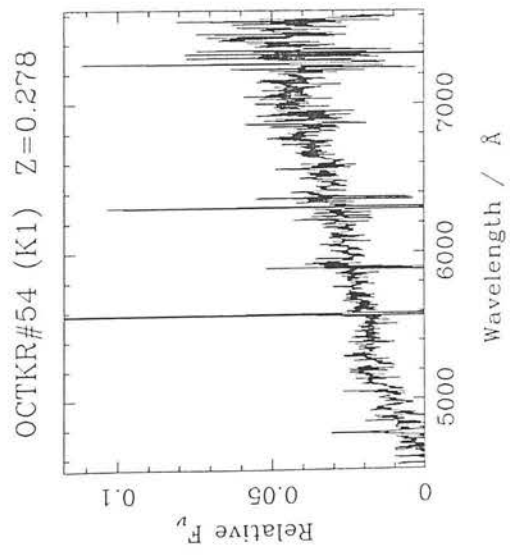
OCTKR#54 (K1) Z=0.278
Relative F_ν
Wavelength / Å

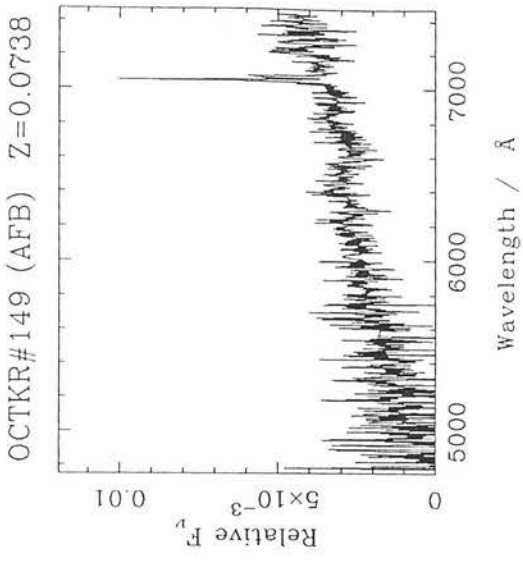
OCTKR#149 (AFB) Z=0.0738
Relative F_ν
0
5×10⁻³
0.01
5000
6000
7000
Wavelength / Å

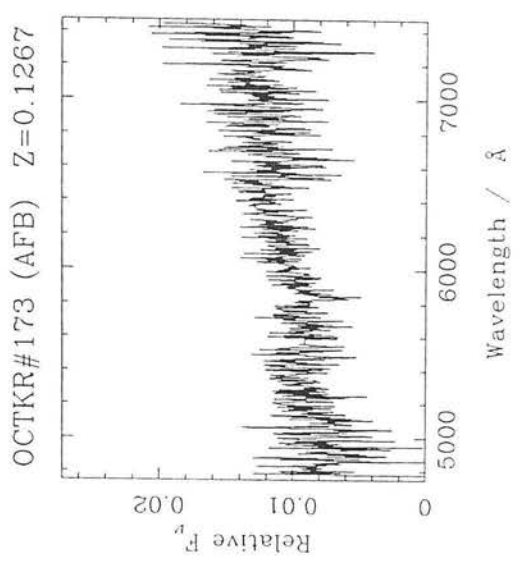
OCTKR#173 (AFB) Z=0.1267
Relative F_ν
0
0.01
0.02
5000
6000
7000
Wavelength / Å

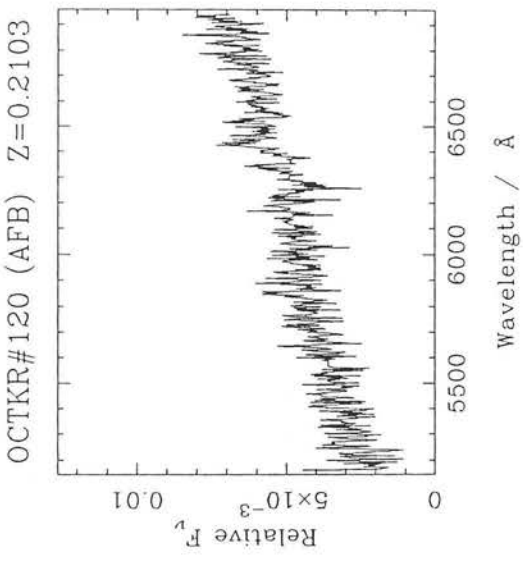
OCTKR#120 (AFB) Z=0.2103
Relative F_ν
0
5×10⁻³
0.01
5500
6000
6500
Wavelength / Å

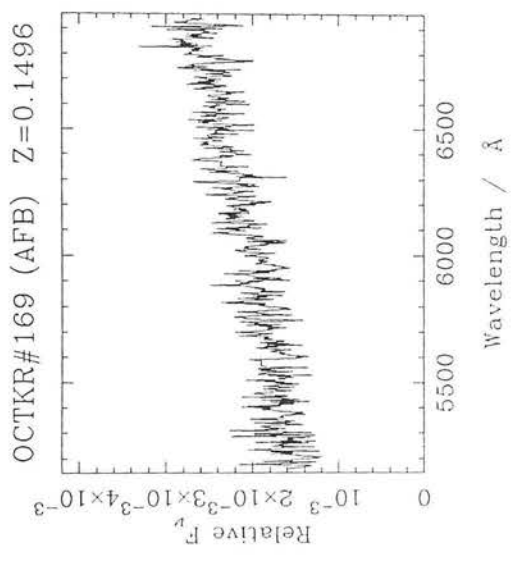
OCTKR#169 (AFB) Z=0.1496
Relative F_ν
0
10⁻³
2×10⁻³
3×10⁻³
4×10⁻³
5500
6000
6500
Wavelength / Å

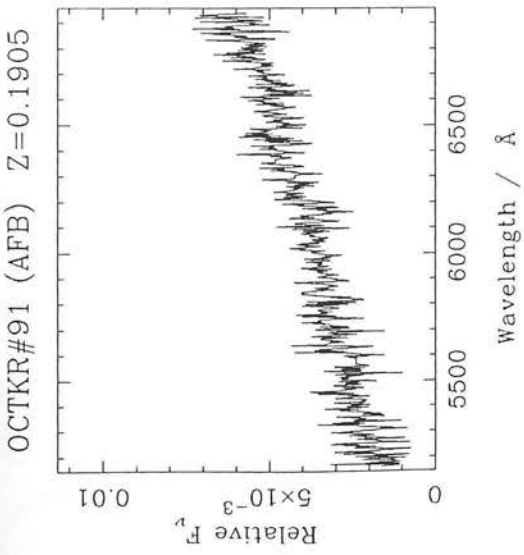
OCTKR#91 (AFB) Z=0.1905
Relative F_ν
0
5×10⁻³
0.01
5500
6000
6500
Wavelength / Å

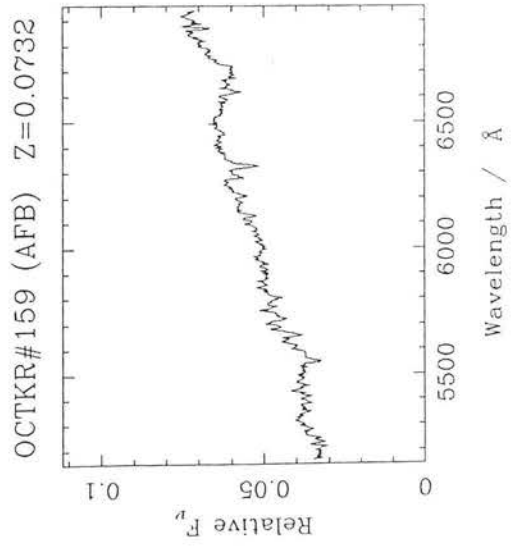
OCTKR#159 (AFB) Z=0.0732
Relative F_ν
0
0.05
0.1
5500
6000
6500
Wavelength / Å

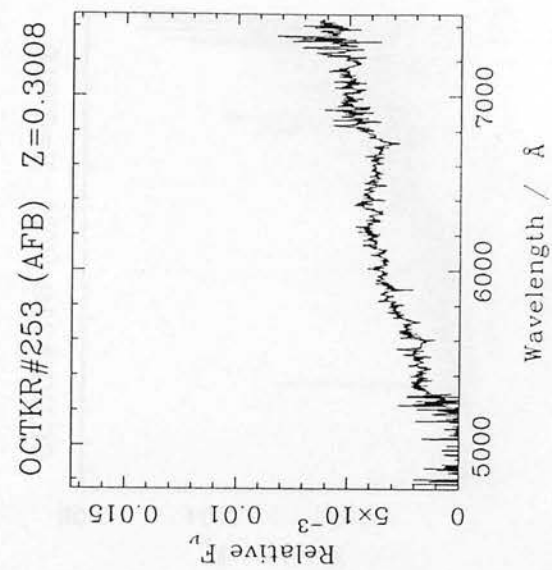
OCTKR#253 (AFB) Z=0.3008
Relative F_ν
0
5×10^{-3}
0.01
0.015
5000
6000
7000
Wavelength / Å

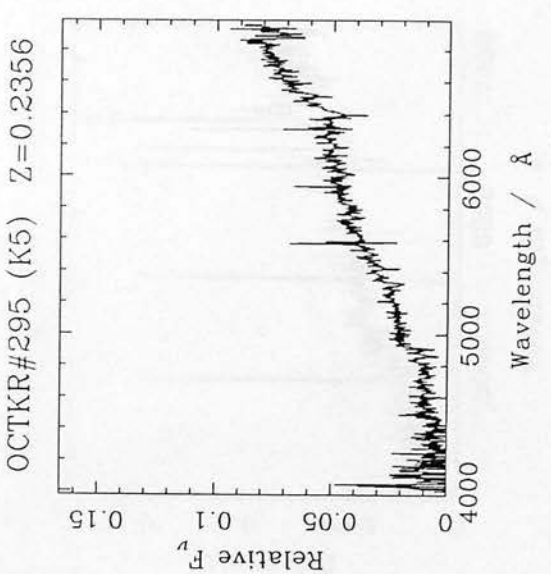
OCTKR#295 (K5) Z=0.2356
Relative F_ν
0
0.05
0.1
0.15
4000
5000
6000
Wavelength / Å

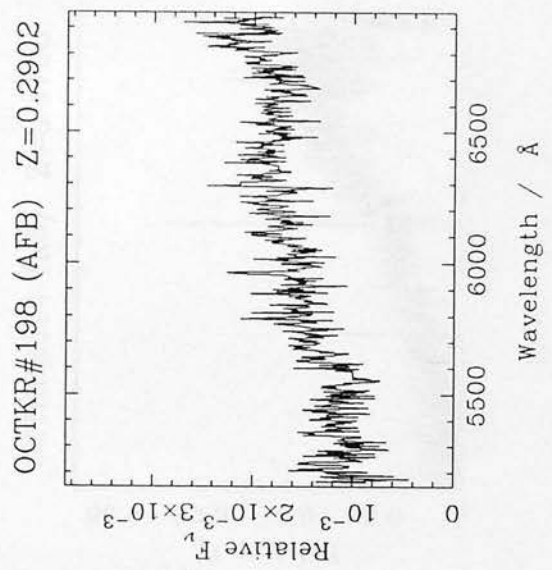
OCTKR#198 (AFB) Z=0.2902
Relative F_ν
0
10^{-3}
2×10^{-3}
3×10^{-3}
5500
6000
6500
Wavelength / Å

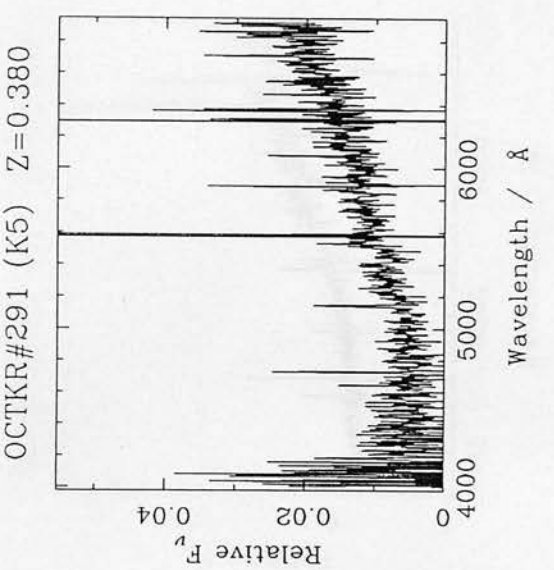
OCTKR#291 (K5) Z=0.380
Relative F_ν
0
0.02
0.04
4000
5000
6000
Wavelength / Å

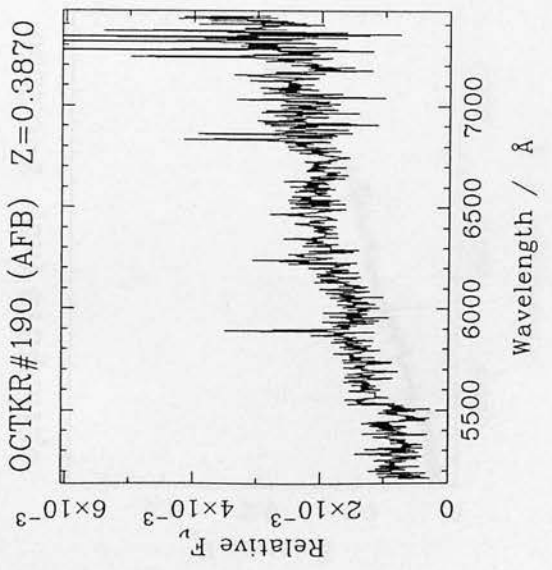
OCTKR#190 (AFB) Z=0.3870
Relative F_ν
0
2×10^{-3}
4×10^{-3}
6×10^{-3}
5500
6000
6500
7000
Wavelength / Å

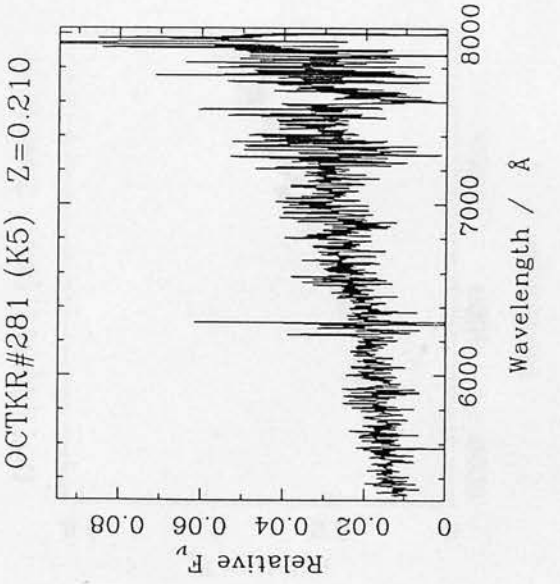
OCTKR#281 (K5) Z=0.210
Relative F_ν
0
0.02
0.04
0.06
0.08
6000
7000
8000
Wavelength / Å

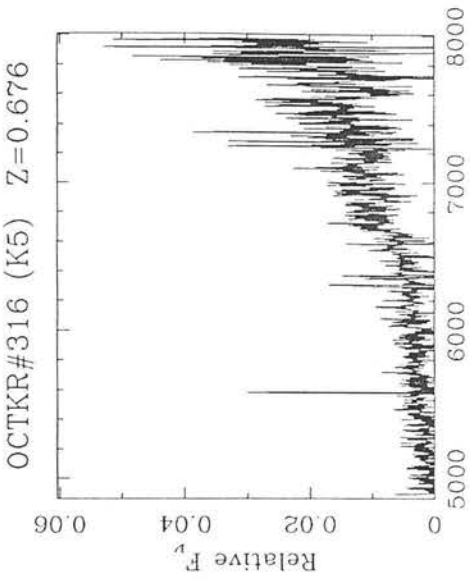
OCTKR#316 (K5) Z=0.676
Relative F_ν
Wavelength / Å

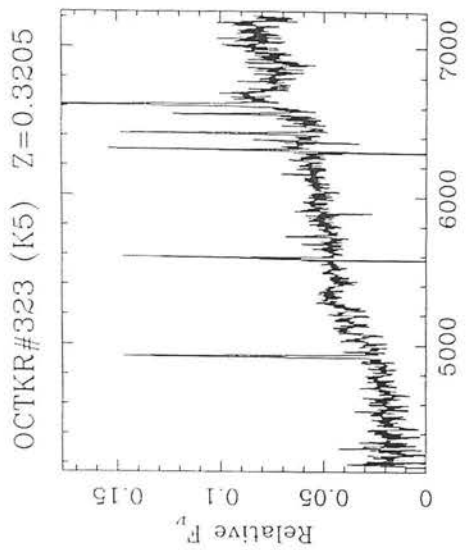
OCTKR#323 (K5) Z=0.3205
Relative F_ν
Wavelength / Å

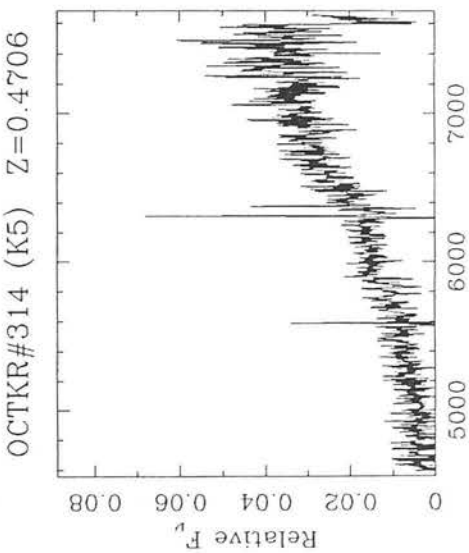
OCTKR#314 (K5) Z=0.4706
Relative F_ν
Wavelength / Å

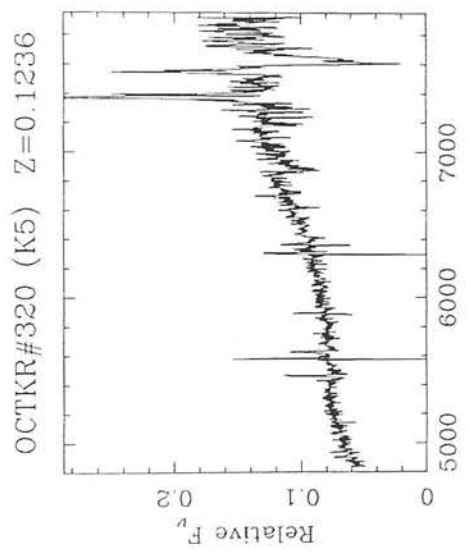
OCTKR#320 (K5) Z=0.1236
Relative F_ν
Wavelength / Å

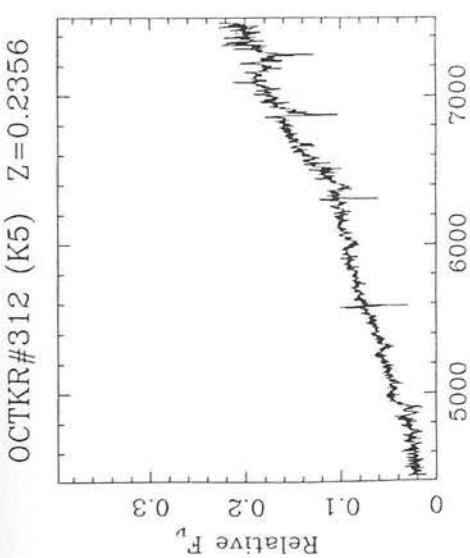
OCTKR#312 (K5) Z=0.2356
Relative F_ν
Wavelength / Å

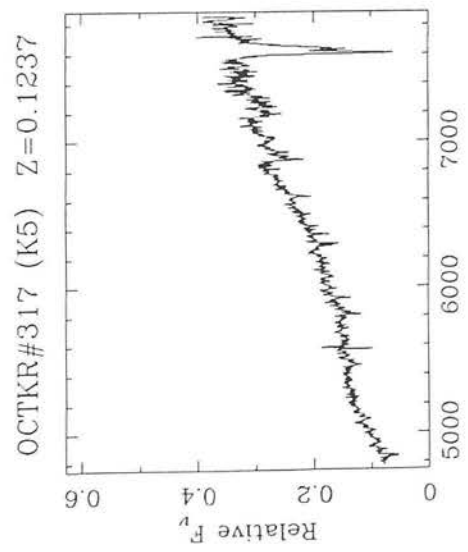
OCTKR#317 (K5) Z=0.1237
Relative F_ν
Wavelength / Å

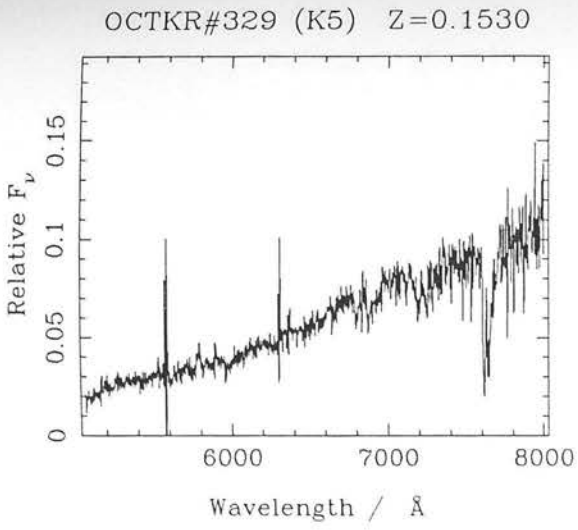
OCTKR#329 (K5) Z=0.1530
Relative F_ν
0
0.05
0.1
0.15
6000
7000
8000
Wavelength / Å

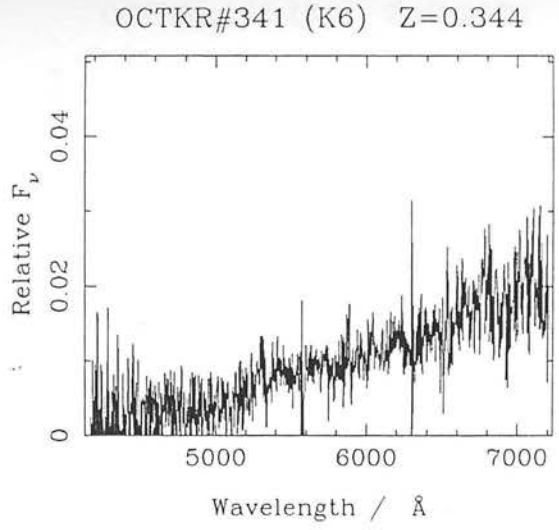
OCTKR#341 (K6) Z=0.344
Relative F_ν
0
0.02
0.04
5000
6000
7000
Wavelength / Å

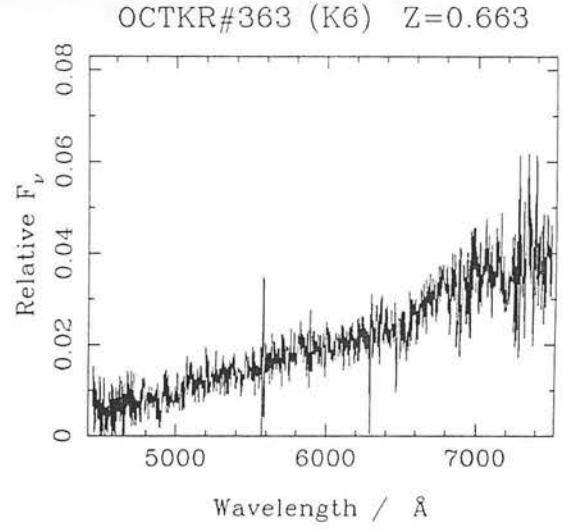
OCTKR#363 (K6) Z=0.663
Relative F_ν
0
0.02
0.04
0.06
0.08
5000
6000
7000
Wavelength / Å

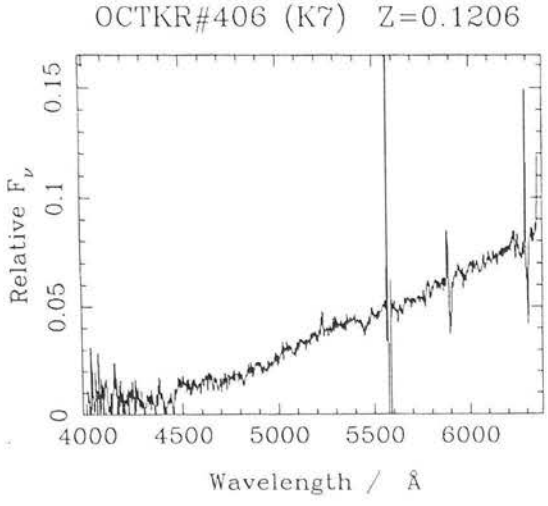
OCTKR#406 (K7) Z=0.1206
Relative F_ν
0
0.05
0.1
0.15
4000
4500
5000
5500
6000
Wavelength / Å

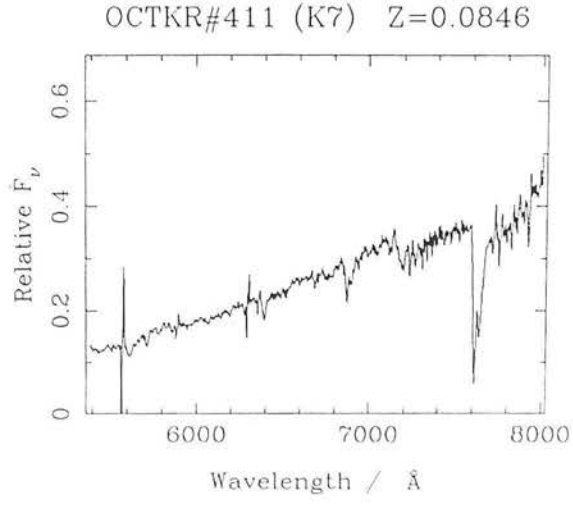
OCTKR#411 (K7) Z=0.0846
Relative F_ν
0
0.2
0.4
0.6
6000
7000
8000
Wavelength / Å

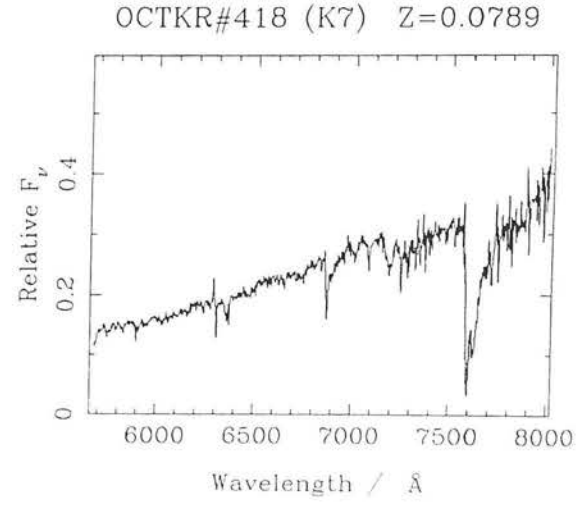
OCTKR#418 (K7) Z=0.0789
Relative F_ν
0
0.2
0.4
6000
6500
7000
7500
8000
Wavelength / Å

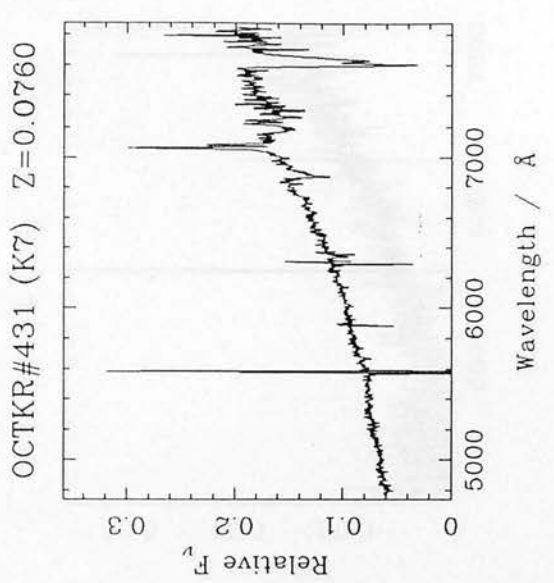
OCTKR#431 (K7) Z=0.0760
Relative F_ν
Wavelength / Å

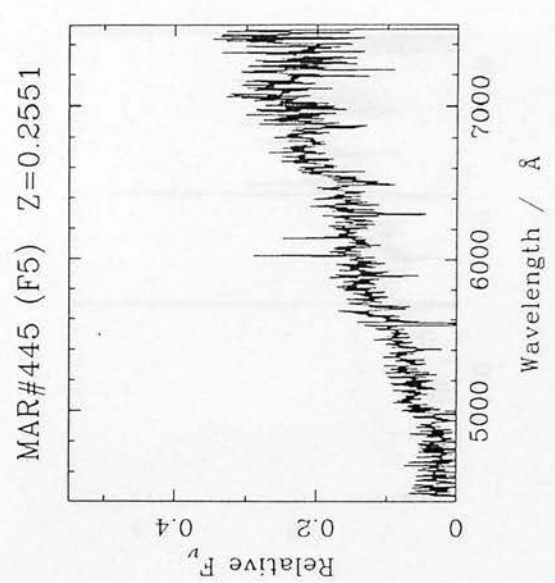
MAR#445 (F5) Z=0.2551
Relative F_ν
Wavelength / Å

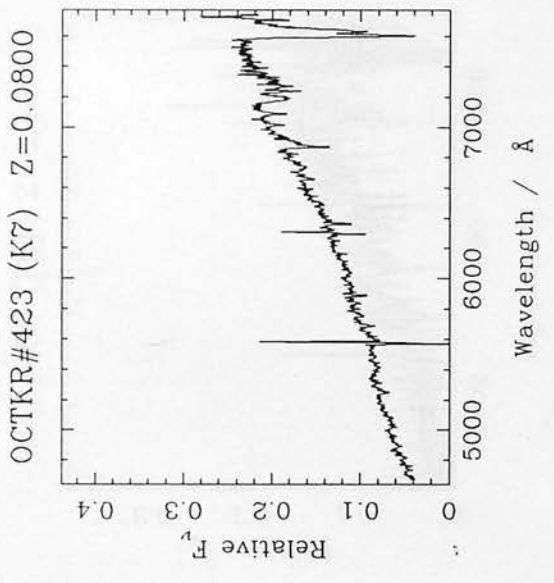
OCTKR#423 (K7) Z=0.0800
Relative F_ν
Wavelength / Å

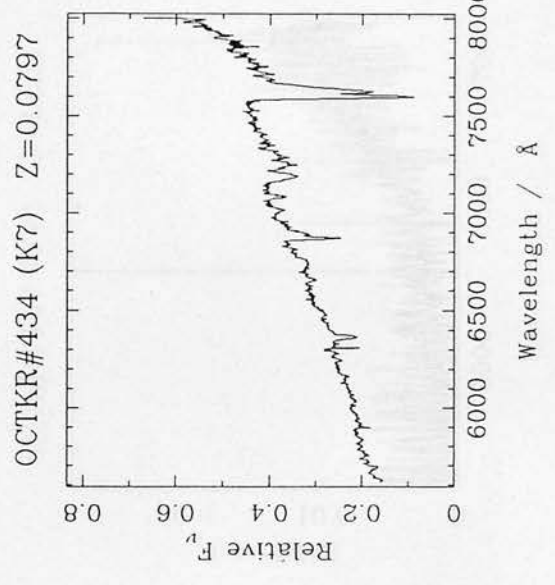
OCTKR#434 (K7) Z=0.0797
Relative F_ν
Wavelength / Å

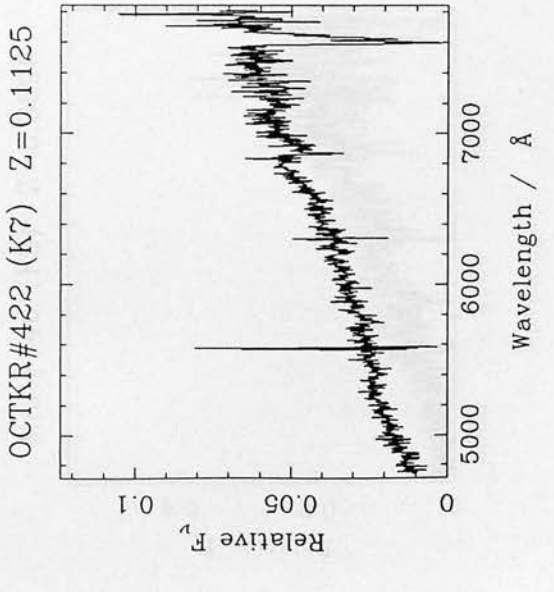
OCTKR#422 (K7) Z=0.1125
Relative F_ν
Wavelength / Å

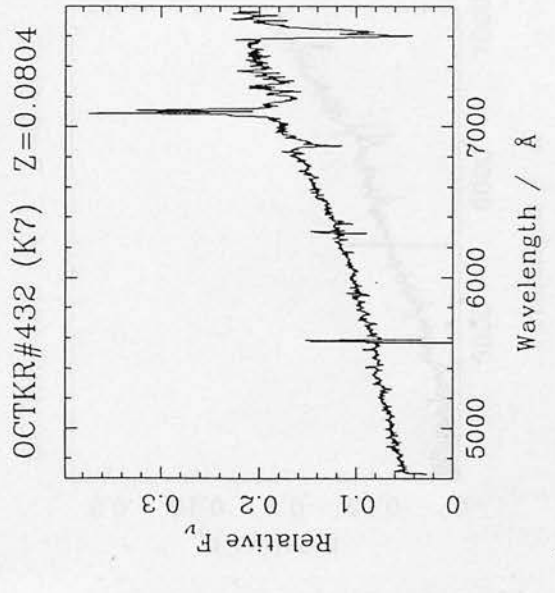
OCTKR#432 (K7) Z=0.0804
Relative F_ν
Wavelength / Å

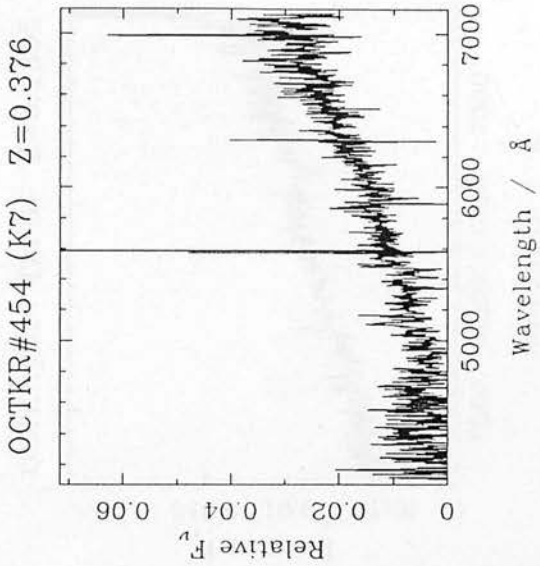
MAR#446 (F5) Z=0.3698
Relative F_ν
0
0.2
0.4
5000
6000
7000
Wavelength / Å

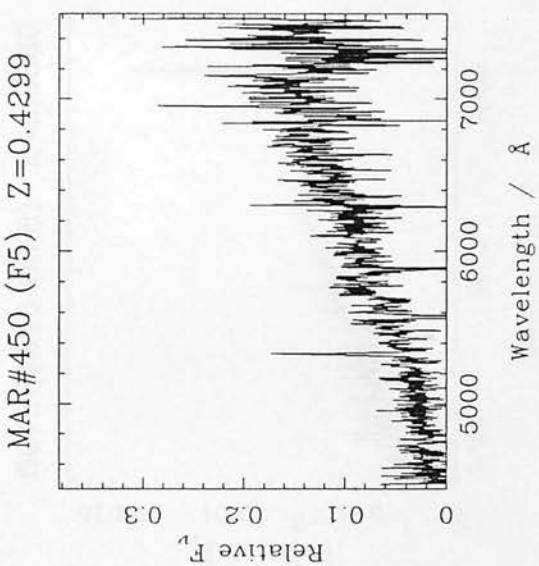
MAR#450 (F5) Z=0.4299
Relative F_ν
0
0.1
0.2
0.3
5000
6000
7000
Wavelength / Å

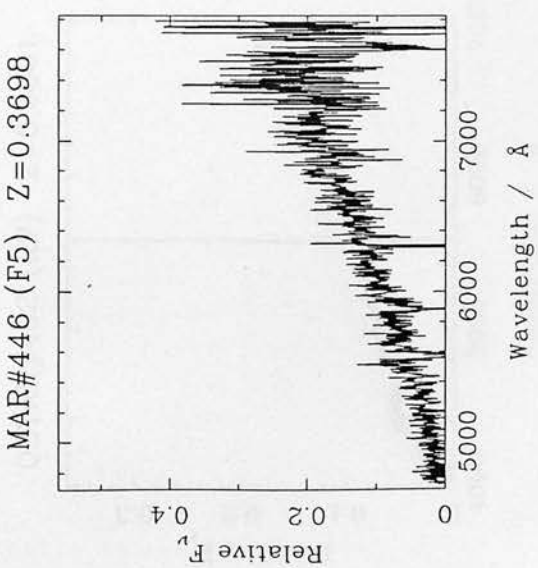
OCTKR#454 (K7) Z=0.376
Relative F_ν
0
0.02
0.04
0.06
5000
6000
7000
Wavelength / Å

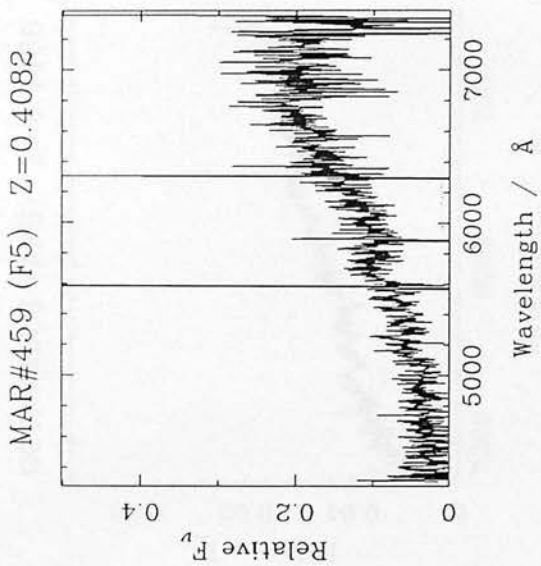
OCTKR#455 (K7) Z=0.2062
Relative F_ν
0
0.05
0.1
0.15
0.2
5000
6000
7000
Wavelength / Å

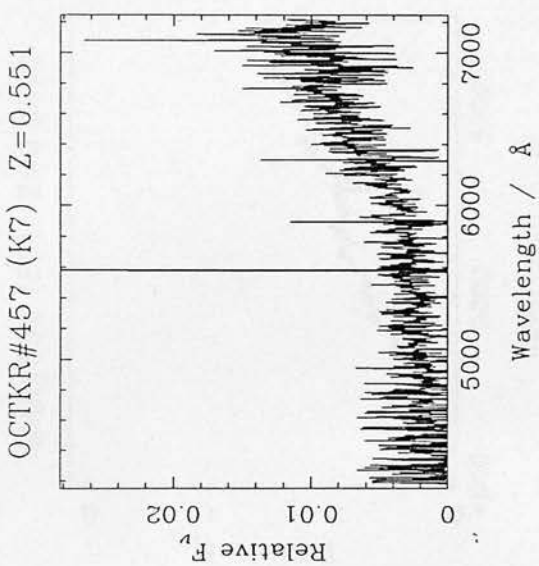
OCTKR#457 (K7) Z=0.551
Relative F_ν
0
0.01
0.02
5000
6000
7000
Wavelength / Å

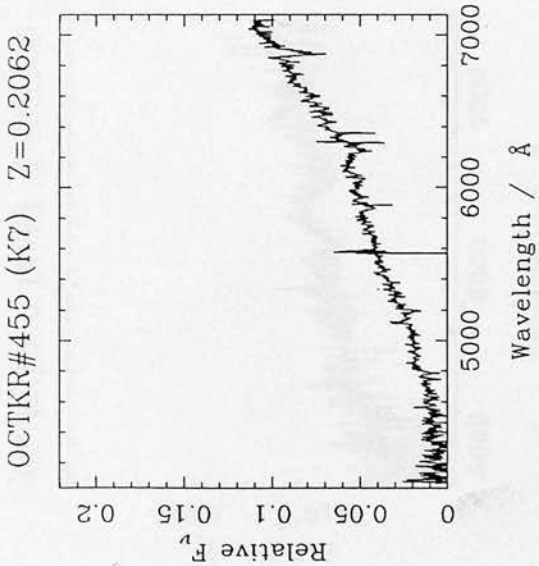
MAR#459 (F5) Z=0.4082
Relative F_ν
0
0.2
0.4
5000
6000
7000
Wavelength / Å

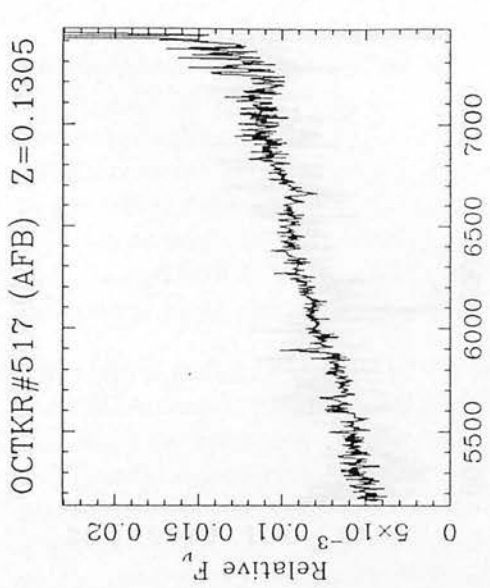
OCTKR#517 (AFB) Z=0.1305
Relative F_ν
Wavelength / Å

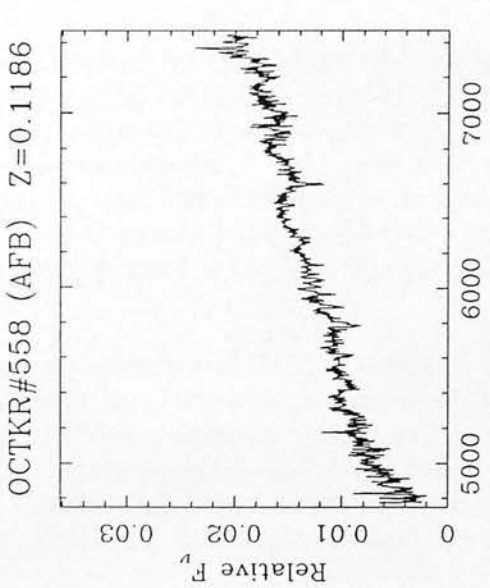
OCTKR#558 (AFB) Z=0.1186
Relative F_ν
Wavelength / Å

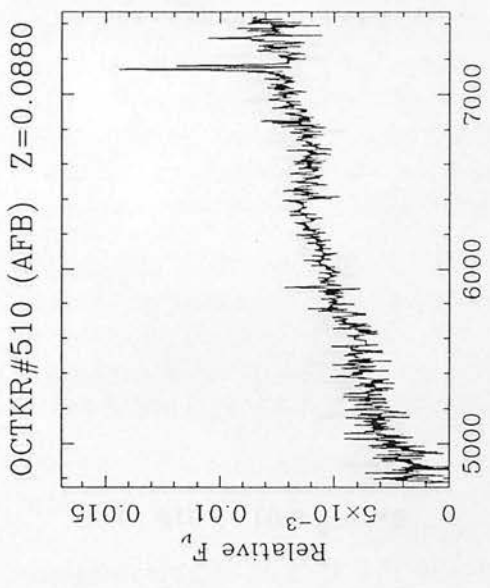
OCTKR#510 (AFB) Z=0.0880
Relative F_ν
Wavelength / Å

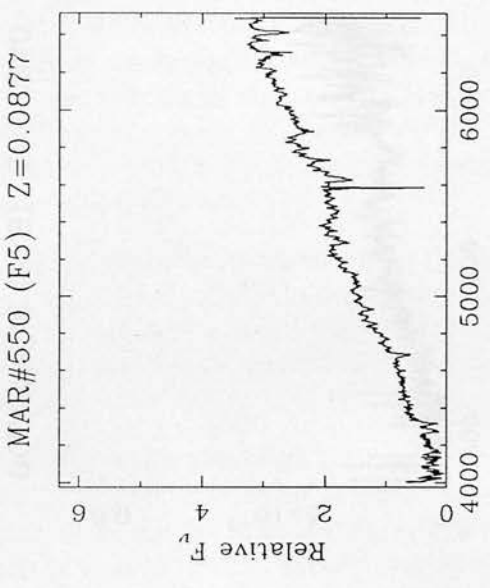
MAR#550 (F5) Z=0.0877
Relative F_ν
Wavelength / Å

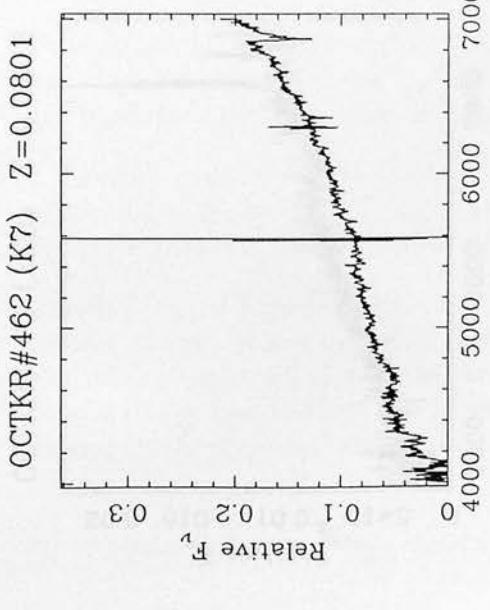
OCTKR#462 (K7) Z=0.0801
Relative F_ν
Wavelength / Å

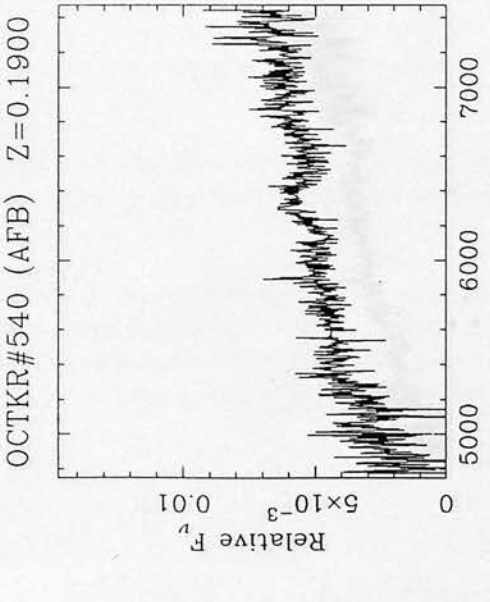
OCTKR#540 (AFB) Z=0.1900
Relative F_ν
Wavelength / Å

ACKNOWLEDGEMENTS

I would like to thank first of all my supervisor John Peacock for the support and guidance which made this work possible. He has also become a good friend over the years. I would like to specially thank him for many interesting and tangential conversations at coffee, for his tolerance of many foolish questions, and for being omnipotent. I owe a great deal, too, to my other mentors, Chris Collins and Lance Miller. Chris showed me that it really is possible to succeed in astronomy, despite being from Catford. Lance taught me how to observe and how to reduce data, and he set this grand project in motion. He also bought me several pints afterwards to make up.

Chapters 5 and 6 also suffered considerably from the presence of Tom Broadhurst, who arrived on the scene in the dying months of my Ph.D. and continually annoyed me with innumerable discussions about the "counts". James Dunlop deserves special mention for being such a great guy, for the many observations which he graciously volunteered, and for his work on the spectral evolution models on which much of my own work was based. I am also very grateful to Richard Ellis for giving me a job, and for his patience and understanding while I finished this thesis.

Of my contemporaries and good friends at ROE there are far too many to name them all. I owe much to Phil Blanco for many cups of coffee and wonderful conversations in the bewitching hours, and for his crazy sanity. Keef deserves mention for bringing new meaning to the word "nice". Sorry Keef. Thanks go to Richard Isadore Jane Davinia Agnes Teresa Dixon (hope that's right) for his room and much violence, to Steeeve for taking me to Schwartz's next September, to Philippe for many lifts home at 2 am, to Dave for innumerable pints, to Bob for his totally lousy impressions, and to Penny for discovering the aurora. I hope she gives me a good write up some day!

Turning to ROE the Next (female) Generation, special mention goes to Pippa for many interesting faces and for letting me feed her cat during a lonely Christmas, to Suzie for her wonderfully mellifluent accent and much healthy exercise, to Isabelle for being much cleverer than me, to Kath for liking my music, and finally to Bob II for being the token Mann (groan). I hope they forgive me for this.

Outside ROE special thanks go to Donald (wherever he is) for introducing me to J.J. Cale, which whiled away many a boring evening. Thanks also go to Mike for being a continual source of amazement, to Roger for not killing me, to Kevin for many pints, to Peter for the postcards, to Patrick for being even more boring than me, to Gina for being so mind-boggling and to all those at the Number Shop for giving me a refuge from astronomy, at a time when I needed it.

I would also like to take this opportunity to thank my parents for so much uncritical love and support over the years, in my varied travels. I so rarely get a chance to show my gratitude for everything they have done.

I am very grateful to the SERC for the provision of the Research Studentship which supported this work and to the taxpayers of this country for their continued support of astronomy, against all utilitarian reason.

Finally I would like to thank two individuals whom I have never met — Donald Knuth author of TEX with which this thesis was written; and Keith Shortridge, creator of the FIGARO package which enabled me to cope with all the astronomical data that threatened to overwhelm me. Both of these items provided a refreshing spark of intellectual elegance during these otherwise tedious chores.